Numerical Methods for Two-particle Fluctuations and Real-time Dynamics of Strongly Correlated Electron Systems

by

Xinyang Dong

A dissertation submitted in partial fulfillment
of the requirements for the degree of
Doctor of Philosophy
(Physics and Scientific Computing)
in the University of Michigan
2022

Doctoral Committee:

Associate Professor Emanuel Gull, Chair
Associate Professor Hugo U.R. Strand, Örebro University
Associate Professor Kai Sun
Associate Professor Dominika Zgid
Assistant Professor Liuyan Zhao

Xinyang Dong
dongxy@umich.edu
ORCID iD: 0000-0002-7414-8476

Acknowledgments

First of all, I would like to give my deepest appreciation to my advisor, Prof. Emanuel Gull, for his continued support during my Ph.D. He always helped me find the right ways of solving the problems I faced, and also told me everyone would make mistakes, so there is no need to overthink them. He gave me enough freedom to work on the things I'm interested in and learn the things I want to know.

My sincere gratitude also goes to Prof. Hugo U.R. Strand, who has been my collaborator and mentor since the third year of my Ph.D. He was patient with me at all times, and trained me in all aspects of research, including math, physics and programming. He always encouraged me to try out new things, and gave me valuable feedback on my work to help me improve. He was also the first reader of this thesis and provided me with detailed feedback for improvement. His rigorous attitude towards science affected me deeply, and will remain as a beneficent influence in my future career. I would also like to thank Dr. Igor Krivenko, who guided me to write my first C++ program, and taught me all sorts of technical skills. I would not be able to accomplish all my research projects without these tools.

Special thanks go to Dr. Sergei Iskakov and Dr. Jia Li, who were great officemates, and provided me help in both physics and programming. I also thank other members of the Gull Group: Dr. Markus Wallerberger, Dr. Joseph Kleinhenz, Chia-Nan Yeh, Runxue Yu, Thomas Blommel, Yang Yu, and Lei Zhang for their friendship and fruitful discussions. I would also like to express great appreciation to Dr. Ceren Burcak Dag, who was my student mentor in my first year at Michigan, and introduced me the life as a graduate student here.

I'm grateful for all the collaborators I had for my research projects: Prof. Andrew J. Millis, Prof. Alessandro Toschi, Prof. Dominika Zgid, Dr. Lorenzo Del Re and Dr. Xi Chen for sharing their knowledge in physics and chemistry. I also thank Prof. Kai Sun for the insightful discussions in theoretical physics.

I would like to thank my committee members: Prof. Hugo U.R. Strand, Prof. Kai Sun, Prof. Dominika Zgid, and Prof. Liuyan Zhao for their time.

Graduate studies at the University of Michigan are an important part of my life. I'm grateful for all the people I met here for the fond memories.

Lastly I would like to give my greatest appreciation to my parents for their unconditional

love. They let me be independent and supported all of my decisions since I was young. This accomplishment would not be possible without them.

Table of Contents

List of Figures

List of Tables

List of Algorithms

List of Appendices

List of Acronyms

AFM antiferromagnetic.

AGF2 auxiliary second-order Green's function perturbation theory.

AIM Anderson impurity model.

AO atomic orbital.

BdG Bogoliubov-de Gennes.

CBS continuous basis set.

CCSD coupled cluster singles doubles.

CCSD(T) coupled cluster singles doubles and non-iterative perturbative triples.

CCSD-EOM coupled cluster singles-doubles equation of motion.

CDMFT cellular dynamical mean-field theory.

CT-AUX continuous-time auxiliary-field Monte Carlo.

CT-HYB continuous-time hybridization expansion Monte Carlo.

CT-INT interaction-expansion continuous time quantum Monte Carlo.

CT-QMC continuous-time quantum Monte Carlo.

DΓA dynamical vertex approximation.

DCA dynamical cluster approximaiton.

DDW d density wave.

DF dual fermion approach.

DLR discrete Lehmann representation.

DMFT dynamical mean-field theory.

DSC $d-$wave superconductivity.

EA electron affinity.

ED exact diagonalization.

EKT extended Koopman's theorem.

FCI full configuration interaction.

GF2 self-consistent second-order Green's function perturbation theory.

HF Hartree-Fock.

IP ionization potential.

IR intermediate representation.

KT Koopman's theorem.

MaxEnt Maximum Entropy.

MP2 second-order Møller–Plesset perturbation theory.

NCA non-crossing approximation.

OCA one-crossing approximation.

PDW p density wave.

Abstract

This thesis contains a series of numerical studies of strongly correlated electron systems. In these systems, interesting emergent properties are brought about by strong electron correlations, leading to unusual fluctuations and phase transitions.

We start with a review of basic concepts in many-body physics from a field theory point of view, including second quantization and path integral formalisms. We then introduce extensions of the single-particle and two-particle Green's function formalisms in the singlet superconducting state, which enable us to extract physical information of the systems in the symmetry-broken phase.

Next, we proceed to the models and numerical methods we use to study the strongly correlated systems. We introduce a low energy effective model – the Hubbard model, which contains a subset of the electron degrees of freedom and can be solved numerically using advanced many-body methods. With the dynamical cluster approximation and continuous-time quantum Monte Carlo impurity solver, we are able to study the competing fluctuations in the paramagnetic state and analyze the fluctuations behind superconductivity in the singlet superconducting state.

We introduce self-consistent diagrammatic methods used in realistic material calculations in the last part of this thesis, with an outline of group theory concepts that can be used to optimize the simulations. Numerical representations and methods for effectively solving equations in realistic material calculations are discussed afterwards. We briefly review some of the developments in this field, and then introduce spectral methods that are based on mathematical properties of Legendre polynomials for solving both the imaginary- and real-time Dyson equations.

Chapter 1

Introduction

Strongly correlated systems, in which physical properties can not be described by one-particle processes or weak-coupling perturbation theory, have attracted increasing attention in the past few decades. Examples of such systems include high temperature superconductors [1], heavy fermion materials [2], and transition metal oxides [3] in which a wide range of emergent phenomena arise from strong electronic interactions. The development of advanced quantum many-body methods for treating the strongly correlated systems is a vivid field of research, and remarkable progress has been achieved on both the theoretical and experimental sides. The core physical quantities in theoretical calculations of these systems are the single- and two-particle Green's functions [4–7]. The single-particle Green's functions describe the propagation of one-electron addition-removal excitations. They can be used to explain experimental results such as electronic spectral functions obtained by angle-resolved photoemission spectroscopy [8]. The theoretical analysis of results from a broader range of experimental techniques such as nuclear magnetic resonance [9], optical spectroscopy [10], and Raman spectroscopy [11] requires two-particle Green's functions, which describe the propagation of excitations associated with a pair of particles.

Despite the progress made in the studies of strongly correlated systems, a large gap still lies between what is observed in experiment and what theories can predict. The theoretical difficulties come from the fact that emergent properties of these systems are not just a simple accumulation of individual quantities, but are brought about by the strong electron-electron interaction. The analytical solution of the Schrödinger equation becomes unreachable for systems with a large number of electrons since the wave function scales exponentially with the number of electrons. A common approach of dealing with this difficulty is to extract a few important degrees of freedom and construct a low-energy effective model. While the effective models still cannot be solved analytically due to the non-perturbative parameter regime relevant to the materials, the models can be solved perturbatively or numerically exactly with advanced many-body methods.

A minimal model that describes many of the salient features of strongly correlated systems is the Hubbard model [12], which includes the motion of electrons in a kinetic energy term and local interactions in the potential energy term. While unable to describe excitations involving high-lying orbitals, this model reproduces much of the low-energy phenomenology observed in experiments on high-temperature superconductors [13, 14]. To solve the Hubbard model, commonly used numerical techniques include diagonalization, diagrammatics, tensor networks, variational methods, series expansion, Monte Carlo, and embedding methods [14]. The dynamical mean-field theory (DMFT) [15], which maps the Hubbard model onto the Anderson impurity model subject to a non-interacting self-consistent bath, provides a powerful tool in the understanding of correlated physics in the Hubbard model. While DMFT is only exact in the limit of infinite coordination number, where quantum fluctuations become purely local, it can successfully capture phenomena such as the Mott metal-insulator transition. To improve on the critical flaw of neglecting the effects of non-local fluctuations in DMFT, extensions such as quantum cluster theories [16], the dual fermion approach (DF) [17], and the dynamical vertex approximation (DΓA) [18] have been proposed. Quantum cluster theories such as dynamical cluster approximaiton (DCA) [19], cellular dynamical mean-field theory (CDMFT) [20] reduce the complexity of the lattice problem by mapping it to a finite-size cluster self-consistently embedded in a dynamical mean-field [16]. The non-local short-range correlations are treated explicitly within the cluster and the long-range correlations are treated on a dynamical mean-field level. The momentum dependent Green's functions provided by the quantum cluster theories give access to features such as the pseudogap and *d*-wave superconductivity [16]. The main limitation of quantum cluster theories come from neglecting long-range fluctuations, which for the two-dimensional Hubbard model yield transitions to ordered states that are forbidden by the Mermin-Wagner theorem [21]. These ordered states, such as the anti-ferromagnetic symmetry breaking in two-dimensional systems, are usually manually suppressed in actual simulations. The capabilities and limitations of quantum cluster theories are explained in detail in Ref. [16]. To solve the cluster impurity problems given by quantum cluster theories, numerical techniques with approximations at different levels have been developed. Commonly used approaches include exact diagonalization (ED) [22], which discretizes the continuous bath into a few sites and performs diagonalization of the whole system; non-crossing approximation (NCA) [23] and one-crossing approximation (OCA) [24, 25], which resum a particular subset of diagrams; as well as various Monte Carlo techniques such as continuous-time quantum Monte Carlo (CT-QMC) [26]. For a review of the impurity solvers see Refs. [15, 16, 26].

While able to drastically reduce the problem size, the analysis of the strongly correlated systems with models will contain systematic uncertainties. Therefore, in addition to the model Hamiltonian approach, ab-initio simulations of solids with “real”, rather than “model”, parameters are also widely used for the study of strongly correlated systems. In ab-initio simulations, a more generalized realistic Hamiltonian is usually solved by perturbation theories and their extensions. The increasing problem size in the simulation of realistic systems requires efficient representations of the Green’s functions and efficient numerical methods for computing mathematical formulas such as derivatives, integrals, and convolutions. This has been an active field of research in both applied mathematics and computational physics.

This thesis includes research topics related with both the simulations of model Hamiltonians, and the simulations of realistic systems.

Chapter 2 reviews basic concepts in non-relativistic quantum field theory that are used in the derivations of this thesis. Chapter 3 provides a detailed analysis of the single- and two-particle Green’s functions in the case of singlet superconducting symmetry breaking. The generalized susceptibilities, vertex functions, and their relations to physical observables are also explained in detail. Chapter 4 starts with introducing the two models: Hubbard model and Anderson impurity model (AIM) that are commonly used in the simulation of strongly correlated system. One of the numerical methods in quantum cluster theories, DCA, is then derived in detail. The generalization of a CT-QMC impurity solver, continuous-time auxiliary-field Monte Carlo (CT-AUX) [27], in the singlet superconducting state is then presented.

The next three chapters summarize simulation results of the two-dimensional single-band Hubbard model within eight-site DCA. Chapter 5 focuses on the analysis of competing fluctuations in the paramagnetic state by comparing the intensity of magnetic, charge, and superconducting fluctuations with different symmetries. Chapter 6 presents the quantified strength of the electron-spin coupling in the singlet superconducting state, and tests the applicability of the one-loop spin fluctuation theory. Chapter 7 analyze the mechanism behind the superconducting order with a generalized fluctuation diagnostic method [28].

The last part of the thesis focuses on the simulation of realistic systems. Chapter 8 introduces the electronic Hamiltonian with realistic basis sets, the self-consistent methods based on low-order diagrams, and the optimizations given by point group symmetry. Chapter 9 provides a brief overview of the developments of compact representations of the Green’s functions and algorithms for solving the Dyson equation. Detailed derivations of the spectral methods for solving the Dyson equation in both imaginary- and real-time and their applications are then presented.

Publications

This thesis is based on work from the following publications:

- **X. Dong**, E. Gull, H.U.R. Strand: *Excitations and spectra from equilibrium real-time Green's functions*, arXiv:2206.04181 (2022).
- **X. Dong**, L. Del Re, A. Toschi, and E. Gull: *Mechanism of Superconductivity in the Hubbard Model at Intermediate Interaction Strength*, arXiv:2205.06286 (2022).
- **X. Dong**, E. Gull, A.J. Millis: *Quantifying the Role of Antiferromagnetic Fluctuations in the Superconductivity of the Doped Hubbard Model*, arXiv:2202.10577 (2022).
- **X. Dong**, E. Gull: *Short-range charge fluctuations in the two-dimensional Hubbard model*, Phys. Rev. B 101, 195115 (2020).
- **X. Dong**, D. Zgid, E. Gull, H.U.R. Strand: *Legendre-spectral Dyson equation solver with super-exponential convergence*, J. Chem. Phys. 152, 134107 (2020).
- **X. Dong**, X. Chen, E. Gull: *Dynamical Charge Susceptibility in the Hubbard Model*, Phys. Rev. B 100, 235107 (2019).

Chapter 2

Field Theory

This chapter summarizes many-body field theory concepts and equations that will be used in the derivations of this thesis. The summary closely follows Ref. [5], and is constrained to the non-symmetry-broken case.

2.1 Many-body Hamiltonian and second quantization

Within the Born-Oppenheimer approximation, without relativistic effects, the Hamiltonian of a quantum many-body problem with N_e electrons in the potential field given by N_I nuclei can be written as

$$\begin{aligned} H &= \sum_{i=1}^{N_e} \left[-\frac{\nabla_{r_i}^2}{2m_e} - \sum_{I=1}^{N_n} \frac{Z_I}{|R_I - r_i|} \right] + \sum_{i=1}^{N_e} \sum_{j=i+1}^{N_e} \frac{1}{|r_i - r_j|} \\ &= \sum_{i=1}^{N_e} h(r_i) + \sum_{i=1}^{N_e} \sum_{j=i+1}^{N_e} \frac{1}{|r_i - r_j|} \,, \end{aligned} \tag{2.1}$$

where r_i and R_I are position coordinates of electrons and nuclei, m_e is the electronic mass, and Z_I is the atomic numbers of the nuclei. The wave function Ψ of the system is the solution of the Schrödinger equation

$$i\partial_t|\Psi\rangle = H|\Psi\rangle \,. \tag{2.2}$$

To avoid the complexity of having $n!$ terms in the wave function of n indistinguishable particles, we introduce the Fock state (occupation number basis) which only counts the number of particles in a specific state, and the field operators that create ($\psi_\sigma^\dagger(r)$) or annihilate ($\psi_\sigma(r)$) a particle with spin σ at position r. To ensure the anti-symmetric property of fermion wave functions, the fermionic field operators obey the anti-commutation relations

$$\{\psi_\sigma(r), \psi_{\sigma'}(r')\} = 0\,, \quad \{\psi_\sigma(r), \psi^\dagger_{\sigma'}(r')\} = \delta_{\sigma\sigma'}\delta(r-r')\,. \tag{2.3}$$

With the field operators, the Hamiltonian in Eq. 2.1 can be expressed in a second-quantized form as

$$\begin{aligned} H = & \sum_\sigma \int dr \psi^\dagger_\sigma(r) \left[-\frac{\nabla^2_r}{2m_e} - \sum_{I=1}^{N_n} \frac{Z_I}{|R_I - r|} \right] \psi_\sigma(r) \\ & + \frac{1}{2} \sum_{\sigma\sigma'} \iint dr_1 dr_2 \psi^\dagger_\sigma(r_1) \psi^\dagger_{\sigma'}(r_2) \frac{1}{|r_1 - r_2|} \psi_{\sigma'}(r_2) \psi_\sigma(r_1)\,. \end{aligned} \tag{2.4}$$

The field operator $\psi_\sigma(r)$ can be expanded with a set of real space single-particle basis functions $\phi_i(r)$

$$\psi_\sigma(r) = \sum_i \phi_i(r) c_{i\sigma}\,, \tag{2.5}$$

where $c_{i\sigma}$ is the second-quantized fermionic annihilation operator which annihilate an electron in basis function ϕ_i with spin σ. Inserting this expansion in Eq. 2.4, the Hamiltonian can be written as

$$H = \sum_{ij} \sum_\sigma h_{ij} c^\dagger_{i\sigma} c_{j\sigma} + \frac{1}{2} \sum_{ijkl} \sum_{\sigma\sigma'} U_{ijkl} c^\dagger_{i\sigma} c^\dagger_{k\sigma'} c_{l\sigma'} c_{j\sigma}\,, \tag{2.6}$$

where h_{ij} is the kinetic and electron-nuclei integral

$$h_{ij} = \int dr \phi^*_i(r) \left[-\frac{\nabla^2_r}{2m_e} - \sum_{I=1}^{N_n} \frac{Z_I}{|R_I - r|} \right] \phi_j(r)\,, \tag{2.7}$$

and U_{ijkl} is the Coulomb repulsion integral

$$U_{ijkl} = \iint dr_1 dr_2 \phi^*_i(r_1) \phi^*_k(r_2) \frac{1}{|r_1 - r_2|} \phi_l(r_2) \phi_j(r_1)\,. \tag{2.8}$$

In general, the basis functions $\phi_i(r)$ are non-orthogonal, with the overlap integral

$$S_{ij} = \int dr \phi^*_i(r) \phi_j(r)\,. \tag{2.9}$$

The anti-commutation relation of the operators $c_{i\sigma}$ can be obtained by inverting Eq. 2.5

$$c_{i\sigma} = \sum_j (S^{-1})_{ij} \int dr \phi_j^*(r) \psi_\sigma(r) \,, \quad \Rightarrow \quad \{c^\dagger_{i\sigma}, c_{j\sigma}\} = (S^{-1})_{ij} \delta_{\sigma\sigma'} \,. \tag{2.10}$$

For simplicity, we will use orthonormal basis functions, where $S = \mathbb{I}$, and omit S in the derivations until chapter 8. Using $S = \mathbb{I}$, the anti-commutation relation between operators in orthonormal basis follows

$$\{c^\dagger_{i\sigma}, c_{j\sigma}\} = \delta_{ij} \delta_{\sigma\sigma'} \,. \tag{2.11}$$

2.2 Coherent state path integral

The coherent state path integral formalism provides a powerful tool in the derivation of many-body theories. It is based on the Feynmann path integral [29], and represents the partition function Z by an integral over field configurations. This section introduces basic concepts of the coherent state path integral formalism that will be useful in later derivations.

2.2.1 Coherent states and Grassmann algebra

A fermionic coherent state $|\eta\rangle$ is defined as an eigenstate of all annihilation operators c_α

$$c_\alpha |\eta\rangle = \eta_\alpha |\eta\rangle \,, \tag{2.12}$$

where $c_\alpha = c_{i\sigma}$, and α is a combined index for both spin σ and site (orbital) i that labels the single particle state $\alpha \equiv (i, \sigma)$. The eigenvalues η_α are anti-commuting Grassmann numbers

$$c_\alpha c_\beta |\eta\rangle = -c_\beta c_\alpha |\eta\rangle \,, \quad \Rightarrow \quad \eta_\alpha \eta_\beta |\eta\rangle = -\eta_\beta \eta_\alpha |\eta\rangle \,, \quad \{\eta_\alpha, \eta_\beta\} = 0 \,, \quad \eta_\alpha \eta_\alpha = 0 \,, \tag{2.13}$$

and satisfy the relations

$$\{\eta_\alpha, c^{(\dagger)}_\beta\} = 0 \,, \quad (\eta_\alpha c_\beta)^\dagger = c^\dagger_\beta \bar{\eta}_\alpha \,, \tag{2.14}$$

where $\bar{\eta}_\alpha$ is the conjugate of η_α, $\overline{\bar{\eta}_\alpha} = \eta_\alpha$. The derivative and integral algebras of Grassmann numbers η_α follow

$$\frac{\partial}{\partial \eta_\alpha} 1 = 0 \,, \quad \frac{\partial}{\partial \eta_\alpha} \eta_\beta = \delta_{\alpha\beta} \,, \quad \frac{\partial}{\partial \eta_\alpha} (\eta_\beta \eta_\alpha) = -\eta_\beta \,, \alpha \neq \beta \,. \tag{2.15}$$

$$\int \mathrm{d}\eta_\alpha \; 1 = 0 \,, \quad \int \mathrm{d}\eta_\alpha \; \eta_\beta = \delta_{\alpha\beta} \,. \tag{2.16}$$

The coherent state $|\eta\rangle$ can be written as

$$|\eta\rangle = e^{-\sum_\alpha \eta_\alpha c^\dagger_\alpha}|0\rangle = \prod_\alpha (1 - \eta_\alpha c^\dagger_\alpha)|0\rangle \,, \tag{2.17}$$

which can be proved to be an eigenstate of c_α [Eq. 2.12]

$$\begin{aligned} c_\alpha|\eta\rangle &= c_\alpha \prod_\beta (1-\eta_\beta c^\dagger_\beta)|0\rangle = \left[\prod_{\beta\neq\alpha}(1-\eta_\beta c^\dagger_\beta)\right] c_\alpha(1-\eta_\alpha c^\dagger_\alpha)|0\rangle \\ &= \left[\prod_{\beta\neq\alpha}(1-\eta_\beta c^\dagger_\beta)\right] \eta_\alpha|0\rangle = \left[\prod_{\beta\neq\alpha}(1-\eta_\beta c^\dagger_\beta)\right] \eta_\alpha(1-\eta_\alpha c^\dagger_\alpha)|0\rangle \\ &= \eta_\alpha \prod_\beta (1-\eta_\beta c^\dagger_\beta)|0\rangle = \eta_\alpha|\eta\rangle \end{aligned} \tag{2.18}$$

using the anti-commutation relations of c_α, $c^\dagger_\alpha$, and η_α. The adjoint $\langle\eta|$ of a coherent state $|\eta\rangle$ can then be expressed as

$$\langle\eta| = \langle 0|e^{-\sum_\alpha c_\alpha \bar{\eta}_\alpha} = \langle 0|e^{\sum_\alpha \bar{\eta}_\alpha c_\alpha} \,, \quad \Rightarrow \quad \langle\eta|c^\dagger_\alpha = \langle\eta|\bar{\eta}_\alpha \,. \tag{2.19}$$

With the derivative algebra given in Eq. 2.15, the action of $c^\dagger_\alpha$ and c_α on a coherent state can be written as

$$c^\dagger_\alpha|\eta\rangle = -\frac{\partial}{\partial\eta_\alpha}|\eta\rangle \,, \quad \langle\eta|c_\alpha = \frac{\partial}{\partial\bar{\eta}_\alpha}\langle\eta| \,. \tag{2.20}$$

The coherent states form an overcomplete basis of an extended Fock space, with the overlap

$$\langle\eta|\eta'\rangle = e^{\sum_\alpha \bar{\eta}_\alpha \eta'_\alpha} \,, \tag{2.21}$$

and the closure relation

$$\int \left(\prod_\alpha d\bar{\eta}_\alpha d\eta_\alpha\right) e^{-\sum_\alpha \bar{\eta}_\alpha \eta_\alpha}|\eta\rangle\langle\eta| = 1 \,. \tag{2.22}$$

Other useful identities associated with Grassmann algebras include the determinant of a positive definite matrix M

$$\int \left(\prod_{\alpha} d\bar{\eta}_{\alpha} d\eta_{\alpha}\right) \exp\left(-\sum_{\beta\gamma} \bar{\eta}_{\beta} M_{\beta\gamma} \eta_{\gamma}\right) = \det M \,, \quad e^{\mathrm{Tr}\ln M} = \det M \,, \tag{2.23}$$

and the Gaussian integral

$$\begin{aligned} &[\det M] \exp\left(\sum_{\alpha\beta} \bar{J}_{\alpha} [M]^{-1}_{\alpha\beta} J_{\beta}\right) \\ &= \int \left(\prod_{\alpha} d\bar{\eta}_{\alpha} d\eta_{\alpha}\right) \exp\left(-\sum_{\beta\gamma} \bar{\eta}_{\beta} M_{\beta\gamma} \eta_{\gamma} + \sum_{\beta} (\bar{\eta}_{\beta} J_{\beta} + \bar{J}_{\beta} \eta_{\beta})\right) . \end{aligned} \tag{2.24}$$

2.2.2 Partition function and path integral

With the definitions of the coherent states and Grassmann numbers, the partition function of the grand canonical ensemble at finite temperature can be expressed as

$$Z = \mathrm{Tr}[e^{-\beta(H-\mu N)}] = \int \left(\prod_{\alpha} d\bar{\eta}_{\alpha} d\eta_{\alpha}\right) e^{-\sum_{\alpha} \bar{\eta}_{\alpha}\eta_{\alpha}} \langle -\eta | e^{-\beta(H-\mu N)} | \eta \rangle \,, \tag{2.25}$$

where $\beta = (k_B T)^{-1}$ is the inverse temperature, μ the chemical potential, and $N = \sum_{\alpha} c^{\dagger}_{\alpha} c_{\alpha}$ the density. The minus sign in $\langle -\eta |$ is given by the anticommutation relation between Grassmann numbers.

In the path integral formalism, the exponential term $e^{-\beta(H-\mu N)}$ is treated as time evolution with the imaginary time $\tau = it \in [0, \beta]$. Discretize the imaginary time interval $[0, \beta]$ into M equal intervals of length $\epsilon = \beta/M$, and insert the closure relation [Eq. 2.22] $M - 1$ times, the partition function Z can be written as

$$\begin{aligned} Z &= \int \left(\prod_{\alpha} d\bar{\eta}_{\alpha} d\eta_{\alpha}\right) e^{-\sum_{\alpha} \bar{\eta}_{\alpha}\eta_{\alpha}} \langle -\eta | e^{-M\epsilon(H-\mu N)} | \eta \rangle \\ &= \int_{\eta^{(0)}=-\eta^{(M)}} \left(\prod_{l=1}^{M} \prod_{\alpha} d\bar{\eta}^{(l)}_{\alpha} d\eta^{(l)}_{\alpha}\right) e^{-\sum_{l=1}^{M} \sum_{\alpha} \bar{\eta}^{(l)}_{\alpha} \eta^{(l)}_{\alpha}} \prod_{l=1}^{M} \left\langle \eta^{(l)} \left| e^{-\epsilon(H-\mu N)} \right| \eta^{(l-1)} \right\rangle \,, \end{aligned} \tag{2.26}$$

where we have used the boundary condition $|\eta^{(0)}\rangle = |-\eta^{(M)}\rangle$. With the exponential term written in a normal ordering form, where all the creation operators are to the left of all the annihilation operators [5]

$$e^{-\epsilon(H-\mu N)} = \; : e^{-\epsilon(H-\mu N)} : + \mathcal{O}(\epsilon^2) \,, \tag{2.27}$$

and in the limit of $M \to \infty$, we have

$$\lim_{M\to\infty} \left\langle \eta^{(l)} \left| e^{-\epsilon(H-\mu N)} \right| \eta^{(l-1)} \right\rangle = \lim_{M\to\infty} \left(e^{\sum_\alpha \bar{\eta}_\alpha^{(l)} \eta_\alpha^{(l-1)}} \right) e^{-\epsilon \left\{ H\left[\bar{\eta}_\alpha^{(l)}, \eta_\alpha^{(l-1)}\right] - \mu \sum_\alpha \bar{\eta}_\alpha^{(l)} \eta_\alpha^{(l-1)} \right\}} , \tag{2.28}$$

where $H\,[\bar{\eta}_\alpha^{(l)}, \eta_\alpha^{(l-1)}] = \frac{\langle \eta^{(l)} | H | \eta^{(l-1)} \rangle}{\langle \eta^{(l)} | \eta^{(l-1)} \rangle}$. Insert this relation in Eq. 2.26, the partition function takes the form

$$\begin{aligned} Z = &\lim_{M\to\infty} \int \left(\prod_{l=1}^{M} \prod_\alpha d\bar{\eta}_\alpha^{(l)} d\eta_\alpha^{(l)} \right) \\ &\qquad \times \exp\left\{ \sum_{k=1}^{M} -\epsilon \left[\sum_\alpha \bar{\eta}_\alpha^{(l)} \left(\frac{\eta_\alpha^{(l)} - \eta_\alpha^{(l-1)}}{\epsilon} - \mu \eta_\alpha^{(l-1)} \right) + H[\bar{\eta}_\alpha^{(l)}, \eta_\alpha^{(l-1)}] \right] \right\} \\ = &\int_{\eta(0)=-\eta(\beta)} \mathcal{D}[\bar{\eta}_\alpha(\tau), \eta_\alpha(\tau)] \\ &\qquad \times \exp\left\{ -\int_0^\beta d\tau \left[\sum_\alpha \bar{\eta}_\alpha(\tau) \left(\partial_\tau - \mu \right) \eta_\alpha(\tau) + H[\bar{\eta}_\alpha(\tau), \eta_\alpha(\tau)] \right] \right\} . \end{aligned} \tag{2.29}$$

Hereafter we will adopt the more compact notation and write the Grassmann numbers with the same letter as the fermionic creation and annihilation operators, i.e. $[\bar{c}, c]$. The partition function will be written as a functional integral over Grassmann fields $\bar{c}$ and c

$$Z = \int \mathcal{D}[\bar{c}, c] e^{-S[\bar{c}, c]} , \tag{2.30}$$

with $S[\bar{c}, c]$ being the action

$$\begin{aligned} S[\bar{c}, c] &= \int_0^\beta d\tau \left[\sum_\alpha \bar{c}_\alpha(\tau)(\partial_\tau - \mu) c_\alpha(\tau) + H[\bar{c}_\alpha(\tau), c_\alpha(\tau)] \right] \\ &= \int dx \left[\bar{c}(x)(\partial_\tau - \mu) c(x) + H[\bar{c}(x), c(x)] \right] , \end{aligned} \tag{2.31}$$

where we have introduced the combined labels

$$x = (\alpha, \tau) , \quad \int dx = \int_0^\beta d\tau \sum_\alpha . \tag{2.32}$$

2.3 Generating functions of many-particle Green's functions

2.3.1 Many-particle Green's functions

One of the central quantities in many-body theory is the many-particle Green's function. In systems without symmetry breaking, it is defined as the time ordered correlation function with equal numbers of creation and annihilation operators

$$G^{(n)}(x_1, \dots, x_n; x'_1, \dots, x'_n) = (-1)^n \langle \mathcal{T} c(x_1) c^\dagger(x'_1), \dots, c(x_n) c^\dagger(x'_n) \rangle \,, \tag{2.33}$$

where $\mathcal{T}$ is the time ordering operator that orders the operators in a form that every operator has only later operators to the left, earlier operators to the right, and

$$c^{(\dagger)}(x) = c^{(\dagger)}_\alpha(\tau) = e^{\tau(H-\mu N)} c^{(\dagger)}_\alpha e^{-\tau(H-\mu N)} \,. \tag{2.34}$$

By defining the partition function with path integral formalism [Eq. 2.30], the expectation value for an imaginary time dependent function can be written as

$$\langle f[\bar{c}(\tau'), c(\tau)] \rangle = \frac{1}{Z} \int \mathcal{D}[\bar{c}, c] e^{-S[\bar{c},c]} f[\bar{c}(\tau'), c(\tau)] \equiv \left\langle \mathcal{T} f[c^\dagger(\tau'), c(\tau)] \right\rangle \,, \tag{2.35}$$

and normal order is taken when two operators are at equal time. The enforcement of time and normal ordering come from the construction of the path integral formalism [Eq. 2.29], where we have inserted a sequence of the closure relation (see Eq. 2.26) and used the normal ordering of operators (see Eq. 2.28). As an example, the single particle Green's function can be written as

$$\begin{aligned} G^{(1)}_{\alpha\gamma}(\tau, \tau') &= -\langle \mathcal{T} c_\alpha(\tau) c^\dagger_\gamma(\tau') \rangle \\ &= -\frac{1}{Z} \mathrm{Tr}[e^{-\beta(H-\mu N)} \mathcal{T} c_\alpha(\tau) c^\dagger_\gamma(\tau')] \\ &= -\frac{1}{Z} \int \mathcal{D}[\bar{c}, c] e^{-S[\bar{c},c]} c_\alpha(\tau) \bar{c}_\gamma(\tau') = -\langle c_\alpha(\tau) \bar{c}_\gamma(\tau') \rangle \,. \end{aligned} \tag{2.36}$$

The many-particle Green's function $G^{(n)}$ can also be written with Grassmann numbers c and $\bar{c}$ as

$$G^{(n)}(x_1, \dots, x_n; x'_1, \dots, x'_n) = (-1)^n \langle c(x_1) \bar{c}(x'_1), \dots, c(x_n) \bar{c}(x'_n) \rangle \,. \tag{2.37}$$

2.3.2 Generating functions

Adding a source term with the Grassmann fields coupled to an external field J to the system gives an extra term in the action S [Eq. 2.31]. Taking the linear source J as an example, the additional term S' can be written as

$$S'[\bar{c}, c] = \int dx[\bar{J}(x)c(x) + \bar{c}(x)J(x)] \,. \tag{2.38}$$

The action with source field gives the generating function $\mathcal{M}[\bar{J}, J]$ of the many-particle Green's function [Eq. 2.37]

$$\begin{aligned}\mathcal{M}[\bar{J}, J] &\equiv \frac{1}{Z}\int \mathcal{D}[\bar{c}, c]e^{-S[\bar{c},c]}e^{-S'[\bar{c},c]} \\ &= \left\langle \exp\left(-\int dx[\bar{J}(x)c(x) + \bar{c}(x)J(x)]\right)\right\rangle_S = \langle \exp\left(-S'\right)\rangle_S \,.\end{aligned} \tag{2.39}$$

Differentiation with respect to the source fields J and $\bar{J}$ yields

$$\frac{\delta \mathcal{M}[\bar{J}, J]}{\delta \bar{J}(x_1)} = -\left\langle c(x_1)e^{-S'}\right\rangle_S \,, \tag{2.40a}$$

$$\frac{\delta \mathcal{M}[\bar{J}, J]}{\delta J(x_1)} = \left\langle \bar{c}(x_1)e^{-S'}\right\rangle_S \,, \tag{2.40b}$$

which gives

$$\begin{aligned}\left.\frac{\delta^{2n}\mathcal{M}[\bar{J}, J]}{\delta \bar{J}\left(x_1\right)\cdots\delta \bar{J}\left(x_n\right)\delta J\left(x'_n\right)\cdots\delta J\left(x'_1\right)}\right|_{\bar{J},J=0} &= \langle \bar{c}(x'_1)\ldots\bar{c}(x'_n)c(x_n)\ldots c(x_1)\rangle \\ &= (-1)^n\langle c(x_1)\bar{c}(x'_1)\ldots c(x_n)\bar{c}(x'_n)\rangle \\ &= G^{(n)}(x_1, \ldots, x_n; x'_1, \ldots, x'_n) \,.\end{aligned} \tag{2.41}$$

A helpful tool in field theory and many-body physics is the Feynman diagrams, which provides a way of graphically displaying physical processes. Detailed explanations of different types of Feynman diagrams can be found in chapter 2 of Ref. [5]. From a diagrammatic point of view, the diagrams for Green's functions defined in Eqs. 2.33 and 2.37 have all the interaction vertices linked to the external points $(x_1, \ldots, x_n)$ and $(x'_1, \ldots, x'_n)$, which are not necessarily all connected [5]. It is useful to define the connected many-particle Green's functions $G^{(n)}_{\text{conn}}(x_1, \ldots, x_n; x'_1, \ldots, x'_n)$, which contains all connected diagrams linked to the external points $(x_1, \ldots, x_n)$ and $(x'_1, \ldots, x'_n)$. The generating function of the connected

Green's functions is given by the logarithm of $\mathcal{M}[\bar{J}, J]$

$$\mathcal{W}[\bar{J}, J] \equiv \ln \mathcal{M}[\bar{J}, J] = \ln \left\langle \exp\left(-\int dx[\bar{J}(x)c(x) + \bar{c}(x)J(x)]\right)\right\rangle_S = \ln \left\langle \exp\left(-S'\right)\right\rangle_S \;, \tag{2.42}$$

which gives

$$\left.\frac{\delta^{2n}\mathcal{W}[\bar{J}, J]}{\delta\bar{J}(x_1)\cdots\delta\bar{J}(x_n)\delta J(x'_n)\cdots\delta J(x'_1)}\right|_{\bar{J},J=0} = G^{(n)}_{\text{conn}}(x_1, \ldots, x_n; x'_1, \ldots, x'_n)\,. \tag{2.43}$$

At first order, $G^{(1)}(x_1; x'_1) = G^{(1)}_{\text{conn}}(x_1; x'_1)$. The first non-trivial relation is given by the second-order Green's functions

$$\begin{aligned}
G^{(2)}_{\text{conn}}(x_1, x_2; x'_1 x'_2) &= \left.\frac{\delta^4\left[\ln\left\langle e^{-S'}\right\rangle_S\right]}{\delta\bar{J}(x_1)\delta\bar{J}(x_2)\delta J(x'_2)\delta J(x'_1)}\right|_{\bar{J},J=0} \\
&= \left.\frac{\delta^2\left[\left\langle e^{-S'}\right\rangle_S^{-1}\left\langle\bar{c}(x'_2)\bar{c}(x'_1)e^{-S'}\right\rangle_S - \left\langle e^{-S'}\right\rangle_S^{-2}\left\langle\bar{c}(x'_2)e^{-S'}\right\rangle_S\left\langle\bar{c}(x'_1)e^{-S'}\right\rangle_S\right]}{\delta\bar{J}(x_1)\delta\bar{J}(x_2)}\right|_{\bar{J},J=0} \\
&= \langle c(x_1)c(x_2)\bar{c}(x'_2)\bar{c}(x'_1)\rangle_S - \langle c(x_2)\bar{c}(x'_2)\rangle_S\langle c(x_1)\bar{c}(x'_1)\rangle_S + \langle c(x_1)\bar{c}(x'_2)\rangle_S\langle c(x_2)\bar{c}(x'_1)\rangle_S \\
&= G^{(2)}(x_1, x_2; x'_1 x'_2) - G^{(1)}(x_1; x'_1)G^{(1)}(x_2; x'_2) + G^{(1)}(x_1; x'_2)G^{(1)}(x_2; x'_1)\,.
\end{aligned} \tag{2.44}$$

2.4 Wick's theorem

In general, computing the n particle Green's function $G^{(n)}$ [Eqs. 2.33, 2.37] is a non-trivial problem. While for non-interacting systems, $G_0^{(n)}$ can be evaluated using the Wick's theorem. In this section we provide a derivation of the Wick's theorem using the generating function $\mathcal{M}$ introduced in section 2.3.2.

Consider a non-interacting Hamiltonian

$$H_0 = \sum_{\alpha\beta} h_{\alpha\beta} c^\dagger_\alpha c_\beta \,, \tag{2.45}$$

the non-interacting action S_0 can be written as

$$S_0 = \iint_0^\beta d\tau d\tau' \sum_{\alpha\beta}\left[\bar{c}_\alpha(\tau)[(\partial_\tau - \mu)\,\delta_{\alpha\beta} + h_{\alpha\beta}]\delta(\tau - \tau')c_\beta(\tau')\right] \,. \tag{2.46}$$

The corresponding non-interacting partition function is in the form

$$Z_0 = \int \mathcal{D}[\bar{c}, c] e^{-S_0[\bar{c},c]} = \det[-g^{-1}] \,, \tag{2.47}$$

where the non-interacting Green's function g is defined with the equation of motion

$$\sum_{\beta} [(\partial_\tau - \mu)\delta_{\alpha\beta} + h_{\alpha\beta}] g_{\beta\gamma}(\tau - \tau') = -\delta_{\alpha\gamma}\delta(\tau - \tau') \,, \tag{2.48}$$

and we have used the identity given in Eq. 2.23 to get the determinant term. Using Eq. 2.39, the generating function $\mathcal{M}_0$ of the non-interacting n-particle Green's function can be written as

$$\begin{aligned} \mathcal{M}_0[\bar{J}, J] &= \frac{1}{Z_0} \int \mathcal{D}[\bar{c}, c] \exp\left(\int dx dx' [\bar{c}(x) g^{-1}(x, x') c(x')] - \int dx [\bar{J}(x) c(x) + \bar{c}(x) J(x)] \right) \\ &= \frac{1}{Z_0} \det[-g^{-1}] \exp\left(- \int dx dx' [\bar{J}(x) g(x, x') J(x')] \right) \\ &= \exp\left(- \int dx dx' [\bar{J}(x) g(x, x') J(x')] \right) \,, \end{aligned} \tag{2.49}$$

where the second equality comes from the Gaussian integral given in Eq. 2.24. The non-interacting n-particle Green's function $G_0^{(n)}$ can then be evaluated using Eq. 2.41

$$\begin{aligned} G_0^{(n)}(x_1, \ldots, x_n;\, x'_1, \ldots, x'_n) &= \left. \frac{\delta^{2n} \mathcal{M}_0[\bar{J}, J]}{\delta \bar{J}(x_1) \ldots \delta \bar{J}(x_n) \delta J(x'_n) \ldots \delta J(x'_1)} \right|_{\bar{J}, J=0} \\ &= \left. \frac{\delta^{2n} \exp\left(- \int dy dy' [\bar{J}(y) g(y, y') J(y')] \right)}{\delta \bar{J}(x_1) \ldots \delta \bar{J}(x_n) \delta J(x'_n) \ldots \delta J(x'_1)} \right|_{\bar{J}, J=0} \\ &= \left. \frac{\delta^n}{\delta \bar{J}(x_1) \ldots \delta \bar{J}(x_n)} \int dy_n \bar{J}(y_n) g(y_n, x'_n) \cdots \int dy_1 \bar{J}(y_1) g(y_1, x'_1) e^{-\int dy dy' [\bar{J}(y) g(y, y') J(y')]} \right|_{\bar{J}, J=0} \\ &= \left. \int dy_n \ldots dy_1 \frac{\delta^n (\bar{J}(y_n) \ldots \bar{J}(y_1))}{\delta \bar{J}(x_1) \ldots \delta \bar{J}(x_n)} g(y_n, x'_n) \ldots g(y_1, x'_1) e^{-\int dy dy' [\bar{J}(y) g(y, y') J(y')]} \right|_{\bar{J}, J=0} \\ &= \sum_P (-1)^P g(x_{P_1}, x'_1) \ldots g(x_{P_n}, x'_n) = \det \mathbf{G}(x_1, \ldots, x_n; x'_1, \ldots, x'_n) \,, \end{aligned} \tag{2.50}$$

where P represents all permutations of the products of one-particle Green's functions, and the sign $(-1)^P$ comes from the Grassmann algebra, that when taking derivative of a Grassmann number, we need to move it to the leftmost of the expression. In the last row, $\mathbf{G}(x_1, \ldots, x_n; x'_1, \ldots, x'_n)$ is a $n \times n$ matrix with the (i, j) element being $g(x_i; x'_j) = G_0^{(1)}(x_i; x'_j)$.

2.5 Effective potential and vertex functions

In section 2.3, we introduced the full and connected Green's functions and their generating functions. In this section, we will introduce another type of function – vertex function and its generating function. The relations between the Green's functions and the vertex functions will also be derived.

2.5.1 Effective potential

In the presence of finite source fields J, $\bar{J}$, the expectation values of $c^{(\dagger)}(x)$ are non-zero as described in section 2.3.2. We can define the average field

$$\phi(x) = \langle c(x) \rangle_{S+S'} = -\frac{\delta}{\delta \bar{J}(x)} \mathcal{W}[\bar{J}, J] \,, \quad \bar{\phi}(x) = \langle \bar{c}(x) \rangle_{S+S'} = \frac{\delta}{\delta J(x)} \mathcal{W}[\bar{J}, J] \,, \tag{2.51}$$

where the thermal averages are taken with respect to the action $S[\bar{c}, c] + S'[\bar{c}, c]$. To obtain a functional of fields $\bar{\phi}$, ϕ instead of $\bar{c}$, c, we perform a Legendre transformation of $\mathcal{W}$. The effective potential is defined as

$$\mathcal{K}[\bar{\phi}, \phi] = -\mathcal{W}[\bar{J}, J] - \int dx [\bar{\phi}(x) J(x) + \bar{J}(x) \phi(x)] \,, \tag{2.52}$$

which satisfies the reciprocity relation

$$\frac{\partial}{\partial \bar{\phi}(x)} \mathcal{K}[\bar{\phi}, \phi] = -J(x) \,, \quad \frac{\partial}{\partial \phi(x)} \mathcal{K}[\bar{\phi}, \phi] = \bar{J}(x) \,. \tag{2.53}$$

Similar to $\mathcal{M}$ and $\mathcal{W}$ that generate full and connected Green's functions, the effective potential $\mathcal{K}$ is the generating function of another type of function – vertex function

$$F_{m\bar{\phi}, k\phi}(x_1, \ldots, x_m; x'_1, \ldots, x'_k) = \left. \frac{\delta^{m+k} \mathcal{K}[\bar{\phi}, \phi]}{\delta \bar{\phi}(x_1) \ldots \delta \bar{\phi}(x_m) \delta \phi(x'_k) \ldots \delta \phi(x'_1)} \right|_{\bar{J}, J=0} \,. \tag{2.54}$$

From a diagrammatic point of view, the vertex functions constructed in this way are one particle irreducible, i.e can not be disconnected by removing one single-particle line [5].

2.5.2 Self-energy and Dyson equation

To describe the interacting behaviour of a system, we need to find the connections between the interacting and non-interacting Green's functions. The vertex functions introduced in the previous subsection are what provide these connections. In this subsection we will introduce the self-energy and derive the Dyson equation for computing the interacting single-particle Green's function.

The functional derivative of a general function $f[\bar{J}, J]$ with respect to the average field $\phi(x)$ can be computed via the chain rule

$$\begin{aligned}
\frac{\delta f[\bar{J}, J]}{\delta \phi(x_1)} &= \int dx_2 \left[\frac{\delta f}{\delta \bar{J}(x_2)} \frac{\delta \bar{J}(x_2)}{\delta \phi(x_1)} + \frac{\delta f}{\delta J(x_2)} \frac{\delta J(x_2)}{\delta \phi(x_1)} \right] \\
&= \int dx_2 \left[\frac{\delta f}{\delta \bar{J}(x_2)} \frac{\delta^2 \mathcal{K}}{\delta \phi(x_1) \delta \phi(x_2)} - \frac{\delta f}{\delta J(x_2)} \frac{\delta^2 \mathcal{K}}{\delta \phi(x_1) \delta \bar{\phi}(x_2)} \right], \qquad (2.55a) \\
\frac{\delta f[\bar{J}, J]}{\delta \bar{\phi}(x_1)} &= \int dx_2 \left[\frac{\delta f}{\delta \bar{J}(x_2)} \frac{\delta^2 \mathcal{K}}{\delta \bar{\phi}(x_1) \delta \phi(x_2)} - \frac{\delta f}{\delta J(x_2)} \frac{\delta^2 \mathcal{K}}{\delta \bar{\phi}(x_1) \delta \bar{\phi}(x_2)} \right]. \qquad (2.55b)
\end{aligned}$$

The lowest order equations related with the vertex functions can be obtained by differentiating the average field introduced in Eq. 2.51

$$\begin{aligned}
\frac{\delta \phi(x_3)}{\delta \phi(x_1)} &= \delta(x_3 - x_1) \\
&= \int x_2 \left[- \frac{\delta^2 \mathcal{W}}{\delta \bar{J}(x_2) \delta \bar{J}(x_3)} \frac{\delta^2 \mathcal{K}}{\delta \phi(x_1) \delta \phi(x_2)} + \frac{\delta^2 \mathcal{W}}{\delta J(x_2) \delta \bar{J}(x_3)} \frac{\delta \mathcal{K}^2}{\delta \phi(x_1) \delta \bar{\phi}(x_2)} \right], \qquad (2.56a) \\
\frac{\delta \bar{\phi}(x_3)}{\delta \bar{\phi}(x_1)} &= \delta(x_3 - x_1) \\
&= \int x_2 \left[\frac{\delta^2 \mathcal{W}}{\delta \bar{J}(x_2) \delta J(x_3)} \frac{\delta^2 \mathcal{K}}{\delta \bar{\phi}(x_1) \delta \phi(x_2)} - \frac{\delta^2 \mathcal{W}}{\delta J(x_2) \delta J(x_3)} \frac{\delta \mathcal{K}^2}{\delta \bar{\phi}(x_1) \delta \bar{\phi}(x_2)} \right], \qquad (2.56b) \\
\frac{\delta \phi(x_3)}{\delta \bar{\phi}(x_1)} &= 0 \\
&= \int x_2 \left[- \frac{\delta^2 \mathcal{W}}{\delta \bar{J}(x_2) \delta \bar{J}(x_3)} \frac{\delta^2 \mathcal{K}}{\delta \bar{\phi}(x_1) \delta \phi(x_2)} + \frac{\delta^2 \mathcal{W}}{\delta J(x_2) \delta \bar{J}(x_3)} \frac{\delta \mathcal{K}^2}{\delta \bar{\phi}(x_1) \delta \bar{\phi}(x_2)} \right], \qquad (2.56c) \\
\frac{\delta \bar{\phi}(x_3)}{\delta \phi(x_1)} &= 0 \\
&= \int x_2 \left[\frac{\delta^2 \mathcal{W}}{\delta \bar{J}(x_2) \delta J(x_3)} \frac{\delta^2 \mathcal{K}}{\delta \phi(x_1) \delta \phi(x_2)} - \frac{\delta^2 \mathcal{W}}{\delta J(x_2) \delta J(x_3)} \frac{\delta \mathcal{K}^2}{\delta \phi(x_1) \delta \bar{\phi}(x_2)} \right]. \qquad (2.56d)
\end{aligned}$$

The equations above may be expressed in a matrix form

$$\int dx_2 \begin{pmatrix} \dfrac{\delta^2 \mathcal{W}}{\delta \bar{J}(x_3) \delta J(x_2)} & -\dfrac{\delta^2 \mathcal{W}}{\delta \bar{J}(x_3) \delta \bar{J}(x_2)} \\ -\dfrac{\delta^2 \mathcal{W}}{\delta J(x_3) \delta J(x_2)} & \dfrac{\delta^2 \mathcal{W}}{\delta J(x_3) \delta \bar{J}(x_2)} \end{pmatrix} \begin{pmatrix} \dfrac{\delta^2 \mathcal{K}}{\delta \bar{J}(x_2) \delta J(x_1)} & \dfrac{\delta^2 \mathcal{K}}{\delta \bar{J}(x_2) \delta \bar{J}(x_1)} \\ \dfrac{\delta^2 \mathcal{K}}{\delta J(x_2) \delta J(x_1)} & \dfrac{\delta^2 \mathcal{K}}{\delta J(x_2) \delta \bar{J}(x_1)} \end{pmatrix} = \delta(x_3 - x_1) \begin{pmatrix} 1 & 0 \\ 0 & 1 \end{pmatrix}. \qquad (2.57)$$

Using the definitions given by Eq. 2.54 and Eq. 2.43, the matrix composed with $F_{\bar{\phi}\phi}$, $F_{\bar{\phi}\bar{\phi}}$,

$F_{\phi\phi}$, $F_{\phi\bar{\phi}}$ is the inverse of the matrix of connected Green's functions

$$\begin{pmatrix} F_{\bar{\phi}\phi} & F_{\bar{\phi}\bar{\phi}} \\ F_{\phi\phi} & F_{\phi\bar{\phi}} \end{pmatrix} = - \begin{pmatrix} \langle c\bar{c} \rangle & \langle cc \rangle \\ \langle \bar{c}\bar{c} \rangle & \langle \bar{c}c \rangle \end{pmatrix}^{-1} , \tag{2.58}$$

where we have used that $G^{(1)}_{\text{conn}}(x_1; x'_1) = G^{(1)}(x_1; x'_1)$. The self-energy Σ is defined as the difference between vertex functions of the interacting and non-interacting systems

$$\begin{pmatrix} F_{\bar{\phi}\phi} & F_{\bar{\phi}\bar{\phi}} \\ F_{\phi\phi} & F_{\phi\bar{\phi}} \end{pmatrix} \equiv \begin{pmatrix} F^{(0)}_{\bar{\phi}\phi} & F^{(0)}_{\bar{\phi}\bar{\phi}} \\ F^{(0)}_{\phi\phi} & F^{(0)}_{\phi\bar{\phi}} \end{pmatrix} - \begin{pmatrix} \Sigma_{\bar{\phi}\phi} & \Sigma_{\bar{\phi}\bar{\phi}} \\ \Sigma_{\phi\phi} & \Sigma_{\phi\bar{\phi}} \end{pmatrix} . \tag{2.59}$$

On Green's function level, this gives the Dyson equation

$$\underline{G}^{-1} = \underline{G}_0^{-1} - \underline{\Sigma} , \tag{2.60}$$

where the underline labels the 2×2 matrix structure. For systems without symmetry breaking, the off-diagonal terms in the matrices are zero, which gives decoupled equations for the diagonal terms in $G^{-1} = G_0^{-1} - \Sigma$, and can be written in an integral form as

$$G^{(1)}(x_1; x'_1) = G^{(1)}_0(x_1; x'_1) + \int dx'_2 dx_3 G^{(1)}_0(x_1; x'_2) \Sigma(x'_2; x_3) G^{(1)}(x_3; x'_1) . \tag{2.61}$$

From a diagrammatic point of view, the self-energy Σ contains all one-particle irreducible amputated diagrams connecting x_1 and x'_1 with the bare propagator G_0 [5].

2.5.3 Higher order vertex functions

To obtain higher order vertex functions from Eq. 2.54, we need to successively take derivatives of the average field. A diagrammatic approach is demonstrated in Ref. [5]. At second order, in the case without symmetry breaking, we get a equation that connects the Green's functions to the vertex functions

$$\begin{aligned} &G^{(2)}_{\text{conn}}(x_1, x_2; x'_1, x'_2) \\ &\quad = - \int dx_3 dx_4 dx'_3 dx'_4 G^{(1)}(x_1; x'_3) G^{(1)}(x_2; x'_4) F_{2\bar{\phi},2\phi}(x'_3, x'_4; x_3, x_4) G^{(1)}(x_3; x'_1) G^{(1)}(x_4; x'_2) . \end{aligned} \tag{2.62}$$

The equation above shows that the two-particle vertex function $F_{2\bar{\phi},2\phi}$ is the sum of all one-particle irreducible amputated connected diagrams with four external legs [5]. The generalization of Eq. 2.62 to symmetry broken case will be discussed in later chapters.

2.6 Luttinger-Ward functional

To analyze the structure of the self-energy, we introduce the Luttinger-Ward functional Φ [30] in this section. The derivation here use the same non-perturbative approach as Refs. [31–34]. For convenience we change the notation of the single particle Green's function $G(x_1; x_1') \to G(x_1; x_2)$.

Consider adding a bilinear source term in the action

$$S'[a, b] = -\int dx_1 dx_2 [a(x_1) J(x_1, x_2) b(x_2)] \,, \tag{2.63}$$

where a and b can be either $\bar{c}$ or c, and the sources $J(x_1, x_2)$ are c-numbers. For non-symmetry-broken systems, we can choose the source term to be

$$S'[\bar{c}, c] = -\int dx_1 dx_2 [\bar{c}(x_1) J(x_1, x_2) c(x_2)] \,. \tag{2.64}$$

The partition function with this source term is in the form

$$\begin{aligned} Z[J] &= \int \mathcal{D}[\bar{c}, c] e^{-S[\bar{c},c]} e^{-S'[\bar{c},c]} \\ &= \int \mathcal{D}[\bar{c}, c] \exp\left(-S[\bar{c}, c] + \int dx_1 dx_2 [\bar{c}(x_1) J(x_1, x_2) c(x_2)]\right) \,. \end{aligned} \tag{2.65}$$

The generating function of Green's functions corresponding to the bilinear source can be defined similar to the generating function $\mathcal{M}[J, \bar{J}]$ introduced in section 2.3.2 as $Z[J]/Z$. To follow the convention used in the derivation of Luttinger-Ward functional, we drop the $1/Z$ pre-factor and define $\mathcal{M}[J] = Z[J]$, $\mathcal{W}[J] = \ln \mathcal{M}[J] = \ln Z[J]$. The one-particle Green's function can then be computed with

$$\begin{aligned} G(x_1; x_2) &= \left.\frac{\delta \mathcal{W}[J]}{\delta J(x_2, x_1)}\right|_{J=0} = \left.\frac{1}{Z} \frac{\delta Z[J]}{\delta J(x_2, x_1)}\right|_{J=0} \\ &= \frac{1}{Z} \int \mathcal{D}[\bar{c}, c] \bar{c}(x_2) c(x_1) e^{-S[\bar{c},c]} = -\langle c(x_1) \bar{c}(x_2) \rangle \,. \end{aligned} \tag{2.66}$$

Performing a Legendre transformation of $\mathcal{W}[J]$ as introduced in section 2.5.1, the effective potential takes the form

$$\mathcal{K}[\tilde{G}] = -\mathcal{W}[J] + \int dx_1 dx_2 \tilde{G}(x_1; x_2) J(x_2, x_1) \,, \tag{2.67}$$

where $\tilde{G}(x_1; x_2) = \frac{\delta \mathcal{W}[J]}{\delta J(x_2, x_1)}$ is an arbitrary variable introduced in the functional. The reciprocal relation (see Eq. 2.53) can be proved by

$$\begin{aligned}\frac{\delta\mathcal{K}[\tilde{G}]}{\delta\tilde{G}(x_1;x_2)} &= -\frac{\delta\mathcal{W}[J]}{\delta\tilde{G}(x_1;x_2)} + J(x_2,x_1) + \int dx_1' dx_2' \tilde{G}(x_1';x_2')\frac{\delta J(x_2',x_1')}{\delta\tilde{G}(x_1;x_2)} \\ &= -\int dx_1' dx_2' \frac{\delta\mathcal{W}[J]}{\delta J(x_2',x_1')}\frac{\delta J(x_2',x_1')}{\delta\tilde{G}(x_1;x_2)} + \int dx_1' dx_2' \frac{\delta\mathcal{W}[J]}{\delta J(x_2',x_1')}\frac{\delta J(x_2',x_1')}{\delta\tilde{G}(x_1;x_2)} + J(x_2,x_1) \\ &= J(x_2,x_1)\,. \end{aligned} \tag{2.68}$$

In the zero source ($J=0$) limit, $\tilde{G}=G$, G is a stationary point of $\mathcal{K}(\tilde{G})$

$$\left.\frac{\delta\mathcal{K}[\tilde{G}]}{\delta\tilde{G}}\right|_{\tilde{G}=G} = 0\,. \tag{2.69}$$

The Luttinger-Ward functional Φ is defined as the difference between the interacting and non-interacting effective potential

$$\Phi[\tilde{G}] = \mathcal{K}[\tilde{G}] - \mathcal{K}_0[\tilde{G}] = \mathcal{K}[\tilde{G}] + \mathcal{W}_0[J] - \mathrm{Tr}[(\tilde{G}J)_0]\,. \tag{2.70}$$

For a non-interacting system with Hamiltonian in Eq. 2.45, $\mathcal{W}_0[J]$ and $\mathrm{Tr}[(\tilde{G}J)_0]$ can be expressed in terms of the non-interacting Green's function g defined in Eq. 2.48 and $\tilde{G}$. With the partition function $Z_0[J]$ written out explicitly using the identity given in Eq. 2.23

$$\begin{aligned} Z_0[J] &= \int \mathcal{D}[\bar{c},c]\exp\left(-\int dx_1 dx_2\,[\bar{c}(x_1)(-g^{-1}(x_1;x_2) - J(x_1,x_2))c(x_2)]\right) \\ &= \det(-g^{-1}-J) = e^{\mathrm{Tr}\ln(-g^{-1}-J)}\,, \end{aligned} \tag{2.71}$$

the generating function $\mathcal{W}_0[J]$ takes the form

$$\mathcal{W}_0[J] = \ln Z_0[J] = \mathrm{Tr}\ln(-g^{-1}-J)\,. \tag{2.72}$$

The relation between J and $\tilde{G}$ can be derived from the definition of $\tilde{G}$

$$\begin{aligned} \tilde{G}(x_1;x_2) &= \frac{\delta\mathcal{W}_0[J]}{\delta J(x_2,x_1)} = \frac{1}{Z_0[J]}\frac{\delta Z_0[J]}{\delta J(x_2,x_1)} \\ &= \int dx_1' dx_2' [(-g^{-1}-J)^{-1}](x_1',x_2')\frac{\delta[-g^{-1}-J](x_2',x_1')}{\delta J(x_2,x_1)} \\ &= [(g^{-1}+J)^{-1}](x_1,x_2)\,, \end{aligned} \tag{2.73}$$

$$\Rightarrow \quad J = \tilde{G}^{-1} - g^{-1}\,. \tag{2.74}$$

The non-interacting effective potential can then be written as

$$\begin{aligned}\mathcal{K}_0[\tilde{G}] &= -\mathcal{W}_0[J] + \mathrm{Tr}[\tilde{G}J]_0 \\ &= -\mathrm{Tr}\ln(-\tilde{G}^{-1}) - \mathrm{Tr}(\tilde{G}g^{-1} - \mathbb{I}) = \mathrm{Tr}\ln(-\tilde{G}) - \mathrm{Tr}(\tilde{G}g^{-1} - \mathbb{I})\,, \end{aligned} \tag{2.75}$$

where we dropped all the indices. With Eq. 2.75, the Luttinger-Ward functional in Eq. 2.70 can be written as

$$\Phi[\tilde{G}] = \mathcal{K}[\tilde{G}] - \mathcal{K}_0[\tilde{G}] = \mathcal{K}[\tilde{G}] - \mathrm{Tr}\ln(-\tilde{G}) + \mathrm{Tr}(\tilde{G}g^{-1} - \mathbb{I})\,. \tag{2.76}$$

The Luttinger-Ward functional is directly related with physical quantities. For example, the self-energy Σ can be defined as the derivative of the Luttinger-Ward functional Φ with respect to $\tilde{G}$ [35, 36]

$$\Sigma[\tilde{G}] \equiv \frac{\delta\Phi[\tilde{G}]}{\delta\tilde{G}}\,. \tag{2.77}$$

Using the expression of $\Phi[\tilde{G}]$ in Eq. 2.76, the derivative in Eq. 2.77 takes the form

$$\begin{aligned}\Sigma[\tilde{G}] \equiv \frac{\delta\Phi[\tilde{G}]}{\delta\tilde{G}} &= \frac{\delta\mathcal{K}[\tilde{G}]}{\delta\tilde{G}} - \frac{\delta}{\delta\tilde{G}}\mathrm{Tr}\ln(-\tilde{G}) + \frac{\delta}{\delta\tilde{G}}\mathrm{Tr}(\tilde{G}g^{-1} - \mathbb{I}) \\ &= \frac{\delta\mathcal{K}[\tilde{G}]}{\delta\tilde{G}} - \tilde{G}^{-1} + g^{-1}\,. \end{aligned} \tag{2.78}$$

Since G is a stationary point of $\mathcal{K}[\tilde{G}]$ [Eq. 2.69], stationarity implies that the self-energy obeys the Dyson equation given by Eq. 2.60

$$\Sigma[G] = g^{-1} - G^{-1}. \tag{2.79}$$

The grand potential of the system can also be expressed with the Luttinger-Ward functional at $\tilde{G} = G$, which gives

$$\begin{aligned}\beta\Omega = -\ln Z = -\mathcal{W}[J=0] &= \Big[\Phi[\tilde{G}] + \mathrm{Tr}\ln(-\tilde{G}) - \mathrm{Tr}(\tilde{G}g^{-1} - \mathbb{I})\Big]_{\tilde{G}=G} \\ &= \Phi[G] + \mathrm{Tr}\ln(-G) - \mathrm{Tr}(G\Sigma)\,. \end{aligned} \tag{2.80}$$

The Luttinger-Ward functional Φ is also useful in diagrammatic self-consistent approximations. Since Φ and Σ both depend on the interaction U, their asymptotic series expansions can be written as [37]

$$\Phi[G;\varepsilon U] = \sum_{l=1}^{\infty} \Phi^{(l)}[G;U]\varepsilon^l \,, \quad \Sigma[G;\varepsilon U] = \sum_{l=1}^{\infty} \Sigma^{(l)}[G;U]\varepsilon^l \,, \tag{2.81}$$

where $\Sigma^{(l)}$ contains all "skeleton" diagrams of order l. The "skeleton" diagrams are two-particle irreducible amputated diagrams where the propagators connecting two points are the bold propagator G. The coefficients $\Phi^{(l)}$ satisfy

$$\Phi^{(l)}[G;U] = \frac{1}{2l}\,\mathrm{Tr}\left[G\Sigma^{(l)}[G;U]\right] \,. \tag{2.82}$$

The applications of the diagrammatic series given by the Luttinger-Ward functional will be introduced in section 8.2.

2.7 Linear response and the Bethe-Salpeter equation

The evaluation of thermal derivatives lead to useful relations connecting the Green's functions with physical observables. Consider adding a bilinear source to the system as in section 2.6

$$S'[\bar{c},c] = -\int dx_1 dx_2 [a(x_1)J(x_1,x_2)b(x_2)] \,, \quad a,b \in \{\bar{c},c\} \,, \tag{2.83}$$

the action can be written as

$$\begin{aligned} Z[J] &= \int \mathcal{D}[\bar{c},c] e^{-S[\bar{c},c]} e^{-S'[\bar{c},c]} \\ &= \int \mathcal{D}[\bar{c},c] \exp\left(-S[\bar{c},c] + \int dx_1 dx_2 [a(x_1)J(x_1,x_2)b(x_2)]\right) \,. \end{aligned} \tag{2.84}$$

The linear response of any correlator $\langle a'(x_1)b'(x_2)\rangle$ ($a', b' \in \{\bar{c},c\}$) to the external field can be computed by taking derivative of the partition function with respect to the source field

$$\begin{aligned} &\left.\frac{\delta\langle a'(x_1)b'(x_2)\rangle_{S+S'}}{\delta J(x_3,x_4)}\right|_{J=0} \\ &= \left.\frac{\delta\left[\frac{1}{Z[J]}\int \mathcal{D}[\bar{c},c]a'(x_1)b'(x_2)\exp\left(-S[\bar{c},c] + \int dx_3 dx_4 a(x_3)J(x_3,x_4)b(x_4)\right)\right]}{\delta J(x_3,x_4)}\right|_{J=0} \\ &= \langle a'(x_1)b'(x_2)a(x_3)b(x_4)\rangle_S - \langle a'(x_1)b'(x_2)\rangle_S \langle a(x_3)b(x_4)\rangle_S \\ &\equiv \chi(x_1,x_2,x_3,x_4) \,, \end{aligned} \tag{2.85}$$

where $\chi(x_1, x_2, x_3, x_4)$ is called the "generalized susceptibility". For systems without symmetry breaking, we can choose the convention $a'(x_1) \to \bar{c}(x_1)$, $b'(x_2) \to c(x_2)$, $a(x_3) \to \bar{c}(x_3)$, $b(x_4) \to c(x_4)$, and define the two-particle Green's function using the particle-hole convention $G^{(2)}(x_2, x_4; x_1, x_3) = \langle \bar{c}(x_1) c(x_2) \bar{c}(x_3) c(x_4) \rangle$. The generalized susceptibility χ can be computed as

$$\begin{aligned} \left. \frac{\delta G^{(1)}(x_2; x_1; J)}{\delta J(x_3, x_4)} \right|_{J=0} &= G^{(2)}(x_2, x_4; x_1, x_3) - G^{(1)}(x_2; x_1) G^{(1)}(x_4; x_3) \\ &\equiv \chi(x_2, x_4; x_1, x_3) \,. \end{aligned} \tag{2.86}$$

In section 2.5.2, we derived the Dyson equation that relates the interacting Green's function G with the bare Green's function G_0. At two-particle level, there is a similar equation for the generalized susceptibility χ which plays an important role in linear response calculations, called the Bethe-Salpeter equation. Following Ref. [32], the Bethe-Salpeter equation can be derived by carrying out derivative of the single-particle Green's function $G^{(1)}$ directly (the superscript in $G^{(1)}$ will be dropped in the following derivation). From the Dyson equation Eq. 2.61

$$G(x_1; x_2) = G_0(x_1; x_2) + \int dx_3 dx_4 G_0(x_1; x_3) \Sigma(x_3; x_4) G(x_4; x_2) \,, \tag{2.87}$$

the derivative of the Green's function can be written as

$$\begin{aligned} \left. \frac{\delta G(x_2; x_1; J)}{\delta J(x_3, x_4)} \right|_{J=0} = \Bigg[& \frac{\delta G_0(x_2; x_1; J)}{\delta J(x_3, x_4)} \\ & + \frac{\delta}{\delta J(x_3, x_4)} \int dx'_3 dx'_4 G_0(x_2; x'_4; J) \Sigma(x'_4; x'_3; J) G(x'_3; x_1; J) \Bigg] \Bigg|_{J=0} \,. \end{aligned} \tag{2.88}$$

The derivatives in Eq. 2.88 can be carried out explicitly, giving the equation [32]

$$\begin{aligned} \left. \frac{\delta G(x_2; x_1; J)}{\delta J(x_3, x_4)} \right|_{J=0} &= -G(x_2; x_3) G(x_4; x_1) \\ &+ \int dx'_1 dx'_2 dx'_3 dx'_4 G(x_2; x'_3) G(x'_4; x_1) \frac{\delta \Sigma(x'_4; x'_3)}{\delta G(x'_2; x'_1)} \left. \frac{\delta G(x'_2; x'_1; J)}{\delta J(x_3, x_4)} \right|_{J=0} \,. \end{aligned} \tag{2.89}$$

Introducing the "irreducible" vertex function

$$\Gamma(x_2, x_4; x_1, x_3) = \frac{\delta \Sigma(x_2; x_1)}{\delta G(x_4; x_3)} \,, \tag{2.90}$$

and the “bare” susceptibilities

$$\chi_0^{=}(x_2,x_4;x_1,x_3) = G(x_2;x_1)G(x_4;x_3)\,, \tag{2.91}$$

$$\chi_0^{\times}(x_2,x_4;x_1,x_3) = -G(x_2;x_3)G(x_4;x_1)\,, \tag{2.92}$$

Eq. 2.89 can be written as a Dyson equation like equation for the generalized susceptibility χ

$$\begin{aligned}\chi(x_2,x_4;x_1,x_3) &= G^{(2)}(x_2,x_4;x_1,x_3) - \chi_0^{=}(x_2,x_4;x_1,x_3) \\ &= \chi_0^{\times}(x_2,x_4;x_1,x_3) \\ &\quad - \int dx_1'dx_2'dx_3'dx_4'\chi_0^{\times}(x_2,x_4';x_1,x_3')\Gamma(x_4',x_2';x_3',x_1')\chi(x_2',x_4;x_1',x_3)\,.\end{aligned} \tag{2.93}$$

Eq. 2.93 is called the Bethe-Salpeter equation. By construction, the “irreducible” vertex Γ contains all two-particle particle-hole irreducible diagrams. The application of this equation will be explained in detail in section 4.3 and chapter 5.

2.8 Schwinger-Dyson equation

Another useful field theoretical relation is the Schwinger-Dyson equation, which we will derive in this section follow Ref. [38]. Consider a partition function with general Grassmann fields $\varphi(x)$ and external source $J(x)$

$$Z[J] = \int \mathcal{D}[\phi]e^{-S+\int dy J(y)\varphi(y)}\,, \tag{2.94}$$

the value of $Z[J]$ is unchanged if we make an infinitesimal shift of the Grassmann field $\varphi(x) \to \varphi(x) + \delta\varphi(x)$,

$$0 = \delta Z[J] = \int \mathcal{D}[\varphi]e^{-S+\int dy J(y)\varphi(y)} \int dx \left(-\frac{\delta S}{\delta\varphi(x)} + J(x)\right)\delta\varphi(x)\,. \tag{2.95}$$

The derivative of $Z[J]$ with respect to J in the zero field limit can be carried out as

$$\frac{\delta}{\delta J(x_1)}\cdots\frac{\delta}{\delta J(x_n)}Z[J]\bigg|_{J=0} = \int \mathcal{D}[\varphi]e^{-S}\varphi(x_1)\cdots\varphi(x_n)\,. \tag{2.96}$$

By taking a series of derivatives of $\delta Z[J]$ with respect to J then setting $J = 0$, we get

$$0 = \int \mathcal{D}[\varphi] e^{-S} \int dx \left(-\frac{\delta S}{\delta \varphi(x)} \phi(x_1) \cdots \varphi(x_n) \right. \\ \left. + \sum_{j=1}^{n} \varphi(x_1) \cdots \varphi(x_{j-1}) \delta(x_j - x) \varphi(x_{j+1}) \cdots \varphi(x_n) \right) \delta\varphi(x) \, . \tag{2.97}$$

Dropping the arbitrary $\delta\varphi(x)$ and the integral over dx, we obtain the Schwinger-Dyson equation

$$\left\langle \frac{\delta S}{\delta \varphi(x)} \varphi(x_1) \cdots \varphi(x_n) \right\rangle = \left\langle \sum_{j=1}^{n} \varphi(x_1) \cdots \varphi(x_{j-1}) \delta(x_j - x) \varphi(x_{j+1}) \cdots \varphi(x_n) \right\rangle \, . \tag{2.98}$$

The application of this equation will be explained in section 3.6.

Chapter 3

Green's Functions and Symmetries

The many-particle Green's functions $G^{(n)}$ introduced in section 2.3 contains important physical information of a system. For example, from the single-particle (or one-particle) Green's functions $G^{(1)}$, which describe the physical processes associated with addition and removal of one electron, spectral functions and other one-particle observables such as density and energy can be extracted. In the mean time, using the two-particle Green's functions $G^{(2)}$, we can analyze how a system responds to external fields (see section 2.7). From Eq. 2.33, we can see that $G^{(n)}$ are explicit functions of the creation operator $c^\dagger(x)$, annihilation operator $c(x)$, and the Hamiltonian H. In general cases that allow for symmetry breaking, it can be written in the form

$$\begin{aligned} G^{(n)}(c, c^\dagger, H) &= G^{(n)}(x_1, \ldots, x_m; x'_1, \ldots, x'_k) \\ &= (-1)^s \langle \mathcal{T} c(x_1), \ldots, c(x_m) c^\dagger(x'_k) \ldots c^\dagger(x'_1) \rangle \,, \end{aligned} \tag{3.1}$$

where $m+k=2n$. Depending on the convention, the order of the operators can be different, and s can be either an even or odd number. Using the short-hand notation introduced in chapter 2, $x \equiv (i, \sigma, \tau)$ is a combined index for site (orbital) i, spin σ, and time τ, such that

$$c^{(\dagger)}(x) = c^{(\dagger)}_{i\sigma}(\tau) = e^{\tau H} c^{(\dagger)}_{i\sigma} e^{-\tau H} \,. \tag{3.2}$$

For clarity, we will label all the indices with number $1, \ldots 2n$ in the following derivations, and will only consider single orbital case so that i only labels the site. All the definitions and derivations can be generalized to multi-orbital case by adding an extra orbital index.

In this chapter, we will introduce general properties of the many-particle Green's functions, with a special focus on the single- and two-particle Green's functions in the singlet superconducting state, in which the condensation of Cooper pairs formed by two electrons or holes of opposite spins is allowed. Two types of spinors: the Bogoliubov-de Gennes (BdG) spinors [39] and the Nambu [4] spinors will be introduced in order to define the Green's functions in a compact form. Other physical quantities such as the generalized susceptibility and vertex function will also be derived and discussed in detail.

3.1 Symmetries

This section summarizes some of the useful symmetry relations of the single- and two-particle Green's functions without detailed derivations. The definitions and derivations closely follow Ref. [40].

Consider a similarity transform $\mathcal{U}$ in the Fock space, the creation and annihilation operators transform as

$$c'^{(\dagger)}_{i\sigma} = \mathcal{U}^{-1} c^{(\dagger)}_{i\sigma} \mathcal{U}\,, \quad c'^{(\dagger)}_{i\sigma}(\tau) = e^{\tau H} \mathcal{U}^{-1} c^{(\dagger)}_{i\sigma} \mathcal{U} e^{-\tau H}\,. \tag{3.3}$$

The transformed Green's function $G^{(n)}(c', c'^{\dagger}, H)$ is a function of c', $c'^{\dagger}$, and H, and the operator chain in the correlator can then be written as

$$\langle \ldots e^{\tau_j H} \mathcal{U}^{-1} c^{(\dagger)}_{i_j \sigma_j} \mathcal{U} e^{-\tau_j H} e^{\tau_l H} \mathcal{U}^{-1} c^{(\dagger)}_{i_l \sigma_l} \mathcal{U} e^{-\tau_l H} \ldots \rangle\,. \tag{3.4}$$

Combining the transformations between operators gives the transformation of the Hamiltonian H

$$\mathcal{U} e^{-\tau_j H} e^{\tau_l H} \mathcal{U}^{-1} = \mathcal{U} e^{-\tau_j H} \mathcal{U}^{-1} \mathcal{U} e^{\tau_l H} \mathcal{U}^{-1} = e^{-\tau_j H'} e^{\tau_l H'}\,, \quad H' = \mathcal{U} H \mathcal{U}^{-1}\,. \tag{3.5}$$

The two transformations at the left and right boundaries can also be combined using the cyclic property of the trace, which eventually gives the equality relation

$$G^{(n)}(c', c'^{\dagger}, H) = G^{(n)}(c, c^{\dagger}, H')\,. \tag{3.6}$$

The operator $\mathcal{U}$ can be called a symmetry of the system if it commutes with the Hamiltonian H. The transformed Hamiltonian H' then equals to the original Hamiltonian H

$$[\mathcal{U}, H] = 0\,, \quad \Rightarrow \quad H' = H\,, \tag{3.7}$$

which gives the equality between the Green's functions before and after transformation $G^{(n)}(c, c^{\dagger}, H') = G^{(n)}(c', c'^{\dagger}, H) = G^{(n)}(c, c^{\dagger}, H)$. This property provides the basis of symmetry analysis of the Green's functions.

3.1.1 Translation symmetry in time and space

For a system in equilibrium with a time independent Hamiltonian H, consider the time translation operator T_τ

$$T_\tau \coloneqq e^{-\tau H}\,, \quad \Rightarrow \quad [T_\tau, H] = 0\,. \tag{3.8}$$

We can transform the operators c and $c^\dagger$ with $\mathcal{U} = T_\tau$. The transformed Green's function reads

$$G'^{(n)}(c', c'^\dagger, H) = (-1)^s \langle e^{(\tau_1-\tau)H} c^{(\dagger)}_{i_1\sigma_1} e^{-(\tau_1-\tau)H} \dots e^{(\tau_{2n}-\tau)H} c^{(\dagger)}_{i_{2n}\sigma_{2n}} e^{-(\tau_{2n}-\tau)H} \rangle\,, \tag{3.9}$$

where we ordered the operators such that $\tau_1 > \tau_2 > \dots \tau_{2n} \geq \tau$. Since the time translational operator commutes with the time independent Hamiltonian, by choosing $\tau = \tau_{2n}$, we have

$$G^{(n)}(\tau_1, \dots, \tau_{2n-1}, \tau_{2n}) = G^{(n)}(\tau_1 - \tau_{2n}, \dots, \tau_{2n-1} - \tau_{2n}, 0)\,, \tag{3.10}$$

where all the site and spin indices are omitted.

In simple models like the Hubbard model, we usually have an analogues symmetry for the spatial degree of freedom, the space translation invariance, which means the system is invariant under a shift by lattice vector r

$$c'^{(\dagger)}_{r_i\sigma} = T_r^{-1} c^{(\dagger)}_{r_i\sigma} T_r = c^{(\dagger)}_{r_i+r,\sigma}\,. \tag{3.11}$$

This invariant gives

$$G^{(n)}(r_1, \dots, r_{2n-1}, r_{2n}) = G^{(n)}(r_1 - r_{2n}, \dots, r_{2n-1} - r_{2n}, r_0)\,, \tag{3.12}$$

where we dropped the unrelated time indices and r_0 is the origin of the lattice.

The time and space translarional invariance correspond to the energy and momentum conservations in Fourier space. The n-particle Green's function in momentum and frequency space can be written as

$$G^{(n)}(k_1\omega_{n_1}, \dots, k_{n_{2n}}\omega_{2n}) = \mathcal{F}[G^{(n)}(r_1\tau_1, \dots r_{2n}\tau_{2n})]\,, \tag{3.13}$$

where $\omega_n = \frac{(2n+1)\pi}{\beta}$ is the fermionic Matsubara frequency, and k labels the momentum of the operator. By defining $(\omega_n)_{c_i^{(\dagger)}}$ as the Matsubara frequency corresponds to the annihilation (creation) operator $c_i^{(\dagger)}$, $k_{c_i^{(\dagger)}}$ as the momentum index corresponds to the annihilation (creation) operator $c_i^{(\dagger)}$, the conservation laws can be written as

$$\sum_i (\omega_n)_{c_i} = \sum_j (\omega_n)_{c_j^\dagger}\,, \quad \sum_i k_{c_i} = \sum_j k_{c_j^\dagger}\,, \tag{3.14}$$

where i (j) runs through all the annihilation (creation) operators. A detailed proof of Eq. 3.14 is presented in Ref. [40].

3.1.2 SU(2) symmetry

For a system that is SU(2) symmetric, the Hamiltonian H commutes with all the spin operators $\hat{S}_i$

$$[H, \hat{S}_i] = 0\,, \quad i = x, y, z\,. \tag{3.15}$$

To define the spin operators $\hat{S}_i$, it is convinient to introduce the Pauli spinors

$$\phi_i = \begin{pmatrix} c_{i\uparrow} \\ c_{i\downarrow} \end{pmatrix}, \quad \phi_i^\dagger = \begin{pmatrix} c_{i\uparrow}^\dagger & c_{i\downarrow}^\dagger \end{pmatrix}, \tag{3.16}$$

where i labels site, and the Pauli matrices

$$\hat{\sigma}_x = \begin{pmatrix} 0 & 1 \\ 1 & 0 \end{pmatrix}, \quad \hat{\sigma}_y = \begin{pmatrix} 0 & -i \\ i & 0 \end{pmatrix}, \quad \hat{\sigma}_z = \begin{pmatrix} 1 & 0 \\ 0 & -1 \end{pmatrix}. \tag{3.17}$$

The Pauli matrices follow the commutation relation $[\hat{\sigma}_i, \hat{\sigma}_j] = 2i\sum_k \varepsilon_{ijk}\hat{\sigma}_k$, and the anti-commutation relation $\{\hat{\sigma}_i, \hat{\sigma}_j\} = 2\delta_{ij}\mathbb{I}_{2\times 2}$, where ε_{ijk} is the Levi-Civita symbol. The spin operators can then be defined as

$$\hat{S}_x = \frac{1}{2}\sum_j \phi_j^\dagger \hat{\sigma}_x \phi_j = \frac{1}{2}\sum_j (c_{j\uparrow}^\dagger c_{j\downarrow} + c_{j\downarrow}^\dagger c_{j\uparrow})\,, \tag{3.18a}$$

$$\hat{S}_y = \frac{1}{2}\sum_j \phi_j^\dagger \hat{\sigma}_y \phi_j = -\frac{i}{2}\sum_j (c_{j\uparrow}^\dagger c_{j\downarrow} - c_{j\downarrow}^\dagger c_{j\uparrow})\,, \tag{3.18b}$$

$$\hat{S}_z = \frac{1}{2}\sum_j \phi_j^\dagger \hat{\sigma}_z \phi_j = \frac{1}{2}\sum_j (c_{j\uparrow}^\dagger c_{j\uparrow} - c_{j\downarrow}^\dagger c_{j\downarrow})\,, \tag{3.18c}$$

where j is the site label. For completeness we also define

$$\hat{S}_0 = \frac{1}{2}\sum_j \phi_j^\dagger \hat{\sigma}_0 \phi_j = \frac{1}{2}\sum_j (c_{j\uparrow}^\dagger c_{j\uparrow} + c_{j\downarrow}^\dagger c_{j\downarrow})\,, \quad \hat{\sigma}_0 = \mathbb{I}_{2\times 2} = \begin{pmatrix} 1 & 0 \\ 0 & 1 \end{pmatrix}, \tag{3.19}$$

which is the density operator.

The first relation given by the SU(2) symmetry is the conservation of total spin in the n-particle Green's function $G^{(n)}$. While this relation holds for any arbitrary direction, we will only discuss the conservation along the z direction. By defining $\sigma_{c_i^{(\dagger)}}$ as the spin that corresponds to the annihilation (creation) operator $c_i^{(\dagger)}$, the conservation law can be written as

$$\sum_i \sigma_{c_i} = \sum_j \sigma_{c_j^\dagger} \,, \tag{3.20}$$

where i (j) runs through all the annihilation (creation) operators in $G^{(n)}$. A detailed proof of this relation can be found in Ref. [40].

Next we consider the generic SU(2) rotation of the Pauli spinor with a rotation operator

$$\mathcal{D}(\vec{n},\theta) = e^{-i\theta\vec{n}\cdot\vec{S}} \,, \quad \vec{n} \in \mathbb{R}^2,\, ||\vec{n}|| = 1,\, \theta \in [0, 2\pi) \,, \quad \vec{S} = (\hat{S}_x, \hat{S}_y, \hat{S}_z). \tag{3.21}$$

The transformation of Pauli spinors follow

$$\phi'^{(\dagger)}(\vec{n},\theta) = e^{i\theta\vec{n}\cdot\vec{S}}\phi^{(\dagger)}e^{-i\theta\vec{n}\cdot\vec{S}} \,. \tag{3.22}$$

The transformed spinor can be computed via the derivative with respect to the rotation angle θ

$$\frac{d}{d\theta}\phi'^{(\dagger)}(\vec{n},\theta) = ie^{i\theta\vec{n}\cdot\vec{S}}[(\vec{n}\cdot\vec{S})\phi^{(\dagger)} - \phi^{(\dagger)}(\vec{n}\cdot\vec{S})]e^{-i\theta\vec{n}\cdot\vec{S}} \overset{(+)}{=-} \frac{1}{2}i(\vec{n}\cdot\vec{\sigma}^{(T)})\phi'^{(\dagger)} \,, \tag{3.23}$$

where $\vec{\sigma}^{(T)} = (\hat{\sigma}_x^{(T)}, \hat{\sigma}_y^{(T)}, \hat{\sigma}_z^{(T)})$, and the minus (plus) sign is associated with ϕ ($\phi^\dagger$). This differential equation has a solution of

$$\phi'^{(\dagger)}(\vec{n},\theta) = e^{\overset{(+)}{-} i\frac{\theta}{2}\vec{n}\cdot\vec{\sigma}^{(T)}}\phi^{(\dagger)} = \left[\cos\left(\frac{\theta}{2}\right)\mathbb{I} \overset{(+)}{-} i\sin\left(\frac{\theta}{2}\right)\vec{n}\cdot\vec{\sigma}^{(T)}\right]\phi^{(\dagger)}(\vec{n},0) \,. \tag{3.24}$$

We consider the rotation along y axis with $\vec{n} = (0,1,0)^T$, which yields

$$\begin{pmatrix} c_\uparrow'^{(\dagger)} \\ c_\downarrow'^{(\dagger)} \end{pmatrix} = \begin{pmatrix} \cos\left(\frac{\theta}{2}\right) & -\sin\left(\frac{\theta}{2}\right) \\ \sin\left(\frac{\theta}{2}\right) & \cos\left(\frac{\theta}{2}\right) \end{pmatrix} \begin{pmatrix} c_\uparrow^{(\dagger)} \\ c_\downarrow^{(\dagger)} \end{pmatrix} \,. \tag{3.25}$$

Relations between operators with different spins can be obtained with two special choices of the rotation angle θ

- $\theta = \pi$, corresponding to spin flip, gives

$$c'^{(\dagger)}_{\sigma} = -2\sigma c^{(\dagger)}_{-\sigma}\,, \quad (2\sigma = \pm 1)\,. \tag{3.26}$$

- $\theta = \frac{\pi}{2}$, corresponding to a spin in z direction is transformed to x direction, gives

$$c'^{(\dagger)}_{\sigma} = \frac{1}{\sqrt{2}}(c^{(\dagger)}_{\sigma} - 2\sigma c^{(\dagger)}_{-\sigma})\,, \quad (2\sigma = \pm 1)\,. \tag{3.27}$$

We will explain how these two relations can be applied to the single- and two-particle Green's functions in section 3.2.

3.1.3 U(1) symmetry

The U(1) group corresponds to the unitary group of degree one, which can be represented by one dimensional unitary matrices $\{e^{i\theta}\}$ with $\theta \in [0, 2\pi)$. The U(1) symmetry is always discussed with the gauge transformation. Under a gauge transformation, creation and annihilation operators for electrons transform like wave functions [41]

$$c_{\sigma} \to e^{ie\alpha} c_{\sigma} = c'_{\sigma}\,, \quad c^{\dagger}_{\sigma} \to e^{-ie\alpha} c^{\dagger}_{\sigma} = c'^{\dagger}_{\sigma}\,, \tag{3.28}$$

where e is the electron charge, α is an arbitrary angle.

For the n-particle Green's functions $G^{(n)}$ defined in Eq. 3.1, if it contains equal numbers of creation and annihilation operators ($m = k$), it will be invariant after the gauge transformation, so that the U(1) symmetry is preserved. For "anomalous" Green's functions with $m \neq k$, the Green's functions after transformation will pick up an extra phase factor $G^{(n)}(c', c'^{\dagger}) = e^{i(m-k)e\alpha} G^{(n)}(c, c^{\dagger})$, and the U(1) symmetry is broken.

3.2 Single- and two-particle Green's functions

In this section, we will define and discuss the single- and two-particle Green's functions in the singlet superconducting state. The discussion of paramagnetic state Green's functions can be found in Ref. [40, 42].

3.2.1 Spinors and single-particle Green's functions

To define the single-particle Green's functions in the singlet superconducting state, we define the BdG spinors [39] in site space

$$\Phi_i = \begin{pmatrix} c_{i\uparrow} \\ c_{i\downarrow} \\ c^\dagger_{i\uparrow} \\ c^\dagger_{i\downarrow} \end{pmatrix} = \left(\frac{\phi_i}{(\phi_i^\dagger)^T} \right) , \quad \Phi_i^\dagger = \begin{pmatrix} c^\dagger_{i\uparrow} & c^\dagger_{i\downarrow} & c_{i\uparrow} & c_{i\downarrow} \end{pmatrix} = \left(\phi_i^\dagger \,\middle|\, \phi_i^T \right) . \tag{3.29}$$

where $\phi_i^{(\dagger)}$ are the Pauli spinors defined in Eq. 3.16. The Fourier transformations of the BdG spinors give

$$\Phi_k = \frac{1}{\sqrt{N}} \sum_i e^{-ik\cdot r_i} \Phi_i = \begin{pmatrix} c_{k\uparrow} \\ c_{k\downarrow} \\ c^\dagger_{-k\uparrow} \\ c^\dagger_{-k\downarrow} \end{pmatrix} , \quad \Phi_k^\dagger = \frac{1}{\sqrt{N}} \sum_i e^{ik\cdot r_i} \Phi_i^\dagger = \begin{pmatrix} c^\dagger_{k\uparrow} & c^\dagger_{k\downarrow} & c_{-k\uparrow} & c_{-k\downarrow} \end{pmatrix} , \tag{3.30}$$

where N is the number of lattice sites. With the BdG spinors, the single-particle Green's function matrix can be written as

$$\begin{aligned} \underline{\mathbf{G}}_{ij}(\tau,\tau') &= -\langle \mathcal{T} \Phi_i(\tau)\Phi_j^\dagger(\tau') \rangle \\ &= -\left\langle \mathcal{T} \begin{pmatrix} c_{i\uparrow}(\tau)c^\dagger_{j\uparrow}(\tau') & c_{i\uparrow}(\tau)c^\dagger_{j\downarrow}(\tau') & c_{i\uparrow}(\tau)c_{j\uparrow}(\tau') & c_{i\uparrow}(\tau)c_{j\downarrow}(\tau') \\ c_{i\downarrow}(\tau)c^\dagger_{j\uparrow}(\tau') & c_{i\downarrow}(\tau)c^\dagger_{j\downarrow}(\tau') & c_{i\downarrow}(\tau)c_{j\uparrow}(\tau') & c_{i\downarrow}(\tau)c_{j\downarrow}(\tau') \\ c^\dagger_{i\uparrow}(\tau)c^\dagger_{j\uparrow}(\tau') & c^\dagger_{i\uparrow}(\tau)c^\dagger_{j\downarrow}(\tau') & c^\dagger_{i\uparrow}(\tau)c_{j\uparrow}(\tau') & c^\dagger_{i\uparrow}(\tau)c_{j\downarrow}(\tau') \\ c^\dagger_{i\downarrow}(\tau)c^\dagger_{j\uparrow}(\tau') & c^\dagger_{i\downarrow}(\tau)c^\dagger_{j\downarrow}(\tau') & c^\dagger_{i\downarrow}(\tau)c_{j\uparrow}(\tau') & c^\dagger_{i\downarrow}(\tau)c_{j\downarrow}(\tau') \end{pmatrix} \right\rangle , \end{aligned} \tag{3.31}$$

which has $4 \times 4 = 16$ terms that include all the possible combinations of operators c_σ and $c^\dagger_\sigma$. With the SU(2) symmetry preserved in the singlet superconducting state, we can simplify the matrix above to a matrix with only four terms:

- According to the spin conservation given by Eq. 3.20, only the eight terms on the diagonal and anti-diagonal will be non-zero.
- According to the spin flip relation given by Eq. 3.26, the remaining eight terms can be grouped into four groups, each containing two terms equal to each other up to a minus

sign

$$\langle \mathcal{T} c_{i\uparrow}(\tau) c^{\dagger}_{j\uparrow}(\tau') \rangle = \langle \mathcal{T} c_{i\downarrow}(\tau) c^{\dagger}_{j\downarrow}(\tau') \rangle \,, \tag{3.32a}$$
$$\langle \mathcal{T} c^{\dagger}_{i\downarrow}(\tau) c_{j\downarrow}(\tau') \rangle = \langle \mathcal{T} c^{\dagger}_{i\uparrow}(\tau) c_{j\uparrow}(\tau') \rangle \,, \tag{3.32b}$$
$$\langle \mathcal{T} c_{i\uparrow}(\tau) c_{j\downarrow}(\tau') \rangle = -\langle \mathcal{T} c_{i\downarrow}(\tau) c_{j\uparrow}(\tau') \rangle \,, \tag{3.32c}$$
$$\langle \mathcal{T} c^{\dagger}_{i\downarrow}(\tau) c^{\dagger}_{j\uparrow}(\tau') \rangle = -\langle \mathcal{T} c^{\dagger}_{i\uparrow}(\tau) c^{\dagger}_{j\downarrow}(\tau') \rangle \,. \tag{3.32d}$$

With these relations, the 4 × 4 matrix in Eq. 3.31 can be block-diagonalized into two 2 × 2 blocks [43, 44]. Taking one of the blocks, the single-particle Green's functions can be defined using the Nambu spinors [4]

$$\psi_i = \begin{pmatrix} c_{i\uparrow} \\ c^{\dagger}_{i\downarrow} \end{pmatrix} \,, \quad \psi^{\dagger}_i = \begin{pmatrix} c^{\dagger}_{i\uparrow} & c_{i\downarrow} \end{pmatrix} \,, \tag{3.33}$$
$$\psi_k = \begin{pmatrix} c_{k\uparrow} \\ c^{\dagger}_{-k\downarrow} \end{pmatrix} \,, \quad \psi^{\dagger}_k = \begin{pmatrix} c^{\dagger}_{k\uparrow} & c_{-k\downarrow} \end{pmatrix} \,, \tag{3.34}$$

which give a compact matrix

$$\underline{G}_{ij}(\tau, \tau') = -\langle \mathcal{T} \psi_i(\tau) \psi^{\dagger}_j(\tau') \rangle = -\langle \mathcal{T} \begin{pmatrix} c_{i\uparrow}(\tau) c^{\dagger}_{j\uparrow}(\tau') & c_{i\uparrow}(\tau) c_{j\downarrow}(\tau') \\ c^{\dagger}_{i\downarrow}(\tau) c^{\dagger}_{j\uparrow}(\tau') & c^{\dagger}_{i\downarrow}(\tau) c_{j\downarrow}(\tau') \end{pmatrix} \rangle \,. \tag{3.35}$$

The two diagonal terms in Eq. 3.35 are usually called the "normal" (N) components and the two off-diagonal terms are usually called the "anomalous" (A) components. The relation between the normal components in $\underline{G}_{ij}(\tau, \tau')$ and the single-particle Green's function defined as $G_{ij,\sigma}(\tau, \tau') = -\langle \mathcal{T} c_{i,\sigma}(\tau) c^{\dagger}_{j,\sigma}(\tau') \rangle$ can be written as

$$G_{ij,00}(\tau, \tau') = G_{ij,\uparrow}(\tau, \tau') \,, \tag{3.36a}$$
$$G_{ij,11}(\tau, \tau') = -G_{ji,\downarrow}(\tau', \tau) \,. \tag{3.36b}$$

The time and space translational invariance explained in Eqs. 3.11 and 3.12 show that the single-particle Green's functions can be simplified to a form with only one time and one space index

$$\underline{G}_{ij}(\tau, \tau') \rightarrow \underline{G}_{r}(\tau - \tau') \,, \quad r = r_i - r_j \,, \tag{3.37}$$

which impose energy and momentum conservations in the frequency and the momentum space, as given by Eq. 3.14. Therefor, the single-particle Green's functions only depend on one momentum and one frequency index in the Fourier space

$$\begin{aligned}\underline{G}_{kk'}(\tau,\tau') &= \sum_{r_i r_j} e^{-i(k\cdot r_i - k'\cdot r_j)}\underline{G}_{r_i r_j}(\tau,\tau') = \sum_{r_i r_j} e^{-ik\cdot(r_i-r_j)+i(k'-k)\cdot r_j}\underline{G}_{r_i-r_j}(\tau,\tau') \\ &= \frac{(2\pi)^d}{V}\delta(k-k')\sum_r e^{-ik\cdot r}\underline{G}_r(\tau,\tau') = \frac{(2\pi)^d}{V}\delta(k-k')\underline{G}_k(\tau,\tau')\,, \end{aligned} \tag{3.38a}$$

$$\underline{G}_k(\tau,\tau') = -\langle\mathcal{T}\begin{pmatrix} c_{k\uparrow}(\tau)c^\dagger_{k\uparrow}(\tau') & c_{k\uparrow}(\tau)c_{-k\downarrow}(\tau') \\ c^\dagger_{-k\downarrow}(\tau)c^\dagger_{k\uparrow}(\tau') & c^\dagger_{-k\downarrow}(\tau)c_{-k\downarrow}(\tau') \end{pmatrix}\rangle\,. \tag{3.38b}$$

$$\begin{aligned}\underline{G}_k(i\omega_n, i\omega'_n) &= \iint_0^\beta d\tau d\tau' e^{i(\omega_n\tau-\omega'_n\tau')}\underline{G}_k(\tau,\tau') \\ &= \iint_0^\beta d\tau d\tau' e^{i\omega_n(\tau-\tau')-i(\omega'_n-\omega_n)\tau'}\underline{G}_k(\tau-\tau') \\ &= \beta\delta_{\omega_n,\omega'_n}\int_0^\beta d\tau e^{i\omega_n\tau}\underline{G}_k(\tau) = \beta\delta_{\omega_n,\omega'_n}\underline{G}_k(i\omega_n)\,, \end{aligned} \tag{3.39}$$

where V is the volume of the unit cell, and $\omega_n = \frac{(2n+1)\pi}{\beta}$ is the fermionic Matsubara frequency. For simplicity, in SU(2) symmetric case, we will only work with the 2×2 Green's function matrix $\underline{G}_k(i\omega_n)$ [Eq. 3.39] and the corresponding self-energy matrix $\underline{\Sigma}_k(i\omega_n)$. The Dyson equation for the matrix Green's function [Eq. 2.60] is diagonal in momentum and frequency space, and can be written as [4, 43]

$$\underline{G}_k^{-1}(i\omega_n) = \underline{G}_{0,k}^{-1}(i\omega_n) - \underline{\Sigma}_k(i\omega_n)\,, \tag{3.40}$$

where $\underline{G}_{0,k}(i\omega_n)$ is the non-interacting Green's function matrix.

For clarity, we will use sub-indices 00, 01, 10, 11 to label the four terms in the 2×2 matrices and move the momentum label into parenthesis in the derivations in this chapter.

3.2.2 Two-particle Green's functions

The two-particle Green's functions in the singlet superconducting state take the form

$$G^{(2)}(x_1,x_2,x_3,x_4) = \langle\mathcal{T}c^{(\dagger)}(x_1)c^{(\dagger)}(x_2)c^{(\dagger)}(x_3)c^{(\dagger)}(x_4)\rangle\,, \tag{3.41}$$

where each operator $c^{(\dagger)}(x) \in \{c_{i\uparrow}(\tau), c^\dagger_{i\uparrow}(\tau), c_{i\downarrow}(\tau), c^\dagger_{i\downarrow}(\tau)\}$ can be either a creation or an annihilation operator with spin up or spin down. With fixed site indices, there are in total $4^4 = 256$ different combinations.

To generate the matrix that contains all possible two-particle Green's functions, we define the generalized Nambu spinors with an extra spin dependence

$$\psi_{i,\sigma} = \begin{pmatrix} c_{i,\sigma} \\ c^\dagger_{i,-\sigma} \end{pmatrix} , \quad \psi^\dagger_{i,\sigma} = \begin{pmatrix} c^\dagger_{i,\sigma} & c_{i,-\sigma} \end{pmatrix} , \tag{3.42}$$

$$\psi_{k,\sigma} = \begin{pmatrix} c_{k,\sigma} \\ c^\dagger_{-k,-\sigma} \end{pmatrix} , \quad \psi^\dagger_{k,\sigma} = \begin{pmatrix} c^\dagger_{k,\sigma} & c_{-k,-\sigma} \end{pmatrix} , \tag{3.43}$$

and the shuffled BdG spinors

$$\Psi_i = \begin{pmatrix} c_{i\uparrow} \\ c^\dagger_{i\downarrow} \\ c_{i\downarrow} \\ c^\dagger_{i\uparrow} \end{pmatrix} = \begin{pmatrix} \psi_{i\uparrow} \\ \hline \psi_{i\downarrow} \end{pmatrix} , \quad \Psi^\dagger_i = \begin{pmatrix} c^\dagger_{i\uparrow} & c_{i\downarrow} & c^\dagger_{i\downarrow} & c_{i\uparrow} \end{pmatrix} = \left(\psi^\dagger_{i\uparrow} \,\middle|\, \psi^\dagger_{i\downarrow} \right) . \tag{3.44}$$

Using these spinors, we are be able to define the two-particle Green's functions using a matrix with a two-level structure, and identify a subset of representative terms with the preserved SU(2) symmetry. For simplicity we will use the combined index $1 \equiv (i_1, \tau_1)$ in the following derivation.

We generate all possible two-particle Green's functions with the Tracy–Singh products $\circ$ [45] of the shuffled BdG spinors. The Tracy–Singh product operates on partitioned matrices and can be considered as Kronecker product at block-level

$$\begin{aligned} \underline{\mathbf{G}}^{(2)}(1234) &= \langle \mathcal{T} \Psi^\dagger_1 \circ \Psi_2 \circ \Psi^\dagger_3 \circ \Psi_4 \rangle \\ &= \left\langle \mathcal{T} \begin{pmatrix} \overbrace{\psi^\dagger_{1\uparrow} \otimes \psi_{2\uparrow} \otimes \psi^\dagger_{3\uparrow} \otimes \psi_{4\uparrow}}^{00} & \psi^\dagger_{1\uparrow} \otimes \psi_{2\uparrow} \otimes \psi^\dagger_{3\downarrow} \otimes \psi_{4\uparrow} & \psi^\dagger_{1\downarrow} \otimes \psi_{2\uparrow} \otimes \psi^\dagger_{3\uparrow} \otimes \psi_{4\uparrow} & \psi^\dagger_{1\downarrow} \otimes \psi_{2\uparrow} \otimes \psi^\dagger_{3\downarrow} \otimes \psi_{4\uparrow} \\ \psi^\dagger_{1\uparrow} \otimes \psi_{2\uparrow} \otimes \psi^\dagger_{3\uparrow} \otimes \psi_{4\downarrow} & \overbrace{\psi^\dagger_{1\uparrow} \otimes \psi_{2\uparrow} \otimes \psi^\dagger_{3\downarrow} \otimes \psi_{4\downarrow}}^{11} & \overbrace{\psi^\dagger_{1\downarrow} \otimes \psi_{2\uparrow} \otimes \psi^\dagger_{3\uparrow} \otimes \psi_{4\downarrow}}^{12} & \psi^\dagger_{1\downarrow} \otimes \psi_{2\uparrow} \otimes \psi^\dagger_{3\downarrow} \otimes \psi_{4\downarrow} \\ \psi^\dagger_{1\uparrow} \otimes \psi_{2\downarrow} \otimes \psi^\dagger_{3\uparrow} \otimes \psi_{4\uparrow} & \overbrace{\psi^\dagger_{1\uparrow} \otimes \psi_{2\downarrow} \otimes \psi^\dagger_{3\downarrow} \otimes \psi_{4\uparrow}}^{21} & \overbrace{\psi^\dagger_{1\downarrow} \otimes \psi_{2\downarrow} \otimes \psi^\dagger_{3\uparrow} \otimes \psi_{4\uparrow}}^{22} & \psi^\dagger_{1\downarrow} \otimes \psi_{2\downarrow} \otimes \psi^\dagger_{3\downarrow} \otimes \psi_{4\uparrow} \\ \psi^\dagger_{1\uparrow} \otimes \psi_{2\downarrow} \otimes \psi^\dagger_{3\uparrow} \otimes \psi_{4\downarrow} & \psi^\dagger_{1\uparrow} \otimes \psi_{2\downarrow} \otimes \psi^\dagger_{3\downarrow} \otimes \psi_{4\downarrow} & \psi^\dagger_{1\downarrow} \otimes \psi_{2\downarrow} \otimes \psi^\dagger_{3\uparrow} \otimes \psi_{4\downarrow} & \overbrace{\psi^\dagger_{1\downarrow} \otimes \psi_{2\downarrow} \otimes \psi^\dagger_{3\downarrow} \otimes \psi_{4\downarrow}}^{33} \end{pmatrix} \right\rangle , \end{aligned} \tag{3.45}$$

where $\otimes$ is the Kronecker product, and $\underline{\mathbf{G}}^{(2)}(1234)$ includes sixteen 4×4 matrices. With the preserved SU(2) symmetry in the singlet superconducting state, we only need to consider a subset of the sixteen matrices

- According to the spin conservation given by Eq. 3.20, only the six matrices that satisfy $\sum_i \sigma_{\psi_i} = \sum_j \sigma_{\psi^\dagger_j}$ will be non zero, which are the 00, 11, 22, 33, 12, 21 terms in the matrix above.

- According to the spin flip relation given by Eq. 3.26, correlators with even number of spin up and spin down operators will be invariant under spin flip, while correlators with odd number of spin up and spin down operators will pick up an extra minus sign. For all terms that fulfill spin conservation, even (odd) number of spin up and down operators also correspond to even (odd) number of creation and annihilation operators. Therefore, we can choose three matrices from the six non-zero matrices as representatives

$$\underline{G}^{(2)}_{00}(1234) = \underline{G}^{(2)}_{\uparrow\uparrow\uparrow\uparrow}(1234) = \langle \mathcal{T}\psi^{\dagger}_{1\uparrow} \otimes \psi_{2\uparrow} \otimes \psi^{\dagger}_{3\uparrow} \otimes \psi_{4\uparrow} \rangle\,, \tag{3.46a}$$

$$\underline{G}^{(2)}_{11}(1234) = \underline{G}^{(2)}_{\uparrow\uparrow\downarrow\downarrow}(1234) = \langle \mathcal{T}\psi^{\dagger}_{1\uparrow} \otimes \psi_{2\uparrow} \otimes \psi^{\dagger}_{3\downarrow} \otimes \psi_{4\downarrow} \rangle\,, \tag{3.46b}$$

$$\underline{G}^{(2)}_{21}(1234) = \underline{G}^{(2)}_{\uparrow\downarrow\downarrow\uparrow}(1234) = \langle \mathcal{T}\psi^{\dagger}_{1\uparrow} \otimes \psi_{2\downarrow} \otimes \psi^{\dagger}_{3\downarrow} \otimes \psi_{4\uparrow} \rangle\,. \tag{3.46c}$$

  For convenience we define the spin labels as in Ref. [42]

$$\underline{G}^{(2)}_{\sigma\sigma'}(1234) \equiv \underline{G}^{(2)}_{\sigma\sigma\sigma'\sigma'}(1234)\,, \tag{3.47a}$$

$$\underline{G}^{(2)}_{\overline{\sigma\sigma'}}(1234) \equiv \underline{G}^{(2)}_{\sigma\sigma'\sigma'\sigma}(1234)\,. \tag{3.47b}$$

- According to the $\frac{\pi}{2}$ spin rotation relation given by Eq. 3.27, the rotation of the annihilation (creation) operators provides the relations

$$c'^{(\dagger)}_{\uparrow} = \frac{1}{\sqrt{2}}(c^{(\dagger)}_{\uparrow} + c^{(\dagger)}_{\downarrow})\,, \quad c'^{(\dagger)}_{\downarrow} = \frac{1}{\sqrt{2}}(c^{(\dagger)}_{\downarrow} - c^{(\dagger)}_{\uparrow})\,. \tag{3.48}$$

  Take the 00 term in each matrix as an example, which is in the form of $\langle c^{\dagger}_{\sigma_1} c_{\sigma_2} c^{\dagger}_{\sigma_3} c_{\sigma_4} \rangle$, the spin conservation and the spin flip relations give

$$\begin{aligned} & G^{(2)}_{\uparrow\uparrow,00}(1234) = G^{(2)}_{\uparrow\downarrow,00}(1234) + G^{(2)}_{\overline{\uparrow\downarrow},00}(1234)\,, \\ \Rightarrow\quad & G^{(2)}_{\overline{\uparrow\downarrow},00}(1234) = G^{(2)}_{\uparrow\uparrow,00}(1234) - G^{(2)}_{\uparrow\downarrow,00}(1234)\,. \end{aligned} \tag{3.49}$$

  All the other terms in the $\underline{G}^{(2)}_{\overline{\uparrow\downarrow}}(1234)$ matrix can be expressed as linear combinations of terms in the $\underline{G}^{(2)}_{\uparrow\uparrow}(1234)$ and $\underline{G}^{(2)}_{\uparrow\downarrow}(1234)$ matrices in a similar way. In most cases, we only need to consider the following two spin configurations

$$\underline{G}^{(2)}_{\uparrow\uparrow}(1234) = \langle \mathcal{T}\psi^{\dagger}_{1\uparrow} \otimes \psi_{2\uparrow} \otimes \psi^{\dagger}_{3\uparrow} \otimes \psi_{4\uparrow} \rangle\,, \tag{3.50a}$$

$$\underline{G}^{(2)}_{\uparrow\downarrow}(1234) = \langle \mathcal{T}\psi^{\dagger}_{1\uparrow} \otimes \psi_{2\uparrow} \otimes \psi^{\dagger}_{3\downarrow} \otimes \psi_{4\downarrow} \rangle\,. \tag{3.50b}$$

The Fourier transformation of the two-particle Green's function matrix $\underline{G}^{(2)}_{\sigma\sigma'}$ can be written out explicitly as

$$
\begin{aligned}
&\underline{G}^{(2)}_{\sigma\sigma'}(k_1\omega_1, k_2\omega_2, k_3\omega_3, k_4\omega_4) \\
&= \sum_{r_1 r_2 r_3 r_4} \iiiint_0^{\beta} d\tau_1 d\tau_2 d\tau_3 d\tau_4 \underline{G}^{(2)}_{\sigma\sigma'}(r_1\tau_1, r_2\tau_2, r_3\tau_3, r_4\tau_4) \\
&\qquad\qquad \times e^{-i(\omega_1\tau_1 - \omega_2\tau_2 + \omega_3\tau_3 - \omega_4\tau_4)} e^{i(k_1\cdot r_1 - k_2\cdot r_2 + k_3\cdot r_3 - k_4\cdot r_4)} \,.
\end{aligned} \tag{3.51}
$$

The time and space translational invariance given in Eqs. 3.11 and 3.12 show that the two-particle Green's functions can be simplified to a form with only three independent time and space indices. This impose momentum and energy conservation relations given by

$$
\sum_i (\omega_n)_{\psi_i} = \sum_j (\omega_n)_{\psi_j^\dagger} \,, \quad \sum_i k_{\psi_i} = \sum_j k_{\psi_j^\dagger} \,, \tag{3.52}
$$

which can be proved in a similar way as in Eqs. 3.38 and 3.39, and give two-particle Green's functions that only depend on three independent momenta (k, k', q) and frequencies $(\omega_n, \omega'_n, \nu_n)$ in the Fourier space. Following the particle-hole notation in Ref. [42], the four momentum and frequency indices in Eq. 3.51 can be chosen as

$$
k_1 = k \,, \quad k_2 = k + q \,, \quad k_3 = k' + q \,, \quad k_4 = k' \,, \tag{3.53a}
$$

$$
\omega_1 = \omega_n \,, \quad \omega_2 = \omega_n + \nu_n \,, \quad \omega_3 = \omega'_n + \nu_n \,, \quad \omega_4 = \omega'_n \,, \tag{3.53b}
$$

where $\omega_n = \frac{(2n+1)\pi}{\beta}$ is the fermionic Matsubara frequency, and $\nu_n = \frac{2n\pi}{\beta}$ is the bosonic Matsubara frequency.

To further analyze the structure of the two-particle Green's functions, we write out the 4×4 matrices explicitly. Introducing combined index 1 as short-hand notation of x_1 to represent either (i_1, τ_1, σ_1) or (k_1, τ_1, σ_1), and -1 to represent either $(i_1, \tau_1, -\sigma_1)$ or $(-k_1, \tau_1, -\sigma_1)$, any two-particle Green's function matrix given by the kronecker product of Nambu spinors is in the form

$$
\begin{aligned}
\underline{G}^{(2)}(1234) &= \langle \mathcal{T} \psi_1^\dagger \otimes \psi_2 \otimes \psi_3^\dagger \otimes \psi_4 \rangle \\
&= \left\langle \mathcal{T} \begin{pmatrix}
c_1^\dagger c_2 c_3^\dagger c_4 & c_1^\dagger c_2 c_{\text{-}3} c_4 & c_{\text{-}1} c_2 c_3^\dagger c_4 & c_{\text{-}1} c_2 c_{\text{-}3} c_4 \\
c_1^\dagger c_2 c_3^\dagger c_{\text{-}4}^\dagger & c_1^\dagger c_2 c_{\text{-}3} c_{\text{-}4}^\dagger & c_{\text{-}1} c_2 c_3^\dagger c_{\text{-}4}^\dagger & c_{\text{-}1} c_2 c_{\text{-}3} c_{\text{-}4}^\dagger \\
c_1^\dagger c_{\text{-}2}^\dagger c_3^\dagger c_4 & c_1^\dagger c_{\text{-}2}^\dagger c_{\text{-}3} c_4 & c_{\text{-}1} c_{\text{-}2}^\dagger c_3^\dagger c_4 & c_{\text{-}1} c_{\text{-}2}^\dagger c_{\text{-}3} c_4 \\
c_1^\dagger c_{\text{-}2}^\dagger c_3^\dagger c_{\text{-}4}^\dagger & c_1^\dagger c_{\text{-}2}^\dagger c_{\text{-}3} c_{\text{-}4}^\dagger & c_{\text{-}1} c_{\text{-}2}^\dagger c_3^\dagger c_{\text{-}4}^\dagger & c_{\text{-}1} c_{\text{-}2}^\dagger c_{\text{-}3} c_{\text{-}4}^\dagger
\end{pmatrix} \right\rangle \,.
\end{aligned} \tag{3.54}
$$

Each term in the $\underline{G}^{(2)}(1234)$ matrix can be decomposed into a disconnected and a connected part

$$\underline{G}^{(2)}(1234) = \underline{G}^{(2)}_{0}(1234) + \underline{G}^{(2)}_{\mathrm{conn}}(1234)\,, \tag{3.55}$$

where the disconnected part is labeled by the subscript 0 since it can be evaluated using the Wick's theorem as the non-interacting two-particle Green's function. The disconnected part of the two-particle Green's function $\langle \mathcal{T} c_1^{(\dagger)} c_2^{(\dagger)} c_3^{(\dagger)} c_4^{(\dagger)} \rangle$ contains three different terms

- The direct term $\chi_0^{=}$: $\langle \mathcal{T}\, \overbracket{c_1^{(\dagger)} c_2^{(\dagger)}}\, \overbracket{c_3^{(\dagger)} c_4^{(\dagger)}} \rangle = \langle \mathcal{T} c_2^{(\dagger)} c_1^{(\dagger)} \rangle \langle \mathcal{T} c_4^{(\dagger)} c_3^{(\dagger)} \rangle$.
- The first exchange term $\chi_0^{\times}$: $\langle \mathcal{T}\, \overbracket{c_1^{(\dagger)} \underbracket{c_2^{(\dagger)} c_3^{(\dagger)}} c_4^{(\dagger)}} \rangle = -\langle \mathcal{T} c_4^{(\dagger)} c_1^{(\dagger)} \rangle \langle \mathcal{T} c_2^{(\dagger)} c_3^{(\dagger)} \rangle$.
- The second exchange term $\chi_0^{\times}$: $\langle \mathcal{T}\, \overbracket{c_1^{(\dagger)} \underbracket{c_2^{(\dagger)} c_3^{(\dagger)}\, c_4^{(\dagger)}}} \rangle = \langle \mathcal{T} c_3^{(\dagger)} c_1^{(\dagger)} \rangle \langle \mathcal{T} c_2^{(\dagger)} c_4^{(\dagger)} \rangle$.

Only one of the two exchange terms is non-zero for each two-particle Green's function due to spin conservation. Take the 00 term as an example and write out the spin indices explicitly, we have

$$\begin{aligned}
\langle \mathcal{T} c^\dagger_{1\uparrow} c_{2\uparrow} c^\dagger_{3\uparrow} c_{4\uparrow} \rangle_0 &= \langle \mathcal{T} c_{2\uparrow} c^\dagger_{1\uparrow} \rangle \langle \mathcal{T} c_{4\uparrow} c^\dagger_{3\uparrow} \rangle - \langle \mathcal{T} c_{4\uparrow} c^\dagger_{1\uparrow} \rangle \langle \mathcal{T} c_{2\uparrow} c^\dagger_{3\uparrow} \rangle + \langle \mathcal{T} c^\dagger_{3\uparrow} c^\dagger_{1\uparrow} \rangle \langle \mathcal{T} c_{2\uparrow} c_{4\uparrow} \rangle \\
&= G_{00}(2,1) G_{00}(4,3) - G_{00}(4,1) G_{00}(2,3) + 0\,, \qquad (3.56\text{a}) \\
\langle \mathcal{T} c^\dagger_{1\uparrow} c_{2\uparrow} c^\dagger_{3\downarrow} c_{4\downarrow} \rangle_0 &= -\langle \mathcal{T} c_{2\uparrow} c^\dagger_{1\uparrow} \rangle \langle \mathcal{T} c^\dagger_{3\downarrow} c_{4\downarrow} \rangle - \langle \mathcal{T} c_{4\downarrow} c^\dagger_{1\uparrow} \rangle \langle \mathcal{T} c_{2\uparrow} c^\dagger_{3\downarrow} \rangle + \langle \mathcal{T} c^\dagger_{3\downarrow} c^\dagger_{1\uparrow} \rangle \langle \mathcal{T} c_{2\uparrow} c_{4\downarrow} \rangle \\
&= -G_{00}(2,1) G_{11}(-3,-4) - 0 + G_{10}(-3,1) G_{01}(2,-4)\,, \qquad (3.56\text{b})
\end{aligned}$$

where the spin indices are dropped from the combined indices $1 \equiv (k_1, \tau_1)$, $-1 \equiv (-k_1, \tau_1)$.

With the momentum and frequency conventions introduced in Eq. 3.53, the two-particle Green's function matrices can be written out explicitly. For $\sigma = \sigma' = \uparrow$, the two-particle Green's function matrix $\underline{G}^{(2)}_{\uparrow\uparrow}$ reads

$$\underline{G}^{(2)}_{\uparrow\uparrow}(k, k+q, k'+q, k') = \langle \mathcal{T} \psi^\dagger_{k\uparrow}(\tau_1) \otimes \psi_{k+q\uparrow}(\tau_2) \otimes \psi^\dagger_{k'+q\uparrow}(\tau_3) \otimes \psi_{k'\uparrow}(\tau_4) \rangle = \tag{3.57}$$

$$\left\langle \mathcal{T} \begin{pmatrix}
c^\dagger_{k\uparrow} c_{k+q\uparrow} c^\dagger_{k'+q\uparrow} c_{k'\uparrow} & c^\dagger_{k\uparrow} c_{k+q\uparrow} c_{-k'-q\downarrow} c_{k'\uparrow} & c_{-k\downarrow} c_{k+q\uparrow} c^\dagger_{k'+q\uparrow} c_{k'\uparrow} & c_{-k\downarrow} c_{k+q\uparrow} c_{-k'-q\downarrow} c_{k'\uparrow} \\
c^\dagger_{k\uparrow} c_{k+q\uparrow} c^\dagger_{k'+q\uparrow} c^\dagger_{-k'\downarrow} & c^\dagger_{k\uparrow} c_{k+q\uparrow} c_{-k'-q\downarrow} c^\dagger_{-k'\downarrow} & c_{-k\downarrow} c_{k+q\uparrow} c^\dagger_{k'+q\uparrow} c^\dagger_{-k'\downarrow} & c_{-k\downarrow} c_{k+q\uparrow} c_{-k'-q\downarrow} c^\dagger_{-k'\downarrow} \\
c^\dagger_{k\uparrow} c^\dagger_{-k-q\downarrow} c^\dagger_{k'+q\uparrow} c_{k'\uparrow} & c^\dagger_{k\uparrow} c^\dagger_{-k-q\downarrow} c_{-k'-q\downarrow} c_{k'\uparrow} & c_{-k\downarrow} c^\dagger_{-k-q\downarrow} c^\dagger_{k'+q\uparrow} c_{k'\uparrow} & c_{-k\downarrow} c^\dagger_{-k-q\downarrow} c_{-k'-q\downarrow} c_{k'\uparrow} \\
c^\dagger_{k\uparrow} c^\dagger_{-k-q\downarrow} c^\dagger_{k'+q\uparrow} c^\dagger_{-k'\downarrow} & c^\dagger_{k\uparrow} c^\dagger_{-k-q\downarrow} c_{-k'-q\downarrow} c^\dagger_{-k'\downarrow} & c_{-k\downarrow} c^\dagger_{-k-q\downarrow} c^\dagger_{k'+q\uparrow} c^\dagger_{-k'\downarrow} & c_{-k\downarrow} c^\dagger_{-k-q\downarrow} c_{-k'-q\downarrow} c^\dagger_{-k'\downarrow}
\end{pmatrix} (\tau_1, \tau_2, \tau_3, \tau_4) \right\rangle .$$

The disconnected part of terms in $\underline{G}^{(2)}_{\uparrow\uparrow}$ can be split into two matrices with either direct and exchange terms

$$\underline{\chi}^{=}_{0,\uparrow\uparrow}(k,k+q,k'+q,k') = \tag{3.58}$$
$$\begin{pmatrix}
G_{00}(k{+}q,k)G_{00}(k',k'{+}q) & G_{00}(k{+}q,k)G_{01}(k',k'{+}q) & G_{01}(k{+}q,k)G_{00}(k',k'{+}q) & G_{01}(k{+}q,k)G_{01}(k',k'{+}q) \\
G_{00}(k{+}q,k)G_{10}(k',k'{+}q) & G_{00}(k{+}q,k)G_{11}(k',k'{+}q) & G_{01}(k{+}q,k)G_{10}(k',k'{+}q) & G_{01}(k{+}q,k)G_{11}(k',k'{+}q) \\
G_{10}(k{+}q,k)G_{00}(k',k'{+}q) & G_{10}(k{+}q,k)G_{01}(k',k'{+}q) & G_{11}(k{+}q,k)G_{00}(k',k'{+}q) & G_{11}(k{+}q,k)G_{01}(k',k'{+}q) \\
G_{10}(k{+}q,k)G_{10}(k',k'{+}q) & G_{10}(k{+}q,k)G_{11}(k',k'{+}q) & G_{11}(k{+}q,k)G_{10}(k',k'{+}q) & G_{11}(k{+}q,k)G_{11}(k',k'{+}q)
\end{pmatrix},$$

$$\underline{\chi}^{\times}_{0,\uparrow\uparrow}(k,k+q,k'+q,k') = -1\times \tag{3.59}$$
$$\begin{pmatrix}
G_{00}(k',k)G_{00}(k{+}q,k'{+}q) & G_{00}(k',k)G_{01}(k{+}q,k'{+}q) & G_{01}(k',k)G_{00}(k{+}q,k'{+}q) & G_{01}(k',k)G_{01}(k{+}q,k'{+}q) \\
G_{10}(k',k)G_{00}(k{+}q,k'{+}q) & G_{10}(k',k)G_{01}(k{+}q,k'{+}q) & G_{11}(k',k)G_{00}(k{+}q,k'{+}q) & G_{11}(k',k)G_{01}(k{+}q,k'{+}q) \\
G_{00}(k',k)G_{10}(k{+}q,k'{+}q) & G_{00}(k',k)G_{11}(k{+}q,k'{+}q) & G_{01}(k',k)G_{10}(k{+}q,k'{+}q) & G_{01}(k',k)G_{11}(k{+}q,k'{+}q) \\
G_{10}(k',k)G_{10}(k{+}q,k'{+}q) & G_{10}(k',k)G_{11}(k{+}q,k'{+}q) & G_{11}(k',k)G_{10}(k{+}q,k'{+}q) & G_{11}(k',k)G_{11}(k{+}q,k'{+}q)
\end{pmatrix},$$

where we have introduced the combined indices $k \equiv (k, i\omega_n)$ and $q \equiv (q, i\nu_n)$ in the $\underline{\chi}_0$ matrices. For $\sigma =\uparrow$, $\sigma' =\downarrow$, the two-particle Green's function matrix $\underline{G}^{(2)}_{\uparrow\downarrow}$ reads

$$\underline{G}^{(2)}_{\uparrow\downarrow}(k,k+q,k'+q,k') = \langle \mathcal{T} \psi^{\dagger}_{k\uparrow}(\tau_1) \otimes \psi_{k+q\uparrow}(\tau_2) \otimes \psi^{\dagger}_{k'+q\downarrow}(\tau_3) \otimes \psi_{k'\downarrow}(\tau_4)\rangle = \tag{3.60}$$
$$\left\langle \mathcal{T} \begin{pmatrix}
c^{\dagger}_{k\uparrow}c_{k+q\uparrow}c^{\dagger}_{k'+q\downarrow}c_{k'\downarrow} & c^{\dagger}_{k\uparrow}c_{k+q\uparrow}c_{-k'-q\uparrow}c_{k'\downarrow} & c_{-k\downarrow}c_{k+q\uparrow}c^{\dagger}_{k'+q\downarrow}c_{k'\downarrow} & c_{-k\downarrow}c_{k+q\uparrow}c_{-k'-q\uparrow}c_{k'\downarrow} \\
c^{\dagger}_{k\uparrow}c_{k+q\uparrow}c^{\dagger}_{k'+q\downarrow}c^{\dagger}_{-k'\uparrow} & c^{\dagger}_{k\uparrow}c_{k+q\uparrow}c_{-k'-q\uparrow}c^{\dagger}_{-k'\uparrow} & c_{-k\downarrow}c_{k+q\uparrow}c^{\dagger}_{k'+q\downarrow}c^{\dagger}_{-k'\uparrow} & c_{-k\downarrow}c_{k+q\uparrow}c_{-k'-q\uparrow}c^{\dagger}_{-k'\uparrow} \\
c^{\dagger}_{k\uparrow}c^{\dagger}_{-k-q\downarrow}c^{\dagger}_{k'+q\downarrow}c_{k'\downarrow} & c^{\dagger}_{k\uparrow}c^{\dagger}_{-k-q\downarrow}c_{-k'-q\uparrow}c_{k'\downarrow} & c_{-k\downarrow}c^{\dagger}_{-k-q\downarrow}c^{\dagger}_{k'+q\downarrow}c_{k'\downarrow} & c_{-k\downarrow}c^{\dagger}_{-k-q\downarrow}c_{-k'-q\uparrow}c_{k'\downarrow} \\
c^{\dagger}_{k\uparrow}c^{\dagger}_{-k-q\downarrow}c^{\dagger}_{k'+q\downarrow}c^{\dagger}_{-k'\uparrow} & c^{\dagger}_{k\uparrow}c^{\dagger}_{-k-q\downarrow}c_{-k'-q\uparrow}c^{\dagger}_{-k'\uparrow} & c_{-k\downarrow}c^{\dagger}_{-k-q\downarrow}c^{\dagger}_{k'+q\downarrow}c^{\dagger}_{-k'\uparrow} & c_{-k\downarrow}c^{\dagger}_{-k-q\downarrow}c_{-k'-q\uparrow}c^{\dagger}_{-k'\uparrow}
\end{pmatrix} (\tau_1,\tau_2,\tau_3,\tau_4) \right\rangle .$$

The two matrices for direct and exchange disconnected parts are

$$\underline{\chi}^{=}_{0,\uparrow\downarrow}(k,k{+}q,k'{+}q,k') = -1\times \tag{3.61}$$
$$\begin{pmatrix}
G_{00}(k{+}q,k)G_{11}(-k'-q,-k') & G_{00}(k{+}q,k)G_{01}(-k'-q,-k') & G_{01}(k{+}q,k)G_{11}(-k'-q,-k') & G_{01}(k{+}q,k)G_{01}(-k'-q,-k') \\
G_{00}(k{+}q,k)G_{10}(-k'-q,-k') & G_{00}(k{+}q,k)G_{00}(-k'-q,-k') & G_{01}(k{+}q,k)G_{10}(-k'-q,-k') & G_{01}(k{+}q,k)G_{00}(-k'-q,-k') \\
G_{10}(k{+}q,k)G_{11}(-k'-q,-k') & G_{10}(k{+}q,k)G_{01}(-k'-q,-k') & G_{11}(k{+}q,k)G_{11}(-k'-q,-k') & G_{11}(k{+}q,k)G_{01}(-k'-q,-k') \\
G_{10}(k{+}q,k)G_{10}(-k'-q,-k') & G_{10}(k{+}q,k)G_{00}(-k'-q,-k') & G_{11}(k{+}q,k)G_{10}(-k'-q,-k') & G_{11}(k{+}q,k)G_{00}(-k'-q,-k')
\end{pmatrix},$$

$$\underline{\chi}^{\times}_{0,\uparrow\downarrow}(k,k{+}q,k'{+}q,k') = \tag{3.62}$$
$$\begin{pmatrix}
G_{10}(-k'-q,k)G_{01}(k{+}q,-k') & G_{00}(-k'-q,k)G_{01}(k{+}q,-k') & G_{11}(-k'-q,k)G_{01}(k{+}q,-k') & G_{01}(-k'-q,k)G_{01}(k{+}q,-k') \\
G_{10}(-k'-q,k)G_{00}(k{+}q,-k') & G_{00}(-k'-q,k)G_{00}(k{+}q,-k') & G_{11}(-k'-q,k)G_{00}(k{+}q,-k') & G_{01}(-k'-q,k)G_{00}(k{+}q,-k') \\
G_{10}(-k'-q,k)G_{11}(k{+}q,-k') & G_{00}(-k'-q,k)G_{11}(k{+}q,-k') & G_{11}(-k'-q,k)G_{11}(k{+}q,-k') & G_{01}(-k'-q,k)G_{11}(k{+}q,-k') \\
G_{10}(-k'-q,k)G_{10}(k{+}q,-k') & G_{00}(-k'-q,k)G_{10}(k{+}q,-k') & G_{11}(-k'-q,k)G_{10}(k{+}q,-k') & G_{01}(-k'-q,k)G_{10}(k{+}q,-k')
\end{pmatrix}.$$

Momentum and energy conservations impose

- $\underline{\chi}^{=}_{0,\uparrow\uparrow}(k, k+q, k'+q, k') \neq 0$ only if $q = 0$.
- $\underline{\chi}^{\times}_{0,\uparrow\uparrow}(k, k+q, k'+q, k') \neq 0$ only if $k = k'$.
- $\underline{\chi}^{=}_{0,\uparrow\downarrow}(k, k+q, k'+q, k') \neq 0$ only if $q = 0$.
- $\underline{\chi}^{\times}_{0,\uparrow\downarrow}(k, k+q, k'+q, k') \neq 0$ only if $k+q = -k'$.

The label of four momentum and frequency indices can be simplified as $(k, k+q, k'+q, k') \to (k, k', q)$. We can define the $\underline{\chi}_0$ matrices with single k dependent single-particle Green's functions, but extra care needs to be taken to make the dimensions match. For example

$$\chi^{\times}_{0,\uparrow\uparrow,00}(k, k', q) = -\frac{1}{\beta N} G_{00}(k', k) G_{00}(k+q, k'+q) = -\beta N G_{00}(k) G_{00}(k+q) \delta_{k,k'} \,, \tag{3.63}$$

where N is the total number of k points.

3.3 Linear response and generalized susceptibilities

One direct application of the two-particle Green's functions is to compute physical susceptibilities. To define the physical susceptibilities, consider adding a field f coupling to an operator A to the original Hamiltonian of the system [7, 32]

$$H' = -fA \,. \tag{3.64}$$

The partition function can be written as (see section 2.7)

$$Z = \int \mathcal{D}[\bar{c}, c] e^{-S[\bar{c},c]} e^{-S'[\bar{c},c]} \,, \tag{3.65}$$

where $S[\bar{c}, c]$ represents the action corresponding to the original Hamiltonian, and $S'[\bar{c}, c] = -\int dx' f(x') A(x')$ is the action corresponding to the added source field. The thermal average of a physical quantity $B(x)$ can then be written as

$$\langle B(x) \rangle_{S+S'} = \frac{1}{Z} \int \mathcal{D}[\bar{c}, c] B(x) e^{-S[\bar{c},c]} e^{-S'[\bar{c},c]} \,. \tag{3.66}$$

The linear response of the physical quantity $B(x)$ to the external field can be computed by taking derivative with respect to the field f [32]

$$\begin{aligned}
&\left.\frac{\delta\langle B(x)\rangle_{S+S'}}{\delta f(x')}\right|_{f=0} \\
&= \frac{1}{Z^2}\left.\left[Z\frac{\delta\int\mathcal{D}[\bar{c},c]B(x)e^{-S[\bar{c},c]}e^{-S'[\bar{c},c]}}{\delta f(x')} - \frac{\delta Z}{\delta f(x')}\int\mathcal{D}[\bar{c},c]B(x)e^{-S[\bar{c},c]}e^{-S'[\bar{c},c]}\right]\right|_{f=0} \\
&= \langle B(x)A(x')\rangle_S - \langle B(x)\rangle_S\langle A(x')\rangle_S \equiv \chi_{BA}(x,x')\,, \qquad (3.67)
\end{aligned}$$

where time ordering in the thermal average is enforced by the Grassmann algebra, and $\chi_{BA}(x,x')$ is called the physical susceptibility.

Taking the spin susceptibility as an example, with the magnetization in z direction defined with the spin operator $\hat{S}_{z,i} = n_{i\uparrow} - n_{i\downarrow}$, $n_{i\sigma} = c^\dagger_{i\sigma}c_{i\sigma}$, the spin susceptibility in momentum space is defined as

$$\chi_{spin}(q,\tau,\tau') = \langle\mathcal{T}\hat{S}_z(q,\tau)\hat{S}_z(-q,\tau')\rangle - \langle\hat{S}_z(q,\tau)\rangle\langle\hat{S}_z(-q,\tau')\rangle\,, \qquad (3.68)$$

which can be computed using the two-particle Green's functions

$$\begin{aligned}
&\chi_{spin}(q,\tau,\tau') \qquad (3.69) \\
&= \frac{1}{N^2}\sum_{kk'}\big[\langle\mathcal{T}c^\dagger_{k\uparrow}(\tau)c_{k+q\uparrow}(\tau)c^\dagger_{k'+q\uparrow}(\tau')c_{k'\uparrow}(\tau')\rangle - \langle\mathcal{T}c^\dagger_{k\uparrow}(\tau)c_{k+q\uparrow}(\tau)\rangle\langle\mathcal{T}c^\dagger_{k'+q\uparrow}(\tau')c_{k'\uparrow}(\tau')\rangle \\
&\qquad -\langle\mathcal{T}c^\dagger_{k\uparrow}(\tau)c_{k+q\uparrow}(\tau)c^\dagger_{k'+q\downarrow}(\tau')c_{k'\downarrow}(\tau')\rangle + \langle\mathcal{T}c^\dagger_{k\uparrow}(\tau)c_{k+q\uparrow}(\tau)\rangle\langle\mathcal{T}c^\dagger_{k'+q\downarrow}(\tau')c_{k'\downarrow}(\tau')\rangle \\
&\qquad +\langle\mathcal{T}c^\dagger_{k\downarrow}(\tau)c_{k+q\downarrow}(\tau)c^\dagger_{k'+q\downarrow}(\tau')c_{k'\downarrow}(\tau')\rangle - \langle\mathcal{T}c^\dagger_{k\downarrow}(\tau)c_{k+q\downarrow}(\tau)\rangle\langle\mathcal{T}c^\dagger_{k'+q\downarrow}(\tau')c_{k'\downarrow}(\tau')\rangle \\
&\qquad -\langle\mathcal{T}c^\dagger_{k\downarrow}(\tau)c_{k+q\downarrow}(\tau)c^\dagger_{k'+q\uparrow}(\tau')c_{k'\uparrow}(\tau')\rangle + \langle\mathcal{T}c^\dagger_{k\downarrow}(\tau)c_{k+q\downarrow}(\tau)\rangle\langle\mathcal{T}c^\dagger_{k'+q\uparrow}(\tau')c_{k'\uparrow}(\tau')\rangle\big]\;.
\end{aligned}$$

With the time translational invariance and the spin flip relation, the magnetic susceptibility in momentum and frequency space can be written as

$$\begin{aligned}
\chi_{spin}(q) &= \int_0^\beta d\tau e^{i\nu_n\tau}\chi_{spin}(q,\tau,0) \qquad (3.70) \\
&= \frac{2}{\beta^2N^2}\sum_{kk'}\Big[G^{(2)}_{\uparrow\uparrow,00}(k,k',q) - \beta N G_{00}(k)G_{00}(k')\delta_{q,0} \\
&\qquad\qquad -G^{(2)}_{\uparrow\downarrow,00}(k,k',q) - \beta N G_{00}(k)G_{11}(-k')\delta_{q,0}\Big]\,,
\end{aligned}$$

where we have used the combined indices $k \equiv (k, i\omega_n)$ and $q \equiv (q, i\nu_n)$, $\sum_{kk'} \equiv \sum_{kk'} \sum_{\omega_n \omega'_n}$. By defining

$$\underline{\chi}_{\sigma\sigma'}(k, k', q) = \underline{G}^{(2)}_{\sigma\sigma'}(k, k', q) - \underline{\chi}^{=}_{0,\sigma\sigma'}(k, k', q)\,, \tag{3.71}$$

the spin susceptibility can be written as

$$\chi_{spin}(q) = \frac{2}{\beta^2 N^2} \sum_{kk'} [\chi_{\uparrow\uparrow,00}(k, k', q) - \chi_{\uparrow\downarrow,00}(k, k', q)] = \frac{2}{\beta^2 N^2} \sum_{kk'} \chi_m(k, k', q)\,, \tag{3.72}$$

where $\chi_m(k, k', q)$ is the generalized susceptibility in the magnetic channel [42]. The charge susceptibility which is defined as the time ordered correlator of the density operator $\hat{N}_i = n_{i\uparrow} + n_{i\downarrow}$ can be written out similarly

$$\chi_{ch}(q) = \frac{2}{\beta^2 N^2} \sum_{kk'} [\chi_{\uparrow\uparrow,00}(k, k', q) + \chi_{\uparrow\downarrow,00}(k, k', q)] = \frac{2}{\beta^2 N^2} \sum_{kk'} \chi_d(k, k', q)\,, \tag{3.73}$$

with $\chi_d(k, k', q)$ the generalized susceptibility in the density channel [42]. In general, all the terms in the $\underline{\chi}_{\sigma\sigma'}(k, k', q)$ matrices can be treated as the linear response of some physical quantities to external fields in different forms, and can be considered as the "generalized" susceptibilities defined in section 2.7.

3.4 Physical Channels

The connections between the generalized susceptibilities $\underline{\chi}_{\sigma\sigma'}(k, k', q)$ and the physical susceptibilities $\chi_{spin/ch}(q)$ motivates the definition of physical channels. By defining a general operator in any physical channel as $\hat{O}^{(a)}$, which is a linear combination of quadratic terms of c and $c^\dagger$, we define physical channels by requiring $\langle \hat{O}^{(a)}_1 \hat{O}^{(b)}_2 \rangle \neq 0$ if a, b belongs to the same channel, and $\langle \hat{O}^{(a)}_1 \hat{O}^{(b)}_2 \rangle = 0$, if a, b belongs to different channels.

In the paramagnetic state, four independent physical channels can be defined [42]: density (d), magnetic (m), spin singlet (s), and spin triplet (t). In the singlet superconducting state, the broken U(1) symmetry reduce the number of independent physical channels to two.

3.4.1 Definition via physical operators

The physical operators $\hat{O}$ can be defined using the BdG spinors introduced in Eq. 3.29 as $\hat{O} = \Phi^\dagger \cdot \tilde{O} \cdot \Phi$, with $\tilde{O}$ a 4×4 matrix in the form of $\hat{\tau}_a \otimes \hat{\sigma}_b$, $\hat{\tau}_a, \hat{\sigma}_b \in \{\hat{\sigma}_0, \hat{\sigma}_x, \hat{\sigma}_y, \hat{\sigma}_z\}$, where $\hat{\tau}_a \equiv \hat{\sigma}_a$, $a = 0, x, y, z$ is introduced to identify the matrices at different sides of $\otimes$. The definitions of the spin and density operators in Eq. 3.18 and Eq. 3.19 can then be extended to a particle hole symmetric form

$$\hat{S}_0 = c^\dagger_\uparrow c_\uparrow + c^\dagger_\downarrow c_\downarrow = \frac{1}{2}(c^\dagger_\uparrow c_\uparrow + c^\dagger_\downarrow c_\downarrow - c_\uparrow c^\dagger_\uparrow - c_\downarrow c^\dagger_\downarrow)\,, \tag{3.74a}$$

$$\hat{S}_x = c^\dagger_\uparrow c_\downarrow + c^\dagger_\downarrow c_\uparrow = \frac{1}{2}(c^\dagger_\uparrow c_\downarrow + c^\dagger_\downarrow c_\uparrow - c_\downarrow c^\dagger_\uparrow - c_\uparrow c^\dagger_\downarrow)\,, \tag{3.74b}$$

$$\hat{S}_y = -i(c^\dagger_\uparrow c_\downarrow - c^\dagger_\downarrow c_\uparrow) = -\frac{i}{2}(c^\dagger_\uparrow c_\downarrow - c^\dagger_\downarrow c_\uparrow - c_\downarrow c^\dagger_\uparrow + c_\uparrow c^\dagger_\downarrow)\,, \tag{3.74c}$$

$$\hat{S}_z = c^\dagger_\uparrow c_\uparrow - c^\dagger_\downarrow c_\downarrow = \frac{1}{2}(c^\dagger_\uparrow c_\uparrow - c^\dagger_\downarrow c_\downarrow - c_\uparrow c^\dagger_\uparrow + c_\downarrow c^\dagger_\downarrow)\,. \tag{3.74d}$$

Dropping the prefactors $\frac{1}{2}$ in the final form, the corresponding matrices can be written as

$$\tilde{S}_0 = \begin{pmatrix} \hat{\sigma}_0 & 0 \\ 0 & -\hat{\sigma}_0 \end{pmatrix} = \hat{\tau}_z \otimes \hat{\sigma}_0\,, \tag{3.75a}$$

$$\tilde{S}_x = \begin{pmatrix} \hat{\sigma}_x & 0 \\ 0 & -\hat{\sigma}_x \end{pmatrix} = \hat{\tau}_z \otimes \hat{\sigma}_x\,, \tag{3.75b}$$

$$\tilde{S}_y = \begin{pmatrix} \hat{\sigma}_y & 0 \\ 0 & \hat{\sigma}_y \end{pmatrix} = \hat{\tau}_0 \otimes \hat{\sigma}_y\,, \tag{3.75c}$$

$$\tilde{S}_z = \begin{pmatrix} \hat{\sigma}_z & 0 \\ 0 & -\hat{\sigma}_z \end{pmatrix} = \hat{\tau}_z \otimes \hat{\sigma}_z\,. \tag{3.75d}$$

In the SU(2) symmetric case, $\langle \hat{S}_a \hat{S}_a \rangle \neq 0$, and $\langle \hat{S}_a \hat{S}_b \rangle = 0$, with $a, b \in \{0, x, y, z\}$, $a \neq b$. Therefore, the four spin and density operators belong to different physical channels. All the 16 matrices in the form of $\hat{\tau}_a \otimes \hat{\sigma}_b$ can be grouped into four groups based on their commutation relations:

1. S_0 (density, d) spin singlet (s) channel (commute with all spin operators):

$$\hat{\tau}_z \otimes \hat{\sigma}_0\,, \quad \hat{\tau}_0 \otimes \hat{\sigma}_0\,, \quad \hat{\tau}_x \otimes \hat{\sigma}_y\,, \quad \hat{\tau}_y \otimes \hat{\sigma}_y\,. \tag{3.76}$$

2. S_x spin triplet channel (only commute with $\hat{S}_x$):

$$\hat{\tau}_z \otimes \hat{\sigma}_x\,, \quad \hat{\tau}_0 \otimes \hat{\sigma}_x\,, \quad \hat{\tau}_x \otimes \hat{\sigma}_z\,, \quad \hat{\tau}_y \otimes \hat{\sigma}_z\,. \tag{3.77}$$

3. S_y spin triplet channel (only commute with $\hat{S}_y$):

$$\hat{\tau}_0 \otimes \hat{\sigma}_y\,, \quad \hat{\tau}_x \otimes \hat{\sigma}_0\,, \quad \hat{\tau}_y \otimes \hat{\sigma}_0\,, \quad \hat{\tau}_z \otimes \hat{\sigma}_y\,. \tag{3.78}$$

4. S_z (magnetic, m) spin triplet (t) channel (only commute with $\hat{S}_z$):

$$\hat{\tau}_z \otimes \hat{\sigma}_z\,, \quad \hat{\tau}_0 \otimes \hat{\sigma}_z\,, \quad \hat{\tau}_x \otimes \hat{\sigma}_x\,, \quad \hat{\tau}_y \otimes \hat{\sigma}_x\,. \tag{3.79}$$

In each channel, the four matrices can be expressed as linear combinations of a set of basis matrices, with separated 2×2 blocks:

1. S_0 (density, d) spin singlet (s) channel

$$S_0 = \begin{pmatrix} \hat{\sigma}_0 & 0 \\ 0 & 0 \end{pmatrix}, \quad T_0 = \begin{pmatrix} 0 & \hat{\sigma}_y \\ 0 & 0 \end{pmatrix}, \tag{3.80a}$$

$$\overline{S}_0 = \begin{pmatrix} 0 & 0 \\ 0 & \hat{\sigma}_0 \end{pmatrix}, \quad \overline{T}_0 = \begin{pmatrix} 0 & 0 \\ \hat{\sigma}_y & 0 \end{pmatrix}. \tag{3.80b}$$

2. S_x spin triplet channel

$$S_x = \begin{pmatrix} \hat{\sigma}_x & 0 \\ 0 & 0 \end{pmatrix}, \quad T_x = \begin{pmatrix} 0 & \hat{\sigma}_z \\ 0 & 0 \end{pmatrix}, \tag{3.81a}$$

$$\overline{S}_x = \begin{pmatrix} 0 & 0 \\ 0 & \hat{\sigma}_x \end{pmatrix}, \quad \overline{T}_x = \begin{pmatrix} 0 & 0 \\ \hat{\sigma}_z & 0 \end{pmatrix}. \tag{3.81b}$$

3. S_y spin triplet channel

$$S_y = \begin{pmatrix} \hat{\sigma}_y & 0 \\ 0 & 0 \end{pmatrix}, \quad T_y = \begin{pmatrix} 0 & \hat{\sigma}_0 \\ 0 & 0 \end{pmatrix}, \tag{3.82a}$$

$$\overline{S}_y = \begin{pmatrix} 0 & 0 \\ 0 & \hat{\sigma}_y \end{pmatrix}, \quad \overline{T}_y = \begin{pmatrix} 0 & 0 \\ \hat{\sigma}_0 & 0 \end{pmatrix}. \tag{3.82b}$$

4. S_z (magnetic, m) spin triplet (t) channel

$$S_z = \begin{pmatrix} \hat{\sigma}_z & 0 \\ 0 & 0 \end{pmatrix}, \quad T_z = \begin{pmatrix} 0 & \hat{\sigma}_x \\ 0 & 0 \end{pmatrix}, \tag{3.83a}$$

$$\overline{S}_z = \begin{pmatrix} 0 & 0 \\ 0 & \hat{\sigma}_z \end{pmatrix}, \quad \overline{T}_z = \begin{pmatrix} 0 & 0 \\ \hat{\sigma}_x & 0 \end{pmatrix}. \tag{3.83b}$$

The three spin triplet channels can be connected by the SU(2) symmetry. Considering the general rotation operation in spin space

$$U_i(\theta) = \exp(-i\tilde{S}_i \frac{\theta}{2}) \,, \quad i = x, y, z, \tag{3.84}$$

where θ is the rotation angle, and $\tilde{S}_i$ one of the matrices defined in Eq. 3.75. The rotation of a matrix in Eqs. 3.81, 3.82, 3.83 is given by

$$M \to U_i^\dagger(\theta) M U_i(\theta) \,. \tag{3.85}$$

The relation between the S_y and S_z channels can be shown by rotating the matrices in the S_y channel [Eq. 3.82] by $\pi/2$ around the x-axis

$$S_y \to -S_z, \quad \overline{S}_y \to \overline{S}_z, \quad T_y \to iT_z, \quad \overline{T}_y \to -i\overline{T}_z \,. \tag{3.86}$$

The relation between the S_x and S_z channels can be shown by rotating the matrices in the S_x channel by $\pi/2$ around the y-axis

$$S_x \to S_z, \quad \overline{S}_x \to \overline{S}_z, \quad T_x \to -T_z, \quad \overline{T}_x \to -\overline{T}_z \,. \tag{3.87}$$

The relation between the S_x and S_y channels can be shown by rotating the matrices in the S_x and S_y channels by $\pi/2$ around the z-axis

$$S_x \to -S_y, \quad \overline{S}_x \to \overline{S}_y, \quad T_x \to iT_y, \quad \overline{T}_x \to -i\overline{T}_y \,, \tag{3.88}$$

$$S_y \to S_x, \quad \overline{S}_y \to -\overline{S}_x, \quad T_y \to iT_x, \quad \overline{T}_y \to -i\overline{T}_x \,. \tag{3.89}$$

Applying the matrices in Eqs. 3.80, 3.81, 3.82, 3.83 to the BdG spinors Φ and $\Phi^\dagger$ [Eq. 3.29], each of the four matrices in each channel would pick out one of the particle-hole (PH), hole-particle (HP), particle-particle (PP), and hole-hole (HH) sectors. Changing all the $\hat{\sigma}_y \to i\hat{\sigma}_y$ to drop the imaginary unit, these operators can be written out explicitly.

The PH sector:

$$\hat{S}_{0,ij} = \phi_i^\dagger \hat{\sigma}_0 \phi_j = c_{i\uparrow}^\dagger c_{j\uparrow} + c_{i\downarrow}^\dagger c_{j\downarrow} \,, \tag{3.90a}$$

$$\hat{S}_{x,ij} = \phi_i^\dagger \hat{\sigma}_x \phi_j = c_{i\uparrow}^\dagger c_{j\downarrow} + c_{i\downarrow}^\dagger c_{j\uparrow} \,, \tag{3.90b}$$

$$\hat{S}_{y,ij} = \phi_i^\dagger (i\hat{\sigma}_y) \phi_j = c_{i\uparrow}^\dagger c_{j\downarrow} - c_{i\downarrow}^\dagger c_{j\uparrow} \,, \tag{3.90c}$$

$$\hat{S}_{z,ij} = \phi_i^\dagger \hat{\sigma}_z \phi_j = c_{i\uparrow}^\dagger c_{j\uparrow} - c_{i\downarrow}^\dagger c_{j\downarrow} \,. \tag{3.90d}$$

The HP sector:

$$\hat{\bar{S}}_{0,ij} = \phi_i^T \hat{\sigma}_0 \phi_j^{\dagger T} = c_{i\uparrow} c_{j\uparrow}^\dagger + c_{i\downarrow} c_{j\downarrow}^\dagger \,, \tag{3.91a}$$

$$\hat{\bar{S}}_{x,ij} = \phi_i^T \hat{\sigma}_x \phi_j^{\dagger T} = c_{i\uparrow} c_{j\downarrow}^\dagger + c_{i\downarrow} c_{j\uparrow}^\dagger \,, \tag{3.91b}$$

$$\hat{\bar{S}}_{y,ij} = \phi_i^T (i\hat{\sigma}_y) \phi_j^{\dagger T} = c_{i\uparrow} c_{j\downarrow}^\dagger - c_{i\downarrow} c_{j\uparrow}^\dagger \,, \tag{3.91c}$$

$$\hat{\bar{S}}_{z,ij} = \phi_i^T \hat{\sigma}_z \phi_j^{\dagger T} = c_{i\uparrow} c_{j\uparrow}^\dagger - c_{i\downarrow} c_{j\downarrow}^\dagger \,. \tag{3.91d}$$

The PP sector:

$$\hat{T}_{0,ij} = \phi_i^\dagger (i\hat{\sigma}_y) \phi_j^{\dagger T} = c_{i\uparrow}^\dagger c_{j\downarrow}^\dagger - c_{i\downarrow}^\dagger c_{j\uparrow}^\dagger \,, \tag{3.92a}$$

$$\hat{T}_{x,ij} = \phi_i^\dagger \hat{\sigma}_z \phi_j^{\dagger T} = c_{i\uparrow}^\dagger c_{j\uparrow}^\dagger - c_{i\downarrow}^\dagger c_{j\downarrow}^\dagger \,, \tag{3.92b}$$

$$\hat{T}_{y,ij} = \phi_i^\dagger \hat{\sigma}_0 \phi_j^{\dagger T} = c_{i\uparrow}^\dagger c_{j\uparrow}^\dagger + c_{i\downarrow}^\dagger c_{j\downarrow}^\dagger \,, \tag{3.92c}$$

$$\hat{T}_{z,ij} = \phi_i^\dagger \hat{\sigma}_x \phi_j^{\dagger T} = c_{i\uparrow}^\dagger c_{j\downarrow}^\dagger + c_{i\downarrow}^\dagger c_{j\uparrow}^\dagger \,. \tag{3.92d}$$

The HH sector:

$$\hat{\bar{T}}_{0,ij} = \phi_i^T (i\hat{\sigma}_y) \phi_j = c_{i\uparrow} c_{j\downarrow} - c_{i\downarrow} c_{j\uparrow} \,, \tag{3.93a}$$

$$\hat{\bar{T}}_{x,ij} = \phi_i^T \hat{\sigma}_z \phi_j = c_{i\uparrow} c_{j\uparrow} - c_{i\downarrow} c_{j\downarrow} \,, \tag{3.93b}$$

$$\hat{\bar{T}}_{y,ij} = \phi_i^T \hat{\sigma}_0 \phi_j = c_{i\uparrow} c_{j\uparrow} + c_{i\downarrow} c_{j\downarrow} \,, \tag{3.93c}$$

$$\hat{\bar{T}}_{z,ij} = \phi_i^T \hat{\sigma}_x \phi_j = c_{i\uparrow} c_{j\downarrow} + c_{i\downarrow} c_{j\uparrow} \,. \tag{3.93d}$$

The rotational relations between the three spin triplet show that there are only two independent channels in the singlet superconducting state, which we will choose to be the S_0 (density spin singlet) channel, and the S_z (magnetic spin triplet) channel.

3.4.2 Definition via group theory

The physical channels can also be defined from a group theory point of view by considering the SO(4) group. The definitions and derivations in this section mainly follow Ref. [46].

The basis of 4×4 matrices and rotations in 4D Euclidian space can be expressed in terms of sixteen matrices [46]

- 1 Identity matrix: $\mathbb{I}_{4\times4}$.
- 4 Γ matrices: Γ_1, Γ_2, Γ_3, Γ_4 .
- 6 Σ matrices: $\Sigma_{ij} = \frac{i}{2}[\Gamma_i, \Gamma_j]$, with $i, j \in \{1, 2, 3, 4\}$, $i < j$.

- 4 $\tilde{\Gamma}$ matrices: $\tilde{\Gamma}_i = i\varepsilon_{ijkl}\Gamma_j\Gamma_k\Gamma_l$, with $i, j, k, l \in \{1, 2, 3, 4\}$, $i \neq j \neq k \neq l$.
- 1 Γ_5 matrix: $\Gamma_5 = \Gamma_1\Gamma_2\Gamma_3\Gamma_4$.

Einstein summation notation and the Levi-Civita symbol ε_{ijkl} are used in the definitions above. The Γ matrices and $\tilde{\Gamma}$ matrices are dual to each other, so we can exchange their notations in the definitions above $\Gamma \leftrightarrow \tilde{\Gamma}$.

In the sixteen matrices above, the six Σ matrices form the generators of an SO(4) group (4D rotation); the identity matrix $\mathbb{I}_{4\times4}$ and Γ_5 are two scalars of the 4D rotation; the four Γ matrices form a 4D vector of the rotation, and the four $\tilde{\Gamma}$ matrices form another 4D vector. We will consider the SO(3) subgroup of the SO(4) group, which corresponds to the SU(2) spin rotations [47, 48].

3.4.2.1 Γ matrices in the chiral representation

Following the chiral representation [49] of the Gamma matrices, we can define a series of reordered Gamma matrices

$$\Gamma_1 = \hat{\tau}_y \otimes \hat{\sigma}_z\,, \quad \Gamma_2 = \hat{\tau}_x \otimes \hat{\sigma}_0\,, \quad \Gamma_3 = \hat{\tau}_y \otimes \hat{\sigma}_x\,, \quad \Gamma_4 = \hat{\tau}_y \otimes \hat{\sigma}_y\,. \tag{3.94}$$

These Γ matrices obey the anti-commutation relation $\{\Gamma_i, \Gamma_j\} = 2\delta_{ij}\mathbb{I}_{4\times4}$. With the four Γ matrices, we can generate all the sixteen matrices mentioned above.

3.4.2.2 Σ matrices in the chiral representation

With the Γ matrices defined in Eq. 3.94, the Σ matrices can be written as

$$\begin{aligned} &\Sigma_{12} = -\hat{\tau}_z \otimes \hat{\sigma}_z\,, \quad \Sigma_{13} = -\hat{\tau}_0 \otimes \hat{\sigma}_y\,, \quad \Sigma_{14} = \hat{\tau}_0 \otimes \hat{\sigma}_x\,, \\ &\Sigma_{23} = \hat{\tau}_z \otimes \hat{\sigma}_x\,, \quad \Sigma_{24} = \hat{\tau}_z \otimes \hat{\sigma}_y\,, \quad \Sigma_{34} = -\hat{\tau}_0 \otimes \hat{\sigma}_z\,. \end{aligned} \tag{3.95}$$

3.4.2.3 $\tilde{\Gamma}$ matrices in the chiral representation

With the Γ matrices defined in Eq. 3.94, the $\tilde{\Gamma}$ matrices are defined as $\tilde{\Gamma}_i = i\varepsilon_{ijkl}\Gamma_j\Gamma_k\Gamma_l$, which are

$$\tilde{\Gamma}_1 = -\hat{\tau}_x \otimes \hat{\sigma}_z\,, \quad \tilde{\Gamma}_2 = \hat{\tau}_y \otimes \hat{\sigma}_0\,, \quad \tilde{\Gamma}_3 = -\hat{\tau}_x \otimes \hat{\sigma}_x\,, \quad \tilde{\Gamma}_4 = \hat{\tau}_x \otimes \hat{\sigma}_y\,. \tag{3.96}$$

The four $\tilde{\Gamma}$ matrices obey the same type of anti-commutation relation, $\{\tilde{\Gamma}_i, \tilde{\Gamma}_j\} = 2\delta_{ij}\mathbb{I}_{4\times4}$, as the Γ matrices.

3.4.2.4 Γ_5 matrix in the chiral representation

The Γ_5 matrix generated by the four Γ matrices defined in Eq. 3.94 can be written as

$$\Gamma_5 = -\hat{\tau}_z \otimes \hat{\sigma}_0 \,. \tag{3.97}$$

3.4.2.5 Relations between matrices generated from Γ and $\tilde{\Gamma}$ matrices

The Σ matrices generated by $\tilde{\Gamma}$ matrices are

$$\tilde{\Sigma}_{ij} = \frac{i}{2}[\tilde{\Gamma}_i, \tilde{\Gamma}_j] = -\Sigma^*_{ij} \,. \tag{3.98}$$

The relations between Γ and $\tilde{\Gamma}$ matrices can be written as

$$-\Gamma_i = i\varepsilon_{ijkl}\tilde{\Gamma}_j\tilde{\Gamma}_k\tilde{\Gamma}_l \,, \quad i,j,k,l \in \{1,2,3,4\} \,, \tag{3.99}$$

$$\tilde{\Gamma}_5 = \tilde{\Gamma}_1\tilde{\Gamma}_2\tilde{\Gamma}_3\tilde{\Gamma}_4 = \Gamma_5 \,. \tag{3.100}$$

3.4.2.6 SU(2) symmetries

The generators $\tilde{S}_i$ of the spin SU(2) rotations can be expressed using the Σ matrices

$$\tilde{S}_x = \frac{1}{2}\Sigma_{23} = \frac{1}{2}(\hat{\tau}_z \otimes \hat{\sigma}_x) \,, \quad \tilde{S}_y = -\frac{1}{2}\Sigma_{13} = \frac{1}{2}(\hat{\tau}_0 \otimes \hat{\sigma}_y) \,, \quad \tilde{S}_z = -\frac{1}{2}\Sigma_{12} = \frac{1}{2}(\hat{\tau}_z \otimes \hat{\sigma}_z) \,. \tag{3.101}$$

These three generators obey the SU(2) commutation relation $[\tilde{S}_i, \tilde{S}_j] = i\varepsilon_{ijk}\tilde{S}_k$.

The sixteen matrices in Eq. 3.94 - Eq. 3.97 form a 16 dimensional representation of the SU(2) group. This group is reducible and can be decomposed into 8 irreducible representations [47, 48], which can be written as

$$0 \oplus 0 \oplus 0 \oplus 0 \oplus 1 \oplus 1 \oplus 1 \oplus 1 \,, \tag{3.102}$$

where we have used angular momentum to label each irreducible representation. The four s-wave representations are scalars with angular momentum 0

$$\mathbb{I}_{4\times 4} \,, \quad \Gamma_4 \,, \quad \tilde{\Gamma}_4 \,, \quad \Gamma_5 \,, \tag{3.103}$$

and the four p-wave representations are vectors ($\vec{O}$) with angular momentum 1

$$\begin{pmatrix} \Gamma_1 \\ \Gamma_2 \\ -\Gamma_3 \end{pmatrix}, \quad \begin{pmatrix} \tilde{\Gamma}_1 \\ -\tilde{\Gamma}_2 \\ -\tilde{\Gamma}_3 \end{pmatrix}, \quad \frac{1}{2}\begin{pmatrix} \Sigma_{23} \\ -\Sigma_{13} \\ -\Sigma_{12} \end{pmatrix}, \quad \frac{1}{2}\begin{pmatrix} \Sigma_{14} \\ -\Sigma_{24} \\ -\Sigma_{34} \end{pmatrix}. \tag{3.104}$$

It can be proved that $[\tilde{S}_i, \tilde{O}_{\text{scalar}}] = 0$, $\forall i \in x, y, z$, so the four scalars do not change under spin rotations. Any of the four vectors $\vec{O}$ in Eq. 3.104 must obey $[\tilde{S}_i, \vec{O}_j] = i\varepsilon_{ijk}\vec{O}_k$, with $i, j, k \in x, y, z$, so the vectors rotate as 3D vectors.

3.4.2.7 Physical channels of correlators

Due to the SU(2) symmetry, the two-particle correlation functions have non-zero expectation values only when transforming as scalar under SU(2) rotations [47, 48]. The product of the two representations follow the relations

$$1 \otimes 0 = 1\,, \quad 0 \otimes 0 = 0\,, \quad 1 \otimes 1 = 0 \oplus 1 \oplus 3\,, \tag{3.105}$$

so there are only 32 non-zero terms

- Product of two scalars: $\langle \tilde{O}_1 \cdot \tilde{O}_2 \rangle \neq 0$ if $\tilde{O}_1, \tilde{O}_2$ are both scalars defined in Eq. 3.103. There are in total $2^4 = 16$ combinations.
- Product of two vectors: $\langle \vec{O}_1 \cdot \vec{O}_2 \rangle \neq 0$ if $\vec{O}_1, \vec{O}_2$ are both vectors defined in Eq. 3.104. There are in total $2^4 = 16$ combinations. The product of these vectors can be written out in three directions separately

  $$\langle \vec{O}_1 \cdot \vec{O}_2 \rangle = \langle O_{1x}O_{2x} + O_{1y}O_{2y} + O_{1z}O_{2z} \rangle\,, \tag{3.106}$$

  and the SU(2) symmetry gives $\langle O_{1x}O_{2x} \rangle = \langle O_{1y}O_{2y} \rangle = \langle O_{1z}O_{2z} \rangle = \frac{1}{3}\langle \vec{O}_1 \cdot \vec{O}_2 \rangle$.

The non-zero correlators found by the group theory derivation are equivalent with the correlators defined with physical operators in section 3.4.1. The four scalars correspond to the four matrices in the spin singlet channel [Eq. 3.76], the four 3D vectors correspond to the 3×4 matrices in the three spin triplet channels [Eqs. 3.77, 3.78, 3.79].

3.4.3 Two-particle Green's functions in physical channels

To define the two-particle Green's functions $G^{(2)}$ in different physical channels, we first transform the operators in Eqs. 3.90 - 3.93 to momentum space using

$$\hat{O}_{kk'} = \sum_{r_i r_j} e^{i(k\cdot r_i - k'\cdot r_j)} \hat{O}_{ij} \, . \tag{3.107}$$

The operators in momentum space are

$$\hat{S}_{0,kq} = c^{\dagger}_{k\uparrow} c_{k+q\uparrow} + c^{\dagger}_{k\downarrow} c_{k+q\downarrow} \, , \tag{3.108a}$$

$$\hat{S}_{x,kq} = c^{\dagger}_{k\uparrow} c_{k+q\downarrow} + c^{\dagger}_{k\downarrow} c_{k+q\uparrow} \, , \tag{3.108b}$$

$$\hat{S}_{y,kq} = c^{\dagger}_{k\uparrow} c_{k+q\downarrow} - c^{\dagger}_{k\downarrow} c_{k+q\uparrow} \, , \tag{3.108c}$$

$$\hat{S}_{z,kq} = c^{\dagger}_{k\uparrow} c_{k+q\uparrow} - c^{\dagger}_{k\downarrow} c_{k+q\downarrow} \, . \tag{3.108d}$$

$$\hat{\overline{S}}_{0,kq} = c_{\text{-}k\uparrow} c^{\dagger}_{\text{-}k\text{-}q,\uparrow} + c_{\text{-}k\downarrow} c^{\dagger}_{\text{-}k\text{-}q\downarrow} \, , \tag{3.109a}$$

$$\hat{\overline{S}}_{x,kq} = c_{\text{-}k\uparrow} c^{\dagger}_{\text{-}k\text{-}q\downarrow} + c_{\text{-}k\downarrow} c^{\dagger}_{\text{-}k\text{-}q\uparrow} \, , \tag{3.109b}$$

$$\hat{\overline{S}}_{y,kq} = c_{\text{-}k\uparrow} c^{\dagger}_{\text{-}k\text{-}q\downarrow} - c_{\text{-}k\downarrow} c^{\dagger}_{\text{-}k\text{-}q\uparrow} \, , \tag{3.109c}$$

$$\hat{\overline{S}}_{z,kq} = c_{\text{-}k\uparrow} c^{\dagger}_{\text{-}k\text{-}q\uparrow} - c_{\text{-}k\downarrow} c^{\dagger}_{\text{-}k\text{-}q\downarrow} \, . \tag{3.109d}$$

$$\hat{T}_{0,kq} = c^{\dagger}_{k\uparrow} c^{\dagger}_{\text{-}k\text{-}q\downarrow} - c^{\dagger}_{k\downarrow} c^{\dagger}_{\text{-}k\text{-}q\uparrow} \, , \tag{3.110a}$$

$$\hat{T}_{x,kq} = c^{\dagger}_{k\uparrow} c^{\dagger}_{\text{-}k\text{-}q\uparrow} - c^{\dagger}_{k\downarrow} c^{\dagger}_{\text{-}k\text{-}q\downarrow} \, , \tag{3.110b}$$

$$\hat{T}_{y,kq} = c^{\dagger}_{k\uparrow} c^{\dagger}_{\text{-}k\text{-}q\uparrow} + c^{\dagger}_{k\downarrow} c^{\dagger}_{\text{-}k\text{-}q\downarrow} \, , \tag{3.110c}$$

$$\hat{T}_{z,kq} = c^{\dagger}_{k\uparrow} c^{\dagger}_{\text{-}k\text{-}q\downarrow} + c^{\dagger}_{k\downarrow} c^{\dagger}_{\text{-}k\text{-}q\uparrow} \, . \tag{3.110d}$$

$$\hat{\overline{T}}_{0,kq} = c_{\text{-}k\uparrow} c_{k+q\downarrow} - c_{\text{-}k\downarrow} c_{k+q\uparrow} \, , \tag{3.111a}$$

$$\hat{\overline{T}}_{x,kq} = c_{\text{-}k\uparrow} c_{k+q\uparrow} - c_{\text{-}k\downarrow} c_{k+q\downarrow} \, , \tag{3.111b}$$

$$\hat{\overline{T}}_{y,kq} = c_{\text{-}k\uparrow} c_{k+q\uparrow} + c_{\text{-}k\downarrow} c_{k+q\downarrow} \, , \tag{3.111c}$$

$$\hat{\overline{T}}_{z,kq} = c_{\text{-}k\uparrow} c_{k+q\downarrow} + c_{\text{-}k\downarrow} c_{k+q\uparrow} \, . \tag{3.111d}$$

The Kronecker product of two Nambu spinors has the form

$$\psi^\dagger_{k_1,\sigma} \otimes \psi_{k_2,\sigma'} = \begin{pmatrix} c^\dagger_{k_1,\sigma} c_{k_2,\sigma'} & c_{-k_1,-\sigma} c_{k_2,\sigma'} \\ c^\dagger_{k_1,\sigma} c^\dagger_{-k_2,-\sigma'} & c^\dagger_{-k_1,-\sigma} c_{-k_2,-\sigma'} \end{pmatrix} . \tag{3.112}$$

Taking the momentum combinations $k_1 = k$, $k_2 = k + q$ as an example, different spin combinations give

$$\psi^\dagger_{k\uparrow} \otimes \psi_{k+q\uparrow} = \frac{1}{2} \begin{pmatrix} \hat{S}_{0,kq} + \hat{S}_{z,kq} & \hat{\bar{T}}_{z,kq} - \hat{\bar{T}}_{0,kq} \\ \hat{T}_{z,kq} + \hat{T}_{0,kq} & \hat{\bar{S}}_{0,kq} - \hat{\bar{S}}_{z,kq} \end{pmatrix} , \tag{3.113a}$$

$$\psi^\dagger_{k\downarrow} \otimes \psi_{k+q\downarrow} = \frac{1}{2} \begin{pmatrix} \hat{S}_{0,kq} - \hat{S}_{z,kq} & \hat{\bar{T}}_{z,kq} + \hat{\bar{T}}_{0,kq} \\ \hat{T}_{z,kq} - \hat{T}_{0,kq} & \hat{\bar{S}}_{0,kq} + \hat{\bar{S}}_{z,kq} \end{pmatrix} , \tag{3.113b}$$

$$\psi^\dagger_{k\uparrow} \otimes \psi_{k+q\downarrow} = \frac{1}{2} \begin{pmatrix} \hat{S}_{x,kq} + \hat{S}_{y,kq} & \hat{\bar{T}}_{y,kq} - \hat{\bar{T}}_{x,kq} \\ \hat{T}_{y,kq} + \hat{T}_{x,kq} & \hat{\bar{S}}_{x,kq} - \hat{\bar{S}}_{y,kq} \end{pmatrix} , \tag{3.113c}$$

$$\psi^\dagger_{k\downarrow} \otimes \psi_{k+q\uparrow} = \frac{1}{2} \begin{pmatrix} \hat{S}_{x,kq} - \hat{S}_{y,kq} & \hat{\bar{T}}_{y,kq} + \hat{\bar{T}}_{x,kq} \\ \hat{T}_{y,kq} - \hat{T}_{x,kq} & \hat{\bar{S}}_{x,kq} + \hat{\bar{S}}_{y,kq} \end{pmatrix} . \tag{3.113d}$$

Therefore, the two particle Green's function matrices $\underline{G}^{(2)}_{\sigma\sigma'}$ in Eq. 3.46 can be written with operators in different physical channels as

$$4\underline{G}^{(2)}_{\uparrow\uparrow}(k, k', q) = 4\langle \mathcal{T} \psi^\dagger_{k\uparrow} \otimes \psi_{k+q\uparrow} \otimes \psi^\dagger_{k'+q\uparrow} \otimes \psi_{k'\uparrow} \rangle \tag{3.114}$$

$$= \begin{pmatrix} \hat{S}_0\hat{S}_0+\hat{S}_0\hat{S}_z+\hat{S}_z\hat{S}_0+\hat{S}_z\hat{S}_z & \hat{S}_0\hat{\bar{T}}_z-\hat{S}_0\hat{\bar{T}}_0+\hat{S}_z\hat{\bar{T}}_z-\hat{S}_z\hat{\bar{T}}_0 & \hat{\bar{T}}_z\hat{S}_0+\hat{\bar{T}}_z\hat{S}_z-\hat{\bar{T}}_0\hat{S}_0-\hat{\bar{T}}_0\hat{S}_z & \hat{\bar{T}}_z\hat{\bar{T}}_z-\hat{\bar{T}}_z\hat{\bar{T}}_0-\hat{\bar{T}}_0\hat{\bar{T}}_z+\hat{\bar{T}}_0\hat{\bar{T}}_0 \\ \hat{S}_0\hat{T}_z+\hat{S}_0\hat{T}_0+\hat{S}_z\hat{T}_z+\hat{S}_z\hat{T}_0 & \hat{S}_0\hat{\bar{S}}_0-\hat{S}_0\hat{\bar{S}}_z+\hat{S}_z\hat{\bar{S}}_0-\hat{S}_z\hat{\bar{S}}_z & \hat{\bar{T}}_z\hat{T}_z+\hat{\bar{T}}_z\hat{T}_0-\hat{\bar{T}}_0\hat{T}_z-\hat{\bar{T}}_0\hat{T}_0 & \hat{\bar{T}}_z\hat{\bar{S}}_0-\hat{\bar{T}}_z\hat{\bar{S}}_z-\hat{\bar{T}}_0\hat{\bar{S}}_0+\hat{\bar{T}}_0\hat{\bar{S}}_z \\ \hat{T}_z\hat{S}_0+\hat{T}_z\hat{S}_z+\hat{T}_0\hat{S}_0+\hat{T}_0\hat{S}_z & \hat{T}_z\hat{\bar{T}}_z-\hat{T}_z\hat{\bar{T}}_0+\hat{T}_0\hat{\bar{T}}_z-\hat{T}_0\hat{\bar{T}}_0 & \hat{\bar{S}}_0\hat{S}_0+\hat{\bar{S}}_0\hat{S}_z-\hat{\bar{S}}_z\hat{S}_0-\hat{\bar{S}}_z\hat{S}_z & \hat{\bar{S}}_0\hat{\bar{T}}_z-\hat{\bar{S}}_0\hat{\bar{T}}_0-\hat{\bar{S}}_z\hat{\bar{T}}_z+\hat{\bar{S}}_z\hat{\bar{T}}_0 \\ \hat{T}_z\hat{T}_z+\hat{T}_z\hat{T}_0+\hat{T}_0\hat{T}_z+\hat{T}_0\hat{T}_0 & \hat{T}_z\hat{\bar{S}}_0-\hat{T}_z\hat{\bar{S}}_z+\hat{T}_0\hat{\bar{S}}_0-\hat{T}_0\hat{\bar{S}}_z & \hat{\bar{S}}_0\hat{T}_z+\hat{\bar{S}}_0\hat{T}_0-\hat{\bar{S}}_z\hat{T}_z-\hat{\bar{S}}_z\hat{T}_0 & \hat{\bar{S}}_0\hat{\bar{S}}_0-\hat{\bar{S}}_0\hat{\bar{S}}_z-\hat{\bar{S}}_z\hat{\bar{S}}_0+\hat{\bar{S}}_z\hat{\bar{S}}_z \end{pmatrix}_{kk'q} ,$$

$$4\underline{G}^{(2)}_{\uparrow\downarrow}(k, k', q) = 4\langle \mathcal{T} \psi^\dagger_{k\uparrow} \otimes \psi_{k+q\uparrow} \otimes \psi^\dagger_{k'+q\downarrow} \otimes \psi_{k'\downarrow} \rangle \tag{3.115}$$

$$= \begin{pmatrix} \hat{S}_0\hat{S}_0-\hat{S}_0\hat{S}_z+\hat{S}_z\hat{S}_0-\hat{S}_z\hat{S}_z & \hat{S}_0\hat{\bar{T}}_z+\hat{S}_0\hat{\bar{T}}_0+\hat{S}_z\hat{\bar{T}}_z+\hat{S}_z\hat{\bar{T}}_0 & \hat{\bar{T}}_z\hat{S}_0-\hat{\bar{T}}_z\hat{S}_z-\hat{\bar{T}}_0\hat{S}_0+\hat{\bar{T}}_0\hat{S}_z & \hat{\bar{T}}_z\hat{\bar{T}}_z+\hat{\bar{T}}_z\hat{\bar{T}}_0-\hat{\bar{T}}_0\hat{\bar{T}}_z-\hat{\bar{T}}_0\hat{\bar{T}}_0 \\ \hat{S}_0\hat{T}_z-\hat{S}_0\hat{T}_0+\hat{S}_z\hat{T}_z-\hat{S}_z\hat{T}_0 & \hat{S}_0\hat{\bar{S}}_0+\hat{S}_0\hat{\bar{S}}_z+\hat{S}_z\hat{\bar{S}}_0+\hat{S}_z\hat{\bar{S}}_z & \hat{\bar{T}}_z\hat{T}_z-\hat{\bar{T}}_z\hat{T}_0-\hat{\bar{T}}_0\hat{T}_z+\hat{\bar{T}}_0\hat{T}_0 & \hat{\bar{T}}_z\hat{\bar{S}}_0+\hat{\bar{T}}_z\hat{\bar{S}}_z-\hat{\bar{T}}_0\hat{\bar{S}}_0-\hat{\bar{T}}_0\hat{\bar{S}}_z \\ \hat{T}_z\hat{S}_0-\hat{T}_z\hat{S}_z+\hat{T}_0\hat{S}_0-\hat{T}_0\hat{S}_z & \hat{T}_z\hat{\bar{T}}_z+\hat{T}_z\hat{\bar{T}}_0+\hat{T}_0\hat{\bar{T}}_z+\hat{T}_0\hat{\bar{T}}_0 & \hat{\bar{S}}_0\hat{S}_0-\hat{\bar{S}}_0\hat{S}_z-\hat{\bar{S}}_z\hat{S}_0-\hat{\bar{S}}_z\hat{S}_z & \hat{\bar{S}}_0\hat{\bar{T}}_z+\hat{\bar{S}}_0\hat{\bar{T}}_0-\hat{\bar{S}}_z\hat{\bar{T}}_z-\hat{\bar{S}}_z\hat{\bar{T}}_0 \\ \hat{T}_z\hat{T}_z-\hat{T}_z\hat{T}_0+\hat{T}_0\hat{T}_z-\hat{T}_0\hat{T}_0 & \hat{T}_z\hat{\bar{S}}_0+\hat{T}_z\hat{\bar{S}}_z+\hat{T}_0\hat{\bar{S}}_0+\hat{T}_0\hat{\bar{S}}_z & \hat{\bar{S}}_0\hat{T}_z-\hat{\bar{S}}_0\hat{T}_0-\hat{\bar{S}}_z\hat{T}_z+\hat{\bar{S}}_z\hat{T}_0 & \hat{\bar{S}}_0\hat{\bar{S}}_0+\hat{\bar{S}}_0\hat{\bar{S}}_z-\hat{\bar{S}}_z\hat{\bar{S}}_0-\hat{\bar{S}}_z\hat{\bar{S}}_z \end{pmatrix}_{kk'q} ,$$

$$4\underline{G}^{(2)}_{\uparrow\downarrow}(k,k',q) = 4\langle \mathcal{T}\psi^{\dagger}_{k\uparrow} \otimes \psi_{k+q\downarrow} \otimes \psi^{\dagger}_{k'+q\downarrow} \otimes \psi_{k'\uparrow}\rangle \tag{3.116}$$

$$= \begin{pmatrix} \hat{S}_x\hat{S}_x - \hat{S}_x\hat{S}_y + \hat{S}_y\hat{S}_x - \hat{S}_y\hat{S}_y & \hat{S}_x\hat{\bar{T}}_y + \hat{S}_x\hat{\bar{T}}_x + \hat{S}_y\hat{\bar{T}}_y + \hat{S}_y\hat{\bar{T}}_x & \hat{\bar{T}}_y\hat{S}_x - \hat{\bar{T}}_y\hat{S}_y - \hat{\bar{T}}_x\hat{S}_x + \hat{\bar{T}}_x\hat{S}_y & \hat{\bar{T}}_y\hat{\bar{T}}_y + \hat{\bar{T}}_y\hat{\bar{T}}_x - \hat{\bar{T}}_x\hat{\bar{T}}_y - \hat{\bar{T}}_x\hat{\bar{T}}_x \\ \hat{S}_x\hat{T}_y - \hat{S}_x\hat{T}_x + \hat{S}_y\hat{T}_y - \hat{S}_y\hat{T}_x & \hat{S}_x\hat{\bar{S}}_x + \hat{S}_x\hat{\bar{S}}_y + \hat{S}_y\hat{\bar{S}}_x + \hat{S}_y\hat{\bar{S}}_y & \hat{\bar{T}}_y\hat{T}_y - \hat{\bar{T}}_y\hat{T}_x - \hat{\bar{T}}_x\hat{T}_y + \hat{\bar{T}}_x\hat{T}_x & \hat{\bar{T}}_y\hat{\bar{S}}_x + \hat{\bar{T}}_y\hat{\bar{S}}_y - \hat{\bar{T}}_x\hat{\bar{S}}_x - \hat{\bar{T}}_x\hat{\bar{S}}_y \\ \hat{T}_y\hat{S}_x - \hat{T}_y\hat{S}_y + \hat{T}_x\hat{S}_x - \hat{T}_x\hat{S}_y & \hat{T}_y\hat{\bar{T}}_y + \hat{T}_y\hat{\bar{T}}_x + \hat{T}_x\hat{\bar{T}}_y + \hat{T}_x\hat{\bar{T}}_x & \hat{\bar{S}}_x\hat{S}_x - \hat{\bar{S}}_x\hat{S}_y - \hat{\bar{S}}_y\hat{S}_x - \hat{\bar{S}}_y\hat{S}_y & \hat{\bar{S}}_x\hat{\bar{T}}_y + \hat{\bar{S}}_x\hat{\bar{T}}_x - \hat{\bar{S}}_y\hat{\bar{T}}_y - \hat{\bar{S}}_y\hat{\bar{T}}_x \\ \hat{T}_y\hat{T}_y - \hat{T}_y\hat{T}_x + \hat{T}_x\hat{T}_y - \hat{T}_x\hat{T}_x & \hat{T}_y\hat{\bar{S}}_x + \hat{T}_y\hat{\bar{S}}_y + \hat{T}_x\hat{\bar{S}}_x + \hat{T}_x\hat{\bar{S}}_y & \hat{\bar{S}}_x\hat{T}_y - \hat{\bar{S}}_x\hat{T}_x - \hat{\bar{S}}_y\hat{T}_y + \hat{\bar{S}}_y\hat{T}_x & \hat{\bar{S}}_x\hat{\bar{S}}_x + \hat{\bar{S}}_x\hat{\bar{S}}_y - \hat{\bar{S}}_y\hat{\bar{S}}_x - \hat{\bar{S}}_y\hat{\bar{S}}_y \end{pmatrix}_{kk'q},$$

in which

$$[\hat{O}^{(a)}\hat{O}^{(b)}]_{kk'q} = \langle \mathcal{T}\hat{O}^{(a)}(k\tau_1,(k+q)\tau_2)\hat{O}^{(b)}((k'+q)\tau_3,k'\tau_4)\rangle\,. \tag{3.117}$$

Since the correlators of operators from different physical channels are zero, each term in the two-particle Green's function matrices can be written as the sum of two terms in two different channels

$$\underline{G}^{(2)}_{\uparrow\uparrow}(k,k',q) = \frac{1}{4}\left[\underline{G}^{(2)}_{\uparrow\uparrow,S_0}(k,k',q) + \underline{G}^{(2)}_{\uparrow\uparrow,S_z}(k,k',q)\right], \tag{3.118a}$$

$$\underline{G}^{(2)}_{\uparrow\downarrow}(k,k',q) = \frac{1}{4}\left[\underline{G}^{(2)}_{\uparrow\downarrow,S_0}(k,k',q) + \underline{G}^{(2)}_{\uparrow\downarrow,S_z}(k,k',q)\right], \tag{3.118b}$$

$$\underline{G}^{(2)}_{\overline{\uparrow\downarrow}}(k,k',q) = \frac{1}{4}\left[\underline{G}^{(2)}_{\overline{\uparrow\downarrow},S_x}(k,k',q) + \underline{G}^{(2)}_{\overline{\uparrow\downarrow},S_y}(k,k',q)\right], \tag{3.118c}$$

with

$$\underline{G}^{(2)}_{\uparrow\uparrow,S_0}(k,k',q) = \begin{pmatrix} \hat{S}_0\hat{S}_0 & -\hat{S}_0\hat{\bar{T}}_0 & -\hat{\bar{T}}_0\hat{S}_0 & \hat{\bar{T}}_0\hat{\bar{T}}_0 \\ \hat{S}_0\hat{T}_0 & \hat{S}_0\hat{\bar{S}}_0 & -\hat{\bar{T}}_0\hat{T}_0 & -\hat{\bar{T}}_0\hat{\bar{S}}_0 \\ \hat{T}_0\hat{S}_0 & -\hat{T}_0\hat{\bar{T}}_0 & \hat{\bar{S}}_0\hat{S}_0 & -\hat{\bar{S}}_0\hat{\bar{T}}_0 \\ \hat{T}_0\hat{T}_0 & \hat{T}_0\hat{\bar{S}}_0 & \hat{\bar{S}}_0\hat{T}_0 & \hat{\bar{S}}_0\hat{\bar{S}}_0 \end{pmatrix}_{kk'q}, \tag{3.119a}$$

$$\underline{G}^{(2)}_{\uparrow\uparrow,S_z}(k,k',q) = \begin{pmatrix} \hat{S}_z\hat{S}_z & \hat{S}_z\hat{\bar{T}}_z & \hat{\bar{T}}_z\hat{S}_z & \hat{\bar{T}}_z\hat{\bar{T}}_z \\ \hat{S}_z\hat{T}_z & -\hat{S}_z\hat{\bar{S}}_z & \hat{\bar{T}}_z\hat{T}_z & -\hat{\bar{T}}_z\hat{\bar{S}}_z \\ \hat{T}_z\hat{S}_z & \hat{T}_z\hat{\bar{T}}_z & -\hat{\bar{S}}_z\hat{S}_z & -\hat{\bar{S}}_z\hat{\bar{T}}_z \\ \hat{T}_z\hat{T}_z & -\hat{T}_z\hat{\bar{S}}_z & -\hat{\bar{S}}_z\hat{T}_z & \hat{\bar{S}}_z\hat{\bar{S}}_z \end{pmatrix}_{kk'q}. \tag{3.119b}$$

$$\underline{G}^{(2)}_{\uparrow\downarrow,S_0}(k,k',q) = \begin{pmatrix} \hat{S}_0\hat{S}_0 & \hat{S}_0\hat{\overline{T}}_0 & -\hat{\overline{T}}_0\hat{S}_0 & -\hat{\overline{T}}_0\hat{\overline{T}}_0 \\ -\hat{S}_0\hat{T}_0 & \hat{S}_0\hat{\overline{S}}_0 & \hat{\overline{T}}_0\hat{T}_0 & -\hat{\overline{T}}_0\hat{\overline{S}}_0 \\ \hat{T}_0\hat{S}_0 & \hat{T}_0\hat{\overline{T}}_0 & \hat{\overline{S}}_0\hat{S}_0 & \hat{\overline{S}}_0\hat{\overline{T}}_0 \\ -\hat{T}_0\hat{T}_0 & \hat{T}_0\hat{\overline{S}}_0 & -\hat{\overline{S}}_0\hat{T}_0 & \hat{\overline{S}}_0\hat{\overline{S}}_0 \end{pmatrix}_{kk'q}, \tag{3.120a}$$

$$\underline{G}^{(2)}_{\uparrow\downarrow,S_z}(k,k',q) = \begin{pmatrix} -\hat{S}_z\hat{S}_z & \hat{S}_z\hat{\overline{T}}_z & -\hat{\overline{T}}_z\hat{S}_z & \hat{\overline{T}}_z\hat{\overline{T}}_z \\ \hat{S}_z\hat{T}_z & \hat{S}_z\hat{\overline{S}}_z & \hat{\overline{T}}_z\hat{T}_z & \hat{\overline{T}}_z\hat{\overline{S}}_z \\ -\hat{T}_z\hat{S}_z & \hat{T}_z\hat{\overline{T}}_z & \hat{\overline{S}}_z\hat{S}_z & -\hat{\overline{S}}_z\hat{\overline{T}}_z \\ \hat{T}_z\hat{T}_z & \hat{T}_z\hat{\overline{S}}_z & -\hat{\overline{S}}_z\hat{T}_z & -\hat{\overline{S}}_z\hat{\overline{S}}_z \end{pmatrix}_{kk'q}. \tag{3.120b}$$

$$\underline{G}^{(2)}_{\uparrow\downarrow,S_x}(k,k',q) = \begin{pmatrix} \hat{S}_x\hat{S}_x & \hat{S}_x\hat{\overline{T}}_x & -\hat{\overline{T}}_x\hat{S}_x & -\hat{\overline{T}}_x\hat{\overline{T}}_x \\ -\hat{S}_x\hat{T}_x & \hat{S}_x\hat{\overline{S}}_x & \hat{\overline{T}}_x\hat{T}_x & -\hat{\overline{T}}_x\hat{\overline{S}}_x \\ \hat{T}_x\hat{S}_x & \hat{T}_x\hat{\overline{T}}_x & \hat{\overline{S}}_x\hat{S}_x & \hat{\overline{S}}_x\hat{\overline{T}}_x \\ -\hat{T}_x\hat{T}_x & \hat{T}_x\hat{\overline{S}}_x & -\hat{\overline{S}}_x\hat{T}_x & \hat{\overline{S}}_x\hat{\overline{S}}_x \end{pmatrix}_{kk'q}, \tag{3.121a}$$

$$\underline{G}^{(2)}_{\uparrow\downarrow,S_y}(k,k',q) = \begin{pmatrix} -\hat{S}_y\hat{S}_y & \hat{S}_y\hat{\overline{T}}_y & -\hat{\overline{T}}_y\hat{S}_y & \hat{\overline{T}}_y\hat{\overline{T}}_y \\ \hat{S}_y\hat{T}_y & \hat{S}_y\hat{\overline{S}}_y & \hat{\overline{T}}_y\hat{T}_y & \hat{\overline{T}}_y\hat{\overline{S}}_y \\ -\hat{T}_y\hat{S}_y & \hat{T}_y\hat{\overline{T}}_y & \hat{\overline{S}}_y\hat{S}_y & -\hat{\overline{S}}_y\hat{\overline{T}}_y \\ \hat{T}_y\hat{T}_y & \hat{T}_y\hat{\overline{S}}_y & -\hat{\overline{S}}_y\hat{T}_y & -\hat{\overline{S}}_y\hat{\overline{S}}_y \end{pmatrix}_{kk'q}. \tag{3.121b}$$

Reordering operators into different orders provides useful relations between the expressions in two different channels. Take the $\underline{G}^{(2)}_{\uparrow\downarrow}(k,k+q,k'+q,k')$ matrix as an example, we can exchange the second and the fourth Nambu spinor

$$\begin{aligned} \underline{G}^{(2)}_{\uparrow\downarrow}(k,k',q) &= \langle \mathcal{T}\psi^{\dagger}_{k\uparrow}(\tau_1)\otimes\psi_{k+q\uparrow}(\tau_2)\otimes\psi^{\dagger}_{k'+q\downarrow}(\tau_3)\otimes\psi_{k'\downarrow}(\tau_4)\rangle \\ &= -P\cdot\langle \mathcal{T}\psi^{\dagger}_{k\uparrow}(\tau_1)\otimes\psi_{k'\downarrow}(\tau_4)\otimes\psi^{\dagger}_{k'+q\downarrow}(\tau_3)\otimes\psi_{k+q\uparrow}(\tau_2)\rangle\cdot P' \\ &= -P\cdot\underline{G}^{(2)}_{\uparrow\downarrow}(k,k+q,k'-k)\cdot P', \end{aligned} \tag{3.122}$$

where P and P' are 4×4 permutation matrices. Writing out the $\underline{G}^{(2)}_{\uparrow\downarrow}(k, k'+q, k'-k)$ matrix explicitly

$$\underline{G}^{(2)}_{\uparrow\downarrow}(k, k+q, k'-k) = \langle \mathcal{T}\psi^{\dagger}_{k\uparrow}(\tau_1)\otimes\psi_{k'\downarrow}(\tau_4)\otimes\psi^{\dagger}_{k'+q\downarrow}(\tau_3)\otimes\psi_{k+q\uparrow}(\tau_2)\rangle = \tag{3.123}$$

$$\left\langle \mathcal{T}\begin{pmatrix} c^{\dagger}_{k\uparrow}c_{k'\downarrow}c^{\dagger}_{k'+q\downarrow}c_{k+q\uparrow} & c^{\dagger}_{k\uparrow}c_{k'\downarrow}c_{-k'-q\uparrow}c_{k+q\uparrow} & c_{-k\downarrow}c_{k'\downarrow}c^{\dagger}_{k'+q\downarrow}c_{k+q\uparrow} & c_{-k\downarrow}c_{k'\downarrow}c_{-k'-q\uparrow}c_{k+q\uparrow} \\ c^{\dagger}_{k\uparrow}c_{k'\downarrow}c^{\dagger}_{k'+q\downarrow}c^{\dagger}_{-k-q\downarrow} & c^{\dagger}_{k\uparrow}c_{k'\downarrow}c_{-k'-q\uparrow}c^{\dagger}_{-k-q\downarrow} & c_{-k\downarrow}c_{k'\downarrow}c^{\dagger}_{k'+q\downarrow}c^{\dagger}_{-k-q\downarrow} & c_{-k\downarrow}c_{k'\downarrow}c_{-k'-q\uparrow}c^{\dagger}_{-k-q\downarrow} \\ c^{\dagger}_{k\uparrow}c^{\dagger}_{-k'\uparrow}c^{\dagger}_{k'+q\downarrow}c_{k+q\uparrow} & c^{\dagger}_{k\uparrow}c^{\dagger}_{-k'\uparrow}c_{-k'-q\uparrow}c_{k+q\uparrow} & c_{-k\downarrow}c^{\dagger}_{-k'\uparrow}c^{\dagger}_{k'+q\downarrow}c_{k+q\uparrow} & c_{-k\downarrow}c^{\dagger}_{-k'\uparrow}c_{-k'-q\uparrow}c_{k+q\uparrow} \\ c^{\dagger}_{k\uparrow}c^{\dagger}_{-k'\uparrow}c^{\dagger}_{k'+q\downarrow}c^{\dagger}_{-k-q\downarrow} & c^{\dagger}_{k\uparrow}c^{\dagger}_{-k'\uparrow}c_{-k'-q\uparrow}c^{\dagger}_{-k-q\downarrow} & c_{-k\downarrow}c^{\dagger}_{-k'\uparrow}c^{\dagger}_{k'+q\downarrow}c^{\dagger}_{-k-q\downarrow} & c_{-k\downarrow}c^{\dagger}_{-k'\uparrow}c_{-k'-q\uparrow}c^{\dagger}_{-k-q\downarrow} \end{pmatrix}(\tau_1,\tau_4,\tau_3,\tau_2)\right\rangle\,,$$

and comparing with Eq. 3.60, we see that the permutation matrices exchange the second and third row of the matrix. With the physical channels defined in Eq. 3.121, the matrix above can be written in S_x and S_y channels separately

$$\underline{G}^{(2)}_{\uparrow\downarrow}(k, k+q, k'-k) = \underline{G}^{(2)}_{\uparrow\downarrow,S_x}(k, k+q, k'-k) + \underline{G}^{(2)}_{\uparrow\downarrow,S_y}(k, k+q, k'-k)\,. \tag{3.124}$$

With the SU(2) rotation relations introduced in Eq. 3.86 and Eq. 3.87, when rotating the matrices in the S_y channel by $\pi/2$ around the x-axis, the operators transform as

$$\hat{S}_y \to -i\hat{S}_z,\quad \overline{S}_y \to i\hat{\overline{S}}_z,\quad \hat{T}_y \to i\hat{T}_z,\quad \hat{\overline{T}}_y \to -i\hat{\overline{T}}_z\,, \tag{3.125}$$

$$\begin{aligned}&\begin{pmatrix} -\hat{S}_y\hat{S}_y & \hat{S}_y\hat{\overline{T}}_y & -\hat{\overline{T}}_y\hat{S}_y & \hat{\overline{T}}_y\hat{\overline{T}}_y \\ \hat{S}_y\hat{T}_y & \hat{S}_y\hat{\overline{S}}_y & \hat{\overline{T}}_y\hat{T}_y & \hat{\overline{T}}_y\hat{\overline{S}}_y \\ -\hat{T}_y\hat{S}_y & \hat{T}_y\hat{\overline{T}}_y & \hat{\overline{S}}_y\hat{S}_y & -\hat{\overline{S}}_y\hat{\overline{T}}_y \\ \hat{T}_y\hat{T}_y & \hat{T}_y\hat{\overline{S}}_y & -\hat{\overline{S}}_y\hat{T}_y & -\hat{\overline{S}}_y\hat{\overline{S}}_y \end{pmatrix}_{k,k+q,k'-k} \\ \Longrightarrow\quad &\begin{pmatrix} \hat{S}_z\hat{S}_z & -\hat{S}_z\hat{\overline{T}}_z & \hat{\overline{T}}_z\hat{S}_z & -\hat{\overline{T}}_z\hat{\overline{T}}_z \\ \hat{S}_z\hat{T}_z & \hat{S}_z\hat{\overline{S}}_z & \hat{\overline{T}}_z\hat{T}_z & \hat{\overline{T}}_z\hat{\overline{S}}_z \\ -\hat{T}_z\hat{S}_z & \hat{T}_z\hat{\overline{T}}_z & \hat{\overline{S}}_z\hat{S}_z & -\hat{\overline{S}}_z\hat{\overline{T}}_z \\ -\hat{T}_z\hat{T}_z & -\hat{T}_z\hat{\overline{S}}_z & \hat{\overline{S}}_z\hat{T}_z & \hat{\overline{S}}_z\hat{\overline{S}}_z \end{pmatrix}_{k,k+q,k'-k}\,.\end{aligned} \tag{3.126}$$

Rotating the matrices in the S_x channel by $\pi/2$ around the y-axis causes the operators to transform as

$$\hat{S}_x \to \hat{S}_z,\quad \hat{\overline{S}}_x \to \hat{\overline{S}}_z,\quad \hat{T}_x \to -\hat{T}_z,\quad \hat{\overline{T}}_x \to -\hat{\overline{T}}_z\,, \tag{3.127}$$

$$\begin{pmatrix} \hat{S}_x\hat{S}_x & \hat{S}_x\hat{\overline{T}}_x & -\hat{\overline{T}}_x\hat{S}_x & -\hat{\overline{T}}_x\hat{\overline{T}}_x \\ -\hat{S}_x\hat{T}_x & \hat{S}_x\hat{\overline{S}}_x & \hat{\overline{T}}_x\hat{T}_x & -\hat{\overline{T}}_x\hat{\overline{S}}_x \\ \hat{T}_x\hat{S}_x & \hat{T}_x\hat{\overline{T}}_x & \hat{\overline{S}}_x\hat{S}_x & \hat{\overline{S}}_x\hat{\overline{T}}_x \\ -\hat{T}_x\hat{T}_x & \hat{T}_x\hat{\overline{S}}_x & -\hat{\overline{S}}_x\hat{T}_x & \hat{\overline{S}}_x\hat{\overline{S}}_x \end{pmatrix}_{k,k'+q,k'-k}$$

$$\Longrightarrow \quad \begin{pmatrix} \hat{S}_z\hat{S}_z & -\hat{S}_z\hat{\overline{T}}_z & \hat{\overline{T}}_z\hat{S}_z & -\hat{\overline{T}}_z\hat{\overline{T}}_z \\ \hat{S}_z\hat{T}_z & \hat{S}_z\hat{\overline{S}}_z & \hat{\overline{T}}_z\hat{T}_z & \hat{\overline{T}}_z\hat{\overline{S}}_z \\ -\hat{T}_z\hat{S}_z & \hat{T}_z\hat{\overline{T}}_z & \hat{\overline{S}}_z\hat{S}_z & -\hat{\overline{S}}_z\hat{\overline{T}}_z \\ -\hat{T}_z\hat{T}_z & -\hat{T}_z\hat{\overline{S}}_z & \hat{\overline{S}}_z\hat{T}_z & \hat{\overline{S}}_z\hat{\overline{S}}_z \end{pmatrix}_{k,k'+q,k'-k} . \tag{3.128}$$

The $\underline{G}^{(2)}_{\uparrow\downarrow}(k,k',q)$ matrix can then be written with correlators in only S_z channel

$$\underline{G}^{(2)}_{\uparrow\downarrow}(k,k',q) = \frac{1}{2}\begin{pmatrix} -\hat{S}_z\hat{S}_z & \hat{S}_z\hat{\overline{T}}_z & -\hat{\overline{T}}_z\hat{S}_z & \hat{\overline{T}}_z\hat{\overline{T}}_z \\ \hat{T}_z\hat{S}_z & -\hat{T}_z\hat{\overline{T}}_z & -\hat{\overline{S}}_z\hat{S}_z & \hat{\overline{S}}_z\hat{\overline{T}}_z \\ -\hat{S}_z\hat{T}_z & -\hat{S}_z\hat{\overline{S}}_z & -\hat{\overline{T}}_z\hat{T}_z & -\hat{\overline{T}}_z\hat{\overline{S}}_z \\ \hat{T}_z\hat{T}_z & \hat{T}_z\hat{\overline{S}}_z & -\hat{\overline{S}}_z\hat{T}_z & -\hat{\overline{S}}_z\hat{\overline{S}}_z \end{pmatrix}_{k,k'+q,k'-k} . \tag{3.129}$$

The definition of physical channels provide a way of extracting physical information from the two-particle Green's functions. These definitions are very important in the fluctuation diagonostic method [28] that we will generalize to the singlet superconducting state in section 3.6 and chapter 7.

3.5 Full vertex functions

As shown in Eq. 3.55, the two-particle Green's function $G^{(2)}$ can be decomposed into a disconnected and a connected term. In interacting systems, the connected part $G^{(2)}$ can be expressed using the full vertex functions (see section 2.5.1), which include all possible two-particle scattering processes. The full vertex functions play an important role in the analysis of two-particle properties, and are the central quantities in the Schwinger-Dyson equation which connects the single-particle self-energy with the two-particle scattering processes [42]. In this section we will provide the derivation for extracting full vertex functions from the single- and two-particle Green's functions.

The relation between $G^{(2)}_{\text{conn}}$ and the full vertex F in the paramagnetic state is written in Eq. 2.62. By introducing notations 1 and $\bar{1}$ to represent the Grassmann numbers c_1 and $\bar{c}_1$

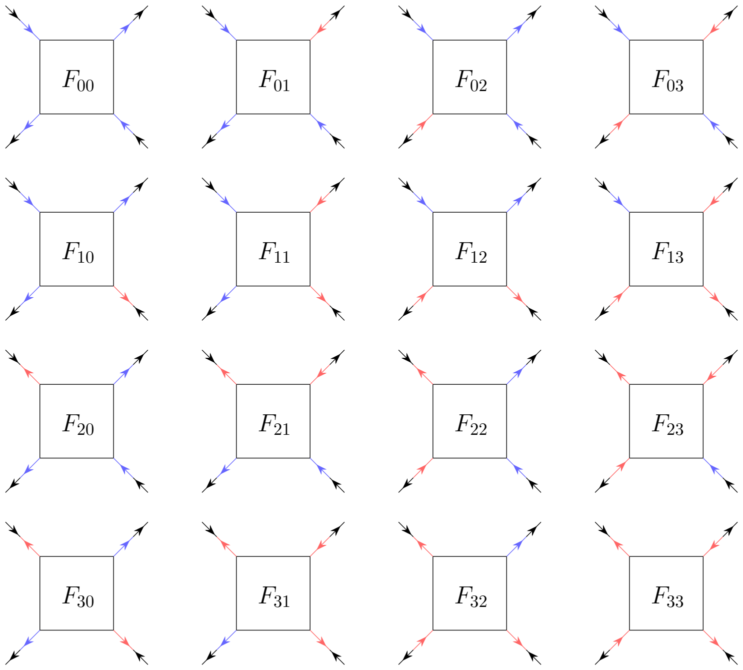

Figure 3.1: Vertex decomposition of the connected part of $G^{(2)}_{00}$. Blue-black arrows represent normal Green's functions, red-black arrows represent anomalous Green's functions.

in the Green's functions, and using Einstein summation, the relation can be written as

$$G^{(2)}_{\text{conn}}(\bar{1}2\bar{3}4) = -G(5\bar{1})G(2\bar{6})F(5\bar{6}7\bar{8})G(7\bar{3})G(4\bar{8})\,. \tag{3.130}$$

Transforming this equation to momentum and frequency space, the Green's functions and full vertex functions should conserve momentum, frequency, and spin, i.e. $G(1\bar{2})$ implies $k_1 = k_2$, $\omega_1 = \omega_2$, $\sigma_1 = \sigma_2$. With the momentum and frequency conventions introduced in Eq. 3.53, the decomposition can be written as

$$\begin{aligned} \chi_{\sigma\sigma'}(k,k',q) &= G^{(2)}_{\sigma\sigma'}(k,k',q) - \chi^{=}_{0,\sigma\sigma'}(k,k',q) \\ &= \chi^{\times}_{0,\sigma\sigma'}(k,k',q) + G^{(2)}_{\text{conn}}(k,k',q) \\ &= \chi^{\times}_{0,\sigma\sigma'}(k,k',q) - \frac{1}{\beta^2N^2}\sum_{k_1k_2}\chi^{\times}_{0,\sigma\sigma}(k,k_1,q)F_{\sigma\sigma'}(k_1,k_2,q)\chi^{\times}_{0,\sigma'\sigma'}(k_2,k',q)\,, \end{aligned} \tag{3.131}$$

where $\chi^{=}_{0,\sigma\sigma'}(k,k',q) = \beta N G_\sigma(k)G_{\sigma'}(k')\delta_{q,0}$, $\chi^{\times}_{0,\sigma\sigma'}(k,k',q) = -\beta N G_\sigma(k)G_\sigma(k+q)\delta_{k,k'}\delta_{\sigma,\sigma'}$, and $\chi^{\times}_{0,\uparrow\uparrow} = \chi^{\times}_{0,\downarrow\downarrow}$. The quantity $A_{\sigma\sigma'}$ is equivalent with $A_{\sigma\sigma',00}$ for $A \in \{G^{(2)}, \chi, \chi^{=}_0, \chi^{\times}_0\}$.

In the superconducting state, the single-particle Green's functions connected to F can be either normal or anomalous line, and there is no constraint on the number of incoming and outgoing legs of the full vertex F. The generalized equation can then be written as

$$G^{(2)}_{\mathrm{conn}}(1234) = -G(51)G(26)F(5678)G(73)G(48)\,, \tag{3.132}$$

where each number labels either c of $\bar{c}$, and the labels on the full vertex F are decided by the Green's functions connected to it. Each leg of F can be either an incoming leg or an outgoing leg, so there are in total $2^4 = 16$ terms in each decomposition. To avoid double counting, we count the number of different terms as follow

- There are $C_4^2 = 6$ terms with 2 in-legs and 2 out-legs.
- There are $C_4^3 = 4$ terms with 3 in-legs and 1 out-leg, and another $C_4^1 = 4$ terms with 1 in-leg and 3 out-legs.
- There are 1 term with 4 in-legs, and another 1 term with 4 out-legs.

We will fix the combinations of incoming and outgoing legs of the full vertex functions, and change the spin of each leg to satisfy spin conservation in our derivation. The 00 term in the two-particle Green's function matrix has the same form as in the paramagnetic state, it can be decomposed as

$$
\begin{aligned}
\langle \bar{c}_{1\sigma} c_{2\sigma} \bar{c}_{3\sigma'} c_{4\sigma'} \rangle_{\text{conn}} = & - \langle c_{5\sigma}\bar{c}_{1\sigma}\rangle\langle c_{2\sigma}\bar{c}_{6\sigma}\rangle F(5\bar{6}7\bar{8})\langle c_{7\sigma'}\bar{c}_{3\sigma'}\rangle\langle c_{4\sigma'}\bar{c}_{8\sigma'}\rangle \\
& + \langle c_{5\sigma}\bar{c}_{1\sigma}\rangle\langle c_{2\sigma}\bar{c}_{6\sigma}\rangle F(5\bar{6}7\bar{8})\langle \bar{c}_{8\text{-}\sigma'}\bar{c}_{3\sigma'}\rangle\langle c_{4\sigma'}c_{7\text{-}\sigma'}\rangle \\
& + \langle \bar{c}_{8\text{-}\sigma}\bar{c}_{1\sigma}\rangle\langle c_{2\sigma}\bar{c}_{6\sigma}\rangle F(5\bar{6}7\bar{8})\langle c_{7\sigma'}\bar{c}_{3\sigma'}\rangle\langle c_{4\sigma'}c_{5\text{-}\sigma'}\rangle \\
& + \langle \bar{c}_{6\text{-}\sigma}\bar{c}_{1\sigma}\rangle\langle c_{2\sigma}c_{5\text{-}\sigma}\rangle F(5\bar{6}7\bar{8})\langle c_{7\sigma'}\bar{c}_{3\sigma'}\rangle\langle c_{4\sigma'}\bar{c}_{8\sigma'}\rangle \\
& + \langle c_{5\sigma}\bar{c}_{1\sigma}\rangle\langle c_{2\sigma}c_{7\text{-}\sigma}\rangle F(5\bar{6}7\bar{8})\langle \bar{c}_{6\text{-}\sigma'}\bar{c}_{3\sigma'}\rangle\langle c_{4\sigma'}\bar{c}_{8\sigma'}\rangle \\
& - \langle \bar{c}_{6\text{-}\sigma}\bar{c}_{1\sigma}\rangle\langle c_{2\sigma}c_{5\text{-}\sigma}\rangle F(5\bar{6}7\bar{8})\langle \bar{c}_{8\text{-}\sigma'}\bar{c}_{3\sigma'}\rangle\langle c_{4\sigma'}c_{7\text{-}\sigma'}\rangle \\[4ex]
& - \langle c_{5\sigma}\bar{c}_{1\sigma}\rangle\langle c_{2\sigma}c_{6\text{-}\sigma}\rangle F(567\bar{8})\langle c_{7\sigma'}\bar{c}_{3\sigma'}\rangle\langle c_{4\sigma'}\bar{c}_{8\sigma'}\rangle \\
& + \langle c_{5\sigma}\bar{c}_{1\sigma}\rangle\langle c_{2\sigma}c_{6\text{-}\sigma}\rangle F(567\bar{8})\langle \bar{c}_{8\text{-}\sigma'}\bar{c}_{3\sigma'}\rangle\langle c_{4\sigma'}c_{7\text{-}\sigma'}\rangle \\
& + \langle c_{5\sigma}\bar{c}_{1\sigma}\rangle\langle c_{2\sigma}\bar{c}_{8\sigma}\rangle F(567\bar{8})\langle c_{7\sigma'}\bar{c}_{3\sigma'}\rangle\langle c_{4\sigma'}c_{6\text{-}\sigma'}\rangle \\
& + \langle \bar{c}_{8\text{-}\sigma}\bar{c}_{1\sigma}\rangle\langle c_{2\sigma}c_{6\text{-}\sigma}\rangle F(567\bar{8})\langle c_{7\sigma'}\bar{c}_{3\sigma'}\rangle\langle c_{4\sigma'}c_{5\text{-}\sigma'}\rangle \\[4ex]
& - \langle c_{5\sigma}\bar{c}_{1\sigma}\rangle\langle c_{2\sigma}\bar{c}_{6\sigma}\rangle F(5\bar{6}\bar{7}\bar{8})\langle \bar{c}_{7\text{-}\sigma'}\bar{c}_{3\sigma'}\rangle\langle c_{4\sigma'}\bar{c}_{8\sigma'}\rangle \\
& + \langle \bar{c}_{6\text{-}\sigma}\bar{c}_{1\sigma}\rangle\langle c_{2\sigma}c_{5\text{-}\sigma}\rangle F(5\bar{6}\bar{7}\bar{8})\langle \bar{c}_{7\text{-}\sigma'}\bar{c}_{3\sigma'}\rangle\langle c_{4\sigma'}\bar{c}_{8\sigma'}\rangle \\
& + \langle \bar{c}_{7\text{-}\sigma}\bar{c}_{1\sigma}\rangle\langle c_{2\sigma}\bar{c}_{6\sigma}\rangle F(5\bar{6}\bar{7}\bar{8})\langle c_{5\sigma'}\bar{c}_{3\sigma'}\rangle\langle c_{4\sigma'}\bar{c}_{8\sigma'}\rangle \\
& + \langle \bar{c}_{8\text{-}\sigma}\bar{c}_{1\sigma}\rangle\langle c_{2\sigma}\bar{c}_{6\sigma}\rangle F(5\bar{6}\bar{7}\bar{8})\langle \bar{c}_{7\text{-}\sigma'}\bar{c}_{3\sigma'}\rangle\langle c_{4\sigma'}c_{5\text{-}\sigma'}\rangle \\[4ex]
& - \langle c_{5\sigma}\bar{c}_{1\sigma}\rangle\langle c_{2\sigma}c_{6\text{-}\sigma}\rangle F(5678)\langle c_{7\sigma'}\bar{c}_{3\sigma'}\rangle\langle c_{4\sigma'}c_{8\text{-}\sigma'}\rangle \\[4ex]
& - \langle \bar{c}_{5\text{-}\sigma}\bar{c}_{1\sigma}\rangle\langle c_{2\sigma}\bar{c}_{6\sigma}\rangle F(\bar{5}\bar{6}\bar{7}\bar{8})\langle \bar{c}_{7\text{-}\sigma'}\bar{c}_{3\sigma'}\rangle\langle c_{4\sigma'}\bar{c}_{8\sigma'}\rangle \, ,
\end{aligned}
\tag{3.133}
$$

where we have used the Grassmann numbers instead of operators to omit the explicit time ordering and introduced the combined index $1 \equiv (i_1, \tau_1)$. Fig. 3.1 gives the diagrams corresponding to the decomposition in Eq. 3.133.

When transforming Eq. 3.133 to momentum and frequency space, the single-particl Green's functions should conserve momentum, frequency, and spin. For example, for $G(12)$, $k_1 = k_2$, $\omega_1 = \omega_2$, $\sigma_1 = \sigma_2$ labels a normal Green's function, and $k_1 = -k_2$, $\omega_1 = -\omega_2$, $\sigma_1 = -\sigma_2$ labels an anomalous Green's function. Using the momentum and frequency conventions introduced in Eq. 3.53, and reorder the labels on F, the decomposition can be written out explicitly for the two spin combinations

$$\begin{aligned}
G^{(2)}_{\uparrow\uparrow,00,\mathrm{conn}}(k,k',q) = &- G_{00}(k)G_{00}(k+q)F_{\uparrow\uparrow,00}(k,k',q)G_{00}(k'+q)G_{00}(k') \\
&- G_{00}(k)G_{00}(k+q)F_{\uparrow\uparrow,11}(k,k',q)G_{10}(k'+q)G_{01}(k') \\
&- G_{10}(k)G_{00}(k+q)F_{\uparrow\uparrow,12}(k,k',q)G_{00}(k'+q)G_{01}(k') \\
&- G_{10}(k)G_{01}(k+q)F_{\uparrow\uparrow,22}(k,k',q)G_{00}(k'+q)G_{00}(k') \\
&- G_{00}(k)G_{01}(k+q)F_{\uparrow\uparrow,21}(k,k',q)G_{10}(k'+q)G_{00}(k') \\
&- G_{10}(k)G_{01}(k+q)F_{\uparrow\uparrow,33}(k,k',q)G_{10}(k'+q)G_{01}(k') \\
\\
&- G_{00}(k)G_{01}(k+q)F_{\uparrow\uparrow,20}(k,k',q)G_{00}(k'+q)G_{00}(k') \\
&- G_{00}(k)G_{01}(k+q)F_{\uparrow\uparrow,31}(k,k',q)G_{10}(k'+q)G_{01}(k') \\
&- G_{00}(k)G_{00}(k+q)F_{\uparrow\uparrow,10}(k,k',q)G_{00}(k'+q)G_{01}(k') \\
&- G_{10}(k)G_{01}(k+q)F_{\uparrow\uparrow,32}(k,k',q)G_{00}(k'+q)G_{01}(k') \\
\\
&- G_{00}(k)G_{00}(k+q)F_{\uparrow\uparrow,01}(k,k',q)G_{10}(k'+q)G_{00}(k') \\
&- G_{10}(k)G_{01}(k+q)F_{\uparrow\uparrow,23}(k,k',q)G_{10}(k'+q)G_{00}(k') \\
&- G_{10}(k)G_{00}(k+q)F_{\uparrow\uparrow,02}(k,k',q)G_{00}(k'+q)G_{00}(k') \\
&- G_{10}(k)G_{00}(k+q)F_{\uparrow\uparrow,13}(k,k',q)G_{10}(k'+q)G_{01}(k') \\
\\
&- G_{00}(k)G_{01}(k+q)F_{\uparrow\uparrow,30}(k,k',q)G_{00}(k'+q)G_{01}(k') \\
\\
&- G_{10}(k)G_{00}(k+q)F_{\uparrow\uparrow,03}(k,k',q)G_{10}(k'+q)G_{00}(k')\,, \qquad (3.134)
\end{aligned}$$

$$
\begin{aligned}
G^{(2)}_{\uparrow\downarrow,00,\mathrm{conn}}(k,k',q) = &- G_{00}(k)G_{00}(k+q)F_{\uparrow\downarrow,00}(k,k',q)G_{11}(-k'-q)G_{11}(-k') \\
&- G_{00}(k)G_{00}(k+q)F_{\uparrow\downarrow,11}(k,k',q)G_{10}(-k'-q)G_{01}(-k') \\
&- G_{10}(k)G_{00}(k+q)F_{\uparrow\downarrow,12}(k,k',q)G_{11}(-k'-q)G_{01}(-k') \\
&- G_{10}(k)G_{01}(k+q)F_{\uparrow\downarrow,22}(k,k',q)G_{11}(-k'-q)G_{11}(-k') \\
&- G_{00}(k)G_{01}(k+q)F_{\uparrow\downarrow,21}(k,k',q)G_{10}(-k'-q)G_{11}(-k') \\
&- G_{10}(k)G_{01}(k+q)F_{\uparrow\downarrow,33}(k,k',q)G_{10}(-k'-q)G_{01}(-k') \\
\\
&- G_{00}(k)G_{01}(k+q)F_{\uparrow\downarrow,20}(k,k',q)G_{11}(-k'-q)G_{11}(-k') \\
&- G_{00}(k)G_{01}(k+q)F_{\uparrow\downarrow,31}(k,k',q)G_{10}(-k'-q)G_{01}(-k') \\
&- G_{00}(k)G_{00}(k+q)F_{\uparrow\downarrow,10}(k,k',q)G_{11}(-k'-q)G_{01}(-k') \\
&- G_{10}(k)G_{01}(k+q)F_{\uparrow\downarrow,32}(k,k',q)G_{11}(-k'-q)G_{01}(-k') \\
\\
&- G_{00}(k)G_{00}(k+q)F_{\uparrow\downarrow,01}(k,k',q)G_{10}(-k'-q)G_{11}(-k') \\
&- G_{10}(k)G_{01}(k+q)F_{\uparrow\downarrow,23}(k,k',q)G_{10}(-k'-q)G_{11}(-k') \\
&- G_{10}(k)G_{00}(k+q)F_{\uparrow\downarrow,02}(k,k',q)G_{11}(-k'-q)G_{11}(-k') \\
&- G_{10}(k)G_{00}(k+q)F_{\uparrow\downarrow,13}(k,k',q)G_{10}(-k'-q)G_{01}(-k') \\
\\
&- G_{00}(k)G_{01}(k+q)F_{\uparrow\downarrow,30}(k,k',q)G_{11}(-k'-q)G_{01}(-k') \\
\\
&- G_{10}(k)G_{00}(k+q)F_{\uparrow\downarrow,03}(k,k',q)G_{10}(-k'-q)G_{11}(-k')\,, \qquad (3.135)
\end{aligned}
$$

where we dropped the explicit summations and normalization factors. All terms in the two-particle Green's function matrices can be decomposed in a similar way. With the $\underline{\chi}_0^{=}$, $\underline{\chi}_0^{\times}$ and $\underline{\chi}$ matrices defined in Eqs. 3.58, 3.59 and Eq. 3.71, the decompositions can be written in a matrix form with proper permutation of matrix elements

$$
PAP' = P \begin{pmatrix} A_{00} & A_{01} & A_{02} & A_{03} \\ A_{10} & A_{11} & A_{12} & A_{13} \\ A_{20} & A_{21} & A_{22} & A_{23} \\ A_{30} & A_{31} & A_{32} & A_{33} \end{pmatrix} P' = \begin{pmatrix} A_{00} & A_{01} & A_{10} & A_{11} \\ A_{20} & A_{21} & A_{30} & A_{31} \\ A_{02} & A_{03} & A_{12} & A_{13} \\ A_{22} & A_{23} & A_{32} & A_{33} \end{pmatrix} = \tilde{A}\,, \qquad (3.136)
$$

$$\begin{aligned}\underline{\tilde{\chi}}_{\sigma\sigma'}(k,k',q) &= \underline{\tilde{G}}^{(2)}_{\sigma\sigma'}(k,k',q) - \underline{\tilde{\chi}}^{=}_{0,\sigma'\sigma'}(k,k',q) \\ &= \underline{\tilde{\chi}}^{\times}_{0,\sigma\sigma'}(k,k',q) - \frac{1}{\beta^2 N^2}\sum_{k_1 k_2}\underline{\tilde{\chi}}^{\times}_{0,\sigma\sigma}(k,k_1,q)\;\underline{\tilde{F}}_{\sigma\sigma'}(k_1,k_2,q)\;\underline{\tilde{\chi}}^{\times}_{0,\sigma'\sigma'}(k_2,k',q)\,.\end{aligned} \tag{3.137}$$

Note that with the SU(2) spin flip relations, the matrices $\underline{\tilde{\chi}}^{\times}_{0,\downarrow\downarrow} \neq \underline{\tilde{\chi}}^{\times}_{0,\uparrow\uparrow}$. The diagonal and anti-diagonal terms in the $\underline{\tilde{\chi}}^{\times}_{0,\downarrow\downarrow}$ matrix equal to those in $\underline{\tilde{\chi}}^{\times}_{0,\uparrow\uparrow}$, while the other terms pick up an extra minus sign.

Eqs. 3.136 and 3.137 provide the equations needed for extracting the full vertex functions $\underline{F}_{\sigma\sigma'}$ from the single- and two-particle Green's functions. The applications of the full vertex functions will be discussed in detail in section 3.6 and chapter 7.

3.6 Schwinger-Dyson equation with full vertex functions

3.6.1 Derivation of the Schwinger-Dyson equation

To find the relations between the self-energies and full vertex functions, we apply the Schwinger-Dyson equation introduced in section 2.8 to the fermionic case $\varphi(x) \to \{c(x), \bar{c}(x)\}$. To derive the Schwinger-Dyson equation in the singlet supreconducting state, we consider the action

$$\begin{aligned}S = &-\int dx_1 dx_2\; \bar{c}(x_1) G^{-1}_{0,00}(x_1,x_2) c(x_2) \\ &+ \frac{1}{2}\int dx_1 dx_2 dx_3 dx_4 U(x_1,x_2;x_3,x_4)\bar{c}(x_1)\bar{c}(x_3)c(x_4)c(x_2)\,,\end{aligned} \tag{3.138}$$

where $G_{0,00}$ represents the 00 term in the non-interacting Green's function matrix $G_{0,00}(x_1,x_2)$ $= -\langle c(x_1)\bar{c}(x_2)\rangle_{S_0}$ for both spin up and spin down. The derivative with respect to the Grassmann number can be written as

$$\begin{aligned}\frac{\delta S}{\delta \bar{c}(x_1)} = &-\int dx_2 G^{-1}_{0,00}(x_1,x_2)c(x_2) \\ &+ \frac{1}{2}\int dx_2 dx_3 dx_4 [U(x_1,x_2,x_3,x_4) - U(x_3,x_2,x_1,x_4)]\bar{c}(x_3)c(x_4)c(x_2)\,.\end{aligned} \tag{3.139}$$

Using the derivative given by Eq. 3.139, the Schwinger-Dyson equation [Eq. 2.98] gives the relation

$$\left\langle \frac{\delta S}{\delta \bar{c}(x_1)} \bar{c}(x_1') \right\rangle = \delta(x_1' - x_1)\,. \tag{3.140}$$

Multiplying Eq. 3.139 with $\bar{c}(x_1')$, the Schwinger-Dyson equation can be written out explicitly as

$$\begin{aligned} \delta(x_1 - x_1') = & - \int dx_2 G^{-1}_{0,00}(x_1, x_2) \langle c(x_2) \bar{c}(x_1') \rangle \\ & + \frac{1}{2} \int dx_2 dx_3 dx_4 [U(x_1, x_2, x_3, x_4) - U(x_3, x_2, x_1, x_4)] \langle \bar{c}(x_3) c(x_4) c(x_2) \bar{c}(x_1') \rangle\,. \end{aligned} \tag{3.141}$$

In the matrix form Dyson equation [Eq. 2.60], which can be written as

$$\int dx_2 \underline{\Sigma}(x_1, x_2) \underline{G}(x_2, x_1') = -\delta(x_1 - x_1') \mathbb{I}_{2\times 2} + \int dx_2 \underline{G_0}^{-1}(x_1, x_2) \underline{G}(x_2, x_1')\,, \tag{3.142}$$

the matrix multiplications can be carried out explicitly

$$\begin{aligned} & \int dx_2 \begin{pmatrix} \Sigma_{00} G_{00} + \Sigma_{01} G_{10} & \Sigma_{00} G_{01} + \Sigma_{01} G_{11} \\ \Sigma_{10} G_{00} + \Sigma_{11} G_{10} & \Sigma_{10} G_{01} + \Sigma_{11} G_{11} \end{pmatrix} (x_1 x_2; x_2 x_1') \\ & = - \begin{pmatrix} \delta(x_1 - x_1') & 0 \\ 0 & \delta(x_1 - x_1') \end{pmatrix} \\ & \quad + \int dx_2 \begin{pmatrix} G^{-1}_{0,00}(x_1, x_2) & 0 \\ 0 & G^{-1}_{0,11}(x_1, x_2) \end{pmatrix} \begin{pmatrix} G_{00}(x_2, x_1') & G_{01}(x_2, x_1') \\ G_{10}(x_2, x_1') & G_{11}(x_2, x_1') \end{pmatrix}\,. \end{aligned} \tag{3.143}$$

Identifying that $-\langle c(x_2) \bar{c}(x_1') \rangle = G_{00}(x_2, x_1')$, Eq. 3.141 can be written as

$$\begin{aligned} & \int dx_2 [\Sigma_{00}(x_1, x_2) G_{00}(x_2, x_1') + \Sigma_{01}(x_1, x_2) G_{10}(x_2, x_1')] \\ & = \frac{1}{2} \int dx_2 dx_3 dx_4 [U(x_1, x_2, x_3, x_4) - U(x_3, x_2, x_1, x_4)] \langle \bar{c}(x_3) c(x_4) c(x_2) \bar{c}(x_1') \rangle\,. \end{aligned} \tag{3.144}$$

Defining the anti-symmetrized interaction $V(x_1, x_2, x_3, x_4) = \frac{1}{2}[U(x_1, x_2, x_3, x_4) - U(x_3, x_2, x_1, x_4)]$, and reordering the operators in the quadruple term, the equation above can be simplified to

$$\begin{aligned} & \int dx_2 [\Sigma_{00}(x_1, x_2) G_{00}(x_2, x_1') + \Sigma_{01}(x_1, x_2) G_{10}(x_2, x_1')] \\ & = \int dx_2 dx_3 dx_4 V(x_1, x_2, x_3, x_4) \langle \bar{c}(x_1') c(x_2) \bar{c}(x_3) c(x_4) \rangle\,. \end{aligned} \tag{3.145}$$

Another equivalent equation for $\int dx_2[\Sigma_{10}(x_1,x_2)G_{01}(x_2,x_1') + \Sigma_{11}(x_1,x_2)G_{11}(x_2,x_1')]$ can be derived by taking derivative of $c(x_2)$, and use $G_{0,11}$ in the action formula. In the following derivation we will only write out equations related with Eq. 3.145 explicitly.

From Eq. 3.145, the two self-energies $\Sigma_{00}(x_1,x_2)$ and $\Sigma_{01}(x_1,x_2)$ can be computed by decomposing the two-particle Green's function $\langle \bar{c}(x_1')c(x_2)\bar{c}(x_3)c(x_4)\rangle$ as in Eq. 3.133. In this calculation, the indices x_2, x_3, x_4 are inter-exchangeable dummy indices, while the index x_1' is a special index. With the explicit decomposition in Eq. 3.133, there are eight terms with $G_{10}(x_2,x_1')$ and another eight terms with $G_{00}(x_2,x_1')$.

We consider a system with SU(2) symmetry and local Hubbard interaction $U(\uparrow,\uparrow,\downarrow,\downarrow) = U(\downarrow,\downarrow,\uparrow,\uparrow) = U$. Using the momentum and energy conventions introduced in Eq. 3.53, and the single-particle Green's function convention introduced in Eq. 3.35 (only spin up), by decomposing $\langle \bar{c}_{k\uparrow}c_{k+q\uparrow}\bar{c}_{k'+q\downarrow}c_{k'\downarrow}\rangle$, which is the 00 term in the $\underline{G}^{(2)}_{\uparrow\downarrow}(k,k',q)$ matrix, the Schwinger-Dyson gives explicit relations between the self-energies and the full vertex functions

$$\begin{aligned}
\Sigma_{00}(k) = \frac{Un}{2} + \frac{U}{\beta^2N^2}\sum_{k'q}[&- G_{00}(k+q)F_{\uparrow\downarrow,00}(k,k',q)G_{11}(-k'-q)G_{11}(-k') \\
&- G_{00}(k+q)F_{\uparrow\downarrow,11}(k,k',q)G_{10}(-k'-q)G_{01}(-k') \\
&- G_{01}(k+q)F_{\uparrow\downarrow,21}(k,k',q)G_{10}(-k'-q)G_{11}(-k') \\
&- G_{01}(k+q)F_{\uparrow\downarrow,20}(k,k',q)G_{11}(-k'-q)G_{11}(-k') \\
&- G_{01}(k+q)F_{\uparrow\downarrow,31}(k,k',q)G_{10}(-k'-q)G_{01}(-k') \\
&- G_{00}(k+q)F_{\uparrow\downarrow,10}(k,k',q)G_{11}(-k'-q)G_{01}(-k') \\
&- G_{00}(k+q)F_{\uparrow\downarrow,01}(k,k',q)G_{10}(-k'-q)G_{11}(-k') \\
&- G_{01}(k+q)F_{\uparrow\downarrow,30}(k,k',q)G_{11}(-k'-q)G_{01}(-k')] \,,
\end{aligned} \tag{3.146a}$$

$$\begin{aligned}
\Sigma_{01}(k) = \;\; 0 \;\; + \frac{U}{\beta^2N^2}\sum_{k'q}[&- G_{00}(k+q)F_{\uparrow\downarrow,12}(k,k',q)G_{11}(-k'-q)G_{01}(-k') \\
&- G_{01}(k+q)F_{\uparrow\downarrow,22}(k,k',q)G_{11}(-k'-q)G_{11}(-k') \\
&- G_{01}(k+q)F_{\uparrow\downarrow,33}(k,k',q)G_{10}(-k'-q)G_{01}(-k') \\
&- G_{01}(k+q)F_{\uparrow\downarrow,32}(k,k',q)G_{11}(-k'-q)G_{01}(-k') \\
&- G_{01}(k+q)F_{\uparrow\downarrow,23}(k,k',q)G_{10}(-k'-q)G_{11}(-k') \\
&- G_{00}(k+q)F_{\uparrow\downarrow,02}(k,k',q)G_{11}(-k'-q)G_{11}(-k') \\
&- G_{00}(k+q)F_{\uparrow\downarrow,13}(k,k',q)G_{10}(-k'-q)G_{01}(-k') \\
&- G_{00}(k+q)F_{\uparrow\downarrow,03}(k,k',q)G_{10}(-k'-q)G_{11}(-k')] \,.
\end{aligned} \tag{3.146b}$$

The other option is to reorder the operators in the quadruple term into $-\langle \bar{c}_\uparrow(x_1')c_\uparrow(x_2)c_\downarrow(x_4)\bar{c}_\downarrow(x_3)\rangle$, which corresponds to the 11 term $\langle \bar{c}_{k\uparrow} c_{k+q\uparrow} c_{-k'-q\downarrow} \bar{c}_{-k'\downarrow} \rangle$ in the $\underline{G}^{(2)}_{\uparrow\uparrow}(k, k', q)$ matrix, we get another set of equations

$$
\begin{aligned}
\Sigma_{00}(k) = \frac{Un}{2} - \frac{U}{\beta^2 N^2} \sum_{k'q} [& - G_{00}(k+q) F_{\uparrow\uparrow,11}(k,k',q) G_{11}(k'+q) G_{11}(k') \\
& - G_{00}(k+q) F_{\uparrow\uparrow,00}(k,k',q) G_{01}(k'+q) G_{10}(k') \\
& - G_{01}(k+q) F_{\uparrow\uparrow,21}(k,k',q) G_{11}(k'+q) G_{10}(k') \\
& - G_{01}(k+q) F_{\uparrow\uparrow,20}(k,k',q) G_{01}(k'+q) G_{10}(k') \\
& - G_{01}(k+q) F_{\uparrow\uparrow,31}(k,k',q) G_{11}(k'+q) G_{11}(k') \\
& - G_{00}(k+q) F_{\uparrow\uparrow,10}(k,k',q) G_{01}(k'+q) G_{11}(k') \\
& - G_{00}(k+q) F_{\uparrow\uparrow,01}(k,k',q) G_{11}(k'+q) G_{10}(k') \\
& - G_{01}(k+q) F_{\uparrow\uparrow,30}(k,k',q) G_{01}(k'+q) G_{11}(k')] \,, \qquad (3.147a)
\end{aligned}
$$

$$
\begin{aligned}
\Sigma_{01}(k) = \quad 0 \quad - \frac{U}{\beta^2 N^2} \sum_{k'q} [& - G_{00}(k+q) F_{\uparrow\uparrow,12}(k,k',q) G_{01}(k'+q) G_{11}(k') \\
& - G_{01}(k+q) F_{\uparrow\uparrow,22}(k,k',q) G_{01}(k'+q) G_{10}(k') \\
& - G_{01}(k+q) F_{\uparrow\uparrow,33}(k,k',q) G_{11}(k'+q) G_{11}(k') \\
& - G_{01}(k+q) F_{\uparrow\uparrow,32}(k,k',q) G_{01}(k'+q) G_{11}(k') \\
& - G_{01}(k+q) F_{\uparrow\uparrow,23}(k,k',q) G_{11}(k'+q) G_{10}(k') \\
& - G_{00}(k+q) F_{\uparrow\uparrow,02}(k,k',q) G_{01}(k'+q) G_{10}(k') \\
& - G_{00}(k+q) F_{\uparrow\uparrow,13}(k,k',q) G_{11}(k'+q) G_{11}(k') \\
& - G_{00}(k+q) F_{\uparrow\uparrow,03}(k,k',q) G_{11}(k'+q) G_{10}(k')] \,. \qquad (3.147b)
\end{aligned}
$$

These two sets of equations are equivalent to each other, we will use Eq. 3.146 in the following derivation to stay consistent with the paramagnetic state equation given in Ref. [28, 42]

$$
\Sigma_\sigma(k) = \frac{1}{2} Un - \frac{U}{\beta^2 N^2} \sum_{k'q} G_\sigma(k) F_{\uparrow\downarrow}(k,k',q) G_{-\sigma}(k+q) G_{-\sigma}(k') \,, \qquad (3.148)
$$

where $F_{\uparrow\downarrow}$ is equivalent with $F_{\uparrow\downarrow,00}$, and the relation between G_σ and terms in the $\underline{G}$ matrix can be found in Eq. 3.36.

The diagrammatic representation of the Schwinger-Dyson equation for the anomalous self-energy [Eq. 3.146b] is shown in the panel (a) of Fig. 3.2. Panel (b) shows two low-order terms of the anomalous self-energy. F, in the case of superconducting order, can have eight possible combinations of incoming or outgoing legs, as illustrated in panel (c). They contain all allowed scattering processes, some of which are illustrated in panel (d).

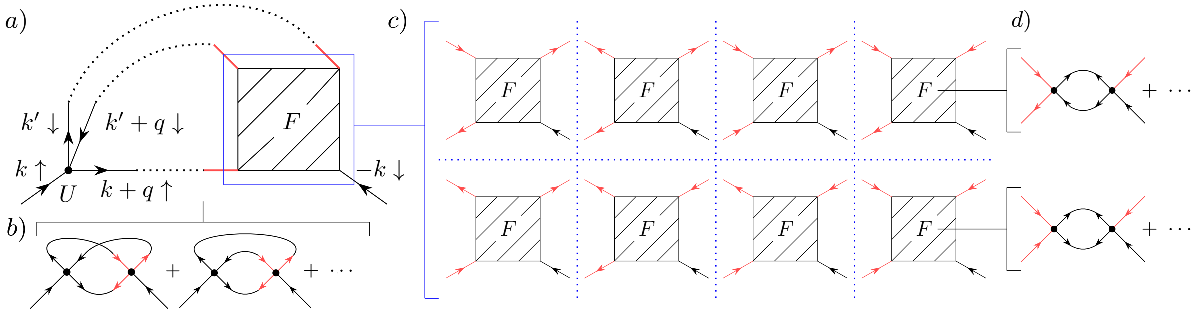

Figure 3.2: Anomalous self-energy diagrams. Panel a: Schwinger Dyson equation [Eq. 3.146b]. Shaded box denotes vertex F with one fixed outgoing leg. Dotted lines: normal or anomalous Green's functions. Panel b: Low-order anomalous self energy diagrams. Panel c: Explicit representation of index combinations of F. Panel d: Some of the low-order diagrams contributing to F. Figure from Ref. [50].

3.6.2 Schwinger-Dyson equations expressed in physical channels

A useful transformation of the Schwinger-Dyson equations [Eqs. 3.146a, 3.146b] is to express the self-energies with vertices in different physical channels defined in section 3.4.3. With the definitions given in Eq. 3.120, the normal and anomalous self-energies in Eqs. 3.146a, 3.146b can be expressed in two separated physical channels S_0 and S_z

$$\Sigma_{00}(k) = \frac{1}{2}[\Sigma_{00,S_0}(k) + \Sigma_{00,S_z}(k)]\,, \tag{3.149a}$$

$$\Sigma_{01}(k) = \frac{1}{2}[\Sigma_{01,S_0}(k) + \Sigma_{01,S_z}(k)]\,. \tag{3.149b}$$

The two different components can be written out explicitly with full vertex functions in one of the physical channels

$$\begin{aligned}\Sigma_{00,S_0}(k) = \frac{Un}{2} + \frac{U}{\beta^2N^2}\sum_{k'q}\big[&- G_{00}(k+q)F_{S_0S_0}(k,k',q)G_{11}(-k'-q)G_{11}(-k') \\ &- G_{00}(k+q)F_{S_0\overline{S}_0}(k,k',q)G_{10}(-k'-q)G_{01}(-k') \\ &- G_{01}(k+q)F_{T_0\overline{T}_0}(k,k',q)G_{10}(-k'-q)G_{11}(-k') \\ &- G_{01}(k+q)F_{T_0S_0}(k,k',q)G_{11}(-k'-q)G_{11}(-k') \\ &- G_{01}(k+q)F_{T_0\overline{S}_0}(k,k',q)G_{10}(-k'-q)G_{01}(-k') \\ &- G_{00}(k+q)F_{\text{-}S_0T_0}(k,k',q)G_{11}(-k'-q)G_{01}(-k') \\ &- G_{00}(k+q)F_{S_0\overline{T}_0}(k,k',q)G_{10}(-k'-q)G_{11}(-k') \\ &- G_{01}(k+q)F_{\text{-}T_0T_0}(k,k',q)G_{11}(-k'-q)G_{01}(-k')\big]\,,\end{aligned} \tag{3.150a}$$

$$
\begin{aligned}
\Sigma_{00,S_z}(k) = \frac{Un}{2} + \frac{U}{\beta^2 N^2} \sum_{k'q} \big[&- G_{00}(k+q) F_{\text{-}S_z S_z}(k,k',q) G_{11}(-k'-q) G_{11}(-k') \\
&- G_{00}(k+q) F_{S_z \overline{S}_z}(k,k',q) G_{10}(-k'-q) G_{01}(-k') \\
&- G_{01}(k+q) F_{T_z \overline{T}_z}(k,k',q) G_{10}(-k'-q) G_{11}(-k') \\
&- G_{01}(k+q) F_{\text{-}T_z S_z}(k,k',q) G_{11}(-k'-q) G_{11}(-k') \\
&- G_{01}(k+q) F_{T_z \overline{S}_z}(k,k',q) G_{10}(-k'-q) G_{01}(-k') \\
&- G_{00}(k+q) F_{S_z T_z}(k,k',q) G_{11}(-k'-q) G_{01}(-k') \\
&- G_{00}(k+q) F_{S_z \overline{T}_z}(k,k',q) G_{10}(-k'-q) G_{11}(-k') \\
&- G_{01}(k+q) F_{T_z T_z}(k,k',q) G_{11}(-k'-q) G_{01}(-k') \big] \,, \qquad (3.150\text{b})
\end{aligned}
$$

$$
\begin{aligned}
\Sigma_{01,S_0}(k) = \; 0 \; + \frac{U}{\beta^2 N^2} \sum_{k'q} \big[&- G_{00}(k+q) F_{\overline{T}_0 T_0}(k,k',q) G_{11}(-k'-q) G_{01}(-k') \\
&- G_{01}(k+q) F_{\overline{S}_0 S_0}(k,k',q) G_{11}(-k'-q) G_{11}(-k') \\
&- G_{01}(k+q) F_{\overline{S}_0 \overline{S}_0}(k,k',q) G_{10}(-k'-q) G_{01}(-k') \\
&- G_{01}(k+q) F_{\text{-}\overline{S}_0 T_0}(k,k',q) G_{11}(-k'-q) G_{01}(-k') \\
&- G_{01}(k+q) F_{\overline{S}_0 \overline{T}_0}(k,k',q) G_{10}(-k'-q) G_{11}(-k') \\
&- G_{00}(k+q) F_{\text{-}\overline{T}_0 S_0}(k,k',q) G_{11}(-k'-q) G_{11}(-k') \\
&- G_{00}(k+q) F_{\text{-}\overline{T}_0 \overline{S}_0}(k,k',q) G_{10}(-k'-q) G_{01}(-k') \\
&- G_{00}(k+q) F_{\text{-}\overline{T}_0 \overline{T}_0}(k,k',q) G_{10}(-k'-q) G_{11}(-k') \big] \,, \qquad (3.151\text{a})
\end{aligned}
$$

$$
\begin{aligned}
\Sigma_{01,S_z}(k) = \; 0 \; + \frac{U}{\beta^2 N^2} \sum_{k'q} \big[&- G_{00}(k+q) F_{\overline{T}_z T_z}(k,k',q) G_{11}(-k'-q) G_{01}(-k') \\
&- G_{01}(k+q) F_{\overline{S}_z S_z}(k,k',q) G_{11}(-k'-q) G_{11}(-k') \\
&- G_{01}(k+q) F_{\text{-}\overline{S}_z \overline{S}_z}(k,k',q) G_{10}(-k'-q) G_{01}(-k') \\
&- G_{01}(k+q) F_{\text{-}\overline{S}_z T_z}(k,k',q) G_{11}(-k'-q) G_{01}(-k') \\
&- G_{01}(k+q) F_{\text{-}\overline{S}_z \overline{T}_z}(k,k',q) G_{10}(-k'-q) G_{11}(-k') \\
&- G_{00}(k+q) F_{\text{-}\overline{T}_z S_z}(k,k',q) G_{11}(-k'-q) G_{11}(-k') \\
&- G_{00}(k+q) F_{\overline{T}_z \overline{S}_z}(k,k',q) G_{10}(-k'-q) G_{01}(-k') \\
&- G_{00}(k+q) F_{\overline{T}_z \overline{T}_z}(k,k',q) G_{10}(-k'-q) G_{11}(-k') \big] \,. \qquad (3.151\text{b})
\end{aligned}
$$

With the definitions given in Eq. 3.129, the normal and anomalous self-energy can also be written in a single channel

$$\begin{aligned}\Sigma_{00}(k) = \frac{Un}{2} + \frac{U}{\beta^2 N^2}\sum_{k'q}\big[&- G_{00}(k+q)F_{\text{-}S_zS_z}(k,k+q,k'-k)G_{11}(-k'-q)G_{11}(-k') \\ &- G_{00}(k+q)F_{\text{-}T_z\overline{T}_z}(k,k+q,k'-k)G_{10}(-k'-q)G_{01}(-k') \\ &- G_{01}(k+q)F_{\text{-}S_z\overline{S}_z}(k,k+q,k'-k)G_{10}(-k'-q)G_{11}(-k') \\ &- G_{01}(k+q)F_{\text{-}S_zT_z}(k,k+q,k'-k)G_{11}(-k'-q)G_{11}(-k') \\ &- G_{01}(k+q)F_{T_z\overline{S}_z}(k,k+q,k'-k)G_{10}(-k'-q)G_{01}(-k') \\ &- G_{00}(k+q)F_{T_zS_z}(k,k+q,k'-k)G_{11}(-k'-q)G_{01}(-k') \\ &- G_{00}(k+q)F_{S_z\overline{T}_z}(k,k+q,k'-k)G_{10}(-k'-q)G_{11}(-k') \\ &- G_{01}(k+q)F_{T_zT_z}(k,k+q,k'-k)G_{11}(-k'-q)G_{01}(-k')\big] \,,\end{aligned} \tag{3.152a}$$

$$\begin{aligned}\Sigma_{01}(k) = \ \ 0 \ \ + \frac{U}{\beta^2 N^2}\sum_{k'q}\big[&- G_{00}(k+q)F_{\text{-}\overline{S}_zS_z}(k,k+q,k'-k)G_{11}(-k'-q)G_{01}(-k') \\ &- G_{01}(k+q)F_{\text{-}\overline{T}_zT_z}(k,k+q,k'-k)G_{11}(-k'-q)G_{11}(-k') \\ &- G_{01}(k+q)F_{\text{-}\overline{S}_z\overline{S}_z}(k,k+q,k'-k)G_{10}(-k'-q)G_{01}(-k') \\ &- G_{01}(k+q)F_{\text{-}\overline{S}_zT_z}(k,k+q,k'-k)G_{11}(-k'-q)G_{01}(-k') \\ &- G_{01}(k+q)F_{\text{-}\overline{T}_z\overline{S}_z}(k,k+q,k'-k)G_{10}(-k'-q)G_{11}(-k') \\ &- G_{00}(k+q)F_{\text{-}\overline{T}_zS_z}(k,k+q,k'-k)G_{11}(-k'-q)G_{11}(-k') \\ &- G_{00}(k+q)F_{\overline{S}_z\overline{T}_z}(k,k+q,k'-k)G_{10}(-k'-q)G_{01}(-k') \\ &- G_{00}(k+q)F_{\overline{T}_z\overline{T}_z}(k,k+q,k'-k)G_{10}(-k'-q)G_{11}(-k')\big] \,.\end{aligned} \tag{3.152b}$$

Changing the dummy indices in Eq. 3.152 as $k+q \to k'$, $k'-k \to q$ and using the relation $G_{00}(k) = -G_{11}(-k)$, we get the equivalence relations

$$\Sigma_{00,S_z}(k) = \Sigma_{00}(k) = \Sigma_{00,S_0}(k) \,, \tag{3.153a}$$

$$\Sigma_{01,S_z}(k) = \Sigma_{01}(k) = \Sigma_{01,S_0}(k) \,, \tag{3.153b}$$

by comparing each line of Eq. 3.152 and Eq. 3.150b, Eq. 3.151b.

The Schwinger-Dyson equations in different physical channels in the paramagnetic state (see Ref. [28]) can be obtained by setting all the anomalous terms to zero. These equations are the central equations for the fluctuation diagnostics method [28], which we will generalize to the singlet superconducting state in chapter 7.

3.7 Bethe-Salpeter equations in different physical channels

In section 2.7 we introduced the two-particle irreducible vertex function and the Bethe-Salpeter equation. In this section, we will summarize the Bethe-Salpeter equations written in different physical channels in the paramagnetic state.

With the momentum and spin conventions defined in Eq. 3.53 and Eq. 3.47a (the particle-hole convention [42]), the Bethe-Salpeter equation in the paramagnetic state can be written as

$$\chi_{\sigma\sigma'}(k,k',q) = \chi^{\times}_{0,\sigma\sigma'}(k,k',q) - \chi^{\times}_{0,\sigma\sigma_1}(k,k_1,q)\Gamma_{\sigma_1\sigma_2}(k_1,k_2,q)\chi_{\sigma_2\sigma'}(k_2,k',q)\,, \tag{3.154}$$

where we have used the Einstein summation notation, and $\chi_{\sigma\sigma'}$ is equivalent with $\chi_{\sigma\sigma',00}$. The two spin configurations $\uparrow\uparrow$ and $\uparrow\downarrow$ are coupled in Eq. 3.154. The physical channels defined in section 3.3 and section 3.4 provide a straight forward way of decoupling different spin combinations. With the definitions

$$\chi_d(k,k',q) = \chi_{\uparrow\uparrow}(k,k',q) + \chi_{\uparrow\downarrow}(k,k',q)\,, \tag{3.155a}$$

$$\chi_m(k,k',q) = \chi_{\uparrow\uparrow}(k,k',q) - \chi_{\uparrow\downarrow}(k,k',q)\,, \tag{3.155b}$$

the Bethe-Salpeter equation can be decoupled in two different channels by "spin diagonalization"

$$\chi_{d,m}(k,k',q) = \chi^{\times}_{0}(k,k',q) - \frac{1}{\beta^2N^2}\sum_{k_1k_2}\chi^{\times}_{0}(k,k_1,q)\Gamma_{d,m}(k_1,k_2,q)\chi_{d,m}(k_2,k',q)\,, \tag{3.156}$$

with the spin indices of $\chi^{\times}_0(k,k',q) = \chi^{\times}_{0,\uparrow\uparrow}(k,k',q) = \chi^{\times}_{0,\downarrow\downarrow}(k,k',q)$ dropped since $\chi^{\times}_{0,\sigma\sigma'}(k,k',q) = 0$, $\sigma \neq \sigma'$.

A similar relation can be derived within the particle-particle convention [42], where the momenta and frequencies are chosen to be

$$k_1 = k\,, \quad k_2 = q-k'\,, \quad k_3 = q-k\,, \quad k_4 = k'\,, \tag{3.157a}$$

$$\omega_1 = \omega_n\,, \quad \omega_2 = \nu_n - \omega'_n\,, \quad \omega_3 = \nu_n - \omega_n\,, \quad \omega_4 = \omega'_n\,. \tag{3.157b}$$

The relation between the particle-hole and particle-particle convention is

$$\chi_{pp,\sigma\sigma'}(k,k',q) = \chi_{\sigma\sigma'}(k,k',q-k-k')\,. \tag{3.158}$$

By carrying out the spin diagonalization in the particle-particle convention [42]

$$\chi_s(k,k',q) = \chi_{pp,\uparrow\downarrow}(k,k',q) - \chi_{pp,\overline{\uparrow\downarrow}}(k,k',q)\,, \tag{3.159a}$$

$$\chi_t(k,k',q) = \chi_{pp,\uparrow\downarrow}(k,k',q) + \chi_{pp,\overline{\uparrow\downarrow}}(k,k',q)\,, \tag{3.159b}$$

the corresponding Bethe-Salpeter equation can be written as

$$\begin{aligned}\chi_s(k,k',q) = &-\chi^{\times}_{0,pp}(k,k',q)\\ &-\frac{1}{2}\frac{1}{\beta^2N^2}\sum_{k_1k_2}(\chi_{0,pp}(k,k_1,q)-\chi_s(k,k_1,q)\Gamma_s(k_1,k_2,q)\chi_{0,pp}(k_2,k',q))\,,\end{aligned} \tag{3.160a}$$

$$\begin{aligned}\chi_t(k,k',q) = &-\chi^{\times}_{0,pp}(k,k',q)\\ &-\frac{1}{2}\frac{1}{\beta^2N^2}\sum_{k_1k_2}(\chi_{0,pp}(k,k_1,q)+\chi_t(k,k_1,q)\Gamma_t(k_1,k_2,q)\chi_{0,pp}(k_2,k',q))\,.\end{aligned} \tag{3.160b}$$

Another useful relation is given by the spin configuration $\chi_{pp,\overline{\uparrow\downarrow}}$, for which the Bethe-Salpeter equation is in the same form as Eq. 3.156

$$\chi_{pp,\overline{\uparrow\downarrow}}(k,k',q) = \chi^{\times}_{0,pp}(k,k',q) - \frac{1}{\beta^2N^2}\sum_{k_1k_2}\chi^{\times}_{0,pp}(k,k_1,q)\Gamma_{pp,\overline{\uparrow\downarrow}}(k_1,k_2,q)\chi_{pp,\overline{\uparrow\downarrow}}(k_2,k',q)\,. \tag{3.161}$$

The Bethe-Salpeter equations [Eqs. 3.156, 3.161] provide the relations between the irreducible vertex Γ and the susceptibility χ in different physical channels. See chapter 5 for their applications.

The generalization of the Bethe-Salpeter equation Eq. 3.154 in the superconducting state can be performed similarly as Eq. 3.137.

Chapter 4

Models and Methods

For strongly correlated systems, solving the many-body Hamiltonian [Eq. 2.6] introduced in section 2.1 exactly is not possible for large systems due to the exponential growth of the Hilbert space with the number of particles. A common approach to get theoretical understandings of strongly correlated systems is to extract a certain subset of the electronic degrees of freedom and construct a low-energy effective model [51]. These models can then be solved numerically with advanced many-body methods. This chapter provides detailed derivations of the models and numerical methods used to obtain the simulation results shown in chapters 5, 6 and 7.

4.1 Hubbard model

The model we address explicitly is the single-band Hubbard model [12], the simplest model of interacting fermions on a discrete lattice. The Hamiltonian has a kinetic term that describes the hopping of electrons, and an interaction term that accounts for the interaction when two fermions occupy the same lattice site

$$H = \sum_{ij,\sigma} t_{ij} c_{i\sigma} c^{\dagger}_{j\sigma} + U \sum_{i} n_{i\uparrow} n_{i\downarrow} - \mu \sum_{i} (n_{i\uparrow} + n_{i\downarrow}) \,, \tag{4.1}$$

where $c^{(\dagger)}_{i\sigma}$ is the annihilation (creation) operator of a fermion on site i with spin σ, t_{ij} is the hopping amplitude between sites i and j, U is the on-site interaction, μ is the chemical potential, and $n_{i\sigma} = c^{\dagger}_{i\sigma} c_{i\sigma}$ is the density operator. On the lattice, the kinetic (hopping) term is diagonal in momentum space due to translational invariance, so the Hamiltonian can be written in a combined form

$$H = \sum_{k\sigma}(\epsilon_k - \mu) c_{k\sigma} c^\dagger_{k\sigma} + U \sum_i n_{i\uparrow} n_{i\downarrow}\,, \tag{4.2}$$

where $c^{(\dagger)}_{k\sigma}$ is the annihilation (creation) operator of a fermion in momentum space, and ϵ_k is the dispersion computed from Fourier transform of the hoppings

$$\epsilon_k = \sum_i t_{i0} e^{-ik\cdot(r_i - r_0)}\,, \tag{4.3}$$

with r_0 the lattice origin.

The typical ordered states (symmetry broken states) of the Hubbard model, which have lower symmetry than the Hamiltonian, include [32]

- Ferromagnetic order, with order parameter $\langle m\rangle = \frac{1}{N}\sum_l \langle n_{l\uparrow} - n_{l\downarrow}\rangle$, breaking spin rotational invariance.

- Antiferromagnetic order, with order parameter $\langle m_\Pi\rangle = \frac{1}{N}\sum_l (-1)^l \langle n_{l\uparrow} - n_{l\downarrow}\rangle$, breaking spin rotational and translational invariance.

- Charge density wave order, with order parameter $\langle n_\Pi\rangle = \frac{1}{N}\sum_l (-1)^l [\langle n_l\rangle - \langle n\rangle]$, breaking translational invariance.

- Singlet superconductivity order, with order parameter $\langle \Delta^\dagger\rangle = \frac{1}{N}\sum_l \langle c^\dagger_{l\uparrow} c^\dagger_{l\downarrow}\rangle$, breaking U(1) gauge symmetry.

4.1.1 Singlet superconducting state

The ordered state we consider in the following derivations is the singlet superconducting state, where the U(1) symmetry is broken, but the SU(2) symmetry is preserved. To enter the singlet superconducting state, one possible way is to add a superconducting source field to the system, meaning an extra term H' is added to the original Hamiltonian

$$H' = -\sum_{ij} (\eta_{ij} c_{i\downarrow} c_{j\uparrow} + \eta^*_{ji} c^\dagger_{j\uparrow} c^\dagger_{i\downarrow})\,, \tag{4.4}$$

with η_{ij} a translational invariant field. With the Nambu spinors introduced in Eq. 3.33 and the Pauli matrices defined in Eq. 3.17, the Hamiltonian with source field [Eqs. 4.1, 4.4] can be written as

$$H = \sum_{ij} t_{ij} \psi_i^\dagger \hat{\sigma}_3 \psi_j - \mu \sum_i \psi_i^\dagger \hat{\sigma}_3 \psi_i - \sum_{ij} \psi_i^\dagger \left[\eta'_{ij} \hat{\sigma}_1 - \eta''_{ij} \hat{\sigma}_2 \right] \psi_j + \frac{U}{2} \sum_i \left[\psi_i^\dagger \hat{\sigma}_3 \psi_i \right] \left[\psi_i^\dagger \hat{\sigma}_3 \psi_i \right] , \tag{4.5}$$

where $\eta'_{ij} = \mathrm{Re}[\eta_{ij}]$, $\eta''_{ij} = \mathrm{Im}[\eta_{ij}]$ are the real and imaginary components of η_{ij}, $\eta_{ij} = \eta'_{ij} + i\eta''_{ij}$, and the chemical potential has been shifted $\mu \to \mu - \frac{U}{2}$.

To identify the symmetry of a translational invariant superconducting field, it is more convenient to partially transform the Hamiltonian to momentum space as in Eq. 4.2, where the kinetic term and the external source field term are diagonal. The Hamiltonian can be written as

$$H = \sum_{k\sigma} (\epsilon_k - \mu) c_{k\sigma} c^\dagger_{k\sigma} - \sum_k (\eta_k c_{-k\downarrow} c_{k\uparrow} + \eta^\dagger_k c^\dagger_{k\uparrow} c^\dagger_{-k\downarrow}) + U \sum_i n_{i\uparrow} n_{i\downarrow} , \tag{4.6}$$

or using the Nambu spinors in the momentum space defined in Eq. 3.34

$$H = \sum_k \psi_k^\dagger \left[(\epsilon_k - \mu) \hat{\sigma}_3 - \eta'_k \hat{\sigma}_1 + \eta''_k \hat{\sigma}_2 \right] \psi_k + \frac{U}{2} \sum_i \left[\psi_i^\dagger \hat{\sigma}_3 \psi_i \right] \left[\psi_i^\dagger \hat{\sigma}_3 \psi_i \right] . \tag{4.7}$$

The spatial symmetry of the superconducting source field η_k can be identified with the momentum dependence of $\eta_k = g(k)\eta$

$$g(k) = \begin{cases} 1 & s \text{ wave} \\ \sin(k_x) & p_x \text{ wave} \\ \sin(k_x)\sin(k_y) & d_{xy} \text{ wave} \\ \cos(k_x) - \cos(k_y) & d_{x^2-y^2} \text{ wave} \end{cases} . \tag{4.8}$$

The Hubbard model [Eqs. 4.2, 4.7] is able to reproduce a large amount of the low-energy phenomenology observed in the high-temperature superconductors [13, 14]. See chapters 5, 6 and 7 for a discussion of the competing fluctuations in the paramagnetic state, and the analysis of the mechanism driving the singlet superconducting state.

4.2 Anderson impurity model

Despite the radical simplification introduced in model Hamiltonians like the Hubbard model [Eq. 4.1] as compared to the full ab-initio Hamiltonian [Eq. 2.6], even simple properties such as the phase diagram are difficult to calculate exactly [51]. In order to extract physics features from the model Hamiltonian numerically, one well established approximation scheme is to map the lattice problem to an auxiliary impurity problem, in which an impurity is embedded in an electronic bath subject to a self-consistent condition. The single-site Anderson impurity model (AIM) was first proposed by Anderson as an effective model for magnetic systems with a magnetic impurity hybridized with metallic bath [52]. Since then, it has been generalized as an effective model for many different systems [26]. This model plays an important role in the dynamical mean-field theory (DMFT) approximation [15], which is a widely used method for solving strongly correlated lattice systems. The effective action of the Anderson impurity model will be derived in this section.

4.2.1 Anderson impurity model without external field

Consider a system without external field, the Hamiltonian of the AIM can be written as

$$H = \sum_{ab} E_{ab} c_a^\dagger c_b + \frac{1}{2} \sum_{abcd} U_{abcd} c_a^\dagger c_b^\dagger c_d c_c + \sum_{\alpha b} (V_{\alpha b} f_\alpha^\dagger c_b + V_{b\alpha}^* c_b^\dagger f_\alpha) + \sum_{\alpha\beta} \epsilon_{\alpha\beta} f_\alpha^\dagger f_\beta \,, \tag{4.9}$$

where the two types of operators, $c_a^{(\dagger)}$ annihilate or create an electron in the impurity, $f_\alpha^{(\dagger)}$ annihilate or create an electron in the bath. a, b, c, d are quantum numbers of the impurity, α, β are (continuous) quantum numbers of the bath. All indices include both spatial and spin degrees of freedom, E_{ab} includes all bare level structures of the impurity, U_{abcd} describes the interaction between the impurity states, $V_{\alpha b}$ is the hybridization between the impurity and bath, $\epsilon_{\alpha\beta}$ describes the energy levels of the non-interacting bath. The corresponding action can be written as

$$S = S_{\text{loc}} + S_{\text{hyb}} + S_{\text{bath}} \,, \tag{4.10}$$

with

$$S_{\text{loc}} = \int_0^\beta d\tau \sum_{ab} \bar{c}_a(\tau)[\delta_{ab}\partial_\tau + E_{ab}] c_b(\tau) + \frac{1}{2} \int_0^\beta d\tau \sum_{abcd} U_{abcd} \bar{c}_a(\tau) \bar{c}_b(\tau) c_d(\tau) c_c(\tau) \,, \tag{4.11a}$$

$$S_{\text{hyb}} = \iint_0^\beta d\tau d\tau' \sum_{\alpha b} [V_{\alpha b} \bar{f}_\alpha(\tau) c_b(\tau') + V_{b\alpha}^* \bar{c}_b(\tau') f_\alpha(\tau)] \,, \tag{4.11b}$$

$$S_{\text{bath}} = \int_0^\beta d\tau \sum_{\alpha\beta} \bar{f}_\alpha(\tau)[\delta_{\alpha\beta}\partial_\tau + \epsilon_{\alpha\beta}] f_\beta(\tau) \,. \tag{4.11c}$$

The partition function for the system within the action formalism depends on both the impurity and the bath Grassmann fields

$$Z = \int \mathcal{D}[\bar{c}, c; \bar{f}, f] e^{-S[\bar{c},c;\bar{f},f]} \,. \tag{4.12}$$

Applying the Gaussian integral transformation Eq. 2.24 to the bath Grassmann fields f and $\bar{f}$, the path integral can be transformed as

$$\int \mathcal{D}[\bar{f}, f] \mathrm{exp}[-\sum_{\alpha\beta} \bar{f}_\alpha A^{-1}_{\alpha\beta} f_\beta + \sum_{\alpha} (\bar{J}_\alpha f_\alpha + \bar{f}_\alpha J_\alpha)] = \det(A^{-1}) \mathrm{exp}[\sum_{\alpha\beta} \bar{J}_\alpha A_{\alpha\beta} J_\beta] \,, \tag{4.13}$$

where $S_{\mathrm{bath}} + S_{\mathrm{hyb}}$ has been transformed together by defining $\sum_b V_{\alpha b} c_b = J_\alpha$, and A is the bath propagator G^{bath} defined with $[\partial_\tau + \epsilon_{\alpha\gamma}] G^{\mathrm{bath}}_{\gamma\beta}(\tau - \tau') = -\delta_{\alpha\beta}\delta(\tau - \tau')$. Integrating out the bath fermions explicitly, we arrive at an effective action formalism for the partition function

$$Z = Z_{\mathrm{bath}} \int \mathcal{D}[\bar{c}, c] e^{-S_{\mathrm{eff}}} \,, \tag{4.14}$$

where the effective action is defined as

$$\begin{aligned} S_{\mathrm{eff}} =& S_{\mathrm{local}} + \iint_0^\beta d\tau d\tau' \sum_{ab} \bar{c}_a(\tau) \Delta_{ab}(\tau - \tau') c_b(\tau') \\ =& \iint_0^\beta d\tau d\tau' \sum_{ab} \bar{c}_a(\tau) [\delta(\tau - \tau')(\delta_{ab}\partial_\tau + E_{ab}) + \Delta_{ab}(\tau - \tau')] c_b(\tau') \\ &+ \frac{1}{2} \int_0^\beta d\tau \sum_{abcd} U_{abcd} \bar{c}_a(\tau) \bar{c}_b(\tau) c_d(\tau) c_c(\tau) \\ =& - \iint_0^\beta d\tau d\tau' \sum_{ab} \bar{c}_a(\tau) \mathcal{G}^{-1}_{ab}(\tau - \tau') c_b(\tau') + \frac{1}{2} \int_0^\beta d\tau \sum_{abcd} U_{abcd} \bar{c}_a(\tau) \bar{c}_b(\tau) c_d(\tau) c_c(\tau) \,, \end{aligned} \tag{4.15}$$

with the hybridization function

$$\Delta_{ab}(\tau - \tau') = \sum_{\alpha\beta} V^\dagger_{a\alpha} G^{\mathrm{bath}}_{\alpha\beta}(\tau - \tau') V_{\beta b} \,, \tag{4.16}$$

and the Weiss field $\mathcal{G}$ of the impurity problem

$$-\mathcal{G}^{-1}_{ab} = \delta(\tau - \tau')(\delta_{ab}\partial_\tau + E_{ab}) + \Delta_{ab}(\tau - \tau') \,. \tag{4.17}$$

The corresponding definitions in the frequency space can be written as

$$\mathcal{G}^{-1}_{ab}(i\omega_n) = (i\omega_n\delta_{ab} - E_{ab}) - \Delta_{ab}(i\omega_n)\,, \tag{4.18}$$

$$\Delta_{ab}(i\omega_n) = \sum_{\alpha\beta} V^{\dagger}_{a\alpha}(i\omega_n - \epsilon_{\alpha\beta})^{-1}V_{\beta b}\,. \tag{4.19}$$

4.2.2 Anderson impurity model with singlet superconducting field

To study a system in the presence of a singlet superconducting source field, we need to add the source field to both the impurity and the bath in the AIM. We will only consider the Hubbard interaction (see section 4.1) and use the Nambu spinors in the following derivations for compactness of the expressions. The Nambu spinors include the spin degree of freedom (see Eq. 3.33), and all the operator indices only contain spatial degrees of freedom. For clarity we change the indices $a, b \to i, j$, $\alpha, \beta \to \iota, \kappa$. The actions of the AIM in Eq. 4.11 can be written as

$$\begin{aligned} S_{\text{loc}} = &\int_0^\beta d\tau \sum_{ij} \bar{\psi}_i(\tau)[\delta_{ij}\partial_\tau\hat{\sigma}_0 + E_{ij}\hat{\sigma}_3 - \eta'_{ij}\hat{\sigma}_1 + \eta''_{ij}\hat{\sigma}_2]\psi_j(\tau) \\ &+ \frac{U}{2}\int_0^\beta d\tau \sum_i [\bar{\psi}_i(\tau)\hat{\sigma}_3\psi_i(\tau)][\bar{\psi}_i(\tau)\hat{\sigma}_3\psi_i(\tau)]\,, \end{aligned} \tag{4.20a}$$

$$\begin{aligned} S_{\text{hyb}} = &\iint_0^\beta d\tau d\tau' \sum_{\iota j}[\bar{\phi}_\iota(\tau)(V_{\iota j}\hat{\sigma}_3 - \eta'_{\iota j}\hat{\sigma}_1 + \eta''_{\iota j}\hat{\sigma}_2)\psi_j(\tau') \\ &+ \bar{\psi}_j(\tau')(V^*_{j\iota}\hat{\sigma}_3 - \eta'_{j\iota}\hat{\sigma}_1 - \eta''_{j\iota}\hat{\sigma}_2)\phi_\iota(\tau)]\,, \end{aligned} \tag{4.20b}$$

$$S_{\text{bath}} = \int_0^\beta d\tau \sum_{\iota\kappa} \bar{\phi}_\iota(\tau)[\delta_{\iota\kappa}\partial_\tau\hat{\sigma}_0 + \epsilon_{\iota\kappa}\hat{\sigma}_3 - \eta'_{\iota\kappa}\hat{\sigma}_1 + \eta''_{\iota\kappa}\hat{\sigma}_2]\phi_\kappa(\tau)\,, \tag{4.20c}$$

where we have used ϕ and $\bar{\phi}$ as the Nambu spinors describing the bath to distinguish with the impurity. With the single-particle Green's function matrix in the singlet superconducting state defined in Eq. 3.35 and Eq. 3.38, the equation of motion of the bath Green's function can be written as

$$[\partial_\tau\hat{\sigma}_0 + \epsilon_{\iota\kappa}\hat{\sigma}_3 - \eta'_{\iota\kappa}\hat{\sigma}_1 + \eta''_{\iota\kappa}\hat{\sigma}_2]\underline{G}^{\text{bath}}_{\iota\kappa}(\tau - \tau') = -\delta_{\iota\kappa}\delta(\tau - \tau')\,. \tag{4.21}$$

With the analogue transformation for the spinors ψ and ϕ as in Eq. 4.13, integrating out the bath explicitly, the effective action is

$$\begin{aligned} S_{\text{eff}} = &- \iint_0^\beta d\tau d\tau' \sum_{ij} \bar{\psi}_i(\tau) \underline{\mathcal{G}}_{ij}^{-1}(\tau - \tau') \psi_j(\tau') \\ &+ \frac{U}{2} \int d\tau \sum_i [\bar{\psi}_i(\tau) \hat{\sigma}_3 \psi_i(\tau)][\bar{\psi}_i(\tau) \hat{\sigma}_3 \psi_i(\tau)] \,, \end{aligned} \tag{4.22}$$

where the Weiss field $\underline{\mathcal{G}}^{-1}$ can be written out explicitly in the frequency space as

$$\underline{\mathcal{G}}_{ij}^{-1}(i\omega_n) = [i\omega_n \hat{\sigma}_0 \delta_{ij} - (E_{ij} - \mu)\hat{\sigma}_3 + \eta'_{ij}\hat{\sigma}_1 - \eta''_{ij}\hat{\sigma}_2] - \underline{\Delta}_{ij}(i\omega_n) \,, \tag{4.23}$$

$$\underline{\Delta}_{ij}(i\omega_n) = \sum_{\iota\kappa} [V_{i\iota}^* \hat{\sigma}_3 - \eta'_{i\iota}\hat{\sigma}_1 - \eta''_{i\iota}\hat{\sigma}_2] \underline{G}_{\iota\kappa}^{\text{bath}}(i\omega_n) [V_{\kappa j}\hat{\sigma}_3 - \eta'_{\kappa j}\hat{\sigma}_1 + \eta''_{\kappa j}\hat{\sigma}_2] \,. \tag{4.24}$$

The main difference between Eqs. 4.18, 4.19, and Eqs. 4.23, 4.24 is that all terms in the Weiss field and the hybridization function are extended from a scalar to a 2 × 2 matrix. Note that even though we specialized to the Hubbard interaction in the derivation above, the interacting term does not enter the transformation used to derive the effective action, and can in general be any type of interaction.

4.3 Dynamical cluster approximation

A common strategy used in theoretical physics to solve a complicated problem is to obtain an approximation to the solution in terms of a more tractable auxiliary problem, specified by a self-consistency condition [26]. DMFT [15], which obtains the approximated solution of a lattice problem using an auxiliary quantum impurity model introduced in section 4.2, has been a powerful tool for studying lattice models. In this section we provide the derivation of DMFT with the single-band Hubbard model [section 4.1] using the cavity construction. We then introduce cluster extensions of DMFT, and derive the dynamical cluster approximaiton (DCA). The derivations in this section closely follow Refs. [15, 16, 53, 54].

4.3.1 Cavity construction

One of the possible ways for deriving the auxiliary problem of the lattice problem is through the cavity construction [15]. The underlying idea is to focus on a cluster in the lattice and explicitly integrate out all the other lattice sites to define an effective dynamics for the selected cluster [15]. Consider the single band Hubbard model without external field [Eq. 4.1], the action at site i can be decomposed into an atomic part and a hopping part [15]

$$S_i^{\mathrm{at}} = \int_0^\beta d\tau \sum_\sigma \bar{c}_{i\sigma}(\tau)[\partial_\tau - \mu]\bar{c}_{i\sigma}(\tau) + U n_{i\uparrow}(\tau) n_{i\downarrow}(\tau)\,, \tag{4.25a}$$

$$S_{ij}^{t} = \int_0^\beta d\tau \sum_\sigma [t_{ij}\bar{c}_{i\sigma}(\tau)c_{j\sigma}(\tau) + t_{ji}\bar{c}_{j\sigma}(\tau)c_{i\sigma}(\tau)]\,. \tag{4.25b}$$

The lattice action can be decomposed into three parts $S = S_C + S^{(0)} + \Delta S$, with cluster sites $i, j \in C$, and sites $x, y \notin C$

$$S_C = \sum_{i\in C} S_i^{\mathrm{at}} + \sum_{i,j\in C} S_{ij}^{t}\,, \quad S^{(0)} = \sum_{x\notin C} S_x^{\mathrm{at}} + \sum_{x,y\notin C} S_{xy}^{t}\,, \quad \Delta S = \sum_{\substack{i\in C\\ x\notin C}} S_{ix}^{t}\,. \tag{4.26}$$

The connection between the chosen cluster and other lattice sites is described by the hybridization term ΔS. With the decomposition in Eq. 4.26, the partition function can be written as

$$\begin{aligned} Z &= \int \prod_{i\in C} \mathcal{D}[\bar{c}_i, c_i] e^{-S_C} \int \prod_{x\notin C} \mathcal{D}[\bar{c}_x, c_x] e^{-S^{(0)}+\Delta S} \\ &= \int \prod_{i\in C} \mathcal{D}[\bar{c}_i, c_i] e^{-S_C} Z^{(0)} \langle e^{-\Delta S}\rangle_{S^{(0)}} \\ &= Z^{(0)} \int \prod_{i\in C} \mathcal{D}[\bar{c}_i, c_i] e^{-S_{\mathrm{eff}}}\,. \end{aligned} \tag{4.27}$$

where we have introduced the effective action

$$S_{\mathrm{eff}} = S_C + \ln\langle e^{-\Delta S}\rangle_{S^{(0)}}\,. \tag{4.28}$$

For the exponential term $\langle e^{-\Delta S}\rangle_{S^{(0)}}$ in the partition function [Eq. 4.27] and the effective action [Eq. 4.28], the thermal average $\langle\cdots\rangle_{S^{(0)}}$ is taken over the cavity action $S^{(0)}$. To have a systematic analysis of this exponential term, we use the generating functions of the full Green's function and the connected Green's function introduced in section 2.3.2

$$\mathcal{M}^{(0)}[\bar{J}, J] = \left\langle \exp\left(-\int_0^\beta d\tau \sum_{x\sigma} [\bar{J}_{x\sigma}(\tau)c_{x\sigma}(\tau) + \bar{c}_{x\sigma}(\tau)J_{x\sigma}(\tau)] \right) \right\rangle_{S^{(0)}}\,, \tag{4.29}$$

$$\mathcal{W}^{(0)}[\bar{J}, J] = \ln \left\langle \exp\left(-\int_0^\beta d\tau \sum_{x\sigma} [\bar{J}_{x\sigma}(\tau)c_{x\sigma}(\tau) + \bar{c}_{x\sigma}(\tau)J_{x\sigma}(\tau)] \right) \right\rangle_{S^{(0)}}\,. \tag{4.30}$$

By defining $\sum_i t_{ix}\bar{c}_{i\sigma} = \bar{J}_{x\sigma}$, the logarithm term in the effective action [Eq. 4.28] can be treated as a generating function

$$\ln\langle e^{-\Delta S}\rangle_{S^{(0)}} = \mathcal{W}^{(0)}[\bar{J}, J]\,, \tag{4.31}$$

and the effective action can be written as

$$S_{\text{eff}} = S_C + \mathcal{W}^{(0)}[\bar{J}, J]\,. \tag{4.32}$$

With the combined index

$$x = (i, \sigma, \tau)\,, \quad \int dx = \int_0^\beta d\tau \sum_i \sum_\sigma\,, \tag{4.33}$$

the connected Green's function can be generated using the generating function $\mathcal{W}$ as

$$\begin{aligned}(G^{(n)}_{\text{conn}})^{(0)}(x_1, \dots x_m; x'_1, \dots x'_k) &= (-1)^k \left.\frac{\delta^{(m+k)}\mathcal{W}^{(0)}(\bar{J}, J)}{\delta\bar{J}(x_1)\dots\delta\bar{J}(x_m)\delta J(x'_k)\dots\delta J(x'_1)}\right|_{\bar{J},J=0} \\ &= \langle\bar{c}(x'_1)\dots\bar{c}(x'_k)c(x_m)\dots c(x_1)\rangle_{S^{(0)},\text{conn}}\,,\end{aligned} \tag{4.34}$$

where $m + k = 2n$. In the paramagnetic state, $G^{(m+k)}_{\text{conn}}$ is only nonzero when $m = k$, while in the superconducting state, the constraint is loosen to $m + k = 2n$ is even. The perturbation expansion of the generating function can then be written as

$$\begin{aligned}\mathcal{W}^{(0)}[\bar{J}, J] = \sum_n \sum_{\substack{m,k \\ m+k=2n}} \frac{(-1)^k}{(2n)!} \int & dx_1 \dots dx_m dx'_1 \dots dx'_k \bar{J}(x_1)\dots\bar{J}(x_m)J(x'_k)\dots J(x'_1) \\ & \times (G^{(n)}_{\text{conn}})^{(0)}(x_1, \dots x_m; x'_1, \dots x'_k)\,.\end{aligned} \tag{4.35}$$

If we only consider the first order terms in Eq. 4.35 ($n = 1$), using the fact that for the single particle Green's functions

$$G^{(1)}_{\text{conn}}(x_1, x_2) = G^{(1)}(x_1, x_2) \in \{\langle c(x_1)\bar{c}(x_2)\rangle, \langle c(x_1)c(x_2)\rangle, \langle\bar{c}(x_1)\bar{c}(x_2)\rangle, \langle\bar{c}(x_1)c(x_2)\rangle\}\,, \tag{4.36}$$

The lowest nontrivial order of $\mathcal{W}^{(0)}$ in the spin singlet superconducting state can be written as

$$\mathcal{W}^{(0)}[\bar{J},J]\big|_{n=1} = \iint_0^\beta d\tau d\tau' \sum_{\substack{i,j\in C\\ x,y\notin C}} \big[- t_{ix}t_{yj}\bar{c}_{i\uparrow}(\tau)\langle -c_{x\uparrow}(\tau)\bar{c}_{y\uparrow}(\tau')\rangle_{S^{(0)}} c_{j\uparrow}(\tau') \\ - t_{xi}t_{jy}c_{i\downarrow}(\tau)\langle -\bar{c}_{x\downarrow}(\tau)c_{y\downarrow}(\tau')\rangle_{S^{(0)}} \bar{c}_{j\downarrow}(\tau') \\ - t_{ix}t_{jy}\bar{c}_{i\uparrow}(\tau)\langle c_{x\uparrow}(\tau)c_{y\downarrow}(\tau')\rangle_{S^{(0)}} \bar{c}_{j\downarrow}(\tau') \\ - t_{xi}t_{yj}c_{i\downarrow}(\tau)\langle \bar{c}_{x\downarrow}(\tau)\bar{c}_{y\uparrow}(\tau')\rangle_{S^{(0)}} c_{j\uparrow}(\tau')\big] \,, \tag{4.37}$$

where we have used the equivalence between spin up and spin down given by the SU(2) symmetry. Using the Nambu spinors [Eq. 3.33], Eq. 4.37 can be written in matrix form

$$\mathcal{W}^{(0)}[\bar{J},J]\big|_{n=1} = -\iint_0^\beta d\tau d\tau' \sum_{\substack{i,j\in C\\ x,y\notin C}} \bar{\psi}_i(\tau)\underline{t}_{ix}\underline{G}^{(0)}_{xy}(\tau-\tau')\underline{t}_{yj}\psi_j(\tau') \,, \tag{4.38}$$

$$\underline{t}_{ix} = \begin{pmatrix} t_{ix} & 0 \\ 0 & -t_{xi} \end{pmatrix} = t_{ix}\hat{\sigma}_3 \,. \tag{4.39}$$

The generalization to systems with superconducting bias field can be carried out straight forwardly by substituting the hopping matrix

$$\underline{t}_{ix} = t_{ix}\hat{\sigma}_3 \quad \rightarrow \quad \underline{t}_{ix} = t_{ix}\hat{\sigma}_3 - \eta'_{ix}\hat{\sigma}_1 + \eta''_{ix}\hat{\sigma}_2 \,. \tag{4.40}$$

4.3.2 Single site DMFT approximation

We first consider the single site case with $i=j=0$. The effective action given by the cavity construction [Eq. 4.28] is still not exact solvable due to the infinite order connected Green's function in Eq. 4.35. In the infinite connectivity limit ($z\to\infty$), it can be shown that only the first order term contribute to the effective potential $\mathcal{W}^{(0)}[\bar{J},J]$ [15, 55]

$$\lim_{z\to\infty} \mathcal{W}^{(0)}(\bar{J},J) = -\iint_0^\beta d\tau d\tau' \sum_{xy} \bar{\psi}_0(\tau)\underline{t}_{0x}\underline{G}^{(0)}_{xy}(\tau-\tau')\underline{t}_{y0}\psi_0(\tau') \,. \tag{4.41}$$

The effective action can then be written as

$$S_{\text{eff}} = -\iint_0^\beta d\tau d\tau' \bar{\psi}_0(\tau)\underline{\mathcal{G}}^{-1}_{00}(\tau-\tau')\psi_0(\tau') + \frac{U}{2}\int d\tau [\bar{\psi}_0(\tau)\hat{\sigma}_3\psi_0(\tau)][\bar{\psi}_0(\tau)\hat{\sigma}_3\psi_0(\tau)] \,, \tag{4.42}$$

where

$$-\underline{\mathcal{G}}^{-1}_{00}(\tau-\tau') = [\partial_\tau\hat{\sigma}_0 - \mu\hat{\sigma}_3]\delta(\tau-\tau') + \sum_{xy} \underline{t}_{0x}\underline{G}^{(0)}_{xy}(\tau-\tau')\underline{t}_{y0} \,. \tag{4.43}$$

The second term of the right hand side in Eq. 4.43 represents the process of hopping from site 0 to site x, propagating on the lattice with cavity from x to y (described by $\underline{G}^{(0)}_{xy}$), and then hopping back from site y to site 0, which takes a much simpler form on a Bethe lattice. When site 0 is removed from the lattice, the nearest neighbors of site 0 are disconnected, so $\underline{G}^{(0)}_{xy} = \underline{G}^{(0)}_{xx}\delta_{xy}$. In the limit of infinite connectivity, the Green's function of the lattice with cavity can be treated as the Green's function of the full lattice, which gives the relations [15, 54]

$$-\underline{\mathcal{G}}^{-1}_{00}(\tau-\tau') = [\partial_\tau\hat{\sigma}_0 - \mu\hat{\sigma}_3]\delta(\tau-\tau') + \underline{t}\;\underline{G}(\tau-\tau')\;\underline{t}\,, \tag{4.44}$$

$$\underline{\mathcal{G}}^{-1}_{00}(i\omega_n) = [i\omega_n\hat{\sigma}_0 + \mu\hat{\sigma}_3] - \underline{t}\;\underline{G}(i\omega_n)\;\underline{t}\,. \tag{4.45}$$

To connect the cavity Weiss field $\mathcal{G}$ to a given Green's function G, we need the relation between the lattice Green's function G and the cavity Green's function $G^{(0)}$, which for a general lattice, reads [15]

$$\underline{G}^{(0)}_{xy}(i\omega_n) = \underline{G}_{xy}(i\omega_n) - \underline{G}_{x0}(i\omega_n)\underline{G}^{-1}_{00}(i\omega_n)\underline{G}_{0y}(i\omega_n)\,. \tag{4.46}$$

Insert this equation into the Eq. 4.43 gives

$$\underline{\mathcal{G}}^{-1}_{00}(i\omega_n) = [i\omega_n\hat{\sigma}_0 + \mu\hat{\sigma}_3] - \sum_{xy}\underline{t}_{0x}[\underline{G}_{xy}(i\omega_n) - \underline{G}_{x0}(i\omega_n)\underline{G}^{-1}_{00}(i\omega_n)\underline{G}_{0y}(i\omega_n)]\underline{t}_{y0}\,. \tag{4.47}$$

Introduce the Fourier transformations of the lattice Green's function and the hopping term

$$\underline{G}_{xy}(i\omega_n) = \frac{1}{N}\sum_k \underline{G}_k(i\omega_n)e^{ik\cdot(r_x-r_y)}\,, \quad \epsilon_k = \sum_x t_{x0}e^{-ik\cdot r_x}\,, \quad \underline{\epsilon}_k = \epsilon_k\hat{\sigma}_3\,, \tag{4.48}$$

the summation in Eq. 4.47 can be expressed as

$$\begin{aligned}\underline{\mathcal{G}}^{-1}_{00}(i\omega_n) = [i\omega_n\hat{\sigma}_0 + \mu\hat{\sigma}_3] - \frac{1}{N}\sum_k \underline{\epsilon}_k\underline{G}_k(i\omega_n)\underline{\epsilon}_k \\ + \frac{1}{N^2}\sum_{kk'}\underline{\epsilon}_k\underline{G}_k(i\omega_n)\underline{G}^{-1}_{00}(i\omega_n)\underline{G}_{k'}(i\omega_n)\underline{\epsilon}_{k'}\,.\end{aligned} \tag{4.49}$$

The central approximation in DMFT is that the self energy $\underline{\Sigma}(i\omega_n)$ is a local quantity. The lattice Green's function can then be expressed in terms of a local term and a hopping term

$$\underline{G}^{-1}_k(i\omega_n) = \underline{\Lambda}(i\omega_n) - \underline{\epsilon}_k\,, \tag{4.50}$$

where the local quantity is defined as $\underline{\Lambda}(i\omega_n) = [i\omega_n\hat{\sigma}_0 + \mu\hat{\sigma}_3] - \underline{\Sigma}(i\omega_n)$. Inserting the hopping term $\underline{\epsilon}_k = \underline{\Lambda}(i\omega_n) - \underline{G}_k^{-1}(i\omega_n)$ into Eq. 4.49, and using $\frac{1}{N}\sum_k \underline{G}_k(i\omega_n) = \underline{G}_{00}(i\omega_n)$, $\sum_k \underline{\epsilon}_k = 0$, we obtain the relation

$$\underline{\mathcal{G}}_{00}^{-1}(i\omega_n) = [i\omega_n\hat{\sigma}_0 + \mu\hat{\sigma}_3] - \underline{\Lambda}(i\omega_n) + \underline{G}_{00}^{-1}(i\omega_n) = \underline{\Sigma}(i\omega_n) + \underline{G}_{00}^{-1}(i\omega_n)\,. \tag{4.51}$$

Comparing Eq. 4.51 with the Weiss field given by the AIM with single site impurity [Eq. 4.23], we get an explicit relation between the lattice Green's function $\underline{G}$, the hybridization function $\underline{\Delta}$, and the self-energy $\underline{\Sigma}$

$$\underline{G}_{00}^{-1}(i\omega_n) = [i\omega_n\hat{\sigma}_0 + \mu\hat{\sigma}_3] - \underline{\Delta}(i\omega_n) - \underline{\Sigma}(i\omega_n)\,. \tag{4.52}$$

This equation provides the self-consistent condition in DMFT. See section 4.3.4 for the self-consistency loop.

4.3.3 Quantum cluster methods

In DMFT, the self-energy is considered as a pure local quantity and momentum conservation is disregarded. To partially restore the momentum dependence, we refer to the cluster extensions of DMFT, also called the quantum cluster theories [16]. One of the cluster extensions, DCA [16, 19], will be derived and discussed in detail in this subsection. In the following derivations, we will only consider systems in the paramagnetic state and omit the spin index for simplicity. The generalization to the singlet superconducting state will be explained at the end of this section.

The derivations in this subsection closely follow Refs. [16, 53]. To follow the notations used in the references, we will use bold $\mathbf{x}$ and bold $\mathbf{k}$ as the symbols for sites and momenta, and move the labels from subscript to parenthesis.

4.3.3.1 General Setup

The quantum cluster approaches reduce the lattice problem to a cluster problem with finite number degrees of freedom. In the general set up of a cluster problem, a D-dimensional N-site lattice is partitioned into clusters with linear size L_c containing $N_c = L_c^D$ sites. Fig. 4.1 shows this type of partitioning with $D = 2$, $N_c = 4$. Following the notation in Ref. [16], we use $\tilde{\mathbf{x}}$ to mark the position of a cluster within the superlattice and $\mathbf{X}$ to label the N_c sites within the cluster. The position of a site in the original lattice is then decomposed into two parts $\mathbf{x} = \tilde{\mathbf{x}} + \mathbf{X}$. Correspondingly, in the reciprocal space, the first Brillouin zone is divided into N_c patches with size $(2\pi/L_c)^D$. The wave vector in the full Brillouin zone can be represented by

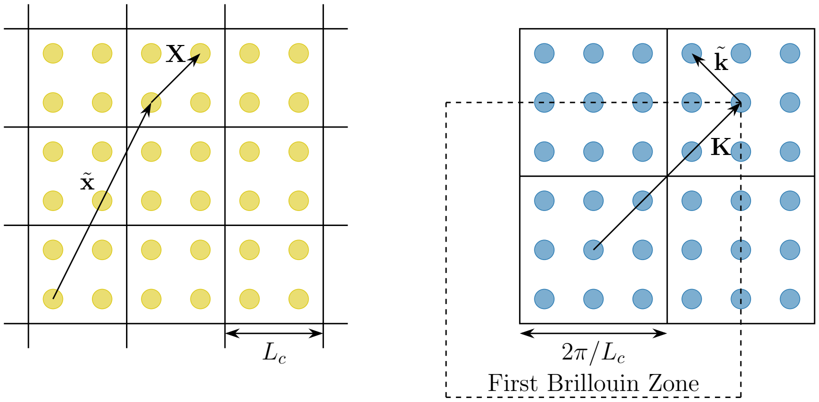

Figure 4.1: Coordinates in a two-dimensional lattice with $N_c = 4$. Left: real space coordinates. $\tilde{\mathbf{x}}$ is the position of a cluster within the superlattice, $\mathbf{X}$ labels the N_c sites within a cluster. Right: momentum space coordinates. $\mathbf{K}$ is the cluster momentum, $\tilde{\mathbf{k}}$ labels the momentum within each patch. Dotted line shows the first Brillouin zone.

$\mathbf{k} = \tilde{\mathbf{k}} + \mathbf{K}$, with $\mathbf{K}$ being the cluster momentum and $\tilde{\mathbf{k}}$ the momentum within the patch. The cluster momentum $\mathbf{K}$ becomes reciprocal lattice vector with $K_\alpha = n_\alpha(2\pi/L_c)$, n_α integer. The Fourier transform of a function within this type of partitioning can be written as [16]

$$f(\mathbf{K},\tilde{\mathbf{k}}) = \sum_{\mathbf{X}\tilde{\mathbf{x}}} f(\mathbf{X},\tilde{\mathbf{x}}) e^{-i[(\mathbf{K}+\tilde{\mathbf{k}})\cdot\mathbf{X}+\tilde{\mathbf{k}}\cdot\tilde{\mathbf{x}}]}\,, \quad f(\mathbf{X},\tilde{\mathbf{x}}) = \frac{1}{N}\sum_{\mathbf{K}\tilde{\mathbf{k}}} f(\mathbf{K},\tilde{\mathbf{k}}) e^{i[(\mathbf{K}+\tilde{\mathbf{k}})\cdot\mathbf{X}+\tilde{\mathbf{k}}\cdot\tilde{\mathbf{x}}]}\,. \tag{4.53}$$

The hopping and the self-energy can also be split into intercluster and intracluster parts [16]

$$t(\tilde{\mathbf{x}}_i - \tilde{\mathbf{x}}_j) = t_c \delta_{\tilde{\mathbf{x}}_i,\tilde{\mathbf{x}}_j} - \delta t(\tilde{\mathbf{x}}_i - \tilde{\mathbf{x}}_j)\,, \tag{4.54}$$

$$\Sigma(\tilde{\mathbf{x}}_i - \tilde{\mathbf{x}}_j, z) = \Sigma_c \delta_{\tilde{\mathbf{x}}_i,\tilde{\mathbf{x}}_j} - \delta\Sigma(\tilde{\mathbf{x}}_i - \tilde{\mathbf{x}}_j, z)\,, \tag{4.55}$$

where all quantities are matrices in cluster sites with dimension $N_c \times N_c$, and $t_c = t(\tilde{\mathbf{x}} = 0)$, $\Sigma_c(z) = \Sigma(\tilde{\mathbf{x}} = 0, z)$ are the intracluster terms, with z being an arbitrary frequency parameter.

4.3.3.2 Locator expansion

The basic idea behind quantum cluster theories is to write down an expansion in space around a finite size cluster, also called a locator expansion [16]. Using the locator expansion around the cluster, with matrix notation of the N_c cluster sites, the Green's function can be written in the form [16]

$$G(\tilde{\mathbf{x}}_i - \tilde{\mathbf{x}}_j, z) = g_c(z)\delta_{\tilde{\mathbf{x}}_i\tilde{\mathbf{x}}_j} + g_c(z)\sum_l \left[\delta t(\tilde{\mathbf{x}}_i - \tilde{\mathbf{x}}_l) + \delta\Sigma(\tilde{\mathbf{x}}_i - \tilde{\mathbf{x}}_l, z)\right] G(\tilde{\mathbf{x}}_l - \tilde{\mathbf{x}}_j, z)\,, \tag{4.56}$$

where $g_c(z)$ is a $N_c \times N_c$ matrix representing the cluster Green's function of an isolated cluster

$$g_c(z) = [(z+\mu) - t_c - \Sigma_c(z)]^{-1}\,. \tag{4.57}$$

With the preserved translational invariance of the superlattice, Eq. 4.56 can be simplified by performing a Fourier transform of the intercluster coordinates [16]

$$G(\tilde{\mathbf{k}}, z) = g_c(z) + g_c(z)[\delta t(\tilde{\mathbf{k}}) + \delta\Sigma(\tilde{\mathbf{k}}, z)]G(\tilde{\mathbf{k}}, z)\,. \tag{4.58}$$

The central approximation of all the cluster formalisms is to truncate the self-energy at cluster level, i.e $\delta\Sigma(\tilde{\mathbf{k}}, z) = 0$. The Green's function then reads

$$G(\tilde{\mathbf{k}}, z) = g_c(z) + g_c(z)\delta t(\tilde{\mathbf{k}})G(\tilde{\mathbf{k}}, z) = [g_c^{-1}(z) - \delta t(\tilde{\mathbf{k}})]^{-1}\,. \tag{4.59}$$

The corresponding hopping integral in momentum space can be computed with the intra-cluster Fourier transform of $\epsilon_{\mathbf{K}+\tilde{\mathbf{k}}}$

$$[t(\tilde{\mathbf{k}})]_{\mathbf{X}_i\mathbf{X}_j} = \frac{1}{N_c}\sum_{\mathbf{K}} e^{i(\mathbf{K}+\tilde{\mathbf{k}})\cdot(\mathbf{X}_i - \mathbf{X}_j)}\epsilon_{\mathbf{K}+\tilde{\mathbf{k}}}\,, \tag{4.60}$$

which violates translational symmetry with respect to the cluster sites $\mathbf{X}$ due to the phase factors $e^{i\tilde{\mathbf{k}}\cdot(\mathbf{X}_i - \mathbf{X}_j)}$.

4.3.3.3 Dynamical cluster approximation

In the Hubbard model [Eq. 4.1], the interaction U is purely local. The momentum dependence of the interaction vertex in diagrammatic expansion is then completely characterized [56] by the Laue function

$$\Delta(\mathbf{k}_1, \mathbf{k}_2, \mathbf{k}_3, \mathbf{k}_4) = \sum_{\mathbf{x}} e^{i(\mathbf{k}_1 - \mathbf{k}_2 + \mathbf{k}_3 - \mathbf{k}_4)\cdot\mathbf{x}}\,. \tag{4.61}$$

In a conventional diagrammatic approach, $\Delta(\mathbf{k}_1, \mathbf{k}_2, \mathbf{k}_3, \mathbf{k}_4) = N\delta(\mathbf{k}_1 - \mathbf{k}_2 + \mathbf{k}_3 - \mathbf{k}_4)$, which refers to momentum conservation at the vertex. In DMFT, $\Delta(\mathbf{k}_1, \mathbf{k}_2, \mathbf{k}_3, \mathbf{k}_4)$ is set to one and momentum conservation is disregarded. The basic idea behind the DCA [16, 19, 53] is to partially restore the translational invariance and momentum conservation at cluster level.

With the definitions of cluster momentum $\mathbf{K}$ and momentum within each path $\tilde{\mathbf{k}}$, the Laue function can be written in terms of [19]

$$\begin{aligned}\Delta(\mathbf{k}_1, \mathbf{k}_2, \mathbf{k}_3, \mathbf{k}_4) &= \sum_{\mathbf{x}} e^{i(\tilde{\mathbf{k}}_1 - \tilde{\mathbf{k}}_2 + \tilde{\mathbf{k}}_3 - \tilde{\mathbf{k}}_4 + \mathbf{K}_1 - \mathbf{K}_2 + \mathbf{K}_3 - \mathbf{K}_4)\cdot\mathbf{x}} \\ &= N_c \delta(\mathbf{K}_1 - \mathbf{K}_2 + \mathbf{K}_3 - \mathbf{K}_4) \sum_n \frac{1}{n!} [(\tilde{\mathbf{k}}_1 - \tilde{\mathbf{k}}_2 + \tilde{\mathbf{k}}_3 - \tilde{\mathbf{k}}_4) \cdot \nabla_{\mathbf{K}_1}]^n \,. \end{aligned} \tag{4.62}$$

In DCA, the Laue function is taken up to the first term with $n = 0$ [19]

$$\Delta_{\mathrm{DCA}}(\mathbf{k}_1, \mathbf{k}_2, \mathbf{k}_3, \mathbf{k}_4) = N_c \delta(\mathbf{M}(\mathbf{k}_1) - \mathbf{M}(\mathbf{k}_2) + \mathbf{M}(\mathbf{k}_3) - \mathbf{M}(\mathbf{k}_4)) \,, \tag{4.63}$$

where $\mathbf{M}$ is a mapping function that maps the lattice momentum $\mathbf{k}$ onto cluster momentum $\mathbf{K}$. Therefore, the cluster momentum is conserved within DCA, and the approximation $\Sigma(\mathbf{k}, z) \approx \Sigma(\mathbf{M}(\mathbf{k}), z)$ follows as a natural consequence [19]. Correspondingly, the translation invariance of the hopping integral can be restored by defining the intracluster hopping

$$[t_{\mathrm{DCA}}(\tilde{\mathbf{k}})]_{\mathbf{X}_i\mathbf{X}_j} = [t(\tilde{\mathbf{k}})]_{\mathbf{X}_i\mathbf{X}_j} e^{-i\tilde{\mathbf{k}}\cdot(\mathbf{X}_i - \mathbf{X}_j)} = \frac{1}{N_c} \sum_{\mathbf{K}} e^{i\mathbf{K}\cdot(\mathbf{X}_i - \mathbf{X}_j)} \epsilon_{\mathbf{K}+\tilde{\mathbf{k}}} \,. \tag{4.64}$$

The intra- and inter-cluster hopping integrals can then be written with the cluster Fourier transform

$$[t_{c,\mathrm{DCA}}]_{\mathbf{X}_i\mathbf{X}_j} = \frac{1}{N_c} \sum_{\mathbf{K}} e^{i\mathbf{K}\cdot(\mathbf{X}_i - \mathbf{X}_j)} \bar{\epsilon}_{\mathbf{K}} \,, \tag{4.65}$$

$$[\delta t_{\mathrm{DCA}}(\tilde{\mathbf{k}})]_{\mathbf{X}_i\mathbf{X}_j} = \frac{1}{N_c} \sum_{\mathbf{K}} e^{i\mathbf{K}\cdot(\mathbf{X}_i - \mathbf{X}_j)} \delta t(\mathbf{K} + \tilde{\mathbf{k}}) \,, \tag{4.66}$$

where

$$\bar{\epsilon}_{\mathbf{K}} = \frac{N_c}{N} \sum_{\tilde{\mathbf{k}}} \epsilon_{\mathbf{K}+\tilde{\mathbf{k}}} \,, \quad \delta t(\mathbf{K} + \tilde{\mathbf{k}}) = \epsilon_{\mathbf{K}+\tilde{\mathbf{k}}} - \bar{\epsilon}_{\mathbf{K}} \,. \tag{4.67}$$

The cluster translational invariant hopping integrals enable a diagonal Green's function in the cluster momentum space

$$\begin{aligned} G(\mathbf{K}+\tilde{\mathbf{k}},z) &= g_c(\mathbf{K},z) + g_c(\mathbf{K},z)\delta t(\mathbf{K}+\tilde{\mathbf{k}})G(\mathbf{K}+\tilde{\mathbf{k}},z) \\ &= \frac{1}{g_c^{-1}(\mathbf{K},z) - \delta t(\mathbf{K}+\tilde{\mathbf{k}})}\,, \end{aligned} \tag{4.68}$$

$$g_c(\mathbf{K},z) = [(z+\mu) - \bar{\epsilon}_{\mathbf{K}} - \Sigma_c(\mathbf{K},z)]^{-1}\,. \tag{4.69}$$

The major approximation in DCA is that the self-energy is a piece-wise constant function of the coarse grained Green's function

$$\begin{aligned} \bar{G}(\mathbf{K},z) &= \frac{N_c}{N}\sum_{\tilde{\mathbf{k}}} G(\mathbf{K}+\tilde{\mathbf{k}},z) \\ &= \frac{N_c}{N}\sum_{\tilde{\mathbf{k}}} [(z+\mu) - \bar{\epsilon}_{\mathbf{K}} - \Sigma_c(\mathbf{K},z) - \delta t(\mathbf{K}+\tilde{\mathbf{k}})]^{-1} \\ &= \frac{N_c}{N}\sum_{\tilde{\mathbf{k}}} [(z+\mu) - \epsilon_{\mathbf{K}+\tilde{\mathbf{k}}} - \Sigma_c(\mathbf{K},z)]^{-1}\,, \end{aligned} \tag{4.70}$$

in which we use the approximation $\Sigma(\mathbf{K}+\tilde{\mathbf{k}},z) = \Sigma_c(\mathbf{K},z)$. The only term containing $\tilde{\mathbf{k}}$ in Eq. 4.70 is $\bar{\epsilon}_{\mathbf{K}+\tilde{\mathbf{k}}}$. By defining a hybridization function

$$\Gamma(\mathbf{K},z) = \frac{\frac{N_c}{N}\sum_{\tilde{\mathbf{k}}} \delta t^2(\mathbf{K}+\tilde{\mathbf{k}})G(\mathbf{K}+\tilde{\mathbf{k}},z)}{1 + \frac{N_c}{N}\sum_{\tilde{\mathbf{k}}} \delta t(\mathbf{K}+\tilde{\mathbf{k}})G(\mathbf{K}+\tilde{\mathbf{k}},z)}\,, \tag{4.71}$$

the coarse grained Green's function can be written as

$$\bar{G}(\mathbf{K},z) = [(z+\mu) - \bar{\epsilon}_{\mathbf{K}} - \Sigma_c(\mathbf{K},z) - \Gamma(\mathbf{K},z)]^{-1}\,. \tag{4.72}$$

The decay of the hybridization function Eq. 4.71 follows $\Gamma(\mathbf{K},z) \sim \mathcal{O}(1/N_c^{2/D})$ [53]. This can be proved by noticing that the momentum $\tilde{\mathbf{k}} \leq \Delta k = 2\pi/N_c^{1/D}$. Since $\epsilon(\mathbf{K}) - \bar{\epsilon}(\mathbf{K}) \sim \mathcal{O}(\Delta k)$, it can be seen from the Taylor expansion of $\delta t(\mathbf{K}+\tilde{\mathbf{k}})$ around the cluster momentum $\mathbf{K}$ that $\delta t(\mathbf{K}+\tilde{\mathbf{k}})$ is of the order $\mathcal{O}(\Delta k)$ and $\Gamma(\mathbf{K},z)$ is of the order $\mathcal{O}((\Delta k)^2)$.

4.3.3.4 Hybridization function from cavity construction

The exact form of the hybridization function $\Gamma(\mathbf{K},i\omega_n)$ can also be computed from an effective cluster problem by focusing on one cluster in the superlattice (labeled by o in the derivations below) [53]. We will summarize the central steps of the derivation provided by Ref. [53] in this subsection, and will temporarily omit the time or frequency label since the analysis are done in site and momentum space.

With the DCA cluster set up, the hybridization term of cluster o can be written as

$$\Gamma_{no} = \sum_{lm} \delta^c_{on} T_{nl} G^{(0)}_{lm} T_{mo}\,, \quad \delta^c_{on} = \frac{N_c}{N} \sum_{\tilde{\mathbf{k}}} e^{i\tilde{\mathbf{k}}\cdot(\mathbf{x}_o - \mathbf{x}_n)}\,, \quad T_{nl} = \frac{1}{N} \sum_{\mathbf{k}} e^{i\mathbf{k}\cdot(\mathbf{x}_n - \mathbf{x}_l)} \delta t(\mathbf{k})\,, \tag{4.73}$$

where δ^c_{on} is a cluster delta function with value 1 for sites n on the impurity cluster and decays fast for sites outside the impurity cluster. $G^{(0)}_{lm}$ is the lattice Green's function with the impurity cluster removed, and T_{nl} is the cluster hopping integral. The cluster Fourier transform of the hybridization function is given by

$$\Gamma(\mathbf{K}) = \sum_n e^{-i\mathbf{K}\cdot(\mathbf{x}_n - \mathbf{x}_o)} \Gamma_{no}\,. \tag{4.74}$$

Similar to the full lattice Green's function [Eq. 4.68], the Green's function on the lattice with cavity removed can be written as

$$G^{(0)}_{lm} = g_{lm}\delta^c_{lm} + \sum_{l'm'}{}' g_{ll'}\delta^c_{ll'} T_{l'm'} G^{(0)}_{m'm}\,, \quad g_{lm} = \frac{1}{N_c} \sum_{\mathbf{K}} e^{i\mathbf{K}\cdot(\mathbf{x}_l - \mathbf{x}_n)} g_c(\mathbf{K})\,, \tag{4.75}$$

where the summation ($\sum{}'$) is restricted to the sites outside the cluster. To compute the hybridization term in Eq. 4.73, we define the quantity

$$\begin{aligned} Q_{lo} &= \sum_m G^{(0)}_{lm} T_{mo} \\ &= \sum_m g_{lm}\delta^c_{lm} T_{mo} + \sum_{l'm'} g_{ll'}\delta^c_{ll'} T_{l'm'} Q_{m'o} + f_{lo}\,, \end{aligned} \tag{4.76}$$

where the summation runs over all lattice sites, and the extra term f_{lo} is added to account for site exclusion and meet the requirement

$$\sum_l \delta^c_{ol} Q_{lo} e^{-i\mathbf{K}\cdot(\mathbf{x}_l - \mathbf{x}_o)} = 0\,, \quad \forall\, \mathbf{K}\,. \tag{4.77}$$

In the momentum space, this constraint can be expressed as

$$\frac{N_c}{N} \sum_{\tilde{\mathbf{k}}} Q(\mathbf{K} + \tilde{\mathbf{k}}) = 0\,, \quad \forall\, \mathbf{K}\,. \tag{4.78}$$

The expression of Q in the momentum space can be computed from the Fourier transform of Eq. 4.76

$$Q(\mathbf{K}+\tilde{\mathbf{k}}) = g_c(\mathbf{K})\delta t(\mathbf{K}+\tilde{\mathbf{k}}) + g_c(\mathbf{K})\delta t(\mathbf{K}+\tilde{\mathbf{k}})Q(\mathbf{K}+\tilde{\mathbf{k}}) \\ - g_c(\mathbf{K})\frac{N_c}{N}\sum_{\tilde{\mathbf{k}}_1}\delta t(\mathbf{K}+\tilde{\mathbf{k}}_1)Q(\mathbf{K}+\tilde{\mathbf{k}}_1)\,. \tag{4.79}$$

The hybridization function in momentum space can then be written as

$$\Gamma(\mathbf{K}) = \sum_{nl} e^{-i\mathbf{K}\cdot(\mathbf{x}_n-\mathbf{x}_o)}\delta^c_{on}T_{nl}Q_{lo} = \frac{N_c}{N}\sum_{\tilde{\mathbf{k}}_1}\delta t(\mathbf{K}+\tilde{\mathbf{k}}_1)Q(\mathbf{K}+\tilde{\mathbf{k}}_1)\,. \tag{4.80}$$

Eqs. 4.79, 4.80 and 4.68 give a set of closed form equations for $Q(\mathbf{K}+\tilde{\mathbf{k}})$ and $\Gamma(\mathbf{K})$, result in

$$Q(\mathbf{K}+\tilde{\mathbf{k}}) = \frac{\delta t(\mathbf{K}+\tilde{\mathbf{k}}) - \Gamma(\mathbf{K})}{g_c^{-1}(\mathbf{K}) - \delta t(\mathbf{K}+\tilde{\mathbf{k}})} = [\delta t(\mathbf{K}+\tilde{\mathbf{k}}) - \Gamma(\mathbf{K})]G(\mathbf{K}+\tilde{\mathbf{k}})\,, \tag{4.81}$$

$$\begin{aligned} \Gamma(\mathbf{K}) &= \frac{N_c}{N}\sum_{\tilde{\mathbf{k}}}\delta t(\mathbf{K}+\tilde{\mathbf{k}})Q(\mathbf{K}+\tilde{\mathbf{k}}) \\ &= \frac{N_c}{N}\sum_{\tilde{\mathbf{k}}}\delta t^2(\mathbf{K}+\tilde{\mathbf{k}}) - \Gamma(\mathbf{K})\frac{N_c}{N}\sum_{\tilde{\mathbf{k}}}\delta t(\mathbf{K}+\tilde{\mathbf{k}})G(\mathbf{K}+\tilde{\mathbf{k}})\,, \\ \Rightarrow \quad \Gamma(\mathbf{K}) &= \frac{\frac{N_c}{N}\sum_{\tilde{\mathbf{k}}}\delta t^2(\mathbf{K}+\tilde{\mathbf{k}})G(\mathbf{K}+\tilde{\mathbf{k}})}{1+\frac{N_c}{N}\sum_{\tilde{\mathbf{k}}}\delta t(\mathbf{K}+\tilde{\mathbf{k}})G(\mathbf{K}+\tilde{\mathbf{k}})}\,. \end{aligned} \tag{4.82}$$

Therefore, the hybridization function given by the cluster impurity method (Eq. 4.82) and the lattice partitioning method (Eq. 4.71) is exactly the same.

4.3.3.5 Connection to impurity model

To connect DCA with DMFT and the AIM introduced in section 4.2, we rewrite the effective action of the cavity construction [Eq. 4.32]

$$S_{\text{eff}} = -\iint_0^\beta d\tau d\tau' \sum_{ij,\sigma}\bar{c}_{i\sigma}(\tau)\mathcal{G}^{-1}_{ij,\sigma}(\tau-\tau')c_{j\sigma}(\tau') \\ + U\int d\tau \sum_i [\bar{c}_{i\uparrow}(\tau)c_{i\uparrow}(\tau)\bar{c}_{i\downarrow}(\tau)c_{i\downarrow}(\tau)]\,, \tag{4.83}$$

with the Weiss field $\mathcal{G}$ in the form

$$\mathcal{G}_{ij}^{-1}(\tau-\tau') = [\partial_\tau + t_{ij} - \mu]\delta(\tau-\tau') - \sum_{xy} t_{ix} G_{xy}^{(0)}(\tau-\tau') t_{yj}\,. \tag{4.84}$$

Transforming the cavity Green's function with the DCA Fourier transform, the Weiss field can be written out similarly as in Eq. 4.49

$$\begin{aligned}\mathcal{G}_c^{-1}(\mathbf{K}, i\omega_n) = [i\omega_n - \bar{\epsilon}_{\mathbf{K}} + \mu] - \frac{N_c}{N}\sum_{\tilde{\mathbf{k}}} \delta t(\mathbf{K}+\tilde{\mathbf{k}}) G(\mathbf{K}+\tilde{\mathbf{k}}, i\omega_n)\delta t(\mathbf{K}+\tilde{\mathbf{k}}) \qquad (4.85)\\ + \frac{N_c^2}{N^2}\sum_{\tilde{\mathbf{k}}\tilde{\mathbf{k}}'} \delta t(\mathbf{K}+\tilde{\mathbf{k}}) G(\mathbf{K}+\tilde{\mathbf{k}}, i\omega_n)\bar{G}^{-1}(\mathbf{K}, i\omega_n) G(\mathbf{K}+\tilde{\mathbf{k}}', i\omega_n)\delta t(\mathbf{K}+\tilde{\mathbf{k}}')\,.\end{aligned}$$

Using the central approximation in DCA that the self-energy only depends on cluster momentum $\mathbf{K}$, the corresponding local quantity can be defined as $\Lambda_c(\mathbf{K}, i\omega_n) = g_c^{-1}(\mathbf{K}, i\omega_n) = [i\omega_n - \bar{\epsilon}_{\mathbf{K}} + \mu] - \Sigma_c(\mathbf{K}, i\omega_n)$, and Eq. 4.68 gives the relation

$$\delta t(\mathbf{K}+\tilde{\mathbf{k}}) = \Lambda_c(\mathbf{K}, i\omega_n) - G^{-1}(\mathbf{K}+\tilde{\mathbf{k}}, i\omega_n)\,. \tag{4.86}$$

Inserting this equation into Eq. 4.85, and using $\bar{G}(\mathbf{K}, i\omega_n) = \frac{N_c}{N}\sum_{\tilde{\mathbf{k}}} G(\mathbf{K}+\tilde{\mathbf{k}}, i\omega_n)$, $\sum_{\tilde{\mathbf{k}}} \delta t(\mathbf{K}+\tilde{\mathbf{k}}) = 0$, the Weiss field can be written as

$$\begin{aligned}\mathcal{G}_c^{-1}(\mathbf{K}, i\omega_n) &= [i\omega_n - \bar{\epsilon}_{\mathbf{K}} + \mu] - \Lambda_c(\mathbf{K}, i\omega_n) + \bar{G}^{-1}(\mathbf{K}, i\omega_n)\\ &= \Sigma_c(\mathbf{K}, i\omega_n) + \bar{G}^{-1}(\mathbf{K}, i\omega_n)\,. \qquad (4.87)\end{aligned}$$

Comparing with Eq. 4.23 given by the AIM, the coarse grained Green's function can be written as

$$\bar{G}^{-1}(\mathbf{K}, i\omega_n) = [i\omega_n - \bar{\epsilon}_{\mathbf{K}} + \mu] - \bar{\Delta}(\mathbf{K}, i\omega_n) - \Sigma_c(\mathbf{K}, i\omega_n)\,, \tag{4.88}$$

which is exactly the same as Eq. 4.72 with $\bar{\Delta}(\mathbf{K}, i\omega_n) = \frac{N_c}{N}\sum_{\tilde{\mathbf{k}}} \Delta(\mathbf{K}+\tilde{\mathbf{k}}, i\omega_n) = \Gamma(\mathbf{K}, i\omega_n)$.

4.3.3.6 Φ functional

As shown by Baym and Kadanoff [35, 36], a thermodynamically consistent approximation can be constructed by requiring the self-energy Σ to be Φ-derivable, where Φ is the Luttinger-Ward functional (see section 2.6)

$$\Sigma = \frac{\delta\Phi[G]}{\delta G}\,. \tag{4.89}$$

It has been proved that both DMFT and DCA fulfill this restriction [15, 19, 53]. With Eq. 2.81 and Eq. 2.82, the Luttinger Ward functional can be written as

$$\Phi[G] = \sum_{l=1}^{\infty} \frac{1}{2l} \mathrm{Tr}\left[G(\mathbf{k})\Sigma^{(l)}(\mathbf{k})\right] . \tag{4.90}$$

Applying the Laue function defined in Eq. 4.63 to the vertices in all the diagrams defining Φ, the DCA Φ functional reads [19, 53]

$$\Phi_{\mathrm{DCA}}[\bar{G}] = \frac{N}{N_c} \sum_{l=1}^{\infty} \frac{1}{2l} \mathrm{Tr}_{\mathrm{c}}\left[\bar{G}(\mathbf{K})\Sigma^{(l)}(\mathbf{K})\right] , \tag{4.91}$$

with $\bar{G}(\mathbf{K})$ defined in Eq. 4.70 and the trace is taken over all the cluster degrees of freedom (including the cluster momentum $\mathbf{K}$). The requirement of a Φ-derivable approximation gives

$$\Sigma(\mathbf{k}) = \frac{\delta\Phi_{\mathrm{DCA}}}{\delta G(\mathbf{k})} = \frac{\delta\Phi_{\mathrm{DCA}}}{\delta\bar{G}(\mathbf{K})}\frac{\delta\bar{G}(\mathbf{K})}{\delta G(\mathbf{k})} = \frac{N}{N_c}\Sigma(\mathbf{K}) \times \frac{N_c}{N}\delta_{\mathbf{K},\mathbf{M}(\mathbf{k})} = \Sigma(\mathbf{M}(\mathbf{k})) . \tag{4.92}$$

The grand potential [Eq. 2.80] can be written out explicitly as

$$\begin{aligned}\Omega &= \frac{1}{\beta}\left[\Phi[G] + \mathrm{Tr}\ln[-G(\mathbf{k})] - \mathrm{Tr}[G(\mathbf{k})\Sigma(\mathbf{k})]\right] \\ &= \frac{1}{\beta}\left[\Phi[G] + \mathrm{Tr}\ln[-G(\mathbf{k})] - \mathrm{Tr}[G(\mathbf{k})G_0^{-1}(\mathbf{k}) - \mathbb{I}]\right] ,\end{aligned} \tag{4.93}$$

which within the DCA approximation reads

$$\Omega_{\mathrm{DCA}} = \frac{1}{\beta}\left[\Phi_{\mathrm{DCA}}[\bar{G}(\mathbf{K})] + \mathrm{Tr}\ln[-G(\mathbf{k})] - \mathrm{Tr}[G(\mathbf{k})G_0^{-1}(\mathbf{k}) - \mathbb{I}]\right] . \tag{4.94}$$

The DCA grand potential is stationary when Σ fulfills the coarse grained Dyson equation

$$\frac{\delta\Omega_{\mathrm{DCA}}}{\delta G(\mathbf{k})} = \frac{1}{\beta}\left[\Sigma(\mathbf{M}(\mathbf{k})) + G_0^{-1}(\mathbf{k}) - G^{-1}(\mathbf{k})\right] = 0 . \tag{4.95}$$

4.3.3.7 DCA approximation at two-particle level

To compute the susceptibilities within DCA, we use the Bethe-Salpeter equation given in Eq. 2.93 and Eq. 3.154. The approximation in DCA at two-particle level is that the two-particle irreducible vertex $\Gamma = \delta\Sigma[G]/\delta G$ is piece-wise constant in the momentum space [16, 19]

$$\Gamma(\mathbf{K}+\tilde{\mathbf{k}},\mathbf{K}'+\tilde{\mathbf{k}}',\mathbf{q}) \approx \Gamma_c(\mathbf{K},\mathbf{K}',\mathbf{q})\,, \tag{4.96}$$

where we omit the frequency labels. The cluster and lattice Bethe-Salpeter equations are in the form

$$\begin{aligned}\chi_{c,\sigma\sigma'}(\mathbf{K},\mathbf{K}',\mathbf{q}) =&\chi^{\times}_{0c,\sigma\sigma'}(\mathbf{K},\mathbf{K}',\mathbf{q}) \\ &- \chi^{\times}_{0c,\sigma\sigma_1}(\mathbf{K},\mathbf{K}_1,\mathbf{q})\Gamma_{c,\sigma_1\sigma_2}(\mathbf{K}_1,\mathbf{K}_2,\mathbf{q})\chi_{c,\sigma_2\sigma'}(\mathbf{K}_2,\mathbf{K}',\mathbf{q})\,, &(4.97)\\ \chi_{l,\sigma\sigma'}(\mathbf{K},\mathbf{K}',\mathbf{q}) =&\chi^{\times}_{0l,\sigma\sigma'}(\mathbf{K},\mathbf{K}',\mathbf{q}) \\ &- \chi^{\times}_{0l,\sigma\sigma_1}(\mathbf{K},\mathbf{K}_1,\mathbf{q})\Gamma_{c,\sigma_1\sigma_2}(\mathbf{K}_1,\mathbf{K}_2,\mathbf{q})\chi_{l,\sigma_2\sigma'}(\mathbf{K}_2,\mathbf{K}',\mathbf{q})\,, &(4.98)\end{aligned}$$

where the cluster and lattice bare susceptibility $\chi_0^{\times}$ are defined as [16]

$$\chi^{\times}_{0c,\sigma\sigma'}(\mathbf{K},\mathbf{K}',\mathbf{q}) = -\beta N_c \bar{G}(\mathbf{K})\bar{G}(\mathbf{K}+\mathbf{q})\delta_{\mathbf{K},\mathbf{K}'}\delta_{\sigma,\sigma'}\,, \tag{4.99}$$

$$\chi^{\times}_{0l,\sigma\sigma'}(\mathbf{K},\mathbf{K}',\mathbf{q}) = -\beta\frac{N_c^2}{N}\sum_{\tilde{\mathbf{k}}} G(\mathbf{K}+\tilde{\mathbf{k}})G(\mathbf{K}+\tilde{\mathbf{k}}+\mathbf{q})\delta_{\mathbf{K},\mathbf{K}'}\delta_{\sigma,\sigma'}\,. \tag{4.100}$$

The lattice susceptibility χ_l can be computed by eliminating Γ_c in Eq. 4.99 and Eq. 4.100, resulting in a matrix form equation

$$\chi_l^{-1} - \chi_{0l}^{\times -1} = \chi_c^{-1} - \chi_{0c}^{\times -1}\,, \tag{4.101}$$

where the matrices are in the space of $\mathbf{K}$, $\mathbf{K}'$ and σ, σ' with fixed $\mathbf{q}$. The decoupling between different spin configurations can be carried out as described in section 3.7.

4.3.3.8 Generalization to symmetry broken state

The momentum space approximation in DCA does not depend on the exact form of the Green's functions and self-energies. All the derivations in this subsection can be generalized to the singlet superconducting state by substituting the scalars with matrix form quantities $G \rightarrow \underline{G}$, $\Sigma \rightarrow \underline{\Sigma}$. See Ref. [16] for more discussions about the generalization to symmetry broken state.

4.3.4 Self-consistency loop

The self-consistent procedure of DMFT and DCA using the self-energy Σ as the adjustable quantity follow the same pattern [15, 16]. The DCA self-consistency loop is shown in Fig. 4.2.

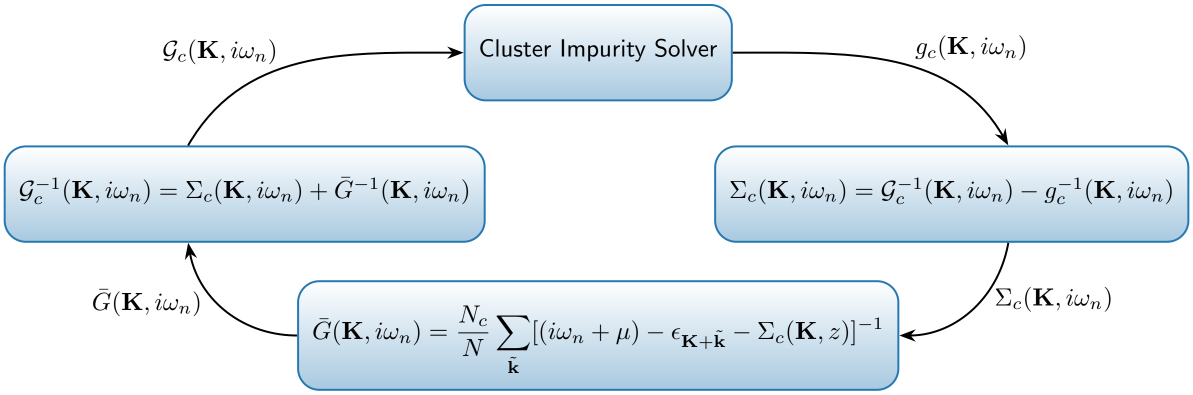

Figure 4.2: DCA self-consistency loop using the self-energy Σ as the adjustable quantity.

This procedure can be written out explicitly using the two central equations Eq. 4.70 and Eq. 4.87 in combine with a cluster impurity solver that can solve the impurity model introduced in section 4.2

1. Start from an initial guess of the self-energy $\Sigma_c(\mathbf{K}, i\omega_n)$, usually zero.
2. Compute the coarse-grained lattice Green's function $\bar{G}(\mathbf{K}, i\omega_n)$ using Eq. 4.70.
3. Compute the Weiss field $\mathcal{G}_c(\mathbf{K}, i\omega_n)$ using Eq. 4.87, which is the input of the impurity solver.
4. Compute the cluster Green's function $g_c(\mathbf{K}, i\omega_n)$ from the impurity solver.
5. Compute the new self-energy $\Sigma_c(\mathbf{K}, i\omega_n)$ with $\Sigma_c(\mathbf{K}, i\omega_n) = \mathcal{G}_c^{-1}(\mathbf{K}, i\omega_n) - g_c^{-1}(\mathbf{K}, i\omega_n)$.
6. Go back to step 2 until convergence.

In general the DCA self-consistency loop is well behaved and can converge within ~ 10 iterations, while critical slowing down will occur around second-order phase transitions.

To enter a spontaneous symmetry broken state, a initial source field will be added during the first iteration of the DCA loop, which will be removed in the subsequent iterations. With an impurity solver that allows for ordering, we identify the ordered state by checking whether the order parameter is finite after the calculation converge to a self-consistent solution.

4.4 Continuous-time auxiliary-field Monte Carlo

The central step in DMFT and DCA simulations is solving the quantum impurity problem, i.e. computing the impurity Green's function, which is a conceptually and algorithmically challenging problem. A wide range of approximate techniques have been developed to solve this problem, including exact diagonalization (ED) with discretized bath [22], numerical renormalization group [57, 58], resummation of particular subset of diagrams (such as the non-crossing approximation (NCA) [23]), etc.

For finite temperature simulations, quantum Monte Carlo techniques provide a general method for solving the quantum impurity problem [26]. The Hirsh-Fye quantum Monte Carlo method [59] has been the principal impurity solver before the developments of continuous-time quantum Monte Carlo (CT-QMC) methods. However, its power is limited by the finite discretization of the imaginary time axis, and the difficulty for simulating systems with general interaction. The CT-QMC methods avoid the time discretization by sampling the partition function with a diagrammatic expansion [26]. The most widely used CT-QMC methods include interaction-expansion continuous time quantum Monte Carlo (CT-INT), continuous-time hybridization expansion Monte Carlo (CT-HYB) [60, 61], and continuous-time auxiliary-field Monte Carlo (CT-AUX) [27]. For a review of the CT-QMC methods see Ref. [26].

This section mainly focuses on the derivations of the CT-AUX method for the single-band Hubbard model in the singlet superconducting state. The derivations closely follow Ref. [26, 27, 62, 63].

4.4.1 Partition function quantum Monte Carlo

The partition function Z of the AIM [Eq. 4.14] can be represented by a sum of the configurations c of weight w_c [63]

$$\begin{aligned} Z &= \int \mathcal{D}[\bar{c}, c] e^{-S_{\text{eff}}[\bar{c},c]} = \int \mathcal{D}[\bar{c}, c] e^{-S_0[\bar{c},c]-S_I[\bar{c},c]} \\ &= \sum_{k=0}^{\infty} \frac{(-1)^k}{k!} \int \mathcal{D}[\bar{c}, c] e^{-S_0} S_I^k = \sum_c w_c \,, \end{aligned} \tag{4.102}$$

where the action is split into an exact solvable part S_0 and a non exact solvable part S_I. In quantum Monte Carlo simulations, we sample the partition function configuration sum using a Markov process. In each simulation, a Markov chain $c_0 \to c_1 \to \cdots$ is generated in the configuration space in a way such that any possible configuration can be reached from another configuration in a finite number of steps (ergodicity) [26], with transition probabilities fulfilling the detailed balance condition [26]

$$|w_i| p(c_i \to c_j) = |w_j| p(c_j \to c_i) \,. \tag{4.103}$$

Here $p(c_i \to c_j)$ is the probability of moving from configuration c_i to configuration c_j, and can be written as

$$p(c_i \to c_j) = p^{\text{prop}}(c_i \to c_j)p^{\text{acc}}(c_i \to c_j)\,, \tag{4.104}$$

with p^{prop} the probability a move is proposed, and p^{acc} the probability a proposed move is accepted. The detailed balance relation [Eq. 4.103] can then be written in the form of

$$\frac{p^{\text{acc}}(c_i \to c_j)}{p^{\text{acc}}(c_j \to c_i)} = \frac{p^{\text{prop}}(c_j \to c_i)}{p^{\text{prop}}(c_i \to c_j)} \frac{|w(c_j)|}{|w(c_i)|}\,. \tag{4.105}$$

In quantum Monte Carlo simulations, the expectation value of an observable can be estimated via the Monte Carlo average

$$\langle O \rangle \approx \langle O \rangle_{\text{MC}} = \frac{\sum_{i=1}^{N} |w_{c_i}| \text{sign}_{c_i} O_{c_i}}{\sum_{i=1}^{N} |w_{c_i}| \text{sign}_{c_i}} = \frac{\langle \text{sign} \cdot O \rangle}{\langle \text{sign} \rangle}\,, \tag{4.106}$$

where O_{c_i} is the measured value at each configuration, and sign_{c_i} is the sign of the weight of each configuration $\text{sign}_{c_i} = w_{c_i}/|w_{c_i}|$. According to the central limit theorem, if the number of configurations is large enough ($N \to \infty$), the expectation value $\langle O \rangle_{\text{MC}}$ will be normally distributed around the true value with variance

$$\text{Var}[\langle O \rangle_{\text{MC}}] = \langle (O_{\text{MC}} - O)^2 \rangle = \frac{\text{Var}[O]}{N}\,. \tag{4.107}$$

The root-mean-square error $\sigma = \sqrt{\text{Var}[\langle O \rangle_{\text{MC}}]} = \sqrt{\text{Var}[\langle O \rangle]}/\sqrt{N}$ of this estimation then has an asymptotic scaling of $\sigma \sim \mathcal{O}(N^{-1/2})$.

4.4.2 Auxiliary-field expansion

The effective action of the cluster AIM associated with the single-band Hubbard model can be written out explicitly as in Eq. 4.15

$$\begin{aligned} S_{\text{eff}} = &- \iint_0^\beta d\tau d\tau' \sum_{ij} \bar{\psi}_i(\tau) \underline{\mathcal{G}}_{ij}^{-1}(\tau - \tau') \psi_j(\tau') \\ &+ \frac{U}{2} \int d\tau \sum_i [\bar{\psi}_i(\tau) \sigma_3 \psi_i(\tau)][\bar{\psi}_i(\tau) \sigma_3 \psi_i(\tau)]\,, \end{aligned} \tag{4.108}$$

with $\underline{\mathcal{G}}_{ij}$ the Weiss field defined in Eq. 4.23. Using the idea of interaction representation [4, 6], the effective action can be split into two parts $S_{\text{eff}} = S_0 + S_I$, with S_0 a quadratic term, and S_I the interacting part

$$S_0 = -\iint_0^\beta d\tau_i d\tau_j \sum_{ij} \bar{\psi}_i(\tau_i)\underline{\mathcal{G}}_{ij}^{-1}(\tau_i, \tau_j)\psi_j(\tau_j)\,, \tag{4.109}$$

$$S_I = \frac{U}{2}\int d\tau_i \sum_i [\bar{\psi}_i(\tau_i)\sigma_3\psi_i(\tau_i)][\bar{\psi}_i(\tau_i)\sigma_3\psi_i(\tau_i)]\,. \tag{4.110}$$

The interacting part is the same in both the paramagnetic and the singlet superconducting state, and can be expressed with the density operator $n_{i\sigma} = \bar{c}_{i\sigma}c_{i\sigma}$

$$S_I = U\int_0^\beta d\tau \sum_i [n_{i\uparrow}(\tau)n_{i\downarrow}(\tau) - \frac{1}{2}(n_{i\uparrow}(\tau) + n_{i\downarrow}(\tau))]\,. \tag{4.111}$$

Within the weak-coupling interaction expansion, the quadratic part of the effective action can be integrated out in the partition function

$$\begin{aligned} Z &= \int \mathcal{D}[\bar{c}, c]e^{-S_{\text{eff}}[\bar{c},c]} = \int \mathcal{D}[\bar{c}, c]e^{-S_0[\bar{c},c]}e^{-S_I[\bar{c},c]} \\ &= \int \mathcal{D}[\bar{c}, c]e^{-S_0[\bar{c},c]}\sum_k \frac{1}{k!}(-S_I[\bar{c}, c])^k = Z_0\sum_k \frac{1}{k!}\langle(-S_I[\bar{c}, c])^k\rangle_0\,, \end{aligned} \tag{4.112}$$

where we have used $\langle\cdot\rangle_0$ to represent the thermal average taken with respect to the quadratic action S_0. The main task in the weak-coupling partition function Monte Carlo simulations is to represent this power series [26, 27, 59, 63–65] .

For the convenience of implementation, we switch to the Hamiltonian formalism and write the partition function Z using operators

$$Z = \text{Tr}[e^{-\beta H}] = \text{Tr}[e^{-\beta H_0}Te^{-\int_0^\beta d\tau H_I(\tau)}]\,, \tag{4.113}$$

where H_0 is a quadratic term, and H_I is the interacting Hamiltonian

$$H_I = U\sum_i [n_{i\uparrow}n_{i\downarrow} - \frac{1}{2}(n_{i\uparrow} + n_{i\downarrow})]\,, \quad n_{i\sigma} = c_{i\sigma}^\dagger c_{i\sigma}\,. \tag{4.114}$$

To decouple the quadruple term in H_I, we define the shifted interacting Hamiltonian with an arbitrary parameter K

$$-\tilde{H}_I = -H_I + \frac{K}{\beta} = \frac{K}{\beta}(1 - \frac{\beta H_I}{K})\,, \tag{4.115}$$

and perform the discrete Hubbard-Stratonovich transformation [59, 66, 67], which gives

$$1 - \frac{\beta H_I}{K} = \frac{1}{2N} \sum_{i,s_i=\pm 1} e^{\gamma s_i (c_{i\uparrow}^\dagger c_{i\uparrow} - c_{i\downarrow}^\dagger c_{i\downarrow})} \,, \tag{4.116}$$

where N is the number of sites i summed over, and $s_i = \pm 1$ are auxiliary spins. The value of γ can be computed by setting $c_{i\uparrow}^\dagger c_{i\uparrow} - c_{i\downarrow}^\dagger c_{i\downarrow} = 1$, which gives

$$\cosh(\gamma) = 1 + \frac{\beta U N}{2K} \,. \tag{4.117}$$

The configuration space of the Monte Carlo sampling is the collection of all auxiliary spin configurations [26]

$$c = \{\{\}, \{(s_1, \tau_1, r_1)\}, \{(s_1, \tau_1, r_1), (s_2, \tau_2, r_2)\}, \ldots \{(s_1, \tau_1, r_1), \ldots (s_k, \tau_k, r_k)\}, \ldots\} \,, \tag{4.118}$$

where $s_i =\uparrow, \downarrow$, τ_i and r_i are labels of the time and position of the ith auxiliary spin. The time ordered exponent in the partition function can be expanded as

$$Z = e^{-K} \sum_k \sum_{\substack{s_i=\pm 1 \\ i=1\cdots k}} \int_0^\beta d\tau_1 \cdots \int_{\tau_{k-1}}^\beta d\tau_k \left(\frac{K}{2\beta N}\right)^k Z_k(\{s_i, \tau_i, r_i\}) \,, \tag{4.119}$$

with $Z_k(\{s_i, \tau_i, x_i\})$ the partition function associated with each configuration

$$Z_k(\{s_i, \tau_i, r_i\}) = \mathrm{Tr}\left[\prod_{i=1}^k e^{-\Delta\tau_i H_0} e^{\gamma s_i (n_{r_i\uparrow} - n_{r_i\downarrow})}\right] \,, \tag{4.120}$$

where $\Delta\tau_i = \tau_{i+1} - \tau_i$ for $i < k$ and $\Delta\tau_k = \beta - \tau_k + \tau_1$. Using the identity

$$\begin{aligned} e^{\gamma s \sigma n_\sigma} &= e^{\gamma s \sigma} n_\sigma + (1 - n_\sigma) = e^{\gamma s \sigma} c_\sigma^\dagger c_\sigma + c_\sigma c_\sigma^\dagger \\ &= e^{\gamma s \sigma} - (e^{\gamma s \sigma} - 1) c_\sigma c_\sigma^\dagger = 1 + (e^{\gamma s \sigma} - 1) c_\sigma^\dagger c_\sigma \,, \end{aligned} \tag{4.121}$$

the trace factor can be expressed in terms of the bare impurity Green's functions $\mathcal{G}$. Take the first order as an example, the partition function can be written as

$$\begin{aligned} &Z_1(\{s_1, \tau_1, r_1\}) \\ &= \mathrm{Tr}\left[e^{-(\beta-\tau_1)H_0} [e^{\gamma s_1} - (e^{\gamma s_1} - 1) c_{r_1\uparrow} c_{r_1\uparrow}^\dagger][e^{-\gamma s_1} - (e^{-\gamma s_1} - 1) c_{r_1\downarrow} c_{r_1\downarrow}^\dagger] e^{-\tau_1 H_1}\right] \,. \end{aligned} \tag{4.122}$$

In the paramagnetic state, only the normal components of the Green's function $\mathcal{G}_{r_i r_j, \sigma} = \langle c_{r_i \sigma}(\tau_i) c_{r_j \sigma}^\dagger(\tau_j)\rangle$ are non-zero. The spin up and spin down contributions to the partition function can be decoupled

$$Z_1(\{s_1,\tau_1,r_1\}) = Z_0[e^{\gamma s_1} - (e^{\gamma s_1}-1)\mathcal{G}_{r_1r_1,\uparrow}(0^+)][e^{-\gamma s_1} - (e^{-\gamma s_1}-1)\mathcal{G}_{r_1r_1,\downarrow}(0^+)]\,. \tag{4.123}$$

Using the Wick's theorem (see section 2.4), the kth order partition function can be written as

$$Z_k(\{s_i,\tau_i,r_i\}) = Z_0\prod_\sigma \det N_\sigma^{-1}(\{s_i,\tau_i,r_i\})\,, \tag{4.124}$$

where N_σ is a $k\times k$ matrix defined as

$$N_\sigma^{-1}(\{s_i,\tau_i,r_i\}) = e^{V_\sigma^{s_i}} - G_{0\sigma}^{\{\tau_i,r_i\}}(e^{V_\sigma^{s_i}} - \mathbb{I})\,, \tag{4.125}$$

$$e^{V_\sigma^{s_i}} = \mathrm{diag}(e^{\gamma(-1)^\sigma s_1},\ldots,e^{\gamma(-1)^\sigma s_i})\,, \tag{4.126}$$

$$(G_{0\sigma}^{\{\tau_i,r_i\}})_{ij} = \mathcal{G}_{r_ir_j,\sigma}(\tau_i-\tau_j)\,,\quad \tau_i-\tau_i = 0^+\,. \tag{4.127}$$

In the singlet superconducting state, both normal and anomalous components of the Green's function are non-zero (see Eq. 3.35). The first order partition function is in the form

$$\begin{aligned}
&Z_1(\{s_1,\tau_1,r_1\}) \\
&= \mathrm{Tr}\left[e^{-(\beta-\tau_1)H_0}[e^{\gamma s_1} - (e^{\gamma s_1}-1)c_{r_1\uparrow}c^\dagger_{r_1\uparrow}][e^{-\gamma s_1} - (e^{-\gamma s_1}-1)c_{r_1\downarrow}c^\dagger_{r_1\downarrow}]e^{-\tau_1H_1}\right] \\
&= \mathrm{Tr}\left[e^{-(\beta-\tau_1)H_0}[e^{\gamma s_1} - (e^{\gamma s_1}-1)c_{r_1\uparrow}c^\dagger_{r_1\uparrow}][1 + (e^{-\gamma s_1}-1)c^\dagger_{r_1\downarrow}c_{r_1\downarrow}]e^{-\tau_1H_1}\right] \\
&= Z_0[e^{\gamma s_1} + e^{\gamma s_1}(e^{-\gamma s_1}-1)\langle c^\dagger_{r_1\downarrow}(\tau_1)c_{r_1\downarrow}(\tau_1)\rangle_0 - (e^{\gamma s_1}-1)\langle c_{r_1\uparrow}(\tau_1)c^\dagger_{r_1\uparrow}(\tau_1)\rangle_0 \\
&\qquad - (e^{\gamma s_1}-1)(e^{-\gamma s_1}-1)\langle c_{r_1\uparrow}(\tau_1)c^\dagger_{r_1\uparrow}(\tau_1)c^\dagger_{r_1\downarrow}(\tau_1)c_{r_1\downarrow}(\tau_1)\rangle_0]\,,
\end{aligned} \tag{4.128}$$

where the quadruple term can be expanded using the Wick's theorem (omitting time argument)

$$\begin{aligned}
\langle c_{r_1\uparrow}c^\dagger_{r_1\uparrow}c^\dagger_{r_1\downarrow}c_{r_1\downarrow}\rangle_0 &= \langle c_{r_1\uparrow}c^\dagger_{r_1\uparrow}\rangle_0\langle c^\dagger_{r_1\downarrow}c_{r_1\downarrow}\rangle_0 - \langle c_{r_1\uparrow}c_{r_1\downarrow}\rangle_0\langle c^\dagger_{r_1\downarrow}c^\dagger_{r_1\uparrow}\rangle_0 \\
&= \det\begin{pmatrix} \langle c_{r_1\uparrow}c^\dagger_{r_1\uparrow}\rangle_0 & \langle c_{r_1\uparrow}c_{r_1\downarrow}\rangle_0 \\ \langle c^\dagger_{r_1\downarrow}c^\dagger_{r_1\uparrow}\rangle_0 & \langle c^\dagger_{r_1\downarrow}c_{r_1\downarrow}\rangle_0 \end{pmatrix} = \det[\langle \psi_{r_1}\psi^\dagger_{r_1}\rangle_0]\,.
\end{aligned} \tag{4.129}$$

Eq. 4.128 can then be written in matrix form

$$
\begin{aligned}
&\frac{Z_1(\{s_1,\tau_1,r_1\})}{Z_0} \qquad (4.130)\\
&= e^{-\gamma s_1}\{e^{2\gamma s_1} - e^{\gamma s_1}(e^{\gamma s_1}-1)\langle c_{r_1\uparrow}c^\dagger_{r_1\uparrow}\rangle_0 - e^{\gamma s_1}(e^{\gamma s_1}-1)\langle c^\dagger_{r_1\downarrow}c_{r_1\downarrow}\rangle_0\\
&\qquad + (e^{\gamma s_1}-1)(e^{\gamma s_1}-1)[\langle c_{r_1\uparrow}c^\dagger_{r_1\uparrow}\rangle_0\langle c^\dagger_{r_1\downarrow}c_{r_1\downarrow}\rangle_0 - \langle c_{r_1\uparrow}c_{r_1\downarrow}\rangle_0\langle c^\dagger_{r_1\downarrow}c^\dagger_{r_1\uparrow}\rangle_0]\}\\
&= e^{-\gamma s_1}\mathrm{det}\left[\begin{pmatrix} e^{\gamma s_1} & 0\\ 0 & e^{\gamma s_1}\end{pmatrix} - \begin{pmatrix}\langle c_{r_1\uparrow}c^\dagger_{r_1\uparrow}\rangle_0 & \langle c_{r_1\uparrow}c_{r_1\downarrow}\rangle_0\\ \langle c^\dagger_{r_1\downarrow}c^\dagger_{r_1\uparrow}\rangle_0 & \langle c^\dagger_{r_1\downarrow}c_{r_1\downarrow}\rangle_0\end{pmatrix}\begin{pmatrix} e^{\gamma s_1}-1 & 0\\ 0 & e^{\gamma s_1}-1\end{pmatrix}\right]\,.
\end{aligned}
$$

For kth order, this expression generalizes to

$$\frac{Z_k(\{s_i,\tau_i,r_i\})}{Z_0} = [\mathrm{det}N^{-1}(\{s_i,\tau_i,r_i\})]\prod_{i=1}^{k} e^{-\gamma_i s_i}\,, \qquad (4.131)$$

where N is a $2k\times 2k$ matrix defined by

$$N^{-1}(\{s_i,\tau_i,r_i\}) = e^{V^{s_i}} - G_0^{\{\tau_i,r_i\}}(e^{V^{s_i}} - \mathbb{I})\,, \qquad (4.132)$$

$$e^{V^{s_i}} = \mathrm{diag}(e^{\gamma s_1}, e^{\gamma s_1}, \ldots, e^{\gamma s_k}, e^{\gamma s_k})\,, \qquad (4.133)$$

$$(G_0^{\{\tau_i,r_i\}})_{ij} = \underline{\mathcal{G}}_{r_i r_j}(\tau_i,\tau_j) = \begin{pmatrix}\mathcal{G}_{r_i r_j,00}(\tau_i,\tau_j) & \mathcal{G}_{r_i r_j,01}(\tau_i,\tau_j)\\ \mathcal{G}_{r_i r_j,10}(\tau_i,\tau_j) & \mathcal{G}_{r_i r_j,11}(\tau_i,\tau_j)\end{pmatrix}\,. \qquad (4.134)$$

For convenience we will always use the symbol $\underline{X}_{ij}$ to represent 2×2 matrix in the following derivations

$$\underline{X}_{ij} = \begin{pmatrix} X_{2i,2j} & X_{2i,2j+1}\\ X_{2i+1,2j} & X_{2i+1,2j+1}\end{pmatrix}\,. \qquad (4.135)$$

4.4.3 Monte Carlo updates

In the random walk updates, the probability of inserting an auxiliary spin in $[0,\beta)$ is $p^{\mathrm{prop}}(k\to k+1) = (1/2)(d\tau/\beta)$; the probability of removing a random auxiliary spin is $p^{\mathrm{prop}}(k+1\to k) = 1/(k+1)$. The acceptance rate of moving from order k to $k+1$ with an extra auxiliary spin $\{s,\tau,r\}$ can be computed from the detailed balance relation Eq. 4.105

$$\frac{p^{\mathrm{acc}}(k\to k+1)}{p^{\mathrm{acc}}(k+1\to k)} = \frac{Ke^{-\gamma s}}{k+1}\frac{\det\left[N^{(k+1)}\right]^{-1}}{\det\left[N^{(k)}\right]^{-1}}\,. \qquad (4.136)$$

The proposed move from order k to $k \pm 1$ is accepted with the probability

$$\min\left[1, \frac{p^{\mathrm{acc}}(k \to k \pm 1)}{p^{\mathrm{acc}}(k \pm 1 \to k)}\right] . \tag{4.137}$$

To compute the acceptance rate in Eq. 4.136, we need to compute the determinant ratio

$$R = \frac{\det\left[N^{(k+1)}\right]^{-1}}{\det\left[N^{(k)}\right]^{-1}} . \tag{4.138}$$

In the Monte Carlo updates in the singlet superconducting state, the N^{-1} matrix will have two new rows and two new columns when inserting a new auxiliary spin

$$(N^{(k+1)})^{-1} = \begin{pmatrix} (N^{(k)})^{-1} & Q \\ R & S \end{pmatrix} , \quad N^{(k+1)} = \begin{pmatrix} \tilde{P} & \tilde{Q} \\ \tilde{R} & \tilde{S} \end{pmatrix} , \tag{4.139}$$

where Q, $\tilde{Q}$ are $(2k \times 2)$ matrices, R, $\tilde{R}$ are $(2 \times 2k)$ matrices, and S, $\tilde{S}$ are (2×2) matrices. Using $\{s, \tau, r\}$ to mark the new auxiliary spin, Q, R, S can be written out explicitly

$$\underline{Q}_l = -\begin{pmatrix} \mathcal{G}_{r_l r,00}(\tau_l, \tau) & \mathcal{G}_{r_l r,01}(\tau_l, \tau) \\ \mathcal{G}_{r_l r,10}(\tau_l, \tau) & \mathcal{G}_{r_l r,11}(\tau_l, \tau) \end{pmatrix} \begin{pmatrix} e^{\gamma s} - 1 & 0 \\ 0 & e^{\gamma s} - 1 \end{pmatrix} , \tag{4.140}$$

$$\underline{R}_m = -\begin{pmatrix} \mathcal{G}_{r r_m,00}(\tau, \tau_m) & \mathcal{G}_{r r_m,01}(\tau, \tau_m) \\ \mathcal{G}_{r r_m,10}(\tau, \tau_m) & \mathcal{G}_{r r_m,11}(\tau, \tau_m) \end{pmatrix} \begin{pmatrix} e^{\gamma s_m} - 1 & 0 \\ 0 & e^{\gamma s_m} - 1 \end{pmatrix} , \tag{4.141}$$

$$\underline{S} = \begin{pmatrix} e^{\gamma s} & 0 \\ 0 & e^{\gamma s} \end{pmatrix} - \begin{pmatrix} \mathcal{G}_{rr,00}(0^+) & \mathcal{G}_{rr,01}(0^+) \\ \mathcal{G}_{rr,10}(0^+) & \mathcal{G}_{rr,11}(0^+) \end{pmatrix} \begin{pmatrix} e^{\gamma s} - 1 & 0 \\ 0 & e^{\gamma s} - 1 \end{pmatrix} . \tag{4.142}$$

The determinant of $(N^{(k+1)})^{-1}$ can be computed using the standard formula of a 2×2 block matrix [27, 59]

$$\det[(N^{(k+1)})^{-1}] = \det[(N^{(k)})^{-1}]\det[S - R(N^{(k)})Q] . \tag{4.143}$$

From the standard inversion equation of the 2×2 block matrix, the four components in the $N^{(k+1)}$ matrix are

$$\tilde{S} = (S - R(N^{(k)})Q)^{-1} \,, \tag{4.144a}$$

$$\tilde{Q} = -[N^{(k)}Q]\tilde{S} \,, \tag{4.144b}$$

$$\tilde{R} = -\tilde{S}[RN^{(k)}] \,, \tag{4.144c}$$

$$\tilde{P} = N^{(k)} + [N^{(k)}Q]\tilde{S}[RN^{(k)}] \,, \tag{4.144d}$$

which give the explicit form of the ratio R

$$R = \frac{\det\left[N^{(k+1)}\right]^{-1}}{\det\left[N^{(k)}\right]^{-1}} = \det[S - R(N^{(k)})Q] = \frac{1}{\det\tilde{S}} \,. \tag{4.145}$$

4.4.4 Measurements of single- and two-particle Green's functions

To compute the four components of the single-particle Green's function at each configuration, we insert the two creation or annihilation operators $d^{(\dagger)}_{r\sigma}$, $d^{(\dagger)}_{r'\sigma'}$ at time τ and τ' into the partition function Z_k [Eq. 4.120]

$$\begin{aligned} G_{rr',\sigma\sigma'}(\tau,\tau')\big|_{Z_k} = \frac{1}{Z_k}\mathrm{Tr}[e^{-(\beta-\tau_k)H_0} \\ \times\, e^{\gamma s_k(n_{r_k\uparrow}-n_{r_k\downarrow})} \ldots e^{-(\tau_{m+1}-\tau)H_0} d^{(\dagger)}_{r\sigma'} e^{-(\tau-\tau_m)H_0} \ldots e^{-(\tau_l-\tau')H_0} d^{(\dagger)}_{r'\sigma'} e^{-(\tau'-\tau_{l-1})H_0} \ldots e^{-\tau_1 H_0}] \,. \end{aligned} \tag{4.146}$$

Take the normal component $G_{rr',00}(\tau-\tau') = \langle \mathcal{T} c_{r\uparrow}(\tau) c^{\dagger}_{r'\uparrow}(\tau')\rangle$ at first order as an example (assume $\tau_1 > \tau > \tau'$)

$$\begin{aligned} G_{rr',00}(\tau,\tau')\big|_{Z_1} &= \frac{1}{Z_1}\mathrm{Tr}[e^{-(\beta-\tau_1)H_0} e^{\gamma s_1(n_{r_1\uparrow}-n_{r_1\downarrow})} e^{-(\tau_1-\tau)H_0} d_{r\uparrow} e^{-(\tau-\tau')H_0} d^{\dagger}_{r'\uparrow} e^{-\tau' H_0}] \\ &= \frac{Z_0}{Z_1}[e^{\gamma s_1} - (e^{\gamma s_1}-1)\langle c^{\dagger}_{r_1\downarrow}(\tau_1) c_{r_1\downarrow}(\tau_1) d_{r\uparrow}(\tau) d^{\dagger}_{r'\uparrow}(\tau')\rangle_0 \\ &\qquad - (e^{\gamma s_1}-1)\langle c_{r_1\uparrow}(\tau_1) c^{\dagger}_{r_1\uparrow}(\tau_1) d_{r\uparrow}(\tau) d^{\dagger}_{r'\uparrow}(\tau')\rangle_0 \\ &\qquad - (e^{\gamma s_1}-1)(e^{-\gamma s_1}-1)\langle c_{r_1\uparrow}(\tau_1) c^{\dagger}_{r_1\uparrow}(\tau_1) c^{\dagger}_{r_1\downarrow}(\tau_1) c_{r_1\downarrow}(\tau_1) d_{r\uparrow}(\tau) d^{\dagger}_{r'\uparrow}(\tau')\rangle_0] \,. \end{aligned} \tag{4.147}$$

Comparing with Eq. 4.128, the order of the correlators in the equation above are increased by one. Using the Wick's theorem, the Green's functions at order k can be computed with a matrix form equation [63] (all auxiliary spin indices are omitted except for time)

$$\underline{G}_{rr'}(\tau,\tau') = \frac{1}{\det(N^{(k)})^{-1}} \det\begin{pmatrix} (N^{(k)})^{-1} & [\underline{G}_{0,r_i r'}(\tau_i,\tau')] \\ -[\underline{G}_{0,rr_j}(\tau,\tau_j)(\underline{e^{V_j}} - \mathbb{I})] & \underline{G}_{0,rr'}(\tau,\tau') \end{pmatrix} \,. \tag{4.148}$$

Carrying out the determinant of the 2×2 block matrix explicitly as in Eq. 4.143, the Green's function matrix can be written as

$$\underline{G}_{rr'}(\tau,\tau') = \underline{G}_{0,rr'}(\tau,\tau') + \sum_{i,j=1}^{k} \underline{G}_{0,rr_j}(\tau,\tau_j)\underline{M}_{ji}\underline{G}_{0,r_ir'}(\tau_i,\tau')\,, \tag{4.149}$$

where the M matrix is the core object for measurements at each configuration, and is defined as

$$\underline{M}_{ji} = \begin{pmatrix} [(e^V-\mathbb{I})N]_{2j,2i} & [(e^V-\mathbb{I})N]_{2j,2i+1} \\ [(e^V-\mathbb{I})N]_{2j+1,2i} & [(e^V-\mathbb{I})N]_{2j+1,2i+1} \end{pmatrix}. \tag{4.150}$$

We may perform a Fourier transform (see Eq. 3.38 and Eq. 3.39) of Eq. 4.149, and measure the single-particle Green's functions in momentum and frequency space directly

$$\begin{aligned}\underline{G}_{kk'}(i\omega_n,i\omega'_n) = {} & \beta N\underline{G}_{0,k}(i\omega_n)\delta_{nn'}\delta_{kk'} \\ & -\sum_{lm}\underline{G}_{0,k}(i\omega_n)e^{ikx_m}e^{i\omega_n\tau_m}\underline{M}_{ml}e^{-i\omega'_n\tau_l}e^{-ik'x_l}\underline{G}_{0,k'}(i\omega'_n)\,.\end{aligned} \tag{4.151}$$

In practice, the Fourier transform of the M matrix is done component-by-component, i.e different terms in the M matrix corresponding to the $00, 01, 10, 11$ components of the Green's function matrix are separated, then the four matrices are transformed separately with same set of coefficients.

Note that for measurements at each configuration, the single-particle Green's functions are not diagonal in momentum and frequency space. The diagonal structure is recovered after the Monte Carlo sum. To compute the single-particle Green's functions, we only need to measure the diagonal terms with $k = k'$, $i\omega_n = i\omega'_n$ in each configuration, while the measurements of the two-particle Green's functions require two-momentum and two-frequency single-particle Green's functions. At each configuration, the two-particle Green's functions can be computed using the Wick's theorem $\underline{G}^{(2)}_{\sigma\sigma'}(k,k+q,k'+q,k') = \underline{\chi}^{=}_{0,\sigma\sigma'}(k,k+q,k'+q,k')+\underline{\chi}^{\times}_{0,\sigma\sigma'}(k,k+q,k'+q,k')$, with the two $\underline{\chi}_{0,\sigma\sigma'}$ matrices defined in Eqs. 3.58, 3.59, 3.61, 3.62.

4.4.5 Sub-matrix updates

From Eq. 4.120, we can see that inserting auxiliary spins with $s = 0$ does not change the partition function Z_k. Using this fact, we can precompute a N matrix with $s = 0$ auxiliary spins, then the insertion and removal of spins are equivalent to spin-flip updates ($s = 0 \leftrightarrow \{-1, 1\}$). The sub-matrix update optimization derived in Ref. [68] can be generalized to the simulation in the singlet superconducting state. Central steps of the sub-matrix updates are summarized here, with detailed derivations in Ref. [68].

Since inserting two “non-interacting” spins $s, s' = 0$ at time τ, τ' does not change the value of the partition function, and the Green’s function calculation can be treated as inserting the creation or annihilation operators at the corresponding times τ, τ', there is a simple relation between N and G (we denote with a tilde with the matrices of size $2k+4$) [27, 62, 68]

$$\tilde{G}^{\{s_i,\tau_i,x_i\}} = \tilde{N}(\{s_i,\tau_i,x_i\})\tilde{G}_0^{\{\tau_i,x_i\}}\,. \tag{4.152}$$

For configurations that have same locations for all vertices but different in value of one auxiliary spin s_p, the matrices G and N are related by [68]

$$\underline{N}'_{ij} = \underline{N}_{ij} + (\underline{G}_{ip} - \delta_{ip}\mathbb{I})\underline{\lambda}_{pp}\underline{N}_{pj}\,, \tag{4.153}$$

$$\underline{G}'_{ij} = \underline{G}_{ij} + (\underline{G}_{ip} - \delta_{ip}\mathbb{I})\underline{\lambda}_{pp}\underline{G}_{pj}\,, \tag{4.154}$$

$$\lambda = e^{V'_p - V_p} - 1 = \mathrm{diag}(0,0,\ldots e^{\gamma s'_p - \gamma s_p}, e^{\gamma s'_p - \gamma s_p},\ldots,0,0) - \mathbb{I}\,. \tag{4.155}$$

At step k of the algorithm, the auxiliary spin s_{p_k} is changed to s'_{p_k}. Defining a new parameter

$$\gamma^k = e^{-\gamma(s'_{p_k} - s_{p_k})} - 1\,, \tag{4.156}$$

λ^k can be expressed as

$$\underline{\lambda}^k_{pp} = (\gamma^k\mathbb{I})[\mathbb{I} + (\mathbb{I} - \underline{G}^k_{pp})(\gamma^k\mathbb{I})]^{-1}\,. \tag{4.157}$$

Defining the inverse of the Green’s function matrix $A^k = (G^k)^{-1}$, with

$$\underline{G}^{k+1}_{ij} = \underline{G}^k_{ij} + (\underline{G}^k_{ip_k} - \delta_{ip_k}\mathbb{I})\underline{\lambda}^k_{p_kp_k}\underline{G}^k_{p_kj}\,, \quad \lambda^k = e^{V'_{p_k} - V_{p_k}} - 1\,, \tag{4.158}$$

the change in A can be written as

$$\begin{aligned}\underline{A}^{k+1}_{ij} &= [\underline{G}^k_{ij} + (\underline{G}^k_{ip} - \delta_{ip}\mathbb{I})\underline{\lambda}^k_{pp}G^k_{pj}]^{-1} \\ &= [\underline{G}^k_{ij} + (\underline{G}^k_{ip} - \delta_{ip}\mathbb{I})(\gamma^k\mathbb{I})[\mathbb{I} + (\mathbb{I} - \underline{G}^k_{pp})(\gamma^k\mathbb{I})]^{-1}G^k_{pj}]^{-1}\,.\end{aligned} \tag{4.159}$$

With the Woodbury formula [69]

$$(G + UCV)^{-1} = G^{-1} - G^{-1}U(C^{-1} + VG^{-1}U)^{-1}VG^{-1}\,, \tag{4.160}$$

Eq. 4.159 can be simplified using

$$C^{-1} + VG^{-1}U^{-1} = [\mathbb{I} + (\mathbb{I} - \underline{G}^k_{pp})(\gamma^k\mathbb{I})](\gamma^k\mathbb{I})^{-1} + \sum_{xy} \underline{G}_{px}\underline{G}^{-1}_{xy}(\underline{G}_{yp} - \delta_{yp}\mathbb{I}) = (\gamma^k\mathbb{I})^{-1}\,, \tag{4.161}$$

which gives A^{k+1} in the form

$$\begin{aligned}\underline{A}^{k+1}_{ij} &= \underline{A}^k_{ij} + \gamma^k(\underline{A}^k_{ip} - \delta_{ip}\mathbb{I})\delta_{pj} \\ &= \underline{A}^k_{ij} + \gamma^k\underline{A}^k_{ip}\delta_{pj} - \gamma^k\delta_{ip}\delta_{pj}\mathbb{I} \\ &= \tilde{\underline{A}}^k_{ij} - \gamma^k\delta_{ip}\delta_{pj}\mathbb{I}\,, \end{aligned} \tag{4.162}$$

where we have defined $\tilde{A}^k$ to represent the matrix A^k with the $(2p)$th and $(2p+1)$th column multiplied by $(1+\gamma^k)$. The determinant of this matrix is then $\det(\tilde{A}^k) = (1+\gamma^k)^2\det(A^k)$. With the matrix determinant lemma [70]

$$\det(A + UV^T) = \det(\mathbb{I} + V^TA^{-1}U)\det A\,, \tag{4.163}$$

the determinant of A^{k+1} is

$$\begin{aligned}\det(A^{k+1}) &= \det(\mathbb{I} - \gamma^k[(\tilde{A}^k)^{-1}]_{pp})\det(\tilde{A}^k) \\ &= (\mathbb{I} - \frac{\gamma^k}{1+\gamma^k}\underline{G}^k_{pp})(1+\gamma^k)^2\det(A^k) \\ &= -\det(A^k)(1+\gamma^k)^2\frac{\gamma^k}{1+\gamma^k}(\underline{G}^k_{pp} - \frac{1+\gamma^k}{\gamma^k}\mathbb{I})\,. \end{aligned} \tag{4.164}$$

The determinant ratio needed for computing the acceptance rate of each update can then be written as

$$\frac{N^k}{N^{k+1}} = -\gamma^k(1+\gamma^k)\det(\underline{G}^k_{pp} - \frac{1+\gamma^k}{\gamma^k}\mathbb{I})\,. \tag{4.165}$$

For multiple spin changes, we can recursively apply Eq. 4.162

$$\underline{A}^{k+1}_{ij} = \underline{A}^0_{ij} + \sum_{l=0}^{k}\gamma^l\underline{A}^0_{ip_l}\delta_{p_lj} - \sum_{l=0}^{k}\gamma^l\delta_{ip_l}\delta_{p_lj}\mathbb{I}\,, \tag{4.166}$$

which means the matrix A^{k+1} is generated from A^0 by successively multiplying columns $2p_l$

and $2p_l + 1$ of matrix A^0 with γ^l, and can be written in matrix form as

$$A^{k+1} = \tilde{A}^k - X^k (Y^k)^T \,, \tag{4.167}$$

where the X and Y matrices are defined as

$$\underline{X}^k_{ij} = \gamma^j \delta_{ip_j} \mathbb{I} \,, \tag{4.168}$$

$$(\underline{Y}^k)^T_{ij} = \delta_{p_i j} \mathbb{I} \,. \tag{4.169}$$

The measurements of the Green's function G^k within spin flip update follow exactly Ref. [68], with the size of each matrix extended from $k_{\max} \times k_{\max}$ to $(2k_{\max}) \times (2k_{\max})$. The acceptance rate of each update can be computed using intermediate matrices defined in Ref. [68] without the necessity of knowing the value of G^k. The main difference in the singlet superconducting state simulation is that each update changes two rows/columns in the corresponding matrices instead of one.

The random walk procedure with the sub-matrix update method is described in detail in Ref. [68]. In general, the random walk process is split into inner and outer loops. In each outer loop, we preform measurements of the observables, then insert $k_{\max}$ random auxiliary spins with $s = 0$ and pre-compute the corresponding N matrix. In each inner loop, we perform $k_{\max}$ times of insertion, removal, or flip of auxiliary spins by changing the value of s in the configuration.

4.4.6 Numerical details

4.4.6.1 Sign problem

A fundamental concern of all the CT-QMC methods is the sign problem (see Eq. 4.106). The analysis of the sign problem is beyond the scope of this thesis. In practice, with the same parameter set, the sign gets improved a bit (closer to 1) when there is a finite singlet superconductivity order.

4.4.6.2 Expansion order

In the absence of a sign problem, the complexity of CT-AUX scales cubically with the average expansion order $\langle k \rangle$ ($\mathcal{O}(\langle k \rangle^3)$), in which $\langle k \rangle^2$ comes from the matrix update, and another $\langle k \rangle$ comes from the auto-correlation time. The average expansion order of the CT-AUX algorithm can be computed from the thermal average of the shifted interacting action $\tilde{S}_I = S_I - K$. Using the expansion of the partition function Z [Eq. 4.112], $\langle \tilde{S}_I \rangle$ can be written as

$$
\begin{aligned}
-\langle \tilde{S}_I \rangle &= -\frac{1}{Z}\int \mathcal{D}[\bar{c},c] e^{-S_0[\bar{c},c]} e^{-\tilde{S}_I[\bar{c},c]} \tilde{S}_I[\bar{c},c] \\
&= -\frac{1}{Z}\int \mathcal{D}[\bar{c},c] e^{-S_0[\bar{c},c]} \sum_k \frac{1}{k!}(-\tilde{S}_I[\bar{c},c])^k \cdot \tilde{S}_I[\bar{c},c] \\
&= \frac{1}{Z}\int \mathcal{D}[\bar{c},c] e^{-S_0[\bar{c},c]} \sum_k \frac{k+1}{(k+1)!}(-\tilde{S}_I[\bar{c},c])^{k+1} \\
&= \langle k \rangle \,. \qquad (4.170)
\end{aligned}
$$

With the explicit expression of the interacting Hamiltonian $\tilde{H}_I$, $\langle \tilde{S}_I \rangle$ can also be written as

$$
-\langle \tilde{S}_I \rangle = -\int_0^\beta d\tau \langle \tilde{H}_I(\tau) \rangle = -\beta \langle \tilde{H}_I \rangle = \beta \left[-U \langle n_\uparrow n_\downarrow - \frac{1}{2}(n_\uparrow + n_\downarrow) \rangle + \frac{K}{\beta} \right] , \qquad (4.171)
$$

in which $n_\sigma = \sum_i n_{i\sigma}$. The average expansion order can then be expressed as

$$
\langle k \rangle = K - \beta U \langle n_\uparrow n_\downarrow - \frac{1}{2}(n_\uparrow + n_\downarrow) \rangle \,. \qquad (4.172)
$$

Therefore, increasing K leads to a higher perturbation order, but also a smaller value of γ (see Eq. 4.117) and thus less polarization of the auxiliary spins [63].

The two thermal averages that determine the average expansion order in Eq. 4.172 corresponding to the kinetic and potential energies of the system. A detailed analysis of these two terms in the singlet superconducting state can be found in Ref. [71].

4.5 Analytical continuation

The many-body correlation functions computed from numerical simulations introduced so far are functions of imaginary time or frequency. When interpreted as response or spectral functions that can be measured in experiments, we need to compute their real axis counterparts. This problem in general is an ill-posed problem, such that small fluctuations in the input data cause drastic changes of the output data. Methods used for doing the analytical continuation include the Maximum Entropy (MaxEnt) method [72, 73], stochastic analytic continuation [74, 75], Pade continued fraction fit [76, 77], and the Nevanlinna continuation method [78]. For noisy data from quantum Monte Carlo simulations, the most commonly used method is the MaxEnt method. In this section, we will briefly introduce the MaxEnt method, and then provide formulas used in the continuation of Green's function, self-energy, and susceptibility. All site and spin indices will be omitted since we're doing analysis of time and frequency. This section closely follows Ref. [73].

Consider the normal component of the single-particle Green's function $G(\tau) = -\langle \mathcal{T} c(\tau) c^\dagger(0) \rangle$, which can be expressed on the Matsubara frequency axis via Fourier transform (see Eq. 3.39)

$$G(i\omega_n) = \int_0^\beta d\tau e^{i\omega_n \tau} G(\tau) \,. \tag{4.173}$$

The Matsubara frequency Green's function is related to the real frequency Green's function via

$$G(i\omega_n) = -\frac{1}{\pi} \int_{-\infty}^{\infty} d\omega \frac{\text{Im} G(\omega)}{i\omega_n - \omega} = \int_{-\infty}^{\infty} d\omega A(\omega) K_n(\omega) \,, \tag{4.174}$$

in which we have defined the spectral function

$$A(\omega) = -\frac{1}{\pi} \text{Im} G(\omega) \,, \tag{4.175}$$

and a integration "kernel"

$$K_n(\omega) = \frac{1}{i\omega_n - \omega} \,. \tag{4.176}$$

In the MaxEnt method, we assume that the Green's function at each sampling points are not known to arbitrary precision. Instead, the values of the Green's function at sampling points are computed by averaging a set of M estimates for each n

$$G_n = G(i\omega_n) = \frac{1}{M} \sum_{j=1}^{M} G_n^{(j)} \,. \tag{4.177}$$

The correlation between the Green's function at different sampling points can be represented by a covariance matrix

$$C_{nm} = \frac{1}{M(M-1)} \sum_{j=1}^{M} (G_n - G_n^{(j)})(G_m - G_m^{(j)}) \,. \tag{4.178}$$

Given a candidate spectral function $A(\omega)$ on the real axis and the associated kernel, the Matsubara frequency Green's function can be evaluated using Eq. 4.174 to create an estimate $\bar{G}_n$ (back-continuation). The "goodness of fit" is measured by the quantity

$$\chi^2 = \sum_{n,m}^{M} (\bar{G}_n - G_n)^* C_{nm}^{-1} (\bar{G}_m - G_m) \,. \tag{4.179}$$

Since the calculation of $G(\omega)$ from $G(i\omega_n)$ is ill conditioned, i.e. there are many solutions of A that satisfy $G = KA$ within the uncertainty given by C_{nm}, calculate A from the direct inversion of K is not applicable. In the MaxEnt method, we minimize the functional

$$Q = \frac{1}{2}\chi^2 - \alpha S[A]\,, \tag{4.180}$$

where α is the Lagrange multiplier and $S[A]$ is the "entropy" that describes likeness with respect to a default model $d(\omega)$

$$S[A] = -\int d\omega A(\omega) \ln \left[\frac{A(\omega)}{d(\omega)}\right]\,. \tag{4.181}$$

Minimizing the functional Q requires a systematic calculation of α and $A(\omega)$. A summary of the algorithms for this procedure can be found in Ref. [73].

Ref. [73] provides a summary of common kernels used in the analytical continuation of physical quantities. Here we list the continuation equations and normalizations for the normal Green's function, self-energy and susceptibility that will be used in later chapters.

1. Fermionic kernels

The normal Green's function and self-energy can be continued using the same kernel. For a function F being either G or Σ, the relation between real and imaginary frequency results can be written as

$$F(i\omega_n) = -\frac{1}{\pi}\int_{-\infty}^{\infty} d\omega \frac{\mathrm{Im}F(\omega)}{i\omega_n - \omega} = \int_{-\infty}^{\infty} d\omega A(\omega) K_n(\omega)\,. \tag{4.182}$$

When $F(i\omega_n)$ is a purely imaginary function, the continuation can be computed with

$$\mathrm{Im}F(i\omega_n) = \frac{1}{\pi}\int_{-\infty}^{\infty} d\omega \mathrm{Im}F(\omega)\frac{\omega_n}{\omega_n^2 + \omega^2} = \int_{-\infty}^{\infty} d\omega A(\omega) K_n'(\omega)\,. \tag{4.183}$$

The normalization used in the analytical continuation of $G(i\omega_n)$ equals to 1, since $\int_{-\infty}^{\infty} d\omega A(\omega) = 1$, $G(i\omega_n)$ decays with $\frac{1}{i\omega_n}$ at high frequency. The asymptotic behaviour of the self-energy $\Sigma(i\omega_n)$ follows [79]

$$\Sigma(i\omega_n) = \Sigma_0 + \frac{\Sigma_1}{i\omega_n} + \mathcal{O}\left[\frac{1}{(i\omega_n)^2}\right]\,, \tag{4.184}$$

where in the Hubbard model without chemical potential shift, $\Sigma_0 = Un$ is the Hartree term, and $\Sigma_1 = Un(n-1)$, with n the density. In practice, the continuation of self-energy is done using the same routine as the Green's function after subtracting the Hartree term and providing a different normalization Σ_1. The kernels $K_n^{(\prime)}$ in Eqs. 4.182, 4.183 are called Fermionic kernels in Ref. [73].

2. Bosonic kernels

For the susceptibility $\chi(i\nu_n)$, the relation between the real and imaginary frequency results can be written as

$$\chi(i\nu_n) = \int_{-\infty}^{\infty} d\nu \frac{\mathrm{Im}\chi(\nu)}{i\nu_n + \nu} = \int_{-\infty}^{\infty} d\nu \frac{\mathrm{Im}\chi(\nu)}{\nu} \frac{\nu}{i\nu_n + \nu} = \int_{-\infty}^{\infty} d\nu B(\nu) K_n(\nu)\,, \tag{4.185}$$

where we have defined the "spectral function" $B(\nu) = \mathrm{Im}\chi(\nu)/\nu$ to avoid having problem at $i\nu_n = \nu = 0$. When $\chi(i\nu_n)$ is a purely real function, the continuation can be computed with

$$\mathrm{Re}\chi(i\nu_n) = \int_{-\infty}^{\infty} d\nu \frac{\mathrm{Im}\chi(\nu)}{\nu} \frac{\nu^2}{\nu_n^2 + \nu^2} = \int_{-\infty}^{\infty} d\nu B(\nu) K_n'(\nu)\,. \tag{4.186}$$

The normalization used in the analytical continuation of $\chi(i\nu_n)$ is given by $\int_{-\infty}^{\infty} d\nu B(\nu) = \chi(i\nu_n = 0)$. The kernels $K_n^{(\prime)}$ in Eqs. 4.185, 4.186 are called Bosonic kernels in Ref. [73].

Chapter 5

Short-Range Charge Fluctuations in the Two-Dimensional Hubbard Model

This chapter is based on *Xinyang Dong, Xi Chen, Emanuel Gull, "Dynamical Charge Susceptibility in the Hubbard Model", Phys. Rev. B 100, 235107 (2019)* [80], and *Xinyang Dong, Emanuel Gull, "Short-Range Charge Fluctuations in the Two-Dimensional Hubbard Model", Phys. Rev. B 101, 195115 (2020)* [81].

5.1 Introduction

The presence of large competing fluctuations of several kinds is one of the defining aspects of correlated electron systems. These fluctuations may then condense into phases that exhibit remarkable properties, including unusually high superconducting transition temperatures and interesting magnetism.

The cuprate superconductors are a paradigmatic example for such a competition. Antiferromagnetic fluctuations are strongest in the 'undoped' parent compounds but present over a large part of phase space. Superconducting fluctuations lead to a superconducting dome for dopings smaller than $\sim 20\%$. Charge phenomena [82–92], such as the famous stripes at 1/8th doping [82, 89] or the features observed in scanning-tunneling experiments [85], are present in several parts of phase space. Charge order with d-wave symmetry has also been found in RXS [93]. Charge fluctuations in the high-temperature superconductors have generated renewed interest, as new experimental probes, such as Resonant inelastic X-ray scattering RIXS [94–99] or Momentum-resolved electron energy-loss spectroscopy M-EELS [100, 101] may be able to directly measure them as a function of momentum and energy.

A minimal model that describes many of the salient features of these materials is the single-band Hubbard model [102, 103]. While unable to describe excitations involving high-lying orbitals, the model reproduces much of the observed low-energy phenomenology, including a pseudogap [104–113], superconductivity [71, 114–121], and the response functions of Raman spectroscopy [117, 122], optical conductivity [113, 123–128], nuclear magnetic resonance [129, 130], and neutron spectroscopy [131]. It is therefore interesting to examine properties of the model in the context of cuprate physics. Due to the non-perturbative parameter regime relevant to the materials, reliable predictions have to resort to numerics, and a wide range of efficient numerical methods are able to describe the relevant parameter regime with consistent results [13].

Hubbard model calculations find spin, charge, and superconducting fluctuations. Spin fluctuations are well understood and mainly dominant near half filling [131–134]. Calculations also find that strong short-wavelength spin fluctuations are primarily responsible for the formation of the pseudogap [28, 135, 136], *i.e.*, the suppression of the density of states near the antinode but not near the node. Superconductivity is found unambiguously in the weak coupling regime [137–139], and strong indications from DCA calculations show that superconductivity does persist to larger couplings [140]. In contrast, results from some newer methods find that in the absence of a next-nearest-neighbor hopping, it is charge (rather than superconducting) order that dominates the ground state [141, 142]. However, all orders are in very close competition. The precision to which the energetics of these phases is known is much better than the uncertainty in the model parameters, indicating that phenomena beyond simple Hubbard model physics may well force the system to choose one order over the other.

At finite temperature, charge fluctuations, in contrast to antiferromagnetic and superconducting fluctuations, are less well investigated for the model without additional nearest-neighbor interactions, whereas the “extended” model has been studied extensively in recent years [143–155]. This is despite the fact that theoretical approaches have proposed unusual charge phenomena, such as the d density wave (DDW) order [156], as candidates responsible for pseudogap physics [157–160]. It is therefore interesting to investigate the extent to which charge fluctuations are present in the model, and the extent to which they correspond to the proposed DDW fluctuations, using numerical methods that generate these fluctuations dynamically from an underlying Hamiltonian.

In this chapter, we will analyze the competing fluctuations in the two-dimensional single band Hubbard model (see section 4.1) in the paramagnetic state using DCA (see section 4.3).

5.2 Methods

This section summarizes the equations and definitions used in the paramagnetic state calculations in this chapter. The definitions mostly follow Ref. [42].

We investigate the two-dimensional single-band Hubbard model on a square lattice with on-site interaction U and chemical potential μ. The Hamiltonian is given by [Eq. 4.2]

$$H = \sum_{k\sigma} (\epsilon_k - \mu) c^\dagger_{k\sigma} c_{k\sigma} + U \sum_i n_{i\uparrow} n_{i\downarrow}. \tag{5.1}$$

Here i labels the lattice site, k the momentum, $c^{(\dagger)}$ annihilation (creation) operators, and n the density. $\epsilon_k = -2t(\cos k_x + \cos k_y) - 4t' \cos k_x \cos k_y$ is the dispersion with hopping t and next-nearest-neighbor hopping t'.

In the paramagnetic state, the single- and two-particle Green's functions are defined as

$$G_\sigma(k_1\tau_1, k_2\tau_2) = -\langle \mathcal{T} c_{k_1\sigma}(\tau_1) c^\dagger_{k_2\sigma}(\tau_2) \rangle \,, \tag{5.2}$$

$$G^{(2)}_{\sigma_1\sigma_2\sigma_3\sigma_4}(k_1\tau_1, k_2\tau_2, k_3\tau_3, k_4\tau_4) = \langle \mathcal{T} c^\dagger_{k_1\sigma_1}(\tau_1) c_{k_2\sigma_2}(\tau_2) c^\dagger_{k_3\sigma_3}(\tau_3) c_{k_4\sigma_4}(\tau_4) \rangle \,, \tag{5.3}$$

and the corresponding generalized susceptibility can be written as

$$\begin{aligned} \chi_{\sigma\sigma'}(k_1\tau_1, k_2\tau_2, k_3\tau_3, k_4\tau_4) = {} & G_{2,\sigma\sigma\sigma'\sigma'}(k_1\tau_1, k_2\tau_2, k_3\tau_3, k_4\tau_4) \\ & - G_\sigma(k_1\tau_1, k_2\tau_2) G_{\sigma'}(k_3\tau_3, k_4\tau_4) \,, \end{aligned} \tag{5.4}$$

The Fourier transform of the generalized susceptibility can be written with particle-hole and particle-particle notation

$$\begin{aligned} \chi^{\omega\omega'\Omega}_{ph,\sigma\sigma'}(k, k', q) = {} & \int_0^\beta d\tau_1 d\tau_2 d\tau_3 \chi_{\sigma\sigma'}(k\tau_1, (k+q)\tau_2, (k'+q)\tau_3, k'0) \\ & \times e^{-i\omega_n\tau_1} e^{i(\omega_n+\Omega_n)\tau_2} e^{-i(\omega'_n+\Omega_n)\tau_3} \,, \end{aligned} \tag{5.5}$$

$$\begin{aligned} \chi^{\omega\omega'\Omega}_{pp,\sigma\sigma'}(k, k', q) = {} & \int_0^\beta d\tau_1 d\tau_2 d\tau_3 \chi_{\sigma\sigma'}(k\tau_1, (q-k')\tau_2, (q-k)\tau_3, k'0) \\ & \times e^{-i\omega_n\tau_1} e^{i(\Omega_n-\omega'_n)\tau_2} e^{-i(\Omega_n-\omega_n)\tau_3} \,, \end{aligned} \tag{5.6}$$

where $\omega_n^{(\prime)}$ is the ferminoic Matsubara frequency, Ω_n is the bosonic Matsubara frequency (equivalent with ν_n used in Chapter 3), and we have used the time and space translational symmetry to get momentum and energy conservations in the Fourier space. The central quantities we use in this chapter are the generalized susceptibility in the density channel

$$\chi_d^{\omega\omega'\Omega}(k,k',q) = \chi_{ph,\uparrow\uparrow}^{\omega\omega'\Omega}(k,k',q) + \chi_{ph,\uparrow\downarrow}^{\omega\omega'\Omega}(k,k',q)\,, \tag{5.7}$$

the generalized susceptibility in the pairing channel

$$\chi_{pp,\overline{\uparrow\downarrow}}^{\omega\omega'\Omega}(k,k',q) = \chi_{pp,\uparrow\uparrow}^{\omega\omega'\Omega}(k,k',q) - \chi_{pp,\uparrow\downarrow}^{\omega\omega'\Omega}(k,k',q)\,, \tag{5.8}$$

and the bare susceptibilities

$$\chi_{0,ph}^{\omega\omega'\Omega}(k,k',q) = -\beta N G_\sigma(k,i\omega_n) G_\sigma(k+q,i\omega_n+i\Omega_n)\delta_{kk'}\delta_{\omega_n\omega'_n}\,, \tag{5.9}$$

$$\chi_{0,pp}^{\omega\omega'\Omega}(k,k',q) = -\beta N G_\sigma(k,i\omega_n) G_\sigma(q-k,i\Omega_n-i\omega_n)\delta_{kk'}\delta_{\omega_n\omega'_n}\,, \tag{5.10}$$

which correspond to $\chi_0^\times$ defined in chapter 3.

The numerical results are obtained using DCA (see section 4.3) on an eight-site cluster with the CT-AUX impurity solver (see section 4.4). Within DCA, the lattice susceptibility can be computed from the cluster susceptibility through the Bethe-Salpeter equation for both χ_d and $\chi_{pp,\overline{\uparrow\downarrow}}$ (see Eqs. 3.156, 3.161 and Eq. 4.101)

$$\chi_l^{-1}(k,k',Q) - \chi_{0l}^{-1}(k,k',Q) = \chi_c^{-1}(K,K',Q) - \chi_{0c}^{-1}(K,K',Q)\,, \tag{5.11}$$

where we have used k, k' and K, K' to distinguish momenta in lattice and cluster susceptibilities, and Q for the transferred momentum in the cluster. All labels contain both momentum and frequency.

In our eight-site simulations, DCA generates strong antiferromagnetic (AFM) fluctuations with a correlation length comparable to the cluster size. If the establishment of long-range AFM order is allowed, the system chooses an ordered state at a temperature above the onset of the pseudogap or superconductivity. This violation of the Mermin-Wagner theorem [21] is a finite size effect. For this reason, we suppress magnetic long-range order and only show results obtained in the paramagnetic state, which have the correlation length of AFM fluctuations restricted to the cluster size [16]. The DCA simulations performed here are insensitive to the stripe order that is widely found in experiment and in numerical ground-state calculations. In order to find a transition to an ordered state in DCA, the ordering vector typically needs to be commensurate with the cluster geometry. However, the stripe orders, *e.g.*, found in Ref. [141] are too large to fit into the DCA cluster studied here. Thus, while the method is sensitive to charge fluctuations on a length scale smaller than the cluster size, DCA is not expected to find the period 4 and period 5 stripes of Ref. [141].

Appropriately chosen larger clusters may find these stripes, but finite size effects would likely overestimate their contribution. The unbiased detection of such orders with DCA or lattice methods is an important open problem.

5.3 Results

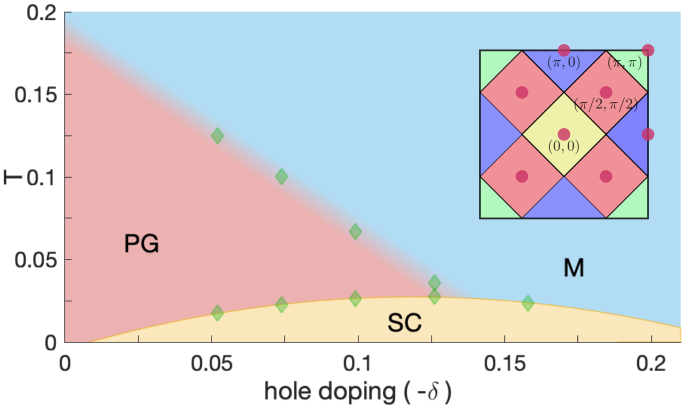

Figure 5.1: 8-site DCA phase diagram of the Hubbard model, with metal (M; blue), pseudogap (PG; red), and superconducting (SC; yellow) regions. In the paper we use $\delta < 0$ for hole doping and $\delta > 0$ for electron doping. Inset: Geometry of the 8-site DCA cluster. Figure from Ref. [80].

Figure 5.1 shows the phase diagram of the model obtained within the eight-site DCA with parameters $U/t = 7$ and $t' = -0.15t$. These parameters are chosen to represent the overall phase diagram common to several cuprates [118]. At these parameters, the model is Mott insulating at half filling, and superconducting at low temperature (the maximum T_c on the eight-site cluster is near T = $1/40\ t$ [71, 118–120, 135]), and exhibits a pseudogap region where the single-particle spectral function at the node stays metallic while the antinode is insulating [135, 161]. The pseudogap regime is obtained by observing a suppression in the single-particle spectral function. The superconducting phase is computed in a Nambu formulation and defined as the area where the anomalous Green's function $G^A(k,\tau) = -\langle \mathcal{T} c_{k\uparrow}(\tau) c_{-k\downarrow}(0)\rangle$ at $k = (0,\pi), (\pi,0)$ becomes nonzero.

5.3.1 Charge susceptibility

To analyze the charge fluctuations, we study the dynamical charge susceptibility, which can be obtained from the generalized susceptibility in the density channel [Eq. 5.7]

$$\chi_{ch}(Q, i\Omega_n) = \frac{2}{\beta^2 N_c^2} \sum_{\omega\omega'} \sum_{kk'} \chi_{l,d}^{\omega\omega'\Omega}(k, k', Q)\,, \tag{5.12}$$

with N_c the number of cluster sites (in our specific case $N_c = 8$). In this subsection, we will present a detailed simulation of the momentum, doping, and temperature dependence of the dynamical charge susceptibility $\chi_{ch}(Q, i\Omega_n)$. These results are needed for the attribution of experimental results to pseudogap physics, as experiments often measure a combination of low-energy physics and higher energy contributions from three-dimensional and atomic physics [97, 162].

Eight-site DCA yields results for eight Q; four of those are equivalent because of symmetry (see inset of Fig. 5.1), such that we have four independent momenta: $Q = (0, 0)$, $Q = (\pi/2, \pi/2)$, $Q = (\pi, 0)$, and $Q = (\pi, \pi)$. We have also performed simulations for 4-site and 16-site clusters at select points and high temperature; these results show qualitatively the same results as 8-site clusters.

We present our simulation data with parameters $U = 7t$ and $t'/t = -0.15$ as a function of Matsubara frequency $i\Omega_n$. In addition, we also show analytically continued result (see section 4.5) of $\mathrm{Im}\chi_{ch}(Q, \Omega)$ as a function of real frequency Ω. Analytical continuation [72, 73] is an uncontrolled procedure that may exponentially amplify statistical uncertainties, especially in the case of bosonic functions such as the charge susceptibility considered here. Values of $\mathrm{Im}\chi_{ch}(Q, \Omega)$ at high frequencies are generally less reliable than at low frequency. Our data mostly results in a single large peak at a characteristic frequency, and continuations with different default models do not lead to appreciable differences in this feature. As we will show below, a simple interpretation of this feature in terms of single-particle quantities is not possible due to the importance of vertex functions. Where we present data in K or eV, we use t $\approx$ 0.35 eV corresponding to high-T_c superconductors [163–166].

Fig. 5.2 shows $\chi_{ch}(Q)$ as a function of frequency at T = 0.1t $\sim$ 400 K, at half filling (Fig. 5.2 a), and in the underdoped (Fig. 5.2 b), optimally doped (Fig. 5.2 c), and overdoped (Fig. 5.2 d) regime. Purple points denote values at $Q = (0, 0)$; the value at $i\Omega_n = 0$ corresponds to the static ($\Omega = 0$) uniform ($Q = (0, 0)$) charge susceptibility which is small in the insulator and generally rises as doping is increased. The zero frequency dependence at higher frequencies is enforced by the Ward identity [35, 167].

Data for susceptibilities at the three-momentum transfer (π, π) (blue), $(\pi, 0)$ [red, degen-

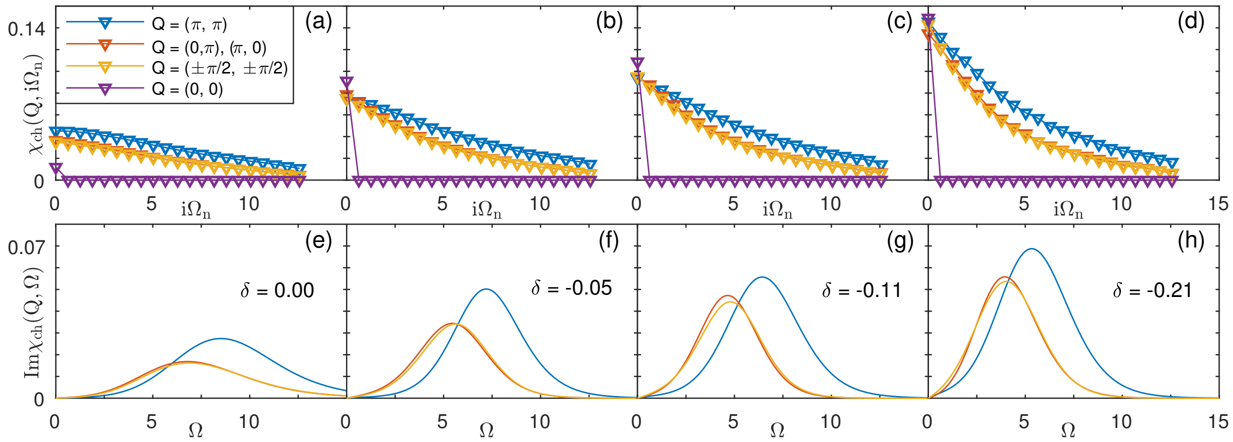

Figure 5.2: Charge susceptibility at $\beta t = 10$ with momentum transfers Q at [(a) and (e)] $\delta = 0$, [(b) and (f)] $\delta = -0.05$, [(c) and (g)] $\delta = -0.11$, and [(d) and (h)] $\delta = -0.21$. [(a)-(d)] are results in Matsubara frequencies, [(e)-(h)] are analytically continued results in real frequency. Figure from Ref. [80].

erate with $(0, \pi)$], and $(\pi/2, \pi/2)$ [orange, degenerate with $(\pm\pi/2, \pm\pi/2)$] exhibit a smooth frequency dependence. Remarkably, data at $Q = (\pi/2, \pi/2)$ and at $Q = (\pi, 0)$ are almost identical, both in the half-filled and in the doped case. The momentum dependence of the charge susceptibility is therefore very different from that of the magnetic susceptibility. For magnetic susceptibility, as found in several approaches [131, 133, 134], the value at $Q = (\pi, \pi)$ is much larger than any other momentum transfer and rapidly grows as temperature decreases. In contrast, within the momentum resolution achievable within DCA, no dominant contribution to the charge susceptibility is found.

In order to make a connection to experiment, we show analytically continued data corresponding to the Matsubara curves in the lower panel [omitting $Q = (0, 0)$]. Within our resolution, our data for $Q = (\pi/2, \pi/2)$ and $Q = (\pi, 0)$ are described well by a single peak with a maximum near $\omega = 7\text{t} \sim 2.45$ eV (half filling) and $4\text{t} \sim 1.40$ eV (overdoped). Data at $Q = (\pi, \pi)$ exhibit a peak at a substantially higher frequency (8.5t $\sim$ 2.97 eV for half filling and 5.5t $\sim$ 1.92 eV for overdoped).

Figure. 5.3 shows the doping dependence of our data at constant temperature T = 0.1t $\sim$ 400 K. The top panels show $Q = (\pi, \pi)$, the middle panels $Q = (0, \pi)$, and the bottom panels $Q = (\pi/2, \pi/2)$. Left panels show Matsubara data, right panels the corresponding analytically continued real frequency data. Four doping points are shown: half filling (purple), underdoped (5% doping, orange), optimally doped (11% doping, red), and overdoped (21% doping, blue).

In Matsubara space, a gradual doping evolution is visible at low frequencies. Zero-frequency values are reduced in comparison to the overdoped values by a factor of about

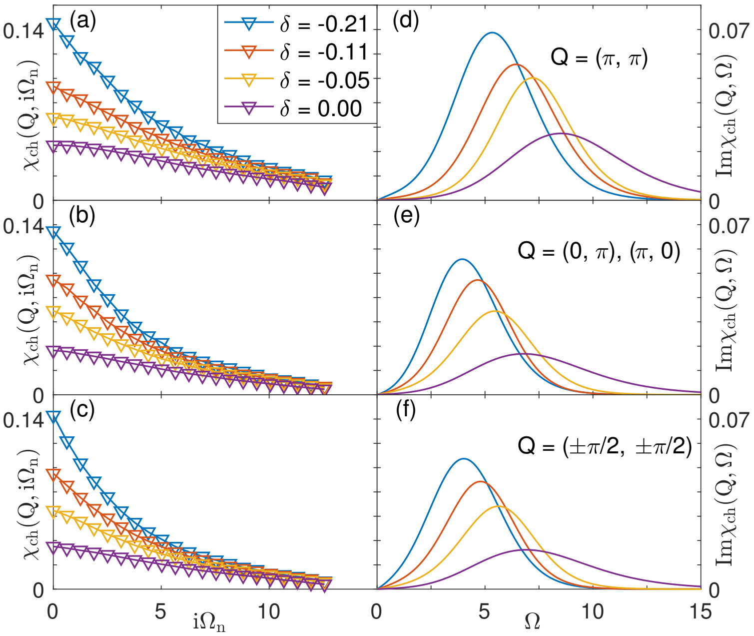

Figure 5.3: Charge susceptibility at $\beta t = 10$ and different dopings with momentum transfer [(a) and (d)] $Q = (\pi, \pi)$, [(b) and (e)] $Q = (0, \pi), (\pi, 0)$, [(c) and (f)] $Q = (\pm\pi/2, \pm\pi/2)$. [(a)-(c)] Results in Matsubara space, [(d)-(f)] results in real space. Figure from Ref. [80].

three, while the high-frequency limit remains unchanged. In the real frequency domain, this corresponds to a lowering of the frequency of the charge susceptibility peak, and a general sharpening. As seen previously, no significant momentum dependence is observed, apart from the Γ point, which is zero due to charge conservation. This doping evolution is similar to what is found at high temperature [134].

Figure. 5.4 shows the temperature dependence of $\chi_{ch}(Q)$ at different doping levels with momentum transfer $Q = (\pm\pi/2, \pm\pi/2)$ at half filling (Figure. 5.4 a), and in the under-doped (Figure. 5.4 b), optimally doped (Figure. 5.4 c), and over-doped (Figure. 5.4 d) regime. Top panels are the result in Matsubara space, and the bottom panels are the corresponding results in real frequency. Four temperatures are considered here: $\beta t = 5$ (T ∼ 800 K, blue), $\beta t = 7.5$ (T ∼ 530 K, orange), $\beta t = 10$ (T ∼ 400 K, yellow), and $\beta t = 15$ (T ∼ 270 K, purple).

As temperature at half filling is decreased, low frequency values are reduced, while the high frequency values remain invariant. In real frequency, the peak of the analytically continued data moves from $\Omega \sim 6t$ to $\Omega \sim 7.5t$. The reduction in low frequency values decreases as we increase doping. All other cases (underdoped, optimally doped, and overdoped) do not show much temperature dependence in both Matsubara and real frequency. The inset of [Figure. 5.4 (b)] shows the temperature dependence of static, uniform $[i\Omega_n = 0, Q = (0, 0)]$ charge

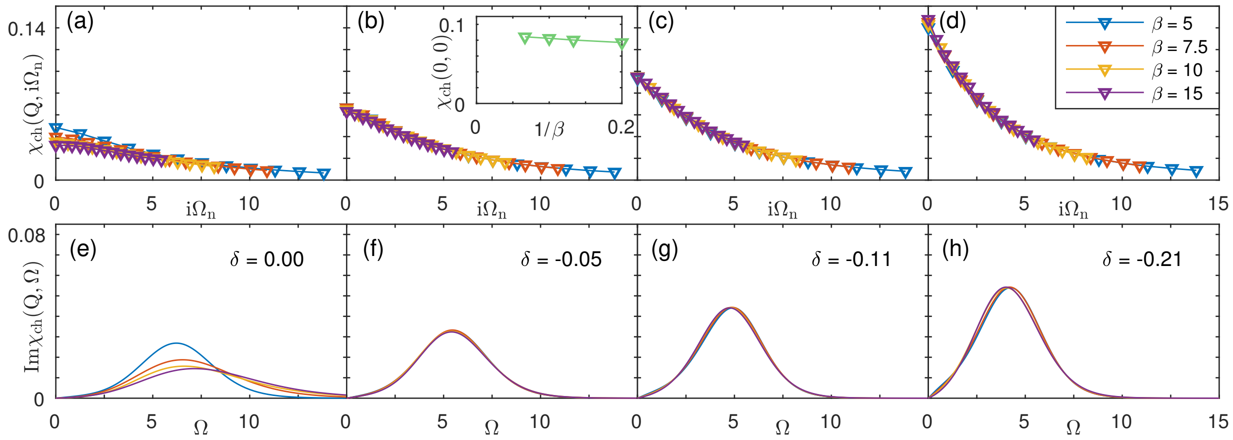

Figure 5.4: Charge susceptibility at different temperatures with momentum transfer $Q = (\pm\pi/2, \pm\pi/2)$ at doping level [(a) and (e)] $\delta = 0$, [(b) and (f)] $\delta = -0.05$, [(c) and (g)] $\delta = -0.11$, [(d) and (h)] $\delta = -0.21$. [(a)-(d)] Results in Matsubara space, [(e)-(h)] results in real space. Inset of (b): Static uniform charge susceptibility $(Q = (0,0), \Omega = 0)$ at doping $\delta = -0.05$. The unit of the temperatures shown in the legend is t^{-1}. Figure from Ref. [80].

susceptibility at doping level $\delta = -0.05$. As shown in Fig. 5.1, at this doping level, we gradually enter the pseudogap regime as temperature is decreased from $\beta t = 5$ to 15. While Ref. [129] shows that $\chi_{spin}(Q = (0,0), 0)$ is strongly suppressed at these parameters, χ_{ch} does not show any signature of the pseudogap. The absence of temperature dependence of χ_{ch} as we enter the pseudogap regime also means that its doping evolution shown in Fig. 5.3 is not caused by the existence of pseudogap.

It is interesting to compare the values from our calculations to those obtained without vertex corrections, where data are obtained by convolving $\chi_0 = G * G$ (see Eq. 5.9). Fig. 5.5 shows value for the zero-frequency part, as a function of both electron and hole doping. Remarkably, the vertex corrections strongly suppress the overall charge susceptibility and eliminate a large part of the momentum dependence. In particular, the dominant contribution at (π, π) is reduced to values similar to the other momenta.

An analysis of the frequency dependence (not shown here) shows the biggest discrepancies at the Γ point, where the violation of the charge conservation in the absence of vertex corrections leads to a large frequency-dependent contribution for nonzero momenta.

Our data also shows a pronounced dependence of the charge fluctuations on t'. Whereas the hole-doped side just shows a slowly increasing momentum-independent charge susceptibility and an overall suppression of the (π, π) susceptibility to the level of the other momenta, the electron-doped side (positive δ, note that approximately $\delta \to -\delta$ for $t' \to -t'$) shows a large enhancement of the (0, 0) susceptibility as compared to other momenta. This region is close to the onset of a first-order coexistence regime [108, 129, 135] in this model. Notably this

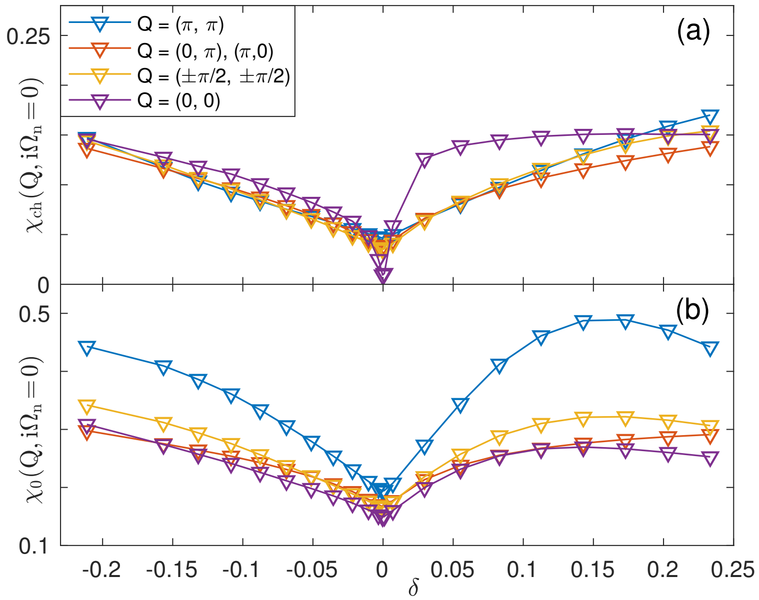

Figure 5.5: (a) Static charge susceptibility and (b) static charge susceptibility without vertex correction. $\beta t = 10$, for different Q at different doping levels. Figure from Ref. [80].

is the same parameter region where strong short-range antiferromagnetic fluctuations are present in the magnetic susceptibility.

5.3.2 Fluctuation diagnostics

Two-particle fluctuations such as the charge fluctuations analyzed in the previous subsection are often interpreted as the underlying cause of changes to single-particle observables. From a computational standpoint, both single- and two-particle quantities are computational outcomes of a simulation of Eq. 5.1. Attributing certain two-particle fluctuations as the "underlying cause" of a change of single-particle features is therefore difficult. However, as defined in Ref. [28], it is possible to express the single-particle self-energy, and thereby correlation contributions to the change of the spectral functions, in terms of two-particle quantities, via the (exact) equation of motion. For magnetic and charge fluctuations, these equations are

$$\tilde{\Sigma}_Q(K) = \frac{U}{\beta^2 N_c} \sum_{K'} F^{KK'Q}_{c,m} G(K')G(K'+Q)G(K+Q) \tag{5.13a}$$

$$= -\frac{U}{\beta^2 N_c} \sum_{K'} F^{KK'Q}_{c,d} G(K')G(K'+Q)G(K+Q) \tag{5.13b}$$

with F_d the corresponding full vertex of χ_d defined in Eq. 5.7, F_m the magnetic analog (for detail mathematical form see Ref. [42]), and K, K', Q representing pairs of frequency and

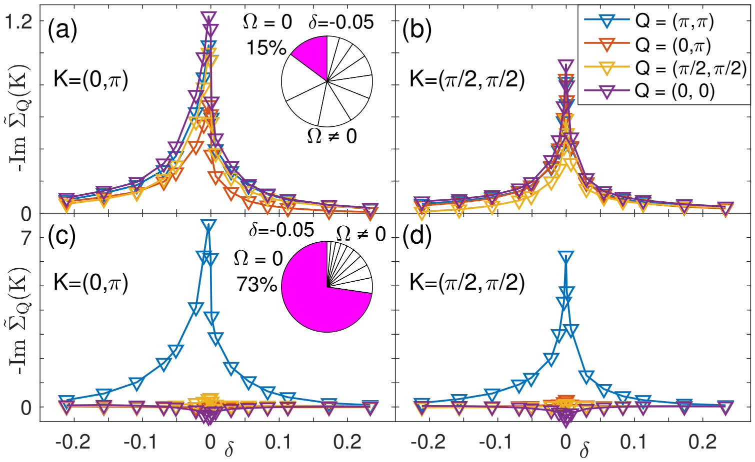

Figure 5.6: Fluctuation diagnostics [28] at $\beta t = 10$. (a) Charge channel, $K = (0, \pi)$; (b) charge channel, $K = (\pi/2, \pi/2)$. (c) Spin channel, $K = (0, \pi)$; (d) spin channel, $K = (\pi/2, \pi/2)$ as a function of doping. Pie chart: relative magnitude of $|\tilde{\Sigma}_Q(K, \pi/\beta)|$ for the first 10 Matsubara frequencies $|\Omega_n|$ in the charge (a) and spin (c) picture. Figure from Ref. [80].

momentum.

If a single momentum comprises the majority of the self-energy, and contributions from low energies are dominant, then a description in terms of bosonic modes of that type is convenient. This procedure, called "fluctuation diagnostics", has been successfully applied to non-Fermi liquid [168, 169] and real-space correlation functions [170].

Fig. 5.6 shows the contributions of fluctuations to the single-particle self-energy at the antinode (left panels) and at the node (right panels) expressed in terms of the charge contributions discussed in this paper (top panels) and in terms of magnetic contributions [131]. As is evident from the lower panels, the pseudogap is well described by short-ranged $Q = (\pi, \pi)$ magnetic fluctuations. A description in terms of charge modes requires similar contributions from all momenta and a much broader frequency range, leading us to conclude that charge fluctuations are not a good way to describe pseudogap physics in the entire parameter range studied here.

For a more detailed description of the fluctuation diagnostics method, see Ref. [28] and chapter 7.

5.3.3 Density wave with different symmetries

Despite the dynamical charge susceptibility, density wave with different symmetry factors are also important for understanding the charge fluctuations in the two-dimensional Hubbard model, especially the DDW fluctuations, which has been proposed as candidates responsible for pseudogap physics. In this subsection, we analyze the density waves and their competition with the $d-$wave superconductivity (DSC) fluctuations.

The density waves can be computed from the linear response introduced in section 3.3 [35]

$$-\frac{1}{N_0}\int_0^\beta d\tau' \sum_{kk'} \frac{\delta G_\sigma(k+q,0,k,0;\Lambda)}{\delta\Lambda(k',\tau')} g(k)g(k')\Big|_{\Lambda=0} = \frac{1}{\beta^2 N_0}\sum_{\omega\omega',kk'} \chi_d^{\omega\omega' 0}(k,k',q)g(k)g(k')\,, \tag{5.14}$$

with $\Lambda(k)$ the source field, $N_0 = \sum_{kk'} |g(k)g(k')|$ a normalization and $g(k)$ a symmetry factor defined in Eq. 4.8. The related order parameter is $D = i\sum_{k,\sigma} g(k)c^\dagger_{k+q,\sigma}c_{k,\sigma}$ [157, 171]. Two of the possible orders are $g(k) = \sin k_x$ for p_x symmetry and $g(k) = \cos k_x - \cos k_y$ for $d_{x^2-y^2}$ symmetry (see Eq. 4.8). The DDW, also called the “staggered flux state”, occurs at $Q = (\pi,\pi)$. The p density wave (PDW), also called the “bond order wave”, happens at $Q = (\pi,\pi)$ and $(\pi,0)$ (we will only consider $Q = (\pi,\pi)$). For a real space representation of DDW, see Fig. 2 of Ref. [156] and Fig. 2 of Ref. [157].

Superconducting fluctuations are related to the susceptibility in the particle-particle channel which follows from an analogous derivation [121],

$$\frac{1}{N_0}\int_0^\beta d\tau' \sum_{kk'} \frac{\delta G^A(k,0;\eta)}{\delta\eta(k',\tau')} g(k)g(k')\Big|_{\eta=0} = \frac{1}{\beta^2 N_0}\sum_{\omega\omega',kk'} \chi_{pp\uparrow\downarrow}^{\omega\omega' 0}(k,k',q=0)g(k)g(k')\,, \tag{5.15}$$

with $G^A(k,\tau) = -\langle \mathcal{T} c_{k\uparrow}(\tau)c_{-k\downarrow}(0)\rangle$ the anomalous Green’s function, and $\eta(k)$ the source field. The related order parameter is $P = \sum_k g(k)c_{k\uparrow}c_{-k\downarrow}$ [171]. We define the right hand side quantity in both Eq.5.14 and Eq. 5.15 as χ_g,

$$\chi_g = \frac{1}{\beta^2 N_0}\sum_{\omega\omega',kk'} \chi^{\omega\omega' 0}(k,k',q)g(k)g(k')\,. \tag{5.16}$$

This is the central quantity investigated in this subsection.

Phase transitions are indicated by a divergence of the susceptibility $\chi^{\omega\omega'\Omega}$. Since we expect large values of $\chi^{\omega\omega'\Omega}$ to be caused by vertex contributions, we define

$$V_g \coloneqq (\chi - \chi_0)_g = \frac{1}{\beta^2 N_0}\sum_{\omega\omega',kk'} g(k)g(k')(\chi^{\omega\omega' 0}(k,k',q) - \chi_0^{\omega\omega' 0}(k,k',q)) \tag{5.17}$$

in analogy to P_g in the superconducting case [121]. This quantity highlights vertex contributions by subtracting band-structure and single-particle effects contained within the bare susceptibility.

In our calculations, only a finite number of frequencies are available, but the asymptotic behavior of χ_0 is known analytically [54]. In the results presented here, we use 36 fermionic frequencies for $\beta t = 5, 10$; 50 fermionic frequencies for $\beta t = 15, 20$; and 80 fermionic frequencies for $\beta t = 30$ on both positive and negative sides to compute the vertices. The relative change for omitting the last eight frequencies on each side is on the order of 10^{-3}. The asymptotic behavior of vertex Γ and F is also analyzed in Ref. [172] which provides an alternative way of treating the high frequency behavior. χ is computed with the number of frequencies listed above for the vertex correction part, plus χ_0 computed with 1024 fermionic frequencies (both positive and negative) and supplemented with an analytically known asymptotic correction.

5.3.3.1 Charge and superconducting fluctuations

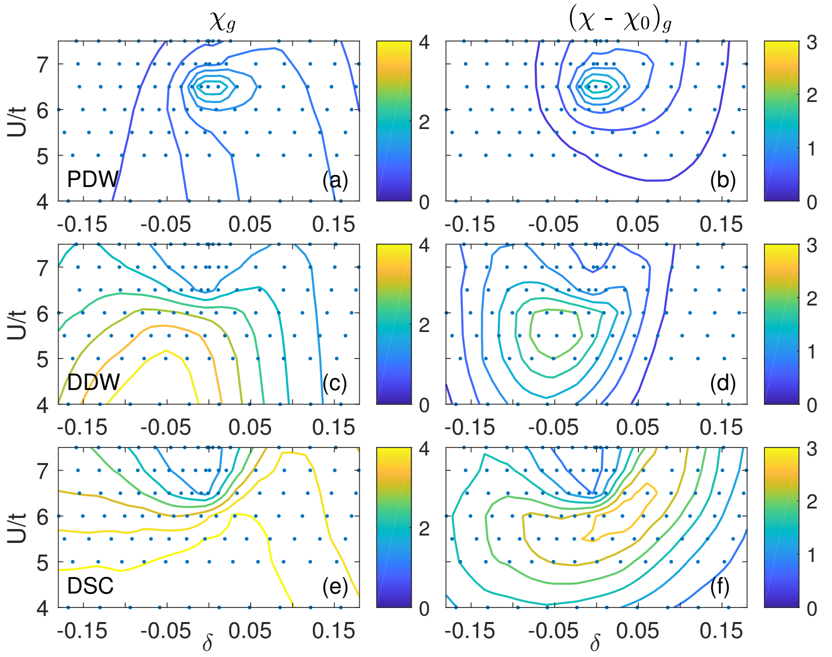

Figure 5.7: Amplitude of the susceptibility χ_g [left panels, Eq. 5.16] and vertex corrections [right panels; Eq. 5.17] for charge fluctuations with p-wave symmetry (top), d-wave symmetry (middle), and d-wave superconductivity (bottom) as a function of doping δ and interaction strength U at $\beta t = 20$, $t' = -0.15t$. Color bars show the strength of the susceptibility. Figure from Ref. [81].

Figure. 5.7 shows six panels for the leading fluctuations at $\beta t = 20$ and $t'/t = -0.15$. The three rows represent p_x and $d_{x^2-y^2}$ density fluctuations, and $d_{x^2-y^2}$ superconducting fluctuations. The left columns show $|\chi_g|$ (see Eq. 5.16), the right columns $|(\chi - \chi_0)_g|$ (see Eq. 5.17). Each panel displays data as a function of U and doping δ, with $\delta = 0$ corresponding to half filling. For superconductivity, only fluctuations with $d_{x^2-y^2}$ symmetry (DSC) are large [121]. Fig. 5.7 (b), (d) and (f) illustrate that χ itself is not a good measure for the correlation contribution that may eventually drive the system to an ordered state, as most of χ stems from $\chi_0 = GG$. Fig. 5.7 (c)-(f) show that the amplitudes of DDW and DSC fluctuations are comparable (at the same order), implying competing fluctuations. However, we find numerically that DSC fluctuations are always larger than DDW for the parameters examined. In a small regime of parameter space, where $U \sim 6.5t$ with slight electron doping, PDW fluctuations are the dominant charge fluctuation (panel (a) and (b)).

The maximum of DSC is on the electron-doped side, while the maximum of DDW is on the hole-doped side, both at intermediate interaction strength U. In addition, DSC fluctuations are suppressed in the pseudogap regime starting from $U \sim 6t$ (see Refs. [121, 135]), while DDW fluctuation starts to show suppression around half filling for $U \sim 6.5t$, which corresponds to the onset of the Mott insulator [135] in this approximation. PDW does not show any suppression by either the pseudogap or the Mott insulating state; its maximum is near $U \sim 6.5t$, which is the same interaction strength where DDW shows a suppression near half filling.

5.3.3.2 Temperature evolution

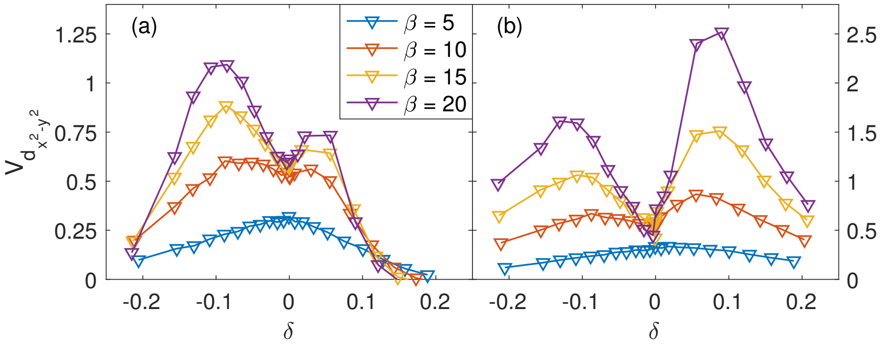

Figure 5.8: Amplitude of vertex correction for DDW and DSC at $U = 7t$, $t' = -0.15t$ for 4 temperatures. We use $t = 1$ here. (a): DDW. (b): DSC. Note that the y ranges of panels (a) and (b) are different. Figure from Ref. [81].

In order to investigate the competition between DDW and DSC fluctuations in more detail, we explore their temperature evolution with different dopings in Fig. 5.8. We show the results at $U = 7t$ and $t' = -0.15t$. Panel (b) shows that away from half filling, the vertex part of DSC increases as temperature decreases for all doping levels investigated (see also Ref. [121]), whereas panel (a) shows that the vertex correction part of DDW increases as temperature decreases in the underdoped regime away from half filling but rapidly decays to zero for large doping. The maximum of the DSC fluctuations are near the maximum T_c [121], while the corresponding maximum DDW fluctuations occur at slightly lower doping. The transition to superconductivity on the hole-doped side will take place near $\beta t = 35$ at

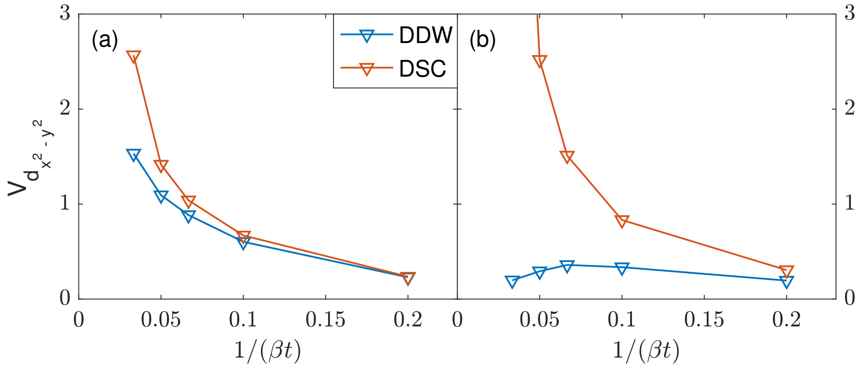

Figure 5.9: Temperature evolution of amplitude of vertex correction for DDW and DSC at $U = 7t$, $t' = -0.15t$, (a) $\mu/t = -1.4$ corresponding to $\delta \sim -0.09$ and (b) $\mu/t = 1$ corresponding to $\delta \sim 0.09$. Figure from Ref. [81].

optimal doping in this model, *i.e.*, at a temperature about twice below where these results have been obtained.

The amplitude of the vertex correction part of DDW and DSC fluctuations as a function of temperature at the doping level corresponding to largest DDW fluctuation and largest DSC fluctuation is shown in Fig. 5.9. These results are obtained in the paramagnetic state but reach temperatures just above the superconducting transition. At the doping level where DDW fluctuations are strongest (corresponding to $\mu/t = -1.4, \delta \sim 0.09$), DSC fluctuations are substantially larger than DDW, and increase faster as temperature decreases. We have been unable to find a region of parameter space where DDW order prevails over DSC around optimal doping. At the doping level corresponding to the largest DSC fluctuation($\mu/t = 1, \delta \sim 0.09$) we could find, DDW fluctuations first increase as temperature decreases, then start to decrease at $\beta t \sim 20$. This result is consistent with the findings of Refs. [171, 173].

5.3.3.3 Particle-hole asymmetry

Figure. 5.10 shows the dependence of PDW and DDW on interaction and doping for three values of t'. t' is to shift the Van Hove singularity of the density of states toward hole doping and destroys particle hole symmetry. We find that as t'/t is changed from 0 to -0.2 and correspondingly the Van Hove singularity more toward the hole-doped side, PDW fluctuations spread out over a larger area of the parameter space at the electron-doped side, but their maximum does not change significantly. On the other hand, the maximum of DDW fluctuations shifts toward hole doping and their intensity decreases substantially. The particle-hole asymmetry of DSC shows a different trend from DDW [121]. As $-t'/t$ increases, the maximum of DSC fluctuations moves to the electron-doped side. This is consistent with a scenario where the establishment of a pseudogap on the hole-doped side suppresses d-wave

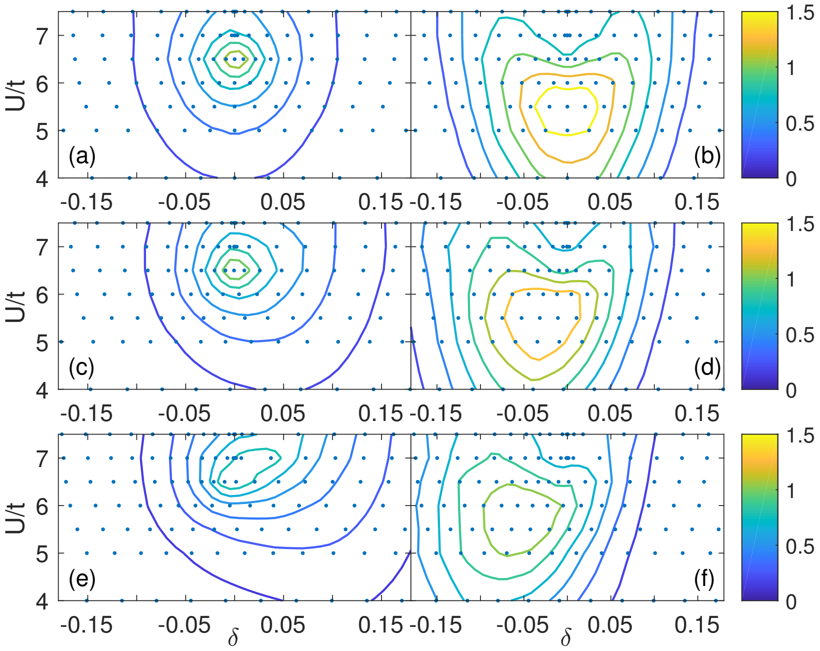

Figure 5.10: Amplitude of vertex correction for p density wave and d density wave at $\beta t = 15$ and different t'. (a): p density wave, $t'/t = 0$. (b): d density wave, $t'/t = 0$. (c): p density wave, $t'/t = -0.10$. (d): d density wave, $t'/t = -0.10$. (e): p density wave, $t'/t = -0.20$. (f): d density wave, $t'/t = -0.20$. The small lack of reflection symmetry of the results at $t' = 0$ is due to Monte Carlo errors. Figure from Ref. [81].

superconducting fluctuations [121].

Panel (a) of Fig. 5.11 shows the amplitude of the vertex corrections of DDW and DSC with different t' at $U = 7t$, $\beta t = 15$, and doping levels corresponding to the largest DDW fluctuations. As $-t'$ increases, the maximum of DDW shifts toward the hole-doped side. Since the overall intensity of the fluctuations decreases, the maximum value of DDW fluctuations saturates and then drops. At the same time, for all the t' values we explore, DDW fluctuations are still weaker than DSC fluctuations around the optimal doping for DDW fluctuations. Panel (b) shows the doping levels where the largest DDW fluctuations are found.

Eight-site DCA shows a narrowing of the pseudogap on the electron-doped side, and for $t' < -0.15t$ has a first-order transition between the Mott insulator and a momentum-dependent Fermi liquid state [135]. This rapid change in the single-particle quantities does not show an analog in the DDW or PDW fluctuations.

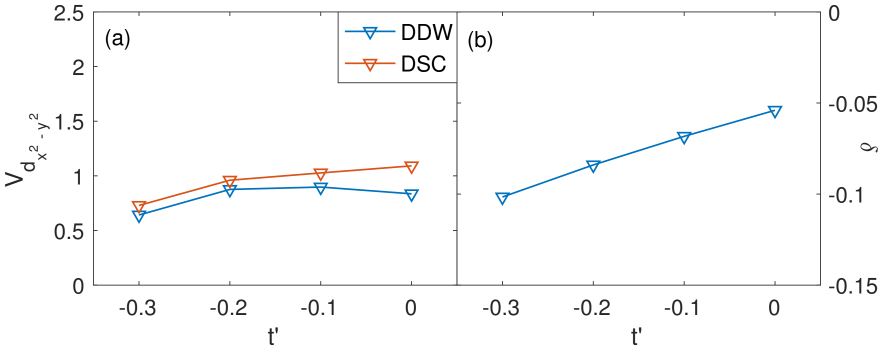

Figure 5.11: (a) t' evolution of vertex correction with $d_{x^2-y^2}$ symmetry [$V_{d_{x^2-y^2}}$, Eq. 5.17] for DDW and DSC at $U = 7t$, $\beta t = 15$ at doping levels corresponding to largest DDW fluctuations. (b) Doping levels corresponding to largest DDW fluctuations.

5.4 Discussion and conclusion

5.4.1 Charge susceptibility

To study the charge fluctuations, we have analyzed the momentum-dependent charge susceptibility in the Hubbard model for a range of dopings and temperatures and for interaction strengths that are thought to be relevant to superconducting cuprates [71, 118]. Experimental progress in M-EELS [100, 101] and RIXS promises to make this quantity accessible and will provide data that is directly comparable to our results. Our analysis has shown that the dynamical charge susceptibility can be represented by a single peak at a characteristic frequency that exhibits remarkably little momentum dependence, almost no temperature dependence, and a doping dependence that predominantly shifts the peak to lower frequencies as doping is increased. Vertex contributions are essential, as they eliminate the momentum dependence and lower the overall magnitude of the bare susceptibility at $Q = (\pi, \pi)$.

5.4.2 d density wave and d-wave superconductivity

The causes and consequences of DDW have been much debated. Early studies [138, 157–160] considered such fluctuations as a candidate for the mechanism of the pseudogap. Numerical calculations of the Hubbard model [171, 173–176] argued that this type of fluctuation is not strong enough to form an ordered state in the strongly correlated region, and is always dominated by DSC fluctuations, while renormalization group studies find that for SU(N), when $N > 6$, DDW becomes the leading instability [177]. Other works have studied the coexistence of DDW and DSC orders [158, 178]. The d-wave fluctuations at $Q = (0, 0)$ or d-nematic fluctuations have been studied in Ref .[173], where it is shown that they grow together with DDW, DSC, and AFM fluctuations.

More recent variational Monte Carlo studies [179, 180] found staggered flux states (DDW states) in the strongly correlated underdoped regime of the Hubbard model, for interactions smaller than the Mott transition. They proposed this state as a candidate for an anomalous "normal state" competing with DSC since its properties are similar to those of the pseudogap. In these more recent works, the state does not coexist with DSC.

Our results clarify some of these arguments. In general, we have found that the dominant charge fluctuations have d-wave symmetry, apart from a small regime near the Mott transition, where we find p-wave charge fluctuation. Our interaction, doping, and t' evolution of DDW correlations show that the evolution of the pseudogap and that of DDW correlations do not track each other. This can be seen from the fact that in the area around half filling, where there is a pseudogap, DDW correlations show a suppression. However, the interaction strength where DDW starts to show a suppression is at $U \sim 6.5t$, not at $U \sim 6t$, where the pseudogap opens. As $-t'/t$ increases, the pseudogap regime moves to the hole-doped side (shown in Fig. 3 and Fig. 4 of Ref. [135]), while the suppression of DDW moves to the electron doped side. These trends show little overall correlation between areas with the largest DDW fluctuations and the appearance of a pseudogap.

Without entering an ordered phase, it is difficult to make statements about a potential coexistence of DDW and DSC. However, comparison between the temperature evolution of DDW and DSC at $U = 7t$ (Fig. 5.8 and Fig. 5.9) clearly shows that around the optimal doping for DDW, DSC correlations are dominant over DDW and will order first. Thus, if there is a coexistence regime, it is likely fully contained inside the DSC dome.

Previous works [171] investigated the competition between DSC and DDW in the Hubbard model with DCA on 4-site clusters at the two doping levels $\delta = -0.05$ and $\delta = -0.25$. The first doping level is in the pseudogap regime, the second far in the overdoped. The main finding, namely that the susceptibility corresponding to the d density wave does not diverge, indicating the absence of a possible transition to the DDW state, is reproduced by our calculations. However, the claim that both DDW and DSC correlation functions are enhanced in the pseudogap regime is inconsistent with our more detailed calculations. The reason is that the intermediate maximum, which we find around $\delta = -0.09$, is missed by the coarse doping resolution employed in Ref. [171].

5.4.3 Fluctuations behind the pseudogap

To analyze the fluctuations behind the pseudogap, we refer to the fluctuation diagnostics method [28], which attributes contributions to the self-energy to fluctuations of different types. Our results show that in the parameter regime we explored, the dominant fluctuation in the paramagnetic state is always magnetic. It is shown in Ref. [28] that these magnetic fluctuations are responsible for the major contribution to the single-particle self-energy, and thereby for the suppression of the density of states. Charge fluctuations are not convenient to understand changes in the single-particle self-energy and spectral function, as terms from all momenta and many frequencies contribute to the self-energy with comparable strength. The pseudogap in the Hubbard model can therefore clearly be attributed to magnetic fluctuations. DDW and DSC fluctuations do not directly contribute to a single-particle self-energy, since the summation of a fluctuation with a d-wave symmetry tends to cancel out in the calculation of the self-energy [28].

Chapter 6

Magnetic Fluctuations and Superconductivity in the Two-Dimensional Hubbard Model

This chapter is based on *Xinyang Dong, Emanuel Gull, Andrew J. Millis "Quantifying the Role of Antiferromagnetic Fluctuations in the Superconductivity of the Doped Hubbard Model", arXiv.2202.10577 (2022)* [181].

6.1 Introduction

Superconductivity arises from the pairing of charge e electrons into charge $2e$ bosons ("Cooper pairs") and their condensation into a coherent quantum state. In conventional superconductors such as lead, a comparison of the frequency dependence of the superconducting gap function to the frequency spectrum of the phonons (quantized lattice vibrations) [182, 183] establishes that the electron-phonon interaction provides the "pairing glue" that binds electrons into Cooper pairs. Many "unconventional" superconductors are now known [184–187] in which the pairing glue is believed not to be provided by phonons. Substantial indirect evidence indicates that in many cases the relevant interaction is the exchange of spin fluctuations [188–192], but direct evidence has been lacking and many other mechanisms have been proposed [193–198].

The theoretical study of the unconventional superconductivity that is believed to arise from strong electron-electron interactions requires a model that captures the essentials of the correlated electron physics, and can be studied non-perturbatively. The Hubbard model has been proposed as the minimal theoretical model of quantum materials such as the copper-oxide based high-T$_c$ superconductors [102, 103]. This model describes electrons hopping among sites of a lattice (here we consider the two dimensional square lattice case with nearest-neighbor hopping of amplitude t) and subject to a site-local repulsive interaction U.

In this chapter, we quantify the strength of the electron-spin fluctuation coupling in the two-dimensional single band model (see section 4.1) within eight-site DCA (see section 4.3) by analysing the frequency dependence of the computationally determined electron self-energy, superconducting gap function and spin fluctuation spectrum.

6.2 Methods

This section summarizes the equations and definitions used in the calculations in this chapter. A more detailed explanation of the single- and two-particle Green's functions can be found in chapter 3, and the model and numerical methods used are introduced in chapter 4.

6.2.1 Measured quantities and numerical methods

We study the two dimensional single band Hubbard model in both the paramagnetic (normal) and the singlet superconducting state

$$H = \sum_{k\sigma} (\epsilon_k - \mu) c^\dagger_{k\sigma} c_{k\sigma} + U \sum_i n_{i\uparrow} n_{i\downarrow} \,, \tag{6.1}$$

with μ the chemical potential, $\epsilon_k = -2t(\cos k_x + \cos k_y)$ the dispersion with nearest neighbor hopping t. U is the strength of the interaction, i labels a lattice site, k labels the momentum, and n is the density operator.

We use the DCA (see section 4.3) to compute the single particle Green's function G and the susceptibility χ. The impurity model is solved with the CT-AUX quantum Monte Carlo impurity solver (see section 4.4).

With the Green's function matrix $\underline{G}(k, i\omega_n)$, the self-energy can be computed from the Dyson equation (see section 3.2.1)

$$\underline{\Sigma}_k(i\omega_n) = \underline{G}^{-1}_{0,k}(i\omega_n) - \underline{G}^{-1}_k(i\omega_n) \,, \tag{6.2}$$

with

$$\underline{G}_k(\tau) = -\langle \mathcal{T} \begin{pmatrix} c_{k\uparrow}(\tau)c^\dagger_{k\uparrow}(0) & c_{k\uparrow}(\tau)c_{-k\downarrow}(0) \\ c^\dagger_{-k\downarrow}(\tau)c^\dagger_{k\uparrow}(0) & c^\dagger_{-k\downarrow}(\tau)c_{-k\downarrow}(0) \end{pmatrix} \rangle \,, \tag{6.3}$$

$$\underline{G}_k(i\omega_n) = \int_0^\beta d\tau e^{i\omega_n\tau} \underline{G}_k(\tau) = \begin{pmatrix} G^N_{k\uparrow}(i\omega_n) & G^A_{k\uparrow}(i\omega_n) \\ G^{A*}_{k\uparrow}(i\omega_n) & -G^N_{-k\downarrow}(-i\omega_n) \end{pmatrix} \,, \tag{6.4}$$

$$\underline{G}^{-1}_{0,k}(i\omega_n) = \begin{pmatrix} i\omega_n - \epsilon_k + \mu & 0 \\ 0 & i\omega_n + \epsilon_k - \mu \end{pmatrix} \,, \tag{6.5}$$

$$\underline{\Sigma}_k(i\omega_n) = \begin{pmatrix} \Sigma^N_{k\uparrow}(i\omega_n) & \Sigma^A_{k\uparrow}(i\omega_n) \\ \Sigma^{A*}_{k\uparrow}(i\omega_n) & -\Sigma^N_{-k\downarrow}(-i\omega_n) \end{pmatrix} \,. \tag{6.6}$$

The SU(2) symmetry of the system gives $G^N_\uparrow = G^N_\downarrow$. For d-wave superconductivity on a lattice with inversion symmetry, $G^{N/A}_k = G^{N/A}_{-k}$, the anomalous Green's function and self-energy can be chosen to be real [199]. In the derivations below we will omit the spin label and use superscripts N and A to mark the normal and anomalous components of the Green's function and self-energy.

The spin susceptibility χ_{spin} is defined with the correlator of the magnetization in z direction $\hat{S}_z = n_\uparrow - n_\downarrow$ (see section 3.3)

$$\chi_{spin}(q,\tau) = \langle \mathcal{T} \hat{S}_z(q,\tau)\hat{S}_z(-q,0)\rangle - \langle \hat{S}_z(q)\rangle^2 \,, \tag{6.7}$$

$$\chi_{spin}(q,i\nu_n) = \int_0^\beta d\tau e^{i\nu_n\tau}\chi_{spin}(q,\tau) \,, \tag{6.8}$$

with ν_n the bosonic Matsubara frequency .

In the DCA simulations performed in this chapter, we have chosen a cluster size $N_c = 8$ which provides sufficient momentum resolution while allowing for calculation of the detailed dynamical information needed here. As explained in chapter 5, small cluster DCA simulations yields an AFM ordered state, causing the lattice susceptibility in the magnetic channel to diverge at $q = (\pi,\pi)$. This ordered state violates the Mermin-Wagner theorem [21] and is caused by finite size effects. Therefore we only analyze the spin susceptibility on cluster level. Note that the Ward identity [35] enforces the spin susceptibility to be zero at $q = (0,0)$ and $\nu_n \neq 0$ [167]. However, in DCA simulations, at cluster level, finite size effects give finite values of $\chi_{spin}(q = (0,0), i\nu_n)$ at $\nu_n \neq 0$. We will use K and Q to label cluster momenta in the rest of this chapter.

In our simulations, the spin susceptibility $\chi_{spin}(Q,\tau)$ is measured on the Chebyshev-Gauss-

Lobatto collocation points, and $\chi_{spin}(Q, i\nu_n)$ are computed via spectral transform [200, 201]. For a detailed explanation of the sampling points and the transformation see chapter 9. We will omit the subscript of χ_{spin} and use $\chi_Q(i\nu_n)$ to represent the spin fluctuation in the rest of this chapter.

6.2.2 Spin fluctuation theory

Figure 6.1: Spin-fluctuation diagrams for normal and anomalous self-energy. Solid lines: Normal or anomalous Green's function; Wavy lines: Spin susceptibility.

Spin fluctuation theories yield the spin fluctuation (SF) contribution to the normal (N) and anomalous (A) self-energies in terms of the spin susceptibility and normal and anomalous components of the Green function $G_K^{N/A}$ as [182, 188, 189, 192] (see Fig. 6.1)

$$\Sigma_K^{SF;N/A}(i\omega_n) = \frac{g^2}{\beta N_c} \sum_{Q, i\nu_n} \chi_Q(i\nu_n) G_{K+Q}^{N/A}(i\omega_n + i\nu_n) \,. \tag{6.9}$$

We assess the relevance of spin fluctuations by using our calculated G and χ, along with an estimated coupling constant g to compare Σ^{SF} [Eq. 6.9] to our numerically calculated self-energies.

6.2.2.1 Coupling constant

To estimate the coupling constant g^2, we partition the exact normal self-energy from DCA into a low frequency part that is supposed to arise mainly from spin fluctuations, and a high frequency part that represents contributions from all other processes

$$\mathrm{Im}\Sigma_K^N(i\omega_n) = \mathrm{Im}\Sigma_K^{SF;N}(i\omega_n) + \mathrm{Im}\Sigma_K^{\mathrm{high;N}}(i\omega_n) \,, \tag{6.10}$$

where the high frequency process is fitted by a minimal two-parameter model

$$\mathrm{Im}\Sigma_K^{\mathrm{fit};N}(i\omega_n) = -\frac{A}{\pi} \frac{\omega_n}{\omega_n^2 + x_0^2} \,, \tag{6.11}$$

with A and x_0 being two fitting parameters. The other relation we impose in the fitting procedure is that the quasi-particle weight $\left[1 - \frac{\partial[\mathrm{Re}\Sigma_K^N(\omega)]}{\partial\omega}\right]^{-1}$ given by the exact self-energy and the approximated self-energy from the spin fluctuation plus the high frequency fitting are approximately the same

$$Z_K^N = Z_K^{\text{fit};N} + Z_K^{SF;N}\,, \tag{6.12a}$$

$$Z_K^N = \frac{\text{Im}(\Sigma_K^N(i\omega_1) - \Sigma_K^N(i\omega_0))}{\omega_1 - \omega_0}\,. \tag{6.12b}$$

The fitting procedure is as follows:

- For a given g^2, compute $\Sigma_K^{SF;N}(i\omega_n)$ as in Eq. 6.9.
- Compute $\text{Im}\Sigma_K^{\text{high};N}(i\omega_n)$ as in Eq. 6.10.
- Fit $\text{Im}\Sigma_K^{\text{fit};N}(i\omega_n)$ to $\text{Im}\Sigma_K^{\text{high};N}(i\omega_n)$ by computing the two fitting parameters A and x_0 from the maximum of $\text{Im}\Sigma_K^{\text{high};N}(i\omega_n)$.
- Compute $\bar{g}^2$ from the requirement of Eq. 6.12.

The value of g^2 is decided by requiring $g^2 = \bar{g}^2$ in the above procedure, under the constraint $A > 0$, $-\text{Im}\Sigma_K^{SF;N}(i\omega_n) \leq -\text{Im}\Sigma_K^N(i\omega_n)$, $\forall n$, $-Z_K^{SF;N} \leq -Z_K^N$.

6.2.2.2 Matsubara sum

The real-frequency normal self-energy given by the spin fluctuation can be computed with the real-frequency normal Green's function and the real-frequency spin susceptibility using Matsubara sum. We will omit all the momentum index in this section since we are doing frequency analysis.

The real-frequency normal Green's function and spin susceptibility can be obtained from the Matsubara frequency results via analytical continuation (see section 4.5) using equations

$$G(i\omega_n) = \int dx \frac{1}{i\omega_n - x} A(x)\,, \tag{6.13}$$

$$\chi(i\nu_n) = \int dy \frac{1}{i\nu_n + y} B(y)\,, \tag{6.14}$$

where we have used $A(x)$ for the fermionic and $B(y)$ the corresponding bosonic spectral functions. The spin fluctuation self-energy can then be written as

$$\Sigma^{SF}(i\omega_n) = \frac{g^2}{\beta} \sum_{i\nu_n} \iint dxdy A(x)B(y) \frac{1}{(i\omega_n + i\nu_n - x)(i\nu_n + y)}\,. \tag{6.15}$$

The frequency sum can be computed using the Cauchy's residue theorem. Consider the Bose distribution function

$$b(z) = \frac{1}{\exp(\beta z) - 1}\,, \tag{6.16}$$

the singular points are at $\exp(\beta z) - 1 = 0$, $z = i\frac{2n\pi}{\beta} = i\nu_n$, which are the bosonic Matsubara frequencies. Define $g(z) = \frac{1}{(i\omega_n + z - x)(z+y)}$, it has singular points at $z_1 = x - i\omega_n$, $z_2 = -y$. The frequency sum can then be written as [7]

$$\begin{aligned}\frac{1}{\beta}\sum_{i\nu_n}\frac{1}{(i\omega_n + i\nu_n - x)(i\nu_n + y)} &= \frac{b(z_1)}{z_1 - z_2} + \frac{b(z_2)}{z_2 - z_1} \\ &= \frac{b(x - i\omega_n)}{x - i\omega_n + y} + \frac{b(-y)}{-y - x + i\omega_n}\,.\end{aligned} \tag{6.17}$$

Consider the Fermi distribution function

$$f(z) = \frac{1}{\exp(\beta z) + 1}\,, \tag{6.18}$$

we have $b(x - i\omega_n) = -f(x)$. Eq. 6.15 can be written as

$$\Sigma^{SF}(i\omega_n) = \iint dxdyA(x)B(y)\frac{f(x) + b(-y)}{i\omega_n - y - x}\,. \tag{6.19}$$

To evaluate the self-energy on real axis, we replace $i\omega_n$ with $\omega + i\delta$, δ an arbitrary small value. The imaginary part of the spin fluctuation self-energy can be written as

$$\begin{aligned}\mathrm{Im}\Sigma^{SF}(\omega) &= \iint dxdyA(x)B(y)[f(x) + b(-y)][-\pi\delta(\omega - y - x)] \\ &= -\pi\int dyA(\omega - y)B(y)[f(\omega - y) + b(-y)] \\ &= \pi\int dyA(\omega - y)B(y)[f(y - \omega) + b(y)]\,,\end{aligned} \tag{6.20}$$

where we have integrated out x explicitly and used the relations $b(-x) = -1 - b(x)$ and $f(-x) = 1 - f(x)$.

6.2.3 Linearized self-energy equation

From the matrix form of the Dyson equation [Eq. 6.2], the Green's functions can be expressed as

$$\underline{G}_k^{-1}(i\omega_n) = \underline{G}_{0,k}^{-1}(i\omega_n) - \underline{\Sigma}_k(i\omega_n)\,, \tag{6.21}$$

$$\begin{pmatrix} G_k^N(i\omega_n) & G_k^A(i\omega_n) \\ G_k^A(i\omega_n) & -G_{-k}^N(-i\omega_n) \end{pmatrix}^{-1} = \begin{pmatrix} i\omega_n - \Sigma_k^N(i\omega_n) - (\epsilon_k - \mu) & -\Sigma_k^A(i\omega_n) \\ -\Sigma_k^A(i\omega_n) & i\omega_n + \Sigma_{-k}^N(-i\omega_n) + (\epsilon_k - \mu) \end{pmatrix}.$$

The anomalous Green's function G^A is thus given by

$$G_k^A(i\omega_n) = \frac{\Sigma_k^A(i\omega_n)}{[i\omega_n - \Sigma_k^N(i\omega_n) - (\epsilon_k - \mu)][i\omega_n + \Sigma_{-k}^N(-i\omega_n) + (\epsilon_k - \mu)] - [\Sigma_k^A(i\omega_n)]^2} \tag{6.22}$$

If we consider a linearized anomalous Green's function equation, the $[\Sigma_k^A(i\omega_n)]^2$ term in the equation above will be dropped, which gives

$$\begin{aligned} G_k^A(i\omega_n) =& \frac{\Sigma_k^A(i\omega_n)}{2i\omega_n - \Sigma_k^N(i\omega_n) + \Sigma_{-k}^N(-i\omega_n)} \\ &\times \left[\frac{1}{i\omega_n - \Sigma_k^N(i\omega_n) - (\epsilon_k - \mu)} + \frac{1}{i\omega_n + \Sigma_{-k}^N(-i\omega_n) + (\epsilon_k - \mu)}\right] \\ =& \frac{\Sigma_k^A(i\omega_n)}{2i\omega_n - 2i\mathrm{Im}\Sigma_k^N(i\omega_n)}[G_k^N(i\omega_n) - G_k^N(-i\omega_n)] \\ =& \frac{\Sigma_k^A(i\omega_n)}{2i\omega_n - 2i\mathrm{Im}\Sigma_k^N(i\omega_n)} 2i\mathrm{Im}G_k^N(i\omega_n) \\ =& \Sigma_k^A(i\omega_n)\frac{\mathrm{Im}G_k^N(i\omega_n)}{\omega_n - \mathrm{Im}\Sigma_k^N(i\omega_n)}\,. \end{aligned} \tag{6.23}$$

In an eight-site DCA simulation with d-wave superconductivity, the anomalous Green's function and self-energy will only be non-zero at $K = (0, \pi)$ and $(\pi, 0)$ and $G_{(0,\pi)}^A(i\omega_n) = -G_{(\pi,0)}^A(i\omega_n)$, $G_{(0,\pi)}^N(i\omega_n) = G_{(\pi,0)}^N(i\omega_n)$. The one-loop spin fluctuations [Eq. 6.9] can then be rewritten as

$$\begin{aligned} \Sigma_{(0,\pi)}^A(i\omega_n) =& \frac{g^2}{\beta N_c}\sum_{\omega_n'}[\chi_{(0,0)}(i\omega_n' - i\omega_n) - \chi_{(\pi,\pi)}(i\omega_n' - i\omega_n)] \\ &\times \frac{\mathrm{Im}G_{(0,\pi)}^N(i\omega_n')}{\omega_n' - \mathrm{Im}\Sigma_{(0,\pi)}^N(i\omega_n')}\Sigma_{(0,\pi)}^A(i\omega_n') \\ =& \sum_{\omega_n'} F(i\omega_n, i\omega_n')\Sigma_{(0,\pi)}^A(i\omega_n')\,, \end{aligned} \tag{6.24}$$

where $F(i\omega_n, i\omega'_n)$ is a matrix in ω_n and ω'_n. The leading eigenvalue λ of this matrix should cross one at T$_c$, if spin fluctuations of this form cause superconductivity, and otherwise denotes the fraction of superconductivity given by one-loop spin fluctuations.

6.2.4 Superconducting gap function

One of the central quantities in the superconductivity theory is the frequency dependent gap function $\Delta(\omega)$ [119, 182, 202]. To derive the superconducting gap function from the single-particle Green's function and self-energy, we start from dividing the normal component of the self-energy into even and odd frequency part

$$\Sigma_k^{N,o,e}(i\omega_n) = \frac{1}{2}\left[\Sigma_k^N(i\omega_n) \mp \Sigma_k^N(-i\omega_n)\right] . \tag{6.25}$$

From Eq. 6.21, the determinant of the inverse Green's function matrix can be written as

$$\begin{aligned}\det(\underline{G}^{-1}) &= [i\omega_n - \Sigma_k^N(i\omega_n) - (\epsilon_k - \mu)][i\omega_n + \Sigma_{-k}^N(-i\omega_n) + (\epsilon_k - \mu)] - [\Sigma_k^A(i\omega_n)]^2 \\ &= \left[1 - \frac{\Sigma_k^{N,o}(i\omega_n)}{i\omega_n}\right]^2 \left[(i\omega_n)^2 - \frac{[(\epsilon_k - \mu) + \Sigma_k^{N,e}(i\omega_n)]^2 + [\Sigma_k^A(i\omega_n)]^2}{\left[1 - \frac{\Sigma_k^{N,o}(i\omega_n)}{i\omega_n}\right]^2}\right] ,\end{aligned} \tag{6.26}$$

where we have used the equivalence relation $\Sigma_k^N = \Sigma_{-k}^N$. The equation for excitations can be extracted from the second term of Eq. 6.26

$$\omega^2 = \mathrm{Re}\left[\frac{[(\epsilon_k - \mu) + \Sigma_k^{N,e}(\omega)]^2 + [\Sigma_k^A(\omega)]^2}{\left[1 - \frac{\Sigma_k^{N,o}(\omega)}{\omega}\right]^2}\right] , \tag{6.27}$$

where the first term shows the modification in propagation of normal particles, and the pairing energetic is given by the gap function [119]

$$\Delta_k(i\omega_n) = \frac{\Sigma_k^A(i\omega_n)}{1 - \frac{\Sigma_k^{N,o}(i\omega_n)}{i\omega_n}} . \tag{6.28}$$

The real-frequency gap function can be obtained from the Matsubara frequency result via analytical continuation (see section 4.5). The spectral representation of the gap function can be written as [119]

$$\Delta(z) = -\int \frac{dx}{\pi} \frac{\mathrm{Im}\Delta(x)}{z - x} , \tag{6.29}$$

where x and z are both complex variables. On the Matsubara axis, $\Delta(i\omega_n)$ is an even function of frequency (see Eq. 6.28), implying that $\mathrm{Im}\Delta(\omega)$ is an odd function of frequency on the real axis. Eq. 6.29 can then be rearranged as

$$\begin{aligned} \Delta(i\omega_n) - \Delta(i\omega_n = 0) &= -\frac{1}{\pi}\int d\omega \frac{\mathrm{Im}\Delta(\omega)}{\omega}\left(\frac{\omega}{i\omega_n - \omega} + 1\right) \\ &= -\frac{i\omega_n}{\pi}\int d\omega \frac{\mathrm{Im}\Delta(\omega)}{\omega}\frac{1}{i\omega_n - \omega}\,, \qquad (6.30) \\ \frac{\Delta(i\omega_n) - \Delta(i\omega_n = 0)}{i\omega_n} &= -\frac{1}{\pi}\int d\omega \frac{\mathrm{Im}\Delta(\omega)}{\omega}\frac{1}{i\omega_n - \omega}\,, \qquad (6.31) \end{aligned}$$

where

$$\Delta(i\omega_n = 0) = \frac{1}{\pi}\int d\omega \frac{\mathrm{Im}\Delta(\omega)}{\omega} \qquad (6.32)$$

is the norm used in the continuation, and can be obtained by fitting $\Delta(i\omega_n)$ at the lowest three Matsubara frequencies to a parabola. The continuation can then be done in a similar way as the normal Green's function with a fermionic kernel (see Ref. [73] and section 4.5).

In our simulation, the anomalous self-energy is chosen to be real, which gives a real gap function on the Matsubara axis. In practice, the continuation can be done using equation

$$\frac{\mathrm{Re}\Delta(i\omega_n) - \mathrm{Re}\Delta(i\omega_n = 0)}{\omega_n} = -\frac{1}{\pi}\int d\omega \frac{\omega_n}{\omega_n^2 + \omega^2}\frac{\mathrm{Im}\Delta(\omega)}{\omega}\,, \qquad (6.33)$$

which is similar to the normal Green's function continuation with particle-hole symmetry [73].

In general, there's no guarantee that $\mathrm{Im}\Delta(\omega)/\omega$ is of definite sign. For a detailed explanation of the validity of the gap function continuation see Ref. [119].

6.3 Results

We investigated several different dopings and interaction strengths. We present here results obtained for doping $x \sim 0.10$ (carrier concentration $n = 1 - x$ per site) and temperatures as low as $T = t/50$. For this carrier concentration at $U = 6t$, the normal state is a momentum-space differentiated Fermi liquid outside the pseudogap regime, corresponding to the overdoped side of the cuprates. The superconducting state, which we explicitly construct, appears below a transition temperature $T_c \approx t/40$. See Fig. 1 in Ref. [118] for the phase diagram at $\beta t = 40$. The choice of parameters is influenced by the following considerations: for higher U, calculations become more difficult [27], while for lower U they are less relevant for strong correlation superconductivity. Higher dopings reduce T_c, whereas lower dopings enhance the effects of the nearby pseudogap and the effects of the AFM state around half filling, making one-loop spin fluctuation theory less likely to succeed. We will comment briefly on the results for different dopings in the conclusions.

6.3.1 Spectral function

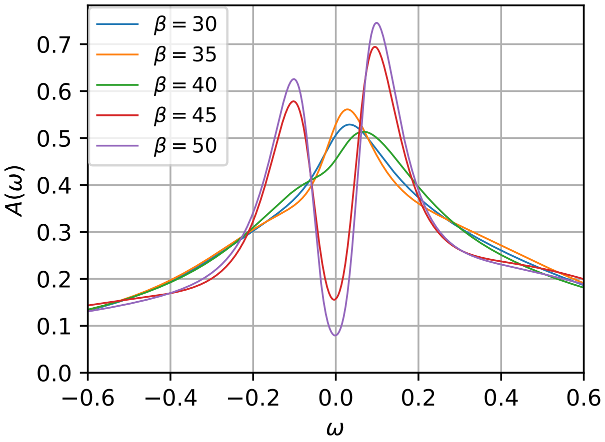

Figure 6.2: Analytically continued spectral function for the antinode $K = (0, \pi)$ at $U = 6t$, $\mu = -1.0t$ and different temperatures. The unit of the temperatures shown in the legend is t^{-1}.

The first signal of the superconductivity can be obtained from the spectral function $A_K(\omega) = -\mathrm{Im}G_K(\omega)/\pi$ at the antinode $K = (0, \pi)$, which can be computed from the normal Green's function $G^N_K(i\omega_n)$ via analytical continuation (see section 4.5). Fig. 6.2 shows the frequency and temperature dependence of $A_{(0,\pi)}(\omega)$. We can see from the temperature evolution that at temperatures above the transition temperature T_c, the spectral function has a peak around zero frequency arising from the van Hove singularity, while as we enter the superconducting state at about $\beta t = 40$, a gap appears. This finding is consistent with the standard theory [203], that the onset of superconductivity is associated with a suppression of density of states at low frequency and with the formation of density of states ("coherence") peaks [118]. See Ref. [118] for results at other dopings.

6.3.2 Spin susceptibility

The real frequency spectral function of the spin susceptibility $B_Q(\nu) = \mathrm{Im}\chi_Q(\nu)/\nu$ at $Q = (\pi, \pi)$, $\nu \to 0$ determines the density of states of low frequency spin excitations and the relaxation rate [130]. In the paramagnetic state, this quantity has a homogeneous increase as

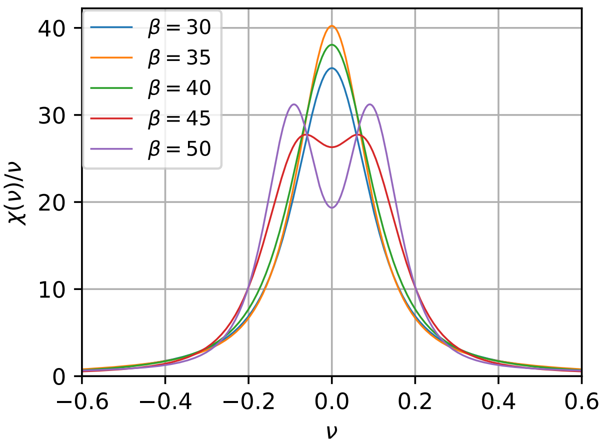

Figure 6.3: Continued spin susceptibility with $Q = (\pi, \pi)$ at $U = 6t$, $\mu = -1.0t$ and different temperatures. The unit of the temperatures shown in the legend is t^{-1}.

temperature decrease [130]. The temperature evolution of $B_{(\pi,\pi)}(\nu)$ across the superconducting transition temperature is shown in Fig. 6.3. We can see from the temperature evolution that as we enter the superconducting state, the spectral function gets suppressed around zero frequency, and a gap gradually appears as we go deeper into the superconducting state.

6.3.3 Self-energy from spin fluctuation theory

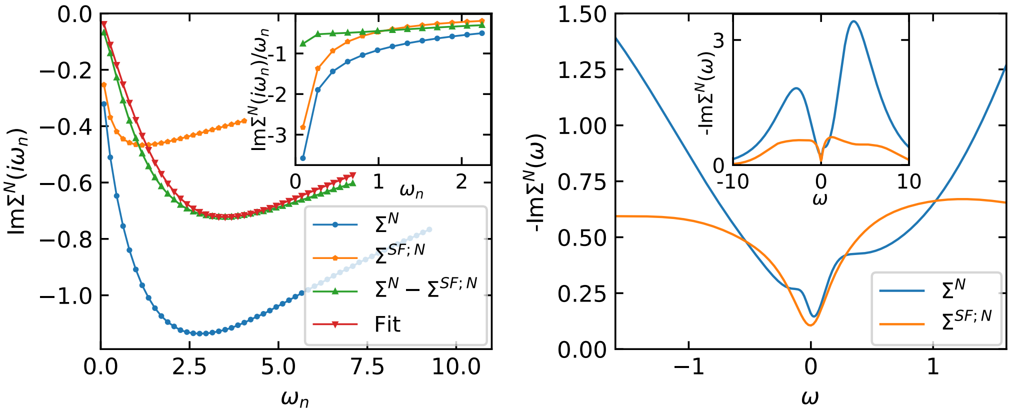

Figure 6.4: Left panel: Imaginary part of the normal component of the Matsubara self-energy for the antinode $K = (0, \pi)$ at $U = 6t$, $\beta t = 35$, and $\mu = -1.0t$ compared to spin fluctuation self-energy computed with $g^2 = 3.8$. Inset: $\mathrm{Im}\Sigma_K^N(i\omega_n)/\omega_n$. Right panel: Negative of the analytically continued real-axis the antinode $(0, \pi)$ self-energy and spin-fluctuation contribution computed with $g^2 = 3.8$. Inset: self-energy over a wide frequency range. Figure from Ref. [181].

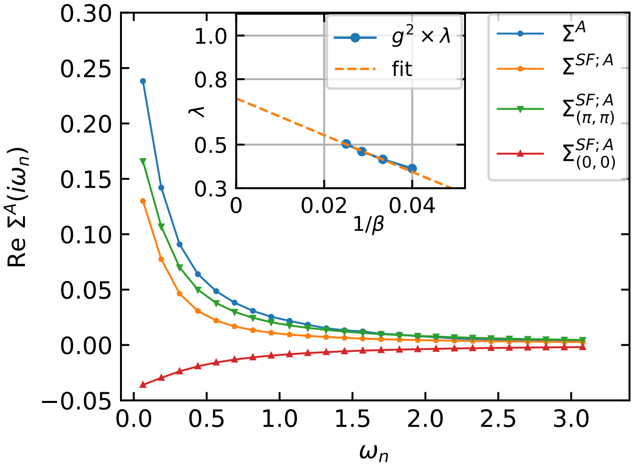

Figure 6.5: Total measured anomalous self-energy Σ^A_K and estimated spin-fluctuation contribution $\Sigma^{SF;A}_K$ of $K = (0, \pi)$ at $U = 6t$, $\beta t = 50$ and $\mu = -1.0t$ ($n = 0.90$). Also shown are the individual contributions to $\Sigma^{SF;A}$ from transferred momenta $Q = (\pi, \pi)$ and $Q = (0, 0)$. Inset: Leading eigenvalues computed from the linearized self-energy equation Eq. 6.24. The value of g^2 is chosen to be 3.8 for all temperatures. Dotted line: Linear fit to $\beta t = 30, 35, 40$. Figure from Ref. [181].

To determine the extent to which superconductivity arises from one-loop spin fluctuations, we compare the anomalous self-energy computed from Eq. 6.9 and directly measured from DCA simulation which gives $d_{x^2-y^2}$ symmetry superconductivity. The method to estimate g^2 is explained in detail in the method section [section 6.2.2]. The upper panel of Fig. 6.4 shows the Matsubara analysis of the normal component of the antinode self-energy, and the lower panel shows the real axis fits. Both cases are consistent with a value of $g^2 = 3.8$ implying that about 2/3 of Z^N comes from the electron-spin fluctuation interaction.

With the spin fluctuation spectrum and the electron-spin fluctuation coupling constant in hand, we begin with the equation for the transition temperature T_c, obtained by linearizing Eq. 6.9 in the anomalous component of the self-energy (see section 6.2.3). The resulting equation is a linear eigenvalue equation for eigenvector $\Sigma^A(i\omega_n)$; the largest eigenvalue λ increases as temperature decreases, and T_c is the temperature at which the leading eigenvalue equals unity (see Eq. 6.24). A $d_{x^2-y^2}$ symmetry gap yields a non-negative eigenvalue. Using our estimated $g^2 = 3.8$, we find that at temperature $T = t/40$ the leading eigenvalue λ is about 0.5 (see inset of Fig. 6.5), so that increasing the net pairing strength by a factor of about two would be needed to bring the leading eigenvalue up to 1 (in fact a larger increase would be required because the coupling constant of the normal state self-energy means the transition temperature does not vary linearly with the coupling).

Figure. 6.5 compares the measured anomalous self-energy to the spin fluctuation self-energy $\Sigma_K^{SF;A}$ at $K = (0, \pi)$. We note that the spin fluctuation interaction has two components, one from fluctuations near the antiferromagnetic wavevector $Q = (\pi, \pi)$ and one from fluctuations at small momenta near $Q = (0, 0)$. The small momentum fluctuations make a negative contribution to Σ_K^A. At the lowest Matsubara frequency the $\Sigma_K^{SF;A}$ produced by the spin fluctuation theory is approximately half of the DCA self-energy, again indicating that spin fluctuation theory [182] alone cannot account for the superconductivity.

6.3.4 Superconducting gap function

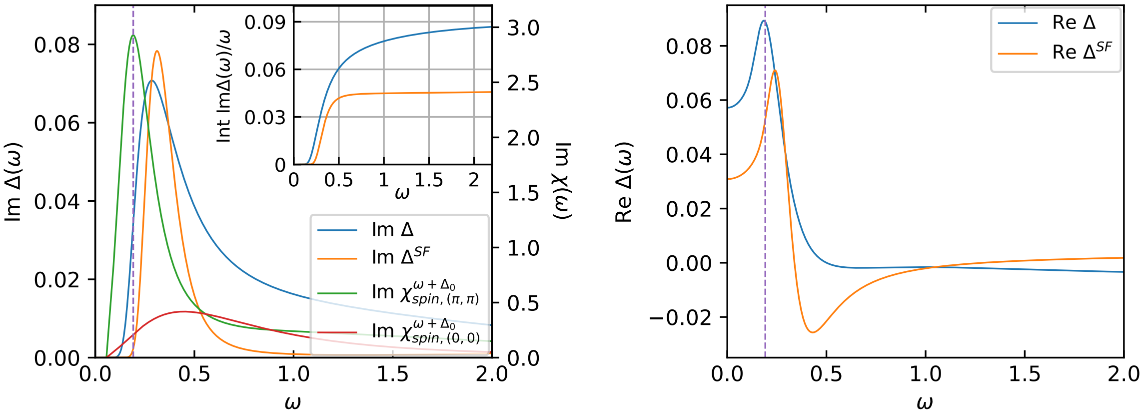

Figure 6.6: Comparison of the true gap function, gap function from spin fluctuation, the AFM susceptibility $\mathrm{Im}\chi^{\omega+\Delta_0}_{spin,(\pi,\pi)}$ and the FM susceptibility $\mathrm{Im}\chi^{\omega+\Delta_0}_{spin,(0,0)}$ shifted by the $\Delta_0 = \mathrm{Re}\Delta(\omega = 0) = 0.057$ at $U = 6t$, $\beta t = 50$ and $\mu = -1.0t$ ($n = 0.90$). Left panel: Imaginary part. Inset: Integral of $\mathrm{Im}\Delta(\omega)/\omega$ starting from $\omega = 0$. Right panel: Real part. Figure from Ref. [181].

We now examine in Fig. 6.6 the frequency dependence of the gap function $\Delta(\omega)$, a complex function of real frequency defined in terms of the normal and anomalous self-energies at $K = (0, \pi)$ (see section 6.2.4).

Following Ref. [182] we compare the frequency dependence of the spin fluctuation spectrum, the imaginary part of the DCA-computed gap function, and the estimated gap function computed by solving Eq. 6.9 using the measured G^A and χ. The real frequency quantities are obtained from maximum entropy analytical continuation of imaginary frequency data obtained at $T = t/50$, well below the superconducting transition temperature. As noted in Ref. [182] the presence of a gap in the electron Green's function means that a peak in χ at a frequency ω_{peak} implies a peak in Δ at $\Delta_0 + \omega_{peak}$ so we shift χ by the zero frequency gap function in the comparison.

We emphasize that the uncertainties in the analytical continuation are not small; while areas are reliably estimated, peak heights and widths are subject to some uncertainty. We see from Fig. 6.6 that while the peaks in the gap function and shifted χ roughly coincide, the spin fluctuation contribution to the imaginary part of the gap function is concentrated at low frequencies, decaying much more rapidly than the DCA-computed gap function, further demonstrating the importance of a high-frequency non-spin-fluctuation contribution to the electron self-energy.

6.4 Discussion and conclusion

Spin fluctuation theories, in which the spin fluctuations (as parametrized by the susceptibility) are treated as a pairing boson within the one loop approximation, are widely considered to be promising candidates for theories of superconductivity. Here we have performed a quantitative study, in a well defined, numerically controlled theory, of the extent to which this is actually the case. The theory produces a superconducting state and a spin fluctuation spectrum, which (taking advantage of recent developments [121]) we can obtain numerically exactly. Access to the spin fluctuation spectrum enables us to compare the spin fluctuation theory calculation of the normal state self-energies to numerically exact results for the same quantities, thereby allowing an estimate of the electron-spin fluctuation coupling constant. Knowledge of the coupling constant then enables a quantitative analysis of the contribution of spin fluctuations to the superconducting transition temperature and to the magnitude and form of the superconducting gap function. In qualitative consistency with previous results [192] we find that low-frequency spin fluctuations contribute to the superconductivity, but we find that quantitatively only about half of the pairing can be attributed to these fluctuations. The other half of the pairing therefore arises from higher frequency fluctuations, whose nature and precise physical origin remains to be determined.

We have similarly examined other doping values and interaction strengths. For $U = 6t,\ \mu = -0.9t$ ($x \sim 0.088$), $U = 6t,\ \mu = -1.1t$ ($x \sim 0.12$), and $U = 5.5t,\ \mu = -0.6t$ ($x \sim 0.066$) our analysis is internally consistent and provides reasonable estimates of the spin fluctuation contribution to the self-energy. We find that as doping is decreased below $x \sim 0.1$ spin fluctuation theory rapidly becomes a much less satisfactory description of the normal state, with the spin fluctuation contribution to Σ^N apparently decreasing, whereas the transition temperature weakly increases. As the doping is increased above $x \sim 0.1$, the spin fluctuation contribution to the normal state self-energy and gap function becomes larger, but the transition temperature rapidly decreases. These results are consistent with our finding that spin fluctuations do not fully account for the superconductivity exhibited by the model.

The numerical method used in this work is the 8-site DCA. The cluster size is chosen based on previous literature to capture the pairing and magnetic fluctuations at reasonable computational expense. DCA does not adequately capture for example the stripe physics [141, 142, 204–206] that may preempt superconductivity in some parameter ranges, and the cluster sizes available, while large enough to provide results that compare well to experiment and more exact calculations, cannot capture many of the interesting specifics of superconducting phenomenology. However, it is important to emphasize that the method provides a single internally consistent computational scheme that produces a well defined locally stable superconducting phase whose properties can be studied, and that provides, at the same level of approximation, normal and anomalous self-energies and spin fluctuation spectra, enabling a theoretically meaningful comparison.

Our finding that spin fluctuations, as parametrized by the spin-spin correlation function χ, and coupled to electrons via the standard one-loop approximation, are not the dominant form of superconductivity suggests more generally that spin fluctuation theories of this type may miss important aspects of correlated electron superconductivity. Our finding also suggests that if the nature of the higher frequency contributions to the pairing could be elucidated, tuning these degrees of freedom might be an effective strategy for raising the transition temperature.

Chapter 7

Fluctuation Diagnostics in the Singlet Superconducting State in the Two-Dimensional Hubbard Model

This chapter is based on *Xinyang Dong, Lorenzo Del Re, Alessandro Toschi, Emanuel Gull "Mechanism of Superconductivity in the Hubbard Model at Intermediate Interaction Strength", arXiv:2205.06286 (2022)* [50].

7.1 Introduction

The microscopic mechanism of unconventional high-temperature superconductivity has been one of the most controversially debated topics in condensed matter physics since the discovery of superconductivity in layered copper-oxides in 1986. While several aspects of the observed physics, such as the $d-$wave symmetry of the order parameter and the proximity to an antiferromagnetic Mott phase, clearly suggest that superconductivity must emerge from strongly correlated electronic processes, the intrinsic quantum many-body nature of the problem has hitherto prevented a rigorous identification of the pairing glue. To explicitly address this point, we present a focused study of the origin of superconductivity in the two-dimensional single band Hubbard model. The Hubbard Hamiltonian, which includes a kinetic term describing the hopping between neighbouring sites on a lattice and a potential-energy term encoding a local electrostatic repulsion, is a minimal theoretical model believed to capture the salient aspects of cuprate superconductivity.

Among the theoretical explanations proposed for the origin of the high-temperature superconductivity in this context, spin fluctuations have been a prominent scenario since the beginning [189–191, 207]. In particular, within in the weak-coupling regime of the Hubbard model, renormalization group techniques [138, 208–210] find d-wave superconductivity in qualitative agreement with spin fluctuation exchange studies [190, 210], consistent with diagrammatic Monte Carlo calculations [139]. At the same time, other, qualitatively different microscopic pictures of superconductivity exist besides the spin fluctuations, including the RVB theory [102], nematic fluctuations [211], loop current order [212], or the “intertwining” of orders of different types [213]. In fact, to what extent the weak-coupling spin fluctuation results apply to the much stronger interaction values, which are typical of cuprate materials, and whether there are other competing or intertwining fluctuations driving the superconductivity remains unresolved.

To provide a conclusive answer, we perform an analysis of the anomalous self-energy in the $d-$wave superconducting state within the method of fluctuation diagnostics [28]. We note that, unlike other diagrammatic approaches, which postulate a specific physical mechanism, analyze its consequences, and then compare to experiments, the fluctuation diagnostics procedure treats fluctuations of all kinds, including those possibly driving superconductivity, on equal footing, and is applicable in all parameter regimes, independent of the degree of correlation. However, the fluctuation diagnostics procedure as derived in [28] was only applicable to the highly symmetric normal state, and thus cannot be used to analyze superconductivity.

In this chapter, we will first generalize this approach to the case of phases with spontaneously broken symmetries and then apply it to identify the dominant fluctuations driving the anomalous self-energy in the superconducting state.

7.2 Methods

This section summarizes the equations and definitions used in the calculations in this chapter. Detail derivations are provided in chapter 3 and chapter 4.

The model we study is the two-dimensional single band Hubbard model (see section 4.1) in the singlet superconducting state

$$H = \sum_{k\sigma} (\epsilon_k - \mu) c^\dagger_{k\sigma} c_{k\sigma} + U \sum_i n_{i\uparrow} n_{i\downarrow} \,, \tag{7.1}$$

with i a lattice site, k momentum, $c^{(\dagger)}$ annihilation (creation) operators, and n the density. $\epsilon_k = -2t(\cos k_x + \cos k_y)$ is the dispersion with hopping t, U the interaction strength, and μ the chemical potential.

We use the DCA (see section 4.3) on a cluster with size $N_c = 8$ with a numerically exact CT-AUX (see section 4.4) impurity solver to enter the superconducting state non-perturbatively [118], and obtain Green’s functions, self-energies, and vertex functions. Within the 8-site DCA approximation, the model exhibits a large and stable d-wave superconducting region [118, 121]. The model is known to also exhibit a stripe phase [141, 142, 204–206], to which our calculation is not sensitive, since its periodicity is larger than the $N_c = 8$ cluster. Recent accurate calculations on different system geometries [142] find that the ground state of the model is charge ordered, rather than superconducting, indicating that the state found by DCA may be competing with a stripe state nearby in energy. Based on the closeness of the energetics, it is reasonable to assume that both states are important [214] and that one or the other will be selected based on minor variations of system geometries, approximations, and model parameters.

To identify the superconducting glue, we apply the fluctuation diagnostics scheme [28] to the anomalous self-energy in the superconducting state. This approach, which so far has been derived [28] and applied [28, 215] only in the paramagnetic normal state, allows for a rigorous identification of the dominant scattering mechanisms responsible for the observed self-energy. The central equation of the fluctuation diagnostics method is the Schwinger-Dyson equation, which can be written in a general form as

$$\Sigma(18) - \Sigma_\infty = -U(1234)G(25)F(5678)G(63)G(74)\,, \tag{7.2}$$

where we have used the Einstein summation notation and introduced the short-hand notation $i = (k_i, \sigma_i, \tau_i)$ for momentum, spin and time indices. The two indices on the self-energy $\Sigma(12)$ and the Green's functions $G(12)$ represent their normal $(1 = 2)$ and anomalous $(1 = -2)$ components, with $-i = (-k_i, -\sigma_i, \tau_i)$. Σ_∞ is the static Hartree contribution for the normal self-energy, and F is the full two-electron scattering amplitude. $U(1234)$ denotes the antisymmetrized interaction which, in the Hubbard model, is proportional to the local interaction U. This expression is exact and relates two-particle fluctuations to single-particle quantities.

The detailed derivation of the Schwinger-Dyson equation can be found in section 3.6, and the corresponding explicit equations for the normal and anomalous self-energies with Hubbard interaction are given in Eq. 3.146. A diagrammatic representation of the anomalous self-energy can be found in Fig. 3.2. The definitions of the single-particle Green's functions and the full vertex functions can be found in section 3.2.1 and section 3.5. In the derivations below we will use the labels combined indices $k \equiv (k, i\omega_n)$ to represent fermionic and $q \equiv (q, i\nu_n)$ to represent bosonic momentum and frequency indices, and will use superscripts N and A to mark the normal and anomalous components of the Green's function and self-energy.

Fluctuation diagnostics exploits symmetries in the Hamiltonian that lead to different expressions for the Schwinger-Dyson equation [Eq. 7.2] of the self-energy Σ. From section 3.4, we know that we can identify four physical channels in the singlet superconducting state, in which two of them are independent, giving two equivalent ways of writing the Schwinger-Dyson equation in the superconducting state (see section 3.6). As F contains all fluctuations of the system, the different expressions of the Schwinger-Dyson equation are equivalent when *all* internal summations are performed. Important additional information about the role played by the different scattering channels can be gained by comparing the expressions of the Schwinger-Dyson equation after *partial* summations over the internal variables k', but not q, are performed. From a physical point of view, each expression can be associated to one of the possible collective modes (e.g., density, magnetic, singlet/triplet pairing) of the electronic system. A large contribution to the final sum over q at low transfer frequency and at a definite momentum signifies a dominant collective mode, in contrast to contributions more evenly distributed over a wide range of frequencies and momenta. We will use K and Q to denote cluster momenta in the rest of this chapter.

7.3 Results

Fig. 7.1 gives the phase diagram of the 2D Hubbard model on the hole-doped side within the DCA approximation at intermediate interaction strength [118] showing the pseudogap (PG), superconducting (SC), and metallic (M) regime. The pseudogap regime is characterized by a suppression of the single particle spectral function, and the superconducting phase corresponds to the region where the anomalous Green's function is non-zero. We present the results for two representative parameter sets without next-nearest neighbor hopping on an eight-site cluster with $U = 6t$, $\beta t = 45$, i.e. $x = 0.031$ ($T_c \in (t/30, t/35]$, corresponding to underdoped (UD) for this value of U) and $x = 0.075$ ($T_c \in (t/30, t/35]$, corresponding to overdoped (OD) for this value of U), see Ref. [118] for a phase diagram. In DCA, both cases considered lie deep in the superconducting phase where the anomalous Green's function G_k^A is non-zero for $K = (0, \pi)$ and $(\pi, 0)$, with relation $G^A_{(0,\pi)} = -G^A_{(\pi,0)}$. Cluster momentum points are shown in the inset of Fig. 7.1. The inset of Fig. 7.1 shows the momentum (Q) and frequency (ν_n) distribution of $|\mathrm{Re}\Sigma^A_{(\pi,0),Q\nu}(i\omega_0)|$, which is computed by summing over fermionic indices k' but *not* over q in Eqs. 3.151a, 3.151b. The pie chart insets show that for both the underdoped and overdoped cases there are a dominant contribution from $Q = (\pi, \pi)$ and $\nu_n = 0$ in the magnetic/triplet channel S_z. In the density/singlet channel S_0, contributions from different momenta and frequencies are evidently distributed much more evenly.

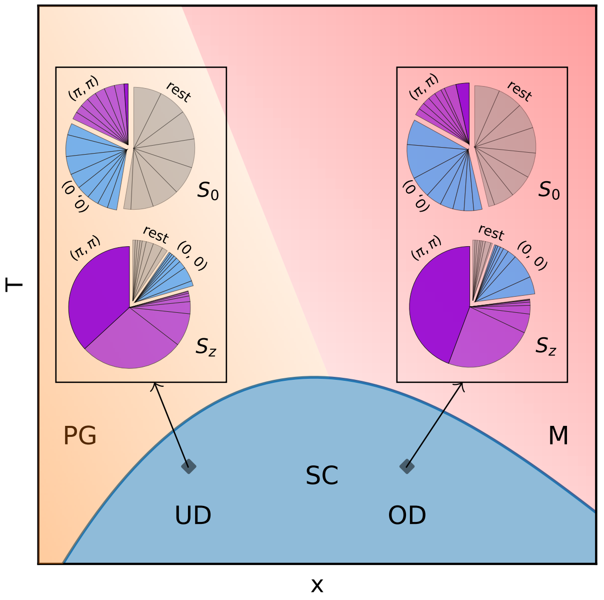

Figure 7.1: Phase diagram sketch, with pseudo-gap (PG, orange), metal (M, red), and superconducting (SC, blue) regimes. Black diamonds denote UD and OD data points analyzed in detail. Inset: Pie chart of $|\mathrm{Re}\Sigma^A_{(\pi,0),Q\nu}(i\omega_0)|$ in the density (S_0) and magnetic (S_z) channels. Counter-clockwise from the top, pieces represent contributions for momentum $Q = (\pi,\pi)$, $Q = (0,0)$ and summation over the remaining momenta in an eight-site cluster. In each slice, separation indicates bosonic frequency ν_n with $n = 0, \pm 1, \ldots \pm 7$. Figure from Ref. [50].

7.3.1 Momentum distribution

We first focus on the momentum distribution of $\mathrm{Re}\Sigma^A_{(\pi,0),Q}(i\omega_n)$ within the two physical channels in Fig. 7.2, computed by summing over all indices in Eqs. 3.151a, 3.151b except for the transferred momentum Q. The inset in the upper left panel shows the momentum points in an eight-site cluster, and the Fermi surface in the non-interacting system for dopings of 0.2 (corresponding to hole doping), 0, -0.2, and -0.4 (corresponding to electron doping). The left two panels show the contribution of different Q in the density channel. The weak Q dependence indicates the absence of a dominant mode in this channel. Results for the magnetic/triplet channel are shown in the right two panels. The transfer momentum $Q = (\pi,\pi)$ associated with AFM fluctuations is clearly the *dominant* mode in both the underdoped and the overdoped regime. We note that a sub-leading, though still sizable, *negative* contribution to the anomalous self-energy is originated by a ferromagnetic mode with $Q = (0,0)$. The black lines with crosses are computed by summing over all different momenta in the cluster, resulting in $\Sigma^A_{S_0}$ and $\Sigma^A_{S_z}$ of Eq. 3.153.

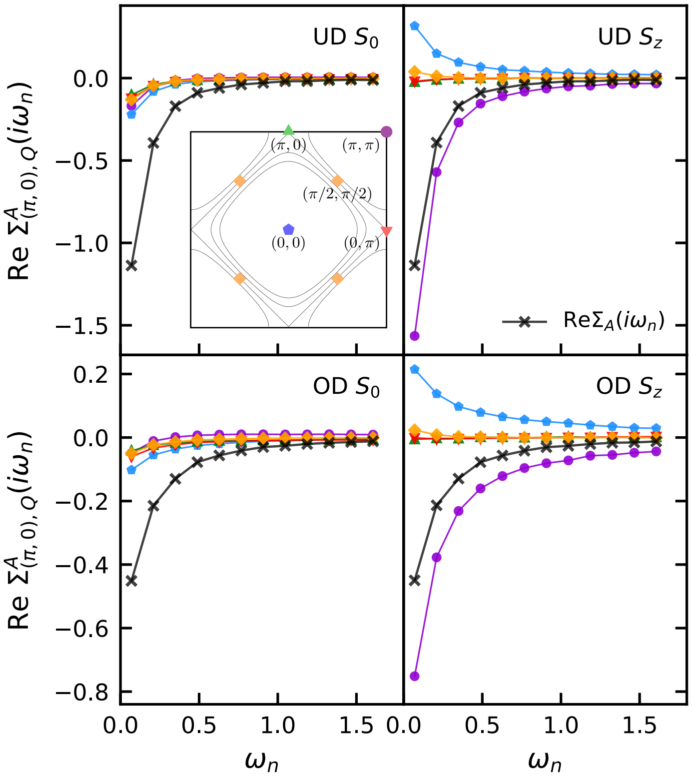

Figure 7.2: Re$\Sigma^A_{(\pi,0),Q}(i\omega_n)$ for several transfer momenta Q in the density (ρ) and magnetic (S) channels. OD and UD correspond to the diamonds in Fig. 7.1. Black line with crosses: total anomalous self-energy after summation over all Q. Inset: non-interacting Fermi surface and location of momentum points corresponding to colors in main panels. Figure from Ref. [50].

7.3.2 Frequency distribution

Important insight can be gained by a complementary analysis in frequency space: Fig. 7.3 shows the frequency dependence of Re$\Sigma^A_{(\pi,0),\nu_n}(i\omega_0)$, corresponding to the result at the lowest fermionic Matsubara frequency $i\omega_0 = \pi/\beta$ after summation over all indices except for bosonic frequency ν_n in Eqs. 3.151a, 3.151b. The low-frequency peak in the magnetic channel identifies the corresponding fluctuation as a well-defined and long lived "mode". In the density representation, the same fluctuations are short range and short lived. This indicates that the density representation is not suitable for a simple interpretation of the superconducting mechanism.

7.4 Discussion and conclusion

By extending the fluctuation diagnostics approach to the superconducting phase, we have been able to unambiguously identify spin fluctuations [189–191, 207] as the dominant con-

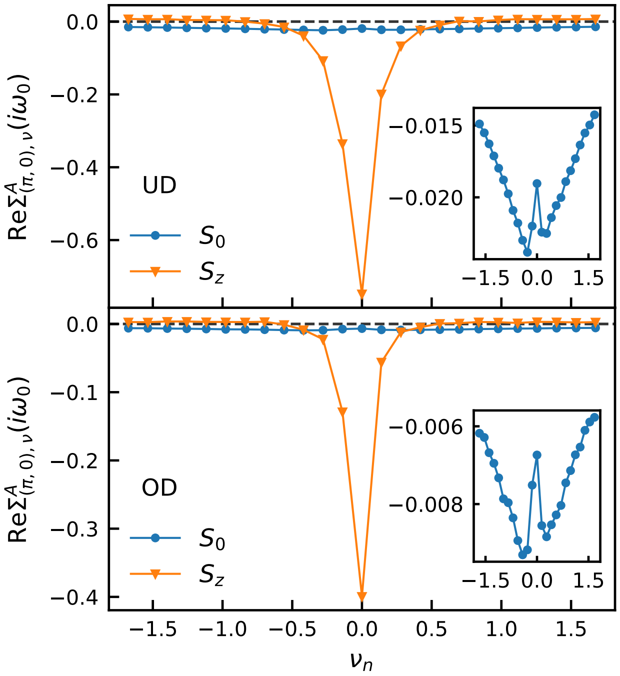

Figure 7.3: Re$\Sigma^A_{(\pi,0),\nu}(i\omega_0)$ in density (ρ) and magnetic (S) channels. OD and UD correspond to the two data points of Fig. 7.1. Inset: Re$\Sigma_{A,\nu}(i\omega_0)$ in density channel with rescaled y axis. Figure from Ref. [50].

tribution to the $d-$wave pairing in the Hubbard model at interaction strengths believed to be relevant for the cuprates, i.e., *beyond* the weak-coupling regime [139, 190, 209, 210]. At the same time, consistent with the existing work in the normal state [28, 80, 168], we do *not* find any indication supporting the alternative scenarios mentioned in the introduction, such as nematic fluctuations [211], loop current order [212], or “intertwining” of different orders [213]. In order for these scenarios to become relevant on larger systems or in other areas of parameter space, superconductivity from spin fluctuations would have to disappear while new mechanisms would have to emerge simultaneously, which we believe to be exceedingly unlikely. In the case of intertwined orders, multiple fluctuations such as density or magnetic ones would contribute synergistically to the pairing, rather than compete, in contradiction with our results. We emphasize that the fluctuation diagnostic is capable of detecting the occurrence of this situation, when it is realized, e.g. in the attractive Hubbard model [28].

Our identification of the superconducting glue agrees with the findings of several experiments. Ref. [216] finds good quantitative agreement between the spectral function computed from conventional spin fluctuation theory with magnetic susceptibility measured by inelastic neutron scattering, and the spectral function measured from angle-resolved photoemission spectroscopy in the superconducting phase of YBCO. Inelastic photon scattering experiments

[217] on Hg1201 and Hg1212 infer that the superconducting temperature T_c can be determined by the strength of the magnetic interactions ("paramagnon signals"), supporting the theory of magnetically mediated high-temperature superconductivity. Other experiments suggest a relation between superconductivity and charge density wave [218], or that the pseudogap and superconductivity may have different origins [219]. Thus, the numerical findings of our study suggest the possibility that the latter class of experiments may be probing aspects of cuprates physics beyond those encoded in the single-orbital Hubbard model on an eight-site DCA cluster.

Independently of the agreement with this multifaceted experimental evidence, our identification of the superconducting glue in terms of spin fluctuations touches a delicate and important aspect of the theoretical description of high-T superconductivity. In particular, conventional spin fluctuation theory [181, 192, 220–223] appears only able to capture a fraction of the pairing contribution [181] (see also chapter 6) or overestimate the results [222], depending on the analysis procedure used. The origin of this discrepancy can be ascribed to the RPA-like one-loop spin fluctuations expressions used in conventional approaches which, outside of the weak-coupling regime, do not capture all spin fluctuation mediated processes [224].

The microscopic picture of superconductivity emerging from our analysis agrees well with recent studies of the description of the *non*-superconducting pseudogap regime: While spin fluctuations were identified as the predominant mechanism of the pseudogap [28, 80, 168], differences with respect to the predictions of conventional spin fluctuation theory were found and traced [225] to the imaginary part of the dynamical scattering amplitude between electrons and spin fluctuations, which is absent in conventional approaches [225].

In conclusion, our fluctuation diagnostics of the superconducting order in the Hubbard model precisely identifies antiferromagnetic spin fluctuations as the glue of the $d-$wave pairing. This conclusion applies to the intermediate-to-large values of the electronic interaction relevant to cuprate physics. For this reason, the spin-fluctuations-driven pairing found in our calculations are expected to differ from conventional spin fluctuation theories.

Chapter 8

Realistic Electron Systems

In chapter 4, we introduced the model Hamiltonians and the corresponding numerical methods for solving the quantum many-body problem described in section 2.1. While the simplified models can be solved with numerical exact methods, they only include a subset of electronic degrees of freedom, which introduce systematic uncertainties. Numerical exact simulations of realistic systems are in general more expensive compared to the simulation of model systems due to the larger size of the configuration space. An alternate approach to embedding methods like DMFT and DCA is to use Green's function perturbation theory based on Feynman diagrams. Controlled approximations can be constructed based on finite-order resummation approximations of the infinite-order diagrams. In this chapter, we will introduce self-consistent methods based on low-order self-energy diagram approximations which are able to partially capture electron correlation effects with relatively low computational cost.

8.1 Molecules and basis sets

For the quantum many-body problem described in section 2.1, the basis functions $\phi_i(r)$ introduced in Eq. 2.5 can in general be non-orthogonal. For realistic electron systems like molecular systems, common choices of the basis functions include plane wave and atomic orbitals (AOs) [226]. We will use AO basis sets in the following derivations.

Accounting for the overlap integral S [Eq. 2.9], the action $\mathcal{S}$ corresponding to the Hamiltonian given by Eq. 2.6 takes the form

$$\begin{aligned}\mathcal{S} = &\int_0^\beta d\tau \sum_{ij} \sum_{\sigma} c^\dagger_{i\sigma}(\tau)[S_{ij}(\partial_\tau - \mu) + h_{ij}] c_{j\sigma}(\tau) \\ &+ \frac{1}{2}\int_0^\beta d\tau \sum_{ijkl} \sum_{\sigma\sigma'} U_{ijkl} c^\dagger_{i\sigma}(\tau) c^\dagger_{k\sigma'}(\tau) c_{l\sigma'}(\tau) c_{j\sigma}(\tau)\,,\end{aligned} \tag{8.1}$$

where i, j, k, l are orbital indices. The quadratic part of the action $\mathcal{S}$ corresponds to the inverse free propagator, c.f., Eq. 2.48, with an extra factor S

$$-g^{-1}_{ij,\sigma}(\tau) = S_{ij}(\partial_\tau - \mu) + h_{ij}\,. \tag{8.2}$$

Equivalently, the Dyson equation [Eq. 2.60] in frequency space becomes

$$G_\sigma(i\omega_n) = [S(i\omega_n + \mu) - h - \Sigma_\sigma(i\omega_n)]^{-1}\,. \tag{8.3}$$

With real basis functions, the interaction tensor U_{ijkl} has the following symmetries [227]

$$U_{ijkl} = U_{jikl} = U_{ijlk} = U_{jilk}\,. \tag{8.4}$$

In numerical simulations of molecular systems, it is sometimes convenient to transform to orthonormal basis. The matrix elements defined in Eqs. 2.7, 2.8, 2.9 can be transformed with a transformation matrix X as

$$S' = X^\dagger S X = \mathbb{I}\,, \quad h' = X^\dagger h X\,, \quad U'_{ijkl} = \sum_{mnpq} X^\dagger_{im} X_{nj} U_{mnpq} X^\dagger_{kp} X_{ql}\,. \tag{8.5}$$

Since the elements in the overlap matrix S is defined as a direct inner product [Eq. 2.9], it is a positive definite Hermitian matrix. In quantum chemistry, there are two common choices of orthogonalization using the eigenvalue decomposition of the overlap matrix $S = \mathcal{U} E \mathcal{U}^\dagger$ [227]

- Canonical orthogonalization: $X = \mathcal{U} E^{-1/2}$.
- Symmetric orthogonalization: $X = \mathcal{U} E^{-1/2} \mathcal{U}^\dagger$.

Similar basis transform will be used in section 8.3 for symmetry transformations.

8.2 Diagrammatic self-consistent approximations

Baym and Kadanoff [35, 36] showed that any approximation to the Luttinger-Ward functional Φ (see section 2.6) by taking a subset of diagrams included in Φ together with the conservation of energy and momentum at each vertex assures the approximation preserves the Ward identity (satisfies conservation laws). The self-consistent methods based on Φ-derivable self-energy approximations usually follow a similar procedure

- Choose an approximation to the Luttinger-Ward functional $\Phi^{\text{approx}}[G]$, and the corresponding approximation to the self-energy $\frac{\Phi^{\text{approx}}[G]}{\delta G} = \Sigma^{\text{approx}}[G]$.
- Perform the self-consistent procedure starting with an initial guess of the Green's function G
    1. Compute the self-energy $\Sigma^{\text{approx}}[G]$.
    2. Compute the Green's function $G[\Sigma]$ from the Dyson equation [Eq. 8.3].
    3. Go back to step 1 until convergence.

In this section, we will introduce two of these self-consistent methods: the Hartree-Fock (HF) approximation [227–229] and the self-consistent second-order Green's function perturbation theory (GF2) [230–234].

8.2.1 Hartree-Fock approximation

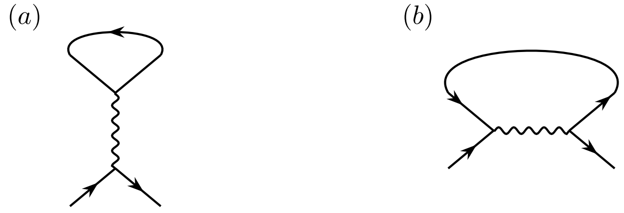

Figure 8.1: Hartree-Fock self-energy diagrams. (a) Hartree diagram. (b) Fock diagram.

The HF approximation corresponds to a truncation of the Φ expansion at first order [227–229]. The corresponding self-energy diagrams are shown in Fig. 8.1, and can be written out explicitly as

$$\Sigma^{(\text{HF})}_{ij,\sigma} = \sum_{kl}\sum_{\sigma'}(U_{ijkl} - U_{ilkj}\delta_{\sigma\sigma'})P_{kl,\sigma'}\,, \quad P_{kl,\sigma'} = G_{lk,\sigma'}(0^-)\,. \tag{8.6}$$

The HF self-energy given in Eq. 8.6 is static (frequency independent) and only depends on the density matrix P. In quantum chemistry, it is typically combined with the kinetic integral h_{ij} [Eq. 2.7] into the so called Fock matrix

$$F_{ij,\sigma} = h_{ij} + \Sigma^{(\mathrm{HF})}_{ij,\sigma} \,. \tag{8.7}$$

The corresponding Green's function at HF level can be written out explicitly as

$$G^{(\mathrm{HF})}_{\sigma}(i\omega_n) = [S(i\omega_n + \mu) - F_\sigma]^{-1} \,. \tag{8.8}$$

The Dyson equation [Eq. 8.3] can also be written using the Fock matrix by changing $h \to F$. This change corresponds to having a different quadratic part of the Hamiltonian. The self-energy will then only contains higher order contributions with asymptotic behaviour $\mathrm{Re}\Sigma(i\omega_n) \sim \mathcal{O}(\frac{1}{(i\omega_n)^2})$ and will decays to zero as $i\omega_n \to \infty$.

8.2.2 GF2

Figure 8.2: Second-order self-energy diagrams. (a) Direct diagram. (b) Exchange diagram.

GF2 adds two additional second-order bold diagrams to the self-energy on top of the HF approximation [230–233] (see Fig. 8.2). The corresponding second order self-energy is given by

$$\Sigma^{(\mathrm{GF2})}_{ij,\sigma}(\tau) = -\sum_{klmnpq} U_{ilnp} G_{lk,\sigma}(\tau) \sum_{\sigma'} G_{pq,\sigma'}(\tau) G_{mn,\sigma'}(-\tau)(U_{kjqm} - U_{qjkm}\delta_{\sigma\sigma'}) \,. \tag{8.9}$$

For closed-shell systems, Eq. 8.9 can be simplified to

$$\Sigma^{(\mathrm{GF2})}_{ij}(\tau) = -\sum_{klmnpq} U_{ilnp}(2U_{kjqm} - U_{qjkm}) G_{lk}(\tau) G_{pq}(\tau) G_{mn}(-\tau) \,, \tag{8.10}$$

using $G = G_\uparrow = G_\downarrow$, $\Sigma = \Sigma_\uparrow = \Sigma_\downarrow$.

For a molecule with N_{ao} orbitals, the naive computational scaling $\mathcal{O}(N_{ao}^6)$ of Eq. 8.9 and Eq. 8.10 can be decreased to $\mathcal{O}(N_{ao}^5)$ with proper tensor contractions. Taking Eq. 8.10 as an example, define $U^{\text{exch}}_{qjkm} = 2U_{kjqm} - U_{qjkm}$, the tensor contractions can be performed as follow

Algorithm 8.1: GF2 self-energy contraction

```
**Input:** Green's function $G_{ij}(\tau)$, interaction tensor $U_{ilnp}$, $U^{\text{exch}}_{qjkm}$.
**Output:** Self-energy $\Sigma_{ij}(\tau)$.
for $0 \leq i < N_{ao}$ do
    $U_i = U[i, :, :, :]$ ;
    $X_{ln,q}(\tau) = \sum_p (U_i)_{ln,p} G_{p,q}(\tau)$ ;
    $Y_{nq,k}(\tau) = \sum_l X_{nq,l} G_{l,k}(\tau)$ ;
    $(Z_i)_{m,qk}(\tau) = \sum_n G_{m,n}(-\tau) Y_{n,qk}$ ;
$\Sigma_{ij}(\tau) = \sum_{(qkm)} Z_{i,qkm}(\tau) U^{\text{exch}}_{qkm,j}$ ;
```

In algorithm 1 we need to pre-allocate two rank-three temporary objects X, Y and one rank-four temporary object Z, and use the symmetries of the interaction tensor [Eq. 8.4]. For applications that are limited by memory, we can instead introduce two rank-three temporary objects and move the last contraction for Σ_{ij} into the loop of i. One of the temporary object can be reused in this procedure, but the tensor contraction in this step would be a matrix vector multiplication instead of matrix matrix multiplication, which is less efficient.

In the following derivations we will omit the spin indices and only consider the closed-shell case.

8.3 Point group symmetry

The system size diagrammatic self-consistent approximations can compute are limited by both the computational cost (GF2 scales as $\mathcal{O}(N_{ao}^5)$) and total memory (U_{ijkl} is a rank 4 tensor). In this section we will describe how to use point group symmetries to block diagonalize the tensors in orbital space. This will reduce both the computational and total memory cost. We will not go deep into the group theory derivations but just state the theorems that are used. Detailed explanations can be found in Refs. [47, 235–238].

8.3.1 Finite groups

The point groups we work with are finite groups G with group elements g, which are closed under multiplications

$$g_1 \cdot g_2 = g_3 \in G\,, \quad \forall g_1, g_2 \in G\,. \tag{8.11}$$

A matrix representation of a group G is a set of matrices $R(g)$ that obey the multiplication table of the group [236]. Two representations $R(g)$ and $R'(g)$ are called equivalent if they are related by a similarity transform

$$R'(g) = \mathcal{U}^{-1} R(g) \mathcal{U}\,, \quad \forall g \in G\,. \tag{8.12}$$

The representation of a finite group can be chosen to be unitary. For two similar unitary representations $R(g)$ and $R'(g)$, the similarity transform $\mathcal{U}$ is also unitary $\mathcal{U}^{-1} = \mathcal{U}^\dagger$. We will only consider unitary representations in the derivations below.

By suitable choice of $\mathcal{U}$, the transformation in Eq. 8.12 can be used to simplify the representation. A representation is said to be reducible if all matrices in the representation can be block diagonalized using one unitary transformation, otherwise it is irreducible. The corresponding block diagonalized reducible representation $R'(g)$ can be written as direct sum of irreducible representations $R^{(i)}(g)$

$$R'(g) = \mathcal{U}^\dagger R(g) \mathcal{U} = \bigoplus_{i=1}^{N} R^{(i)}(g)\,, \tag{8.13}$$

where N is the number of blocks.

Schur's lemma states that a matrix that commutes with all matrices of an irreducible representation must be a multiple of the identity matrix. Consider a reducible representation that can be written as the direct sum of n irreducible representations $R^{(i)}$ repeated a_i times. A general matrix B that commutes with all group elements $[B, R(g)] = 0$, $\forall g \in G$ can be written in the form [236]

$$B' = \mathcal{U}^\dagger B \mathcal{U} = \bigoplus_{i=1}^{n} (b^{(i)} \otimes \mathbb{I}_{d_i})\,, \tag{8.14}$$

where $b^{(i)}$ is $a_i \times a_i$ matrix, d_i is the dimension of $R^{(i)}$. The number of non-zero coefficients in the matrix after the decomposition is $N_{B'} = \sum_{i=1}^{n} (a_i d_i)^2$, lower than the coefficients in the original matrix $N_B = (\sum_{i=1}^{n} a_i d_i)^2$. Therefore, imposing the symmetries reduces the number of coefficients needed to represent B.

8.3.2 Unitary transformation

To find the transformation matrix $\mathcal{U}$ that block diagonalize the matrices (tensors) in orbital space using point group symmetries of a molecule, there are in general two steps: 1) Build the matrix representation of the group, then 2) find the unitary transformation $\mathcal{U}$ that does the block diagonalization. In this subsection we will describe how these two steps are preformed in practice.

8.3.2.1 Building the matrix representation

To build the representation matrices of a given molecule and basis functions with its symmetry group, we first generate the permutation table for symmetry related atoms. The permutation table determines which atom gets mapped into which atom under each symmetry operation of the group. With the atom positions r_i and the real space rotation matrices $Q(g)$ corresponding to the group elements g, the algorithm for generating the full permutation table $P(g)$ is as the follows:

Algorithm 8.2: Permutation table for atoms in molecule

```
Input: Molecule ($N_{atom}$ atoms with positions $r_i$), $n_g$ group operations $Q(g)$.
Output: $n_g$ permutation table $P(g)$ with size $N_{atom} \times N_{atom}$.
for $\forall g \in G$ do
    Create a zero matrix $P(g)$ with size $N_{atom} \times N_{atom}$ ;
    for $0 \leq i < N_{atom}$ do
        $r_{trans} = Q(g) * r_i$ ;
        Find $j \in [0, N_{atom})$ such that $r_j = r_{trans}$ ;
        $[P(g)]_{ij} = 1$ ;
```

Next, we need to find out how the basis functions of the molecule transform under symmetry operations. With AOs, the angular momentum part of the basis functions are real spherical Harmonics Y_{lm}, which are linear combinations of complex spherical Harmonics Y_l^m

$$Y_{lm} = TY_l^m \,. \tag{8.15}$$

The rotation of the orbitals can be computed from the Wigner D-matrix that characterize the rotation of complex spherical Harmonics [236, 239]. For a given total angular momentum l (azimuthal quantum number), the D matrices determine how different magnetic quantum number ms are mixed after symmetry operation g

$$(Y_l^m)' = D(g,l)Y_l^m \,. \tag{8.16}$$

The rotation of real spherical Harmonics can then be written as

$$Y'_{lm} = \tilde{D}(g,l)Y_{lm} = TD(g,l)T^{-1}Y_{lm} \,. \tag{8.17}$$

With the permutation table and the D-matrix, the full representation matrix for each group element $R(g)$ can be built in the following way:

1. Block diagonalize the permutation matrix $P(g)$ to get a new permutation matrix $P'(g)$, with each block in $P'(g)$ containing atoms that are symmetry related with each other under operation g

   $$P'(g) = X^\dagger P(g)X = \bigoplus_{i=1}^{n} p^{(i)}(g) \,, \tag{8.18}$$

   where n is the number of "independent" groups of atoms that are not symmetry related under g, and $P'(g)$ can be considered as the permutation matrix for reordered atoms. The matrix X is also a permutation matrix with only one non-zero unit entry of in each row and column.

2. Build the representation matrix $R'(g)$ for the reordered atoms with basis functions. For each block $p^{(i)}(g)$ in $P'(g)$, the corresponding block in $R'(g)$ can be computed with

   $$R'(g) = \bigoplus_{i=1}^{n} r^{(i)}(g) \,, \tag{8.19}$$

   $$r^{(i)}(g) = p^{(i)}(g) \otimes \left(\bigoplus_{k=1}^{L^{(i)}} \tilde{D}(g,l_k) \right) \,, \tag{8.20}$$

   where k runs through all l of the atomic orbitals of atom i, $\sum_{k=1}^{L^{(i)}}(2l_k+1) = n_{ao}^{(i)}$.

3. Compute $R(g)$ from $R'(g)$

   $$R(g) = Z^\dagger R'(g)Z \,, \tag{8.21}$$

   where the matrix $Z^\dagger$ can be constructed from the matrix X by extending each $X_{ij} = 1$ in the X matrix to an identity matrix $\mathbb{I}_{n_{ao}^{(j)}}$ and fill other places with suitably sized zero matrices. The $Z^\dagger$ matrix constructed in this way has dimension $\sum_{j=1}^{N_{atom}} n_{ao}^{(j)} = N_{ao}$.

8.3.2.2 Find unitary transform for block diagonalization

There are several different ways to find the unitary transforms that block diagonalize the representation matrices $R(g)$ into a direct sum of irreducible representations. This includes building a projection matrix with the projection operators associated with irreducible representations, or by simultaneous diagonalization of the Dirac characters. Detailed explanations these two methods can be found in Refs. [236, 238], and we will briefly summarize the second way which do not require the information of irreducible representations as a priori.

To find the unitary transformation that decomposes the representation into block diagonalized form (irreducible representations), we first introduce the concept of conjugacy classes. The conjugacy classes C of a group G are defined as subsets of elements $g \in G$ that satisfy the conjugate relation

$$g_1, g_2 \in C \iff \exists g \in G,\ s.t.\ g_1 = g^{-1} g_2 g\,. \tag{8.22}$$

The relation between classes and irreducible representations can be characterized by the character $\chi(g)$, which is defined as the trace of the representation matrix $R(g)$

$$\chi(g) = \mathrm{Tr}[R(g)] = \chi(C)\,, \quad \forall g \in C\,, \tag{8.23}$$

where the second equity is due to the cyclicity of the trace. Hence, the character $\chi(g)$ for each element in a class is the same. It can be proved that the characters of two irreducible representations $\chi^{(i)}$ obey the orthogonality relation (the "wonderful orthogonality" theorem [236, 238])

$$\frac{1}{n_g} \sum_{g\in G} \chi^{(i)}(g) \chi^{(i')}(g)^* = \delta_{i,i'}\,, \tag{8.24}$$

which can be used to prove that the number of irreducible representations is equal to the number of classes (see Ref. [238]).

The quantity associated with classes that facilitates the construction of irreducible representations is the Dirac character Ω_C, which is defined as the sum of all elements in a class

$$\Omega_C = \frac{1}{n_{cg}} \sum_{g\in C} R(g) = \frac{1}{n_g} \sum_{g\in G} R^\dagger(g) R(g') R(g)\,, \quad \forall g' \in C\,, \tag{8.25}$$

where n_{cg} is the number of elements in class C. Due to the class rearrangement theorem [236], the Dirac characters commute with all group elements and with each other $[\Omega_C, R(g)] = 0$,

$[\Omega_C, \Omega_{C'}] = 0$ [236]. Therefore, simultaneous diagonalization of all the Dirac characters Ω_C gives a unitary transform $\mathcal{U}$ that diagonalizes $R(g)$ into blocks corresponding to different irreducible representations $R^{(i)}(g)$ [236].

In practice, to use the block diagonalized tensors in orbital space, we need to know the size of each block, which is associated with the repetition and dimension of each irreducible representation. The size of each block can be extracted from the n_c diagonalized Dirac characters. The eigenvalues of Ω_C are related to the characters of the irreducible representations. With the diagonal terms

$$\omega_C = \mathrm{diag}(\mathcal{U}^\dagger \Omega_C \mathcal{U}) \,, \tag{8.26}$$

different irreducible representations correspond to different constants in each ω_C. The sizes of the blocks can be computed by finding the shortest common constant piceses in all ω_C.

However, the unitary transform $\mathcal{U}$ given by simultaneous diagonalization can not separate repeated irreducible representations, since the eigenvalues of Ω_C are the same for equivalent irreducible representations. The separation of repeated irreducible representation is not required for obtaining a block diagonalized form of the matrix in Eq. 8.14, but might be necessary for other applications. The method for separating repeated irreducible representations can be found in Ref. [240].

8.3.3 Transformation in orbital space

With the unitary matrix $\mathcal{U}$, tensors with two orbital indices (overlap matrix S, Fock matrix F, Green's function G, and self-energy Σ) transform as

$$M' = \mathcal{U}^\dagger M \mathcal{U} \,. \tag{8.27}$$

In the orbital space, M' has $n = n_C$ blocks, with the size of block i being $a_i d_i \times a_i d_i$. The rank four interaction tensor transform as

$$U'_{ijkl} = \sum_{mnpq} \mathcal{U}^\dagger_{im} \mathcal{U}_{nj} U_{mnpq} \mathcal{U}^\dagger_{kp} \mathcal{U}_{ql} \,. \tag{8.28}$$

The U'_{ijkl} tensor after transformation can be considered as tensor blocks labeled with four irreducible representation indices. In practice, one can loop over all the combinations of irreducible representations to find and store the non-zero blocks.

In numerical simulations, besides being able to reduce both the computational cost and total memory, the block structure of the tensors also provides a natural way of performing parallelization, since different symmetry blocks do not mix with each other.

Chapter 9

Dyson Equation Solvers with Spectral Methods

This chapter is based on *Xinyang Dong, Emanuel Gull, Dominika Zgid, Hugo U.R. Strand "Legendre-spectral Dyson equation solver with super-exponential convergence", J. Chem. Phys. 152, 134107 (2020)* [241], and *Xinyang Dong, Emanuel Gull, Hugo U.R. Strand "Excitations and spectra from equilibrium real-time Green's functions", in preparation* [242].

9.1 Introduction

While the finite temperature Green's function formalism is very successful in applications to model Hamiltonians, its applicability to quantum chemistry and materials science remains limited to simple molecular and periodic problems. This is due to the necessity of simultaneously describing both the core and valence orbitals, with vastly different energy scales spanning several orders of magnitude. To describe these realistic systems, a compact representation of the Green's function is required.

In all diagrammatic self-consistent methods introduced in section 8.2, a central step is to solve the Dyson equation [Eq. 8.3] for the single-particle Green's function. In equilibrium simulations, the Dyson equation is diagonal in frequency space and can be readily solved. However, the self-energy contractions in diagrammatic methods are usually direct products of the Green's functions in time space. If one chooses to solve the Dyson equation in frequency space, an efficient transform between time and frequency space is necessary for self-consistent methods. Within the imaginary time and Matsubara frequency formalisms, with the standard approach using equidistant Matsubara frequency grids [243] and a finite frequency cut-off, the imaginary time Green's function only converges to the analytical result linearly with the number of Matsubara frequencies. Amending the representation with a low order high frequency expansion results in polynomial convergence [244–246]. In practice, this is problematic, since for systems with a wide range of energy scales, the number of coefficients is controlled by the largest energy scale [247]. An alternate approach is to solve the Dyson equation in imaginary time, which is a non-trivial integro-differential equation.

In the mean time, using the full real-time contour Green's function formalism [248] to handle general time dependent and non-equilibrium situations remains challenging due to the requirement of both high time resolution and long simulation times. Current methods are built on an equidistant discretization in real-time which evolved from second order explicit methods [249] to the current state-of-the-art sixth order multistep method [250]. Even though significant progress has been made for non-equilibrium Green's functions with two time arguments using matrix compression techniques [251] as well as adaptive time-stepping methods [252], compact discretizations and high order methods in real-time have not been explored.

The developments of compact representations of the Green's functions and algorithms for solving the Dyson equation is an active field of research. In this chapter, we briefly review some of the developments and introduce spectral methods for solving both the imaginary- and real-time Dyson equations.

9.2 Real-time contour Green's functions

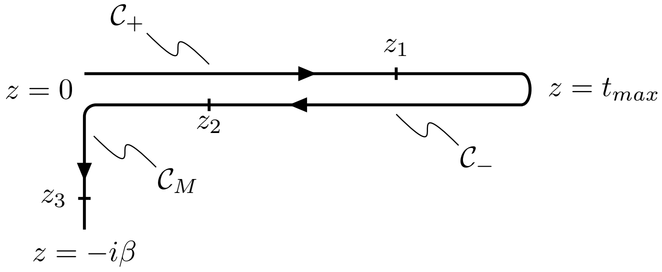

Figure 9.1: Real-time contour for systems in initial thermal equilibrium at inverse temperature β. Figure from Ref. [242].

For finite temperature calculations, imaginary-time and Matsubara frequency formalisms are sufficient to describe thermal equilibrium properties. To describe both thermal and temporal quantum correlations, we introduce the contour Green's function on the L-shaped time contour $\mathcal{C}$ [248]

$$G_{ij}(z,z') = -i\langle T_{\mathcal{C}} c_i(z) c_j^\dagger(z')\rangle = \frac{-i}{Z}\mathrm{Tr}[T_{\mathcal{C}} e^{-\mathcal{S}} c_i(z) c_j^\dagger(z')]\,, \quad z,z'\in\mathcal{C}\,, \tag{9.1}$$

where $T_{\mathcal{C}}$ is the contour time ordering operator ($z_1 < z_2 < z_3$ in Fig. 9.1), the operator $c_i^\dagger(z')$ ($c_j(z)$) creates (annihilates) a particle in the orbital i (j) at the contour time z' (z), $\mathcal{S} = i\int_{\mathcal{C}} dz H(z)$ is the action for the (time dependent) Hamiltonain H. In the following derivations we will omit the orbital indices for readability.

The contour $\mathcal{C}$ consists of three branches $\mathcal{C} = \mathcal{C}_+ \cup \mathcal{C}_- \cup \mathcal{C}_M$, where the branch $\mathcal{C}_+$ is the forward propagation in real-time from $z = 0$ to some maximal time $z = t_{\max}$, $\mathcal{C}_-$ the backward propagation in real-time, and $\mathcal{C}_M$ is the propagation in imaginary-time to the final time $z = -i\beta$ given by the inverse teperature β of the initial state. The time arguments z and z' of the Green's function can be constrained to one of the three branches of the contour. All the Keldysh components can be defined as [250]

$$G^M(\tau-\tau') = -iG(z,z')\,, \quad z,z'\in\mathcal{C}_M\,, \tag{9.2a}$$

$$G^>(t,t') = G(z,z')\,, \quad z\in\mathcal{C}_-\,,\; z'\in\mathcal{C}_+\,, \tag{9.2b}$$

$$G^<(t,t') = G(z,z')\,, \quad z\in\mathcal{C}_+\,,\; z'\in\mathcal{C}_-\,, \tag{9.2c}$$

$$G^\rceil(t,\tau') = G(z,z')\,, \quad z\in\mathcal{C}_\pm\,,\; z'\in\mathcal{C}_M\,, \tag{9.2d}$$

$$G^\ulcorner(\tau,t') = G(z,z')\,, \quad z\in\mathcal{C}_M\,,\; z'\in\mathcal{C}_\pm\,, \tag{9.2e}$$

$$G^{\mathrm{T}}(t,t') = G(z,z')\,, \quad z,z'\in\mathcal{C}_+\,, \tag{9.2f}$$

$$G^{\bar{\mathrm{T}}}(t,t') = G(z,z')\,, \quad z,z'\in\mathcal{C}_-\,, \tag{9.2g}$$

where $G^M(\tau)$ is the imaginary-time, $G^\gtrless(t,t')$ the greater/lesser, $G^\rceil(t,\tau')$ the right mixing, $G^\ulcorner(\tau,t')$ the left mixing, and $G^{\mathrm{T}}(t,t')$ the causal, $G^{\bar{\mathrm{T}}}(t,t')$ the anti-causal Green's function. The retarded and advanced Green's function can also be defined in addition

$$G^R(t,t') = \theta(t-t')[G^>(t,t') - G^<(t,t')]\,, \tag{9.3}$$

$$G^A(t,t') = \theta(t'-t)[G^<(t,t') - G^>(t,t')]\,, \tag{9.4}$$

with $\theta(t)$ the Heaviside step function. The symmetry relations of different real-time components can be written as [253]

$$
\begin{aligned}
G^{<,>}(t,t')^{\dagger} &= -G^{<,>}(t',t)\,, && \text{(9.5a)}\\
G^{\rceil}(t,\tau')^{\dagger} &= -\xi G^{\lceil}(\beta-\tau',t)\,, && \text{(9.5b)}\\
G^{\lceil}(\tau,t')^{\dagger} &= -\xi G^{\rceil}(t',\beta-\tau)\,, && \text{(9.5c)}\\
G^{R}(t,t')^{\dagger} &= G^{A}(t',t)\,, && \text{(9.5d)}
\end{aligned}
$$

where we introduced the parameter $\xi = -1$ for fermions and $\xi = 1$ for bosons.

The Dyson equation of the contour Green's function can be written in an integro-differential form [250, 253]

$$
(iS\partial_z - F(z))G(z,z') - \int_{\mathcal{C}} d\bar{z}\,\Sigma(z,\bar{z})G(\bar{z},z') = \delta_{\mathcal{C}}(z,z')\,, \tag{9.6}
$$

in combination with the Kubo-Martin-Schwinger (KMS) boundary conditions $G(0^-,z') = \xi G(-i\beta,z')$ and $G(z,0^-) = \xi G(z,-i\beta)$. The overlap integral S is defined in Eq. 2.9, $F(z)$ is the time dependent Fock matrix. $\delta_{\mathcal{C}}$ is the contour Dirac delta function defined through $\int_{\mathcal{C}} d\bar{z} f(\bar{z})\delta_{\mathcal{C}}(z,\bar{z}) = f(z)$, which requires

$$
\delta_{\mathcal{C}}\left(z,z'\right) = \begin{cases} \delta(z-z')\,, & z,z' \in \mathcal{C}_1 \\ -\delta(z-z')\,, & z,z' \in \mathcal{C}_2 \\ i\delta(z-z')\,, & z,z' \in \mathcal{C}_3 \\ 0\,, & \text{otherwise} \end{cases}\,. \tag{9.7}
$$

In non-equilibrium simulations, it is possible to work with only a reduced set of components of the Green's function using the symmetry properties of G [Eq. 9.5], one possible choice is the set $\{G^{<}, G^{R}, G^{\rceil}, G^{M}\}$ [250, 253].

In the following derivations, we will only consider the case of equilibrium real-time evolution [254, 255], i.e. the time evolution of system is governed by the same time-independent Hamiltonian as the initial thermal equilibrium state. In this case the Fock matrix is time independnet $F(z) = F$, the greater and lesser Green's functions $G^{\gtrless}$ are time translation invariant, $G^{\gtrless}(t,t') = G^{\gtrless}(t-t')$ and can be inferred from the mixing Green's function $G^{\rceil}$ as

$$
G^{<}(t) = G^{\rceil}(t,0)\,, \quad G^{>}(t) = -G^{>}(-t)^{\dagger} = -[G^{\lceil}(0,t)]^{\dagger} = \xi G^{\rceil}(t,\beta)\,. \tag{9.8}
$$

The retarded Green's function can then be written as

$$G^R(t,t') = \theta(t-t')[G^>(t,t') - G^<(t,t')] = \theta(t)[\xi G^\urcorner(t,\beta) - G^\urcorner(t,0)]\,. \tag{9.9}$$

With the initial state determined by $G^M(\tau)$, all real-time behaviour of the system can be described by $G^\urcorner(t,\tau')$, and it's sufficient to solve the Dyson equations for $G^M(\tau)$ and $G^\urcorner(t,\tau')$ to get all the Green's function components. The Dyson equation for these two components can be written out explicitly using the Langreth rules [256] (see Appendix A)

$$(-S\partial_\tau - F)G^M(\tau) - \int_0^\beta d\bar{\tau}\, \Sigma^M(\tau-\bar{\tau})G^M(\bar{\tau}) = 0\,, \quad \text{b.c. } [G(0) - \xi G(\beta)]S = -\mathbb{I}\,, \tag{9.10}$$

$$\begin{aligned}(iS\partial_t - F)G^\urcorner(t,\tau) - \int_0^t d\bar{t}\, \Sigma^R(t-\bar{t})G^\urcorner(\bar{t},\tau) &= Q^\urcorner(t,\tau)\,, \quad \text{b.c. } G^\urcorner(0,\tau) = iG^M(-\tau)\,, \\ &= \int_0^\beta d\bar{\tau}\, \Sigma^\urcorner(t,\bar{\tau})G^M(\bar{\tau}-\tau)\,, \end{aligned} \tag{9.11}$$

where the boundary condition in Eq. 9.10 comes from the anticommutation relation of the operators [Eq. 2.10], and the boundary condition in Eq. 9.11 comes from the continuity at $\tau = 0$. Combining the Dyson equations [Eqs. 9.10, 9.11] with the expressions for the self-energies

$$\Sigma^M = \Sigma^M[G^M]\,, \quad \Sigma^\urcorner = \Sigma^\urcorner[G^\urcorner] \tag{9.12}$$

gives the closed set of equations that can be solved first in the imaginary-time for $G^M(\tau)$ and then in real-time for $G^\urcorner(t,\tau)$.

In practice, many physical properties only depend on the retarded component of Green's function and self-energy. The Dyson equation for the retarded component can be written as

$$(iS\partial_t - F)G^R(t) - \int_0^t d\bar{t}\, \Sigma^R(t-\bar{t})G^R(\bar{t}) = 0\,, \quad \text{b.c. } [G^R(0)]S = -i\mathbb{I}\,. \tag{9.13}$$

Solving the Dyson equations [Eqs. 9.10, 9.11, 9.13] for the Green's functions in time is a non-trivial problem. In the following sections, we will introduce efficient representations of the Green's functions using polynomial expansions [200], and efficient methods for solving the Dyson equations in these representations.

9.3 Polynomial expansion and quadratures

This section introduces the basic ideas of spectral methods. The derivations closely follow Ref. [200].

The starting point of spectral methods is to approximate a continuous function by a finite sum [200]

$$f(x) \approx f_N(x) = \sum_{n=0}^{N} f_n u_n(x)\,, \tag{9.14}$$

where $\{u_n\}_{n=0}^{N}$ are the basis functions, and $\{f_n\}_{n=0}^{N}$ are the coefficients need to be determined. The basis functions employed are smooth functions, with common choices of trigonometric functions or orthogonal polynomials [200]. For our specific applications to represent the Green's functions, we choose to expand in orthogonal polynomials. Two functions f and g are said to be orthogonal with respect to a generic weight function w on (a, b) if

$$(f, g)_w = \int_a^b dx f(x)g(x)w(x) = 0\,, \tag{9.15}$$

and the continuous function norm is defined as $||f||_w = \sqrt{(f, f)_w}$.

Two widely used orthogonal polynomials are the Legendre polynomials ($P_n(x)$) and Chebyshev polynomials of the first kind ($T_n(x)$) [200]. The Legendre polynomials $P_n(x)$ obey the three-term recurrence relation

$$P_0(x) = 1, \quad P_1(x) = x\,, \tag{9.16}$$

$$(n+1)P_{n+1}(x) = (2n+1)xP_n(x) - nP_{n-1}(x)\,, \quad n \geq 1\,. \tag{9.17}$$

They are mutually orthogonal with respect to the uniform weight function $w(x) = 1$ on $[-1, 1]$

$$\int_{-1}^{1} dx P_m(x)P_n(x) = \delta_{m,n}\frac{2}{2n+1}\,. \tag{9.18}$$

The three-term recurrence relation for the Chebyshev polynomials is

$$T_0(x) = 1, \quad T_1(x) = x\,, \tag{9.19}$$

$$T_{n+1}(x) = 2xT_n(x) - T_{n-1}(x)\,, \quad n \geq 1\,. \tag{9.20}$$

They are mutually orthogonal with respect to the weight function $w(x) = \frac{1}{\sqrt{1-x^2}}$

$$\int_{-1}^{1} dx T_m(x) T_n(x) \frac{1}{\sqrt{1-x^2}} = \delta_{m,n} \frac{c_n \pi}{2}\,, \quad \text{with } c_0 = 2\,,\ \text{and } c_n = 1\,, \text{ for } n \geq 1\,. \tag{9.21}$$

In the derivations below, we denote an orthogonal polynomial of degree n by

$$l_n(x) = k_n x^n + \ldots k_1 x + k_0\,, \quad k_n \neq 0\,,\ \{k_i\} \in \mathbb{R}\,, \tag{9.22}$$

and the set of all polynomials of degree $\leq n$ is denoted by

$$L_n = \text{span}\{1, x, \ldots x^n\} = \text{span}\{l_0, l_1, \ldots l_n\}\,. \tag{9.23}$$

One important topic related with orthogonal polynomials is their relation with Gauss-type integration formulas. The basic idea of Gauss-type quadrature is to seek the best numerical approximation of an integral by selecting optimal nodes at which the integrand is evaluated [200]. For numerical quadratures

$$\int_a^b dx f(x) w(x) = \sum_{i=0}^{N} f(x_i) w_i + E_N[f]\,, \tag{9.24}$$

where $\{x_i\}_{i=0}^N$ are the quadrature nodes (collocation points), $\{w_i\}_{i=0}^N$ the quadrature weights, and $E_N[f]$ is the quadrature error, the quadrature formula is exact if $E_N[f] = 0$.

For a given weight function $w(x)$, there are in general three types of Gauss quadrature nodes, with a unique set of quadrature weights $\{w_i\}_{i=0}^N$ such that

$$\int_a^b dx f(x) w(x) = \sum_{i=0}^{N} f(x_i) w_i\,, \quad \forall\, f \in L_{2N+\delta}\,. \tag{9.25}$$

The three types are [200]:

1. Gauss quadrature: $\delta = 1$, with $x_i \in \{l_{N+1}(x) = 0\}$.

2. Gauss-Radau quadrature: $\delta = 0$, with $x_0 = a$ the left end point, $\{x_i\}_{i=1}^N$ the set of zeros of

$$q_N(x) = \frac{l_{N+1}(x) + \alpha_N l_N(x)}{x - a}\,, \quad \alpha_N = -\frac{l_{N+1}(a)}{l_N(a)}\,. \tag{9.26}$$

3. Gauss-Lobatto quadrature: $\delta = -1$, with $x_0 = a$, $x_N = b$ the left and right end point,

$\{x_i\}_{i=1}^{N-1}$ the set of zeros of

$$z_{N-1}(x) = \frac{l_{N+1}(x) + \alpha_N l_N(x) + \beta_N l_{N-1}(x)}{(x-a)(b-x)}\,, \tag{9.27}$$

where α_N and β_N are chosen such that

$$l_{N+1}(x) + \alpha_N l_N(x) + \beta_N l_{N-1}(x) = 0\,, \quad x \in \{a, b\}\,. \tag{9.28}$$

In general, including each boundary of the integration interval decreases the exact polynomial order by one. The general definition of the weights $\{w_i\}$ and the proof of the quadrature rules can be found in Ref. [200]. Explicit forms of Legendre and Chebyshev quadrature nodes and weights are summarized in Appendix B.

The discrete inner product and norm corresponding to the quadrature nodes x_i and weights w_i are defined as

$$\langle f, g\rangle_{N,w} = \sum_{i=0}^{N} f(x_i)g(x_i)w_i\,, \quad ||f||_{N,w} = \sqrt{\langle f, f\rangle_{N,w}}\,, \tag{9.29}$$

which can be connected to the continuous integral using the exactness of Gauss type quadratures

$$\langle f, g\rangle_{N,w} = (f, g)_w\,, \quad \forall\, f \cdot g \in L_{2N+\delta}\,. \tag{9.30}$$

With the exact discrete inner product, the backward and forward discrete polynomial transforms can be written as matrix-vector multiplications

$$f(x_i) = \sum_{n=0}^{N} l_n(x_i) f_n = L_{in} f_n\,, \quad 0 \le i \le N\,, \tag{9.31a}$$

$$f_n = \frac{\langle l_n, f\rangle_{N,w}}{\langle l_n, l_n\rangle_{N,w}} = \frac{1}{W_n}\sum_{i=0}^{N} f(x_i) l_n(x_i) w_i = S_{ni} f(x_i), \quad 0 \le n \le N\,, \tag{9.31b}$$

where $W_n = ||l_n||_w^2$ for $0 \le n \le N-1$ and

$$W_N = \begin{cases} ||l_N||_w^2\,, & \text{for Gauss and Gauss-Radau,} \\ \langle l_N, l_N\rangle_{N,w}\,, & \text{for Gauss-Lobatto.} \end{cases} \tag{9.32}$$

The normalization is different for different quadratures because Eq. 9.30 is only exact up to $2N-1$ for the Gauss-Lobatto quadrature, but the integrand in the normalization is an order

$2N$ polynomial. The two transformation matrices L_{in} and S_{ni} are well-conditioned matrices. To transform between the sampling points and the expansion coefficients, Eq. 9.31 provides stable transformations with computational complexity $\mathcal{O}(N^2)$. For Chebyshev polynomials, the scaling of the transformation can be improved to $\mathcal{O}(N\log(N))$ using the fast cosine transformation [257] since the quadrature nodes are known analytically as cosines. The scaling of transformations with Legendre polynomials can be improved by changing the problem to transformations with Chebyshev polynomials using the fast transform between Legendre and Chebyshev coefficients that scales as $\mathcal{O}(N(\log N)^2/\log\log N)$ [258].

9.4 Representation of Green's functions

Solving the Dyson equations [Eqs. 9.10, 9.11, 9.13] numerically requires a finite discretization of both the imaginary- and real-time axis. For continuous functions, finite orthogonal polynomial expansions converge super-geometrically [259], and stable high-order integro-differential solvers can be readily formulated for this class of expansions [200, 260]. This section summarizes the representations of Green's functions based on polynomial expansions.

9.4.1 Imaginary-time polynomial expansion

Using orthogonal polynomials, a function with one imaginary-time argument $f(\tau)$ (such as $G^M(\tau)$ and $\Sigma^M(\tau)$) can be represented by a finite order expansion

$$f(\tau) \approx \sum_{m=0}^{N_\tau-1} f_m l_m[\psi_M(\tau)]\,, \tag{9.33}$$

where f_m are the expansion coefficients of $f(\tau)$, $l_m(x)$ is the mth orthogonal polynomial supported on $x \in [-1,1]$, and the linear function

$$\psi_M(\tau) = \frac{2\tau}{\beta} - 1 \tag{9.34}$$

maps imaginary-time $\tau \in [0,\beta]$ to $\psi_M(\tau) \in [-1,1]$.

Detailed descriptions of representing imaginary-time functions with Legendre and Chebyshev polynomials can be found in Refs. [201, 261]. The sampling points needed for representing $G^M(\tau)$ with orthogonal polynomials scales as $\sqrt{\beta}$ [262]. The discussion of other more efficient representations optimized specifically to capture the exponential decay around 0 and β for $G^M(\tau)$, which give a $\log(\beta)$ scaling, such as the intermediate representation (IR)

[262, 263] and the discrete Lehmann representation (DLR) [264] is beyond the scope of this thesis and can be found in the references.

9.4.2 Real-time panel expansion

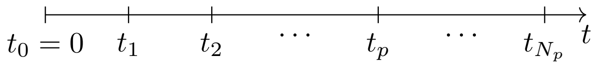

Figure 9.2: Real-time panel representation. Figure from Ref. [242].

To represent a function $f(t)$ with one real-time argument, we construct equidistant points on the real-time axis $t_p = \Delta t \cdot p$ with $p = 0, 1, \ldots, N_p$. The real-time panels are defined as the sub-intervals

$$\mathcal{T}_p \equiv [t_p, t_{p+1}] = [p\Delta t, (p+1)\Delta t] \,, \quad p \in 0, 1, ..., N_p - 1 \,. \tag{9.35}$$

For a time point $t \in \mathcal{T}_p$, the real-time dependent function $f(t)$ can be represented by a discretized function using finite order orthogonal polynomials on panel p

$$t \in \mathcal{T}_p \,, \quad f(t) \approx f_p(t) = \sum_{n}^{N_t - 1} f_{p,n} l_n[\psi_p(t)] \,, \tag{9.36}$$

where the linear function

$$\psi_p(t) = 2\left(\frac{t}{\Delta t} - p\right) - 1 \tag{9.37}$$

maps times $t \in \mathcal{T}_p$ back to the interval $\psi_p(t) \in [-1, 1]$. The function $f(t)$ for all t can be expressed as the direct sum of the panel expansions $f_p(t)$

$$f(t) \approx \sum_{p=0}^{N_p - 1} f_p(t) = \sum_{p=0}^{N_p - 1} \left[\sum_{n=0}^{N_t - 1} f_{p,n} l_n[\psi_p(t)] \right] \,, \tag{9.38}$$

by defining $l_n(x) = 0$ for $x \notin [-1, 1]$.

9.4.3 Imaginary- and real-time product basis

For a function $f(t, \tau)$ with both imaginary- and real-time arguments (such as the mixed Green's function $G^{\urcorner}(t, \tau)$), we combine the Legendre expansion in imaginary-time τ and the Legendre panel based expansion in real-time t by forming a direct product basis of Eqs. 9.33

and 9.38. The resulting discretization of $f(t,\tau)$ takes the form

$$f(t,\tau) \approx \sum_{p=0}^{N_p-1} f_p(t,\tau) = \sum_{p=0}^{N_p-1} \left[\sum_{n=0}^{N_t-1} \sum_{m=0}^{N_\tau-1} f_{p,nm} P_n[\psi_p(t)] P_m[\psi_M(\tau)] \right] , \tag{9.39}$$

where $f_{p,nm}$ is a rank-3 tensor of Legendre polynomial coefficients, N_τ and N_t are the polynomial expansion order on the imaginary- and real-time axis.

9.4.4 Transformation with quadratures

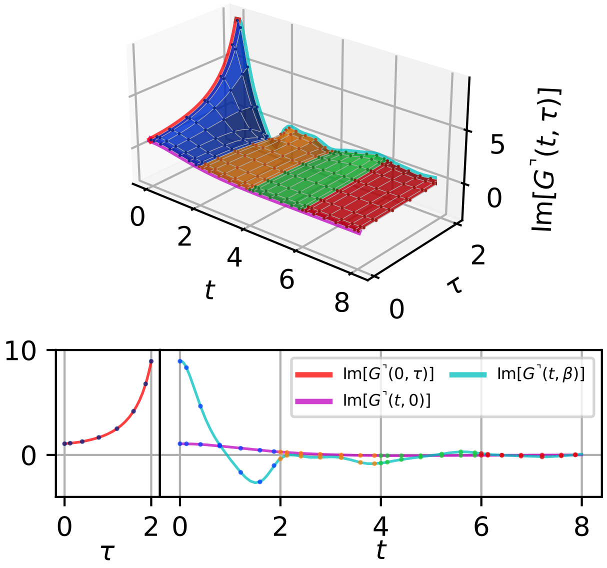

Figure 9.3: Real- and imaginary-time panel representation of the mixed Green's function $G^\rceil(t,\tau)$ for a H_2 dimer at $\beta = 2\,\mathrm{Ha}^{-1}$ and hydrogen distance $r = 0.5$ Å. Upper panel: Product representation using four panels (blue, yellow, green, and red surfaces). Each panel has a product basis with eight order polynomials both in time t and imaginary-time τ, $N_t = 8$, $N_\tau = 8$. The corresponding collocation nodes are also shown (dark circle markers). Lower left panel: Initial imaginary-time solution at $t = 0$, where $\mathrm{Im}[G^\rceil(0,\tau)] = -G^M(\beta-\tau)$ in terms of its polynomial expansion (red) and collocation nodes (dark blue). Lower right panel: Time evolution of $G^\rceil(t,\tau)$ at $\tau = 0$ and β (cyan and magenta lines respectively) related to the lesser and greater Green's functions, see Eq. 9.8. Figure from Ref. [242].

The stable transformations between the real- and imaginary-time space and the expansion coefficients can be obtained by sampling the functions on collocation points (quadrature nodes) and using the transformations in Eq. 9.31. The real- and imaginary-time collocation points $t_{p,i}$ and τ_j, are given by the inverse of the linear maps in Eqs. 9.34 and 9.37

$$t_{p,i} = \psi_p^{-1}(x_i)\,, \quad \tau_j = \psi_M^{-1}(x_j)\,. \tag{9.40}$$

The explicit transformations take the form

$$f(t_{p,i}) = \sum_{n=0}^{N_t-1} f_{p,n} l_n[\psi_p(t_i)] = \sum_{n=0}^{N_t-1} L_{in} f_{p,n}\,, \tag{9.41a}$$

$$f_{p,n} = \frac{1}{W_n} \sum_{i=0}^{N_t-1} f(t_{p,i}) l_n[\psi_p(t_i)] w_i = \sum_{i=0}^{N_t-1} S_{ni} f(t_{p,i})\,, \tag{9.41b}$$

$$f(\tau_j) = \sum_{m=0}^{N_\tau-1} f_m l_m[\psi_M(\tau_j)] = \sum_{m=0}^{N_\tau-1} L_{im} f_m\,, \tag{9.42a}$$

$$f_m = \frac{1}{W_m} \sum_{i=0}^{N_\tau-1} f(\tau_j) l_m[\psi_M(\tau_j)] w_i = \sum_{i=0}^{N_\tau-1} S_{mj} f(\tau_j)\,. \tag{9.42b}$$

The transformation of the product basis is the direct product of the two transformations, which can be written as

$$f(t_{p,i}, \tau_j) = \sum_{n=0}^{N_t-1} \sum_{m=0}^{N_\tau-1} L_{in} L_{jm} f_{p,nm}\,, \tag{9.43a}$$

$$f_{p,nm} = \sum_{i=0}^{N_t-1} \sum_{j=0}^{N_\tau-1} S_{ni} S_{mj} f(t_{p,i}, \tau_j)\,. \tag{9.43b}$$

Fig. 9.3 gives an example of using collocation points as sampling points in imaginary- and real-time product basis.

For an entire function $f(t,\tau)$ on real- and imaginary-time axis, the polynomial coefficients decay supergeometrically with n and m, i.e. the polynomial coefficients decay faster than exponentially [259] with respect to N_t and N_τ.

9.4.5 Matsubara frequency representation

With the polynomial expansion of the an imaginary-time function [Eq. 9.33], the expansion of the corresponding Matsubara function can be computed from the Fourier transform directly [265]

$$f(i\omega_n) = \int_0^\beta d\tau f(\tau) e^{i\omega_n \tau} \approx \sum_{m=0}^{N-1} f_m \hat{l}_m[i\omega_n]\,, \tag{9.44}$$

$$\hat{l}_m[i\omega_n] = \int_0^\beta d\tau l_m[\psi_M(\tau)] e^{i\omega_n \tau}\,, \tag{9.45}$$

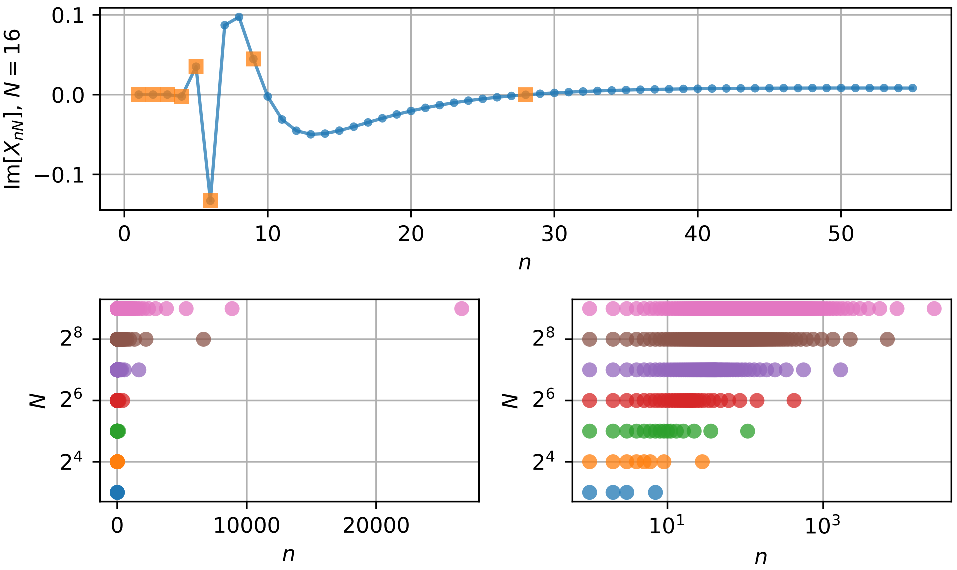

Figure 9.4: Sparse-sampling Matsubara frequency grids based on Legendre polynomials of order N. Upper panel: Matsubara frequency transform of the Legendre polynomial $P_N(x)$ for $N = 16$ (blue dots) and the sparse-sampling frequencies (orange squares). The selected Matsubara frequency indices n are shown for different orders N on a linear (middle panel) and logarithmic grid (lower panel). Figure from Ref. [242].

where $\omega_n = \frac{(2n+\zeta)\pi}{\beta}$, $\zeta = 1$ for fermions and $\zeta = 0$ for bosons.

The choice of Matsubara sampling points follow the same idea of Gauss quadrature, by finding the approximated zeros of the next basis function of the Matsubara expansion $\hat{l}_N(i\omega_n)$. The derivations for the Fourier transform of Chebyshev polynomials can be found in Ref. [201], and the Fourier transform of the Legendre polynomials can be expressed in terms of Bessel functions of the first kind [266]

$$\mathcal{F}\{P_m\} = \int_{-1}^{1} dx e^{-i\omega x} P_m(x) = 2(-i)^m j_m(\omega)\,, \tag{9.46}$$

$$\mathcal{F}^{-1}\{P_m\} = \int_{-1}^{1} dx e^{i\omega x} P_m(x) = 2i^m j_m(\omega)\,, \tag{9.47}$$

where $j_m(z)$ is the mth spherical Bessel function.

The transformation between the expansion coefficients and the Matsubara frequency for Chebyshev polynomials can be found in Ref. [265]. The transformation matrix for Legendre polynomials can be derived directly from the Fourier transform [Eqs. 9.46, 9.47]

$$f(i\omega_n) = \int_0^\beta d\tau e^{i\omega_n\tau} f(\tau) = \int_0^\beta d\tau e^{i\omega_n\tau} \sum_{m=0}^{N-1} f_m P_m[\psi_M(\tau_i)]$$
$$= \sum_{m=0}^{N-1} f_m \int_0^\beta d\tau e^{i\omega_n\tau} P_m[\psi_M(\tau_i)] = \sum_{m=0}^{N-1} X_{nm} f_m \,, \tag{9.48}$$

$$X_{nm} = \int_0^\beta d\tau e^{i\omega_n\tau} P_m[\psi_M(\tau)] = \frac{\beta}{2}\int_{-1}^{1} dx e^{i\omega_n\frac{\beta}{2}(x+1)} P_m[\psi_M(\tau)]$$
$$= \frac{\beta}{2} e^{i\frac{\beta}{2}\omega_n} \int_{-1}^{1} dx e^{i\omega_n\frac{\beta}{2}x} P_m[\psi_M(\tau)] = \frac{\beta}{2} e^{i\frac{\beta}{2}\omega_n} 2 i^m j_m\left(\frac{\beta}{2}\omega_n\right) . \tag{9.49}$$

With $\omega_n = \frac{(2n+\zeta)\pi}{\beta}$, the exponential term $e^{i\frac{\beta}{2}\omega_n} = e^{in\pi} \times e^{i\zeta\frac{\pi}{2}} = i^\zeta(-1)^n$. The transformation matrix can be written as

$$X_{nm} = \beta(-1)^n (i)^{m+\zeta} j_m\left(\frac{\beta}{2}\omega_n\right)$$
$$= \beta(-1)^n (i)^{m+\zeta} j_m\left(\frac{(2n+\zeta)\pi}{2}\right) , \tag{9.50}$$

and the inverse transform can be carried out using the inverse transformation matrix

$$f_m = \sum_{n=0}^{N-1} Y_{mn} f(i\omega_n) \,, \quad X_{nm} Y_{mn} = \mathbb{I} \,. \tag{9.51}$$

In practice, fermionic systems and bosonic systems lead to different choices of the expansion order N. For fermions, N is chosen to be even, $\hat{l}_N[i\omega_n]$ has N roots on the imaginary frequency axis $(-i\infty, i\infty)$. For bosons, N is chosen to be odd, $\hat{l}_N[i\omega_n]$ has $N-1$ roots on the imaginary frequency axis $(-i\infty, i\infty)$. The sampling points can be chosen as the Matsubara frequency points closest to the roots of $\hat{l}_N[i\omega_n]$ (or sign change points), and an extra sampling point $i\omega_n = 0$ is taken in the bosonic case [265]. The resulting Matsubara frequency grids select a number of equidistant Matsubara frequencies at low frequencies and only a few (non-linearly spaced) points at high-frequency, see Fig. 9.4.

9.4.6 Imaginary-time Dyson solver with sparse sampling method

With the imaginary-time and Matsubara frequency representations introduced in sections 9.4.1, 9.4.4 and 9.4.5, the transformation between $G^M(\tau)$ and $G^M(i\omega_n)$ can be done via the coefficients G^M_m

$$G^M(\tau_j) \underset{S_{mj}}{\overset{L_{jm}}{\rightleftharpoons}} G^M_m \underset{X_{nm}}{\overset{Y_{mn}}{\rightleftharpoons}} G^M(i\omega_n)\,. \tag{9.52}$$

To compute $G^M(\tau)$ from the Dyson equation, we can solve the frequency space Dyson equation [Eq. 8.3] to get $G^M(i\omega_n)$, then transform the results to the imaginary-time space via the transformation in Eq. 9.52. For a detailed description of solving the Dyson equation with sparse sampling method see Ref. [265].

9.5 Dyson solvers with Legendre spectral method

In this section, we employ the Legendre polynomial basis to solve the integro-differential form Dyson equations [Eqs. 9.10, 9.11, 9.13], since it is possible to express the Fredholm and Volterra integrals directly in Legendre coefficient space, using a recursive algorithm [266]. The derivations in this section are published in Refs. [241, 242].

9.5.1 Imaginary-time Dyson solver

With the imaginary-time expansion introduced in section 9.4.1, the imaginary-time integro-differential Dyson equation [Eq. 9.10] can be reformulated completely in the space of Legendre coefficients.

9.5.1.1 Derivative operator

The derivative operator ∂_τ acting on Legendre polynomials takes the form

$$\begin{aligned}\partial_\tau P_m[\psi_M(\tau)] &= \frac{2}{\beta}\partial_x P_m(x) = \frac{2}{\beta}\sum_{\substack{k=0,\\ k+m\,\text{odd}}}^{m-1}(2k+1)P_k(x)\\ &= \frac{2}{\beta}\sum_k \tilde{D}_{mk}P_k(x) = \sum_k D_{mk}P_k(x)\,,\end{aligned} \tag{9.53}$$

where $\tilde{D}_{mk}$ is the upper triangular matrix

$$\tilde{D}_{mk} \equiv \begin{cases} 2k+1, & 0 \le k \le m,\ k+m\ \text{odd} \\ 0, & \text{elsewhere} \end{cases}\,. \tag{9.54}$$

9.5.1.2 Imaginary-time integral

The imaginary-time convolution $[\Sigma^M * G^M]$ can be separated into two terms of Volterra type

$$\begin{aligned}[\Sigma^M * G^M](\tau) &= \int_0^\beta d\bar{\tau}\Sigma^M(\tau-\bar{\tau})G^M(\bar{\tau}) \\ &= \int_0^\tau d\bar{\tau}\Sigma^M(\tau-\bar{\tau})G^M(\bar{\tau}) + \int_\tau^\beta d\bar{\tau}\xi\Sigma^M(\beta+\tau-\bar{\tau})G^M(\bar{\tau}),\end{aligned} \tag{9.55}$$

using the periodicity property $\Sigma^M(-\tau) = \xi\Sigma^M(\beta-\tau)$, such that $\Sigma(\tau)$ is only evaluated in $[0, \beta]$, avoiding the discontinuity at $\tau = 0$.

With Legendre-Gauss type collocation points, the convolution integrals in Eq. 9.55 can be computed using reinterpolated quadrature, which scales cubically with the number of sampling points ($\sim \mathcal{O}(N_\tau^3)$) [200]. In Legendre coefficient space, the convolution operator $[\Sigma^M *]$ can be written as a sum of two matrices $B^{\lessgtr}_{mk}$ representing the two Volterra terms in Eq. 9.55

$$[\Sigma^M *]_{mk} \equiv \frac{\beta}{2}[B^{<}_{mk} + \xi B^{>}_{mk}], \tag{9.56}$$

where the $B^{\lessgtr}_{mk}$ matrices are the convolution matrices for a function $f(x)$ defined on $[-1, 1]$. Stable recursion relations for $B^{\lessgtr}_{mk}$ have been derived by Hale and Townsend [266] using the Fourier connection between Legendre polynomials and spherical Bessel functions [Eqs. 9.46, 9.47]. This algorithm scales quadratically with the number of coefficients ($\sim \mathcal{O}(N_\tau^2)$). We will only state the result here, and provide a detailed derivation in Appendix C.

The coefficients in the $B^{\lessgtr}_{mk}$ matrices are related by the recursion relation

$$B^{\lessgtr}_{m,k+1} = -\frac{2k+1}{2m+3}B^{\lessgtr}_{m+1,k} + \frac{2k+1}{2m-1}B^{\lessgtr}_{m-1,k} + B^{\lessgtr}_{m,k-1}, \tag{9.57}$$

in which computing each column requires two previous columns to be known. The recursion relation is only stable for the lower triangular coefficients in $B^{\lessgtr}_{mk}$. The upper triangular coefficients are computed using the transpose relation

$$B^{\lessgtr}_{m,k} = (-1)^{k+m}\frac{2m+1}{2k+1}B^{\lessgtr}_{k,m}. \tag{9.58}$$

The two first columns are given by the starting relations

$$B^{\lessgtr}_{m,0} = \begin{cases} f_0 \pm \frac{f_1}{3}\,, & m = 0 \\ \pm(\frac{f_{m-1}}{2m-1} - \frac{f_{m+1}}{2m+3})\,, & m \geq 1 \end{cases}\,, \tag{9.59a}$$

$$B^{\lessgtr}_{m,1} = \begin{cases} \mp B^{\lessgtr}_{1,0}/3\,, & m = 0 \\ \mp B^{\lessgtr}_{m,0} + \frac{B^{\lessgtr}_{m-1,0}}{2m-1} - \frac{B^{\lessgtr}_{m+1,0}}{2m+3}\,, & m \geq 1 \end{cases}\,. \tag{9.59b}$$

For the convolution operator $[\Sigma^M *]_{mk}$, $f_m = \Sigma^M_m$, with Σ^M_m the Legendre coefficients of the self-energy $\Sigma^M(\tau)$ (see section 9.4.1).

9.5.1.3 Boundary condition

The boundary condition of the imaginary-time Green's function in Eq. 9.10 can be reformulated in Legendre coefficient space using $P_k(\pm 1) = (\pm 1)^k$ as

$$-\mathbb{I} = S[G^M(0) - \xi G^M(\beta)] = \sum_k S[(-1)^k - \xi] G^M_k\,. \tag{9.60}$$

9.5.1.4 Linear system

With the derivative opeartor [Eq. 9.53] and the convolution operator [Eq. 9.56], the imaginary-time Dyson equation [Eq. 9.10] can be written entirely in the Legendre coefficient space as

$$\sum_{k=0}^{N_\tau - 1} (-S D_{mk} - F\delta_{m,k} - [\Sigma^M *]_{mk}) G^M_k = \mathbf{0}_m\,. \tag{9.61}$$

The boundary condition [Eq. 9.60] is enforced by setting the last row of the matrices on the left hand side and the right hand side of Eq. 9.61 to satisfy the relation given by Eq. 9.60.

9.5.2 Real-time Dyson solver

With the real-time panel expansion and imaginary- and real-time product basis introduced in sections 9.4.2 and 9.4.3, the integro-differential equation for the mixed and retarded Green's functions [Eqs. 9.11, 9.13] can be reformulated completely in the space of Legendre coefficients. We will provide derivation for the Dyson equation that gives $G^{\urcorner}(t,\tau)$ [Eq. 9.11] in detail. The equations used to solve for $G^R(t)$ [Eq. 9.13] can be derived in a similar way.

9.5.2.1 Derivative operator

The action of the partial derivative ∂_t on the real-time Legendre polynomial basis functions $P_n(\psi_p(t))$ of panel p is given by

$$\partial_t P_n[\psi_p(t)] = \frac{2}{\Delta t}\partial_x P_n(x) = \frac{2}{\Delta t}\sum_{n'} \tilde{D}_{nn'} P_{n'}(x) = \sum_{n'} D_{nn'} P_{n'}(x)\,, \tag{9.62}$$

where $\tilde{D}_{nn'}$ is the upper triangular matrix defined in Eq. 9.54.

9.5.2.2 Real-time history integral

Using the real-time panel notations in section 9.4.2, the history integral $I(t,\tau)$ in the Dyson equation for $G^{\rceil}(t,\tau)$ [Eq. 9.11] can be written as a sum of functions $I_p(t,\tau)$ supported on panel p

$$I(t,\tau) = \int_0^t d\bar{t}\,\Sigma^R(t-\bar{t})G^{\rceil}(\bar{t},\tau) = \sum_{p=0}^{N_p-1} I_p(t,\tau)\,, \quad I_p(t,\tau) \equiv 0\,, \forall\, t \notin \mathcal{T}_p\,. \tag{9.63}$$

Each function $I_p(t,\tau)$ can be written as a sum of integrals over the panel components of the mixed Green's function $G^{\rceil}_p(t,\tau)$ defined in Eq. 9.39

$$I_p(t,\tau) = \sum_{k=0}^{p} \int_0^t d\bar{t}\,\Sigma^R(t-\bar{t})G^{\rceil}_k(\bar{t},\tau)\,, \quad G^{\rceil}_k(\bar{t},\tau) \equiv 0\,, \forall\, \bar{t} \notin \mathcal{T}_k\,. \tag{9.64}$$

The finite support in t and $\bar{t}$ also restricts the integration argument of $\Sigma^R(t-\bar{t})$ in each term of Eq. 9.64. With $t \in \mathcal{T}_n$ and $\bar{t} \in \mathcal{T}_k$, the argument $t - \bar{t}$ lies on the interval

$$\begin{aligned} t - \bar{t} \in [\min \mathcal{T}_p - \max \mathcal{T}_k, \max \mathcal{T}_p - \min \mathcal{T}_k] &= [t_p - t_{k+1}, t_{p+1} - t_k] \\ &= [t_{p-k-1}, t_{p-k+1}] \\ &= \mathcal{T}_{p-k-1} \bigcup \mathcal{T}_{p-k}\,. \end{aligned} \tag{9.65}$$

The constraints of time arguments leaves only two panels of $\Sigma^R(t-\bar{t})$ contributing in Eq. 9.64. For $t \in \mathcal{T}_p$

$$\begin{aligned} \int_0^t d\bar{t}\,\Sigma^R(t-\bar{t})G^{\rceil}_k(\bar{t},\tau) &= \int_0^t d\bar{t}\,\Sigma^R_{p-k-1}(t-\bar{t})G^{\rceil}_k(\bar{t},\tau) + \int_0^t d\bar{t}\,\Sigma^R_{p-k}(t-\bar{t})G^{\rceil}_k(\bar{t},\tau) \\ &= \Sigma^R_{p-k-1} \overset{>}{*} G^{\rceil}_k + \Sigma^R_{p-k} \overset{<}{*} G^{\rceil}_k\,. \end{aligned} \tag{9.66}$$

Using the short-hand notation introduced in the last step of Eq. 9.66, the history integral $I_p(t, \tau)$ [Eq. 9.64] can be written as

$$I_p(t, \tau) = \mathcal{I}_p(t, \tau) + \Sigma_p^R \overset{<}{*} G_0^{\rceil} + \Sigma_0^R \overset{<}{*} G_p^{\rceil} , \tag{9.67}$$

where the integrals depend on Σ_p^R and $G_p^{\rceil}$ have been separated from the integrals over earlier panels

$$\mathcal{I}_p(t, \tau) \equiv \sum_{k=0}^{p-1} \left(\Sigma_{p-1-k}^R \overset{>}{*} G_k^{\rceil} \right) + \sum_{k=1}^{p-1} \left(\Sigma_{p-k}^R \overset{<}{*} G_k^{\rceil} \right) . \tag{9.68}$$

The two panel integrals in Eq. 9.66 can be computed in Legendre coefficient space directly. In both cases, the integral bounds are determined by the support of the Σ^R and $G^{\rceil}$ panel components

$$\begin{aligned} \Sigma_{p-k-1}^R \overset{>}{*} G_k^{\rceil} &\equiv \int_0^t d\bar{t}\, \Sigma_{p-k-1}^R(t - \bar{t}) G_k^{\rceil}(\bar{t}, \tau) \\ &= \int_{\max(t_k, t - t_{p-k})}^{\min(t_{k+1}, t - t_{p-k-1})} d\bar{t}\, \Sigma_{p-k-1}^R(t - \bar{t}) G_k^{\rceil}(\bar{t}, \tau) \\ &= \int_{t - t_{p-k}}^{t_{k+1}} d\bar{t}\, \Sigma_{p-k-1}^R(t - \bar{t}) G_k^{\rceil}(\bar{t}, \tau) , \end{aligned} \tag{9.69}$$

and analogously

$$\begin{aligned} \Sigma_{p-k}^R \overset{<}{*} G_k^{\rceil} &\equiv \int_0^t d\bar{t}\, \Sigma_{p-k}^R(t - \bar{t}) G_k^{\rceil}(\bar{t}, \tau) \\ &= \int_{t_k}^{t - t_{p-k}} d\bar{t}\, \Sigma_{p-k}^R(t - \bar{t}) G_k^{\rceil}(\bar{t}, \tau) . \end{aligned} \tag{9.70}$$

The convolution operators corresponding to the two integrals are given by

$$[\Sigma_q^R \overset{\lessgtr}{*}] = \frac{\Delta t}{2} B^{\lessgtr}[\Sigma_q^R] , \tag{9.71}$$

where the $B^{\lessgtr}$ matrices are given by exactly the same recursion relation as in Eqs. 9.57, 9.58, 9.59, with f_n in the initial conditions being the real-time panel Legendre coefficients of the retarded self-energy on panel q, $f_n = \Sigma_{q,n}^R$.

The product basis Legendre coefficients $I_{p,nm}$ [Eq. 9.39] of the history integral $I_p(t, \tau)$ can be calculated using matrix products in Legendre coefficient space according to

$$I_{p,nm} = \mathcal{I}_{p,nm} + \sum_{n'=0}^{N_t - 1} [\Sigma_p^R \overset{<}{*}]_{nn'} G_{0,n'm}^{\rceil} + \sum_{n'=0}^{N_t - 1} [\Sigma_0^R \overset{<}{*}]_{nn'} G_{p,n'm}^{\rceil} , \tag{9.72}$$

where $G^{\rceil}_{p,nm}$ are the real-time panel Legendre coefficients of $G^{\rceil}$ on panel p, and $\mathcal{I}_{p,nm}$ are the product basis Legendre coefficients of $\mathcal{I}_p(t,\tau)$ given by

$$\mathcal{I}_{p,nm} = \sum_{k=0}^{p-1} \sum_{n'=0}^{N_t-1} [\Sigma^R_{p-1-k} \overset{>}{*}]_{nn'} G^{\rceil}_{k,n'm} + \sum_{k=1}^{p-1} \sum_{n'=0}^{N_t-1} [\Sigma^R_{p-k} \overset{<}{*}]_{nn'} G^{\rceil}_{k,n'm} \,. \tag{9.73}$$

9.5.2.3 Real-time panel right hand side

The right hand side $Q^{\rceil}(t,\tau)$ in Eq. (9.11) can also be expressed as a sum of panel restricted functions

$$Q^{\rceil}(t,\tau) = \sum_{p=0}^{N_p-1} Q^{\rceil}_p(t,\tau) \,, \quad Q^{\rceil}_p(t,\tau) \equiv 0 \,, \forall t \notin \mathcal{T}_p \,, \tag{9.74}$$

where $Q^{\rceil}_p(t,\tau)$ is given by

$$Q^{\rceil}_p(t,\tau) = \int_0^\beta d\bar{\tau} \, \Sigma^{\rceil}_p(t,\bar{\tau}) G^M(\bar{\tau} - \tau) \,. \tag{9.75}$$

This class of integrals can be computed in Legendre coefficient space using similar algorithm as in Eq. 9.55, which pertains to the imaginary-time convolution integral

$$[A*]B \equiv \int_0^\beta d\bar{\tau} A(\tau - \bar{\tau}) B(\bar{\tau}) \,. \tag{9.76}$$

Comparing with the imaginary-time integral for the right-hand side term $Q^{\rceil}_p(t,\tau)$ in Eq. 9.75 we have

$$A(\tau) \equiv G^M(-\tau) \,, \quad B(\tau) \equiv \Sigma^{\rceil}_p(t,\tau) \,. \tag{9.77}$$

The fermionic antiperiodicity $G^M(-\tau) = -G^M(\beta - \tau)$ in combination with the Legendre expansion of $G^M(\tau)$ in Eq. 9.33 gives

$$\begin{aligned} A(\tau) &= -\sum_m G^M_m P_m[\psi_M(\beta - \tau)] \\ &= \sum_m (-1)^{m+1} G^M_m P_m[\psi_M(\tau)] \\ &= \sum_m A_m P_m[\psi_M(\tau)] \,, \end{aligned} \tag{9.78}$$

where we have used $\psi_M(\beta - \tau) = -\psi_M(\tau)$ (see Eq. 9.34), and $P_m(-x) = (-1)^m P_m(x)$. The panel Legendre expansion of $Q^\rceil_p(t, \tau)$ can be expressed as

$$Q^\rceil_{p,nm} = \sum_{m'} [\tilde{G}^M *]_{mm'} \Sigma^\rceil_{p,nm'} \, , \tag{9.79}$$

where the operator $[\tilde{G}^M *]$ is given by

$$[\tilde{G}^M *] = \frac{\beta}{2} \left(B^<[\tilde{G}^M] - B^>[\tilde{G}^M] \right) \, . \tag{9.80}$$

The $B^{\lessgtr}$ matrices are given by Eqs. 9.57, 9.58 and 9.59 with the modified Legendre coefficients $f_m = \tilde{G}^M_m = (-1)^{m+1} G^M_m$.

9.5.2.4 Boundary condition

The boundary condition of the integro-differential equation [Eq. 9.11] at each panel p is given by the initial boundary condition and the continuity of $G^\rceil(t, \tau)$ between panels

$$G^\rceil(0, \tau) = i\xi G^M(\beta - \tau) \, , \quad \text{for } p = 0 \, , \tag{9.81a}$$

$$G^\rceil_p(t_p, \tau) = G^\rceil_{p-1}(t_p, \tau) \, , \quad \text{for } p > 0 \, . \tag{9.81b}$$

which can be reformulated in Legendre coefficient space using $P_n(\pm 1) = (\pm 1)^n$

$$\sum_n (-1)^n G^\rceil_{p,nm} = i\xi (-1)^m G^M_m \, , \quad \text{for } p = 0 \, , \tag{9.82a}$$

$$\sum_n (-1)^n G^\rceil_{p,nm} = \sum_n G^\rceil_{p-1,nm} \, , \quad \text{for } p > 0 \, . \tag{9.82b}$$

9.5.2.5 Linear system

Using the panel expression for both the history integral $I(t, \tau)$ in Eq. 9.63 and Eq. 9.67, and the right-hand side $Q^\rceil(t, \tau)$ in Eq. 9.74, the real-time panel Dyson equation for $G^\rceil_p(t, \tau)$ becomes

$$(iS\partial_t - F - \Sigma^R_0 \overset{<}{*}) G^\rceil_p(t, \tau) = Q^\rceil_p(t, \tau) + \mathcal{I}_p(t, \tau) + [\Sigma^R_p \overset{<}{*} G^\rceil_0](t, \tau) \, . \tag{9.83}$$

With the derivative operator [Eq. 9.62], the history integral [Eq. 9.72], and right-hand side [Eq. 9.79], the Dyson equation for the mixed Green's function at each panel p [Eq. 9.83] can

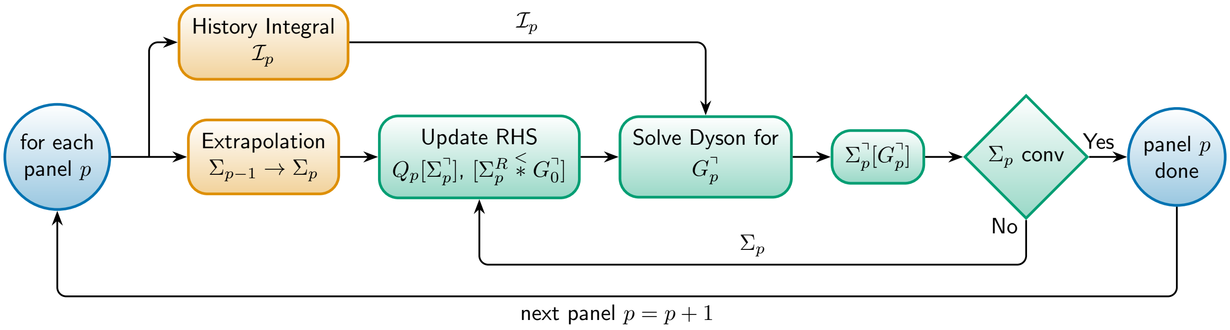

Figure 9.5: Schematic real-time panel propagation of $G_p^\rceil$ with self-energy self consistency imposed per panel. The history integral and extrapolation (orange boxes) is performed once per panel, while the Dyson equation and self-energy (green boxes) are iterated to self consistency in Σ_p.

be written entirely in the Legendre coefficient space

$$\sum_{n'} \left(iSD_{nn'} - F\delta_{n,n'} - [\Sigma_0^{R} \overset{<}{*}]_{nn'} \right) G^\rceil_{p,n'm} = Q^\rceil_{p,nm} + \mathcal{I}_{p,nm} + [\Sigma_p^R \overset{<}{*} G_0^\rceil]_{p,nm} \,. \tag{9.84}$$

The boundary condition [Eq. 9.82] is enforced by setting the last row of the matrices on the left hand side and the right hand side of Eq. 9.84 to satisfy the relations in Eq. 9.82 depending on the panels.

9.5.2.6 Time propagation

In this section we summarize the algorithm for time propagation of the equilibrium real-time problem formulated in section 9.2. The goal is to determine the mixed Green's function $G^\rceil(t, \tau)$ by self-consistently solving the real-time Dyson equation Eq. 9.11 in combination with the self-energy relation $\Sigma^\rceil = \Sigma^\rceil[G^\rceil]$ of Eq. 9.12.

The real-time panel subdivision of section 9.4.2 gives a real-time Dyson equation [Eq. 9.83] that can be solved successively for each panel p, and its reformulation in Legendre coefficient space [Eq. 9.84] produces a linear system equation for $G^\rceil$. The required calculation steps for the time propagation on panel p are shown in Fig. 9.5.

For each panel p, the history integral $\mathcal{I}_p$ given by Eq. 9.73 is only computed once, since it depends on the Green's function $G_q^\rceil$ and self-energy $\Sigma_q^\rceil$ on earlier panels $q < p$. For $p > 0$, an initial guess for the panel self-energy Σ_p is obtained by extrapolation of Σ_{p-1} using linear prediction [267], inorder to reduce the number of the self-energy self-consistent steps. To emphasize that these two steps are only performed once per panel they are shown as orange boxes in Fig. 9.5.

The Dyson equation and self-energy self-consistency is performed by the steps represented as green boxes in Fig. 9.5. First, given the self-energy Σ_p on the current panel p, the right-hand side terms in the Dyson eqation [Eq. 9.84], $Q_p[\Sigma^\rceil]$ and $[\Sigma^R_p \overset{<}{*} G^\rceil_0]$ are constructed. Then the panel Dyson equation [Eq. 9.84] is solved for the panel Green's function $G^\rceil_p$, which in turn is used to compute the self-energy Σ_p using Eq. 9.12. If the induced change in the self-energy Σ_p is above a given threshold another self-energy self-consistent iteration is performed. For the systems considered here, the relative change in the self-energy per iteration reaches machine precision in less than ten self-consistent iterations. Once the self-energy is converged, the calculation for panel p is complete and the time propagation proceeds to the next panel $p + 1$.

For long time simulations we observe spectral aliasing in the Legendre coefficients in imaginary time of $G^\rceil(t, \tau)$ (not shown). This phenomenon is well understood [259, 268] and is resolved by using spectral-blocking in terms of Orzag's two-thirds rule [259]. In other words, the self-energy $\Sigma^\rceil(t, \tau)$ is evaluated on a denser collocation grid in imaginary time and only 2/3 of the resulting Legendre coefficients are used in the solution of the Dyson equation. This prevents the spectral aliasing and gives stable time-panel stepping.

9.5.3 Convergence and scaling

9.5.3.1 Imaginary-time Dyson solver

The overview of different imaginary-time Dyson solvers can be found in Table I in Ref. [241]. For simulations of realistic systems with large energy scales at low temperature, sparse sampling method [265] with IR [262, 263] or DLR [264] basis is the most efficient method. The imaginary-time Legendre spectral Dyson solver introduced in this chapter, in which the linear system [Eq. 9.61] can be solved using GMRES [269] with a Matsubara frequency sparse sampling preconditioner, gives a slightly better accuracy but is less efficient in practice.

9.5.3.2 Real-time Dyson solver

To benchmark the convergence properties of the Legendre-panel based Dyson solver, we use an analytically solvable two level system with energies ϵ_1 and ϵ_2 and hybridization V, giving the matrix valued quadratic Hamiltonian

$$h = \begin{bmatrix} \epsilon_1 & V \\ V & \epsilon_2 \end{bmatrix} . \tag{9.85}$$

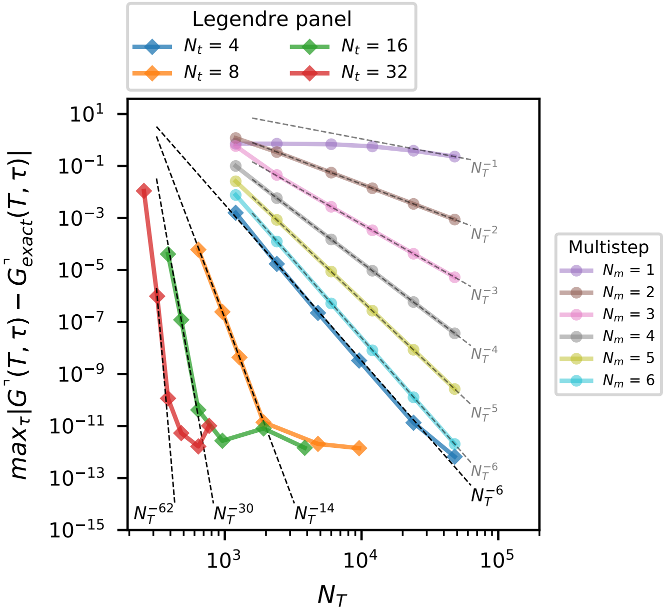

Figure 9.6: Error convergence of the equilibrium real-time Green's function $G^\rceil_{11}(t,\tau)$ for a two-level system at final time T, as a function of time discretization points N_T. The real-time panel Dyson solver result for the panel expansion orders $N_t = 4$, 8, 16 and 32 (diamonds), and the results of the equidistant multistep method of Ref. [250] up to maximal order $N_m = 6$ (circles) are shown together with asymptotic convergence rates (dotted lines). Figure from Ref. [242].

The matrix-valued contour Green's function G_{ij} for this non-interacing system is given by

$$(i\mathbf{1}\partial_z - h)G = \delta_\mathcal{C}\,, \tag{9.86}$$

and is analytically solvable by diagonalization. The G_{11} component of the Green's function also obeys the scalar Dyson equation of motion

$$(i\partial_z - \epsilon_1)G_{11} - \int_\mathcal{C} d\bar{z}\Sigma(z,\bar{z})G_{11}(\bar{z},z) = \delta_\mathcal{C}\,, \tag{9.87}$$

with the self-energy Σ given by $\Sigma = Vg_2V$ with g_2 the solution of $(i\partial_z - \epsilon_2)g_2 = \delta_\mathcal{C}$. To derive Eq. 9.87 from Eq. 9.86, the inversion formulas for two-by-two block matrices can be used. Another way of thinking this problem is treating site 2 as the bath site of site 1, the self-energy of site 1 is then given by the hybridization function introduced in section 4.2.

To benchmark our real-time panel Dyson equation solver we solve Eq. 9.87 for $G^\rceil(t,\tau)$ in the equilibrium case $\epsilon_1 = -1$, $\epsilon_2 = 5$, $V = 6$ at inverse temperature $\beta = 3$ and compare to the analytical solution obtained from Eq. 9.86 at the final time $T = 48$, see Fig. 9.6. We use Legendre-Gauss-Lobatto quadrature in our implementation. To be able to compare the results for the real-time panel expansion orders $N_t = 4$, 8, 16, and 32 we study the error as a function of total number N_T of time discretization points used, given by $N_T = N_p \cdot N_t$ where N_p is the number of real-time panels. For all N_t we observe the asymptotic convergence rate

$$\max_{\tau} |G^{\rceil}(T, \tau) - G^{\rceil}_{\text{exact}}(T, \tau)| \sim \mathcal{O}(N_T^{-2(N_t - 1)}) \, . \tag{9.88}$$

We note that there is no inherent limitation of the expansion order N_t, and a high order expansions like $N_t = 32$ gives an even higher order convergence rate $\sim \mathcal{O}(N_T^{-62})$.

We attribute the unexpected factor of two in the exponent of Eq. 9.88 to the superconvergence phenomenon [270] present in the family of Galerkin methods of our Dyson solver [Eq. 9.84]. Numerical tests show that the convergence properties remain the same for $\Sigma = 0$ where Eq. 9.84 simplifies to a series of coupled first order initial value problems. As shown in the literature [271–274], and confirmed by our numerical tests, the high order superconvergence of Eq. 9.88 is only attained at the panel boundaries, while the remaining Legendre-Gauss-Lobatto collocation points (used for the self-energy evaluation) converge as $\mathcal{O}(N_T^{-(N_t+2)})$. The observed superconvergence on the panel boundaries is beneficial since the initial value for each real-time panel [Eq. 9.81] is known to high accuracy.

To put the convergence properties of our real-time panel Dyson solver in perspective, we also solve Eq. 9.87 using the state-of-the-art multistep method for the real-time Dyson equation of Ref. [250]. The multistep method uses an equidistant real-time discretization, the Gregory quadrature, and backward differentiation. At order N_m the asymptotic convergence of the multistep method is given by $\sim \mathcal{O}(N_T^{-N_m})$. However, due to the inherent high-order instability of backward differentiation the order N_m of the multistep method is limited to $N_m \leq 6$ [250]. The convergence of the muiltistep method at all possible orders N_m applied to the two level benchmark system is also shown in Fig. 9.6.

Comparing the performance of the two methods in Fig. 9.6 explicitly shows the efficiency of high order polynomial panel expansions in real-time. At equal orders N_t and N_m the asymptotic scaling of the multistep solver $N_T^{-N_m}$ is much slower than the $N_T^{-2(N_t-1)}$ rate of the real-time panel solver. Hence, already at expansion order $N_t = 4$ the real-time panel solver (blue diamonds) has the same asymptotic error scaling $\mathcal{O}(N_T^{-6})$ as the maximum order $N_m = 6$ multistep method (cyan circles), see Fig. 9.6. In contrast to the multistep algorithm, the order N_t of the Legendre-panel solver is not limited. Going to high polynomial order gives a dramatic reduction in the total number of time discretization points N_T required to reach high accuracy. For example, reaching an accuracy of 10^{-11} using expansion order $N_t = 4$ requires $N_T \sim 10^4$ points, while using expansion order $N_t = 32$ reduces the required number of required real-time points to $N_T \sim 10^2$, i.e. by almost two orders of magnitude. Thus, for a fixed time T and accuracy the number of real-time discretization points N_T required to store the equilibrium real-time Green's function can be drastically reduced when using the high order real-time panel Dyson solver. This is an important advance since calculations in general are memory limited, in particular when using the multistep method. Using the high-order real-time panel expansion will therefore enable the study of both larger systems and longer simulation times.

	Multistep	Legendre-Panel	Eq.
Linear system	N_T	$N_T \cdot N_t^2$ [1]	9.84
History integral	N_T^2	N_T^2	9.73

Table 9.1: Asymptotic computational complexity as a function of time discretization points N_T for the multistep method of Ref. [250] and the real-time panel method at panel expansion order N_t.

[1] $N_T \cdot N_t$ with iterative linear solver.

The enhanced performance of the real-time panel expansion comes at the price of a moderate increase of computational complexity (see Tab. 9.1). The main difference between the multistep solver and the real-time panel solver is that the panel based approach requires solving Eq. (9.84) for all time points within a panel at once. This amounts to solving a per-panel linear system with a naive cubic scaling $\mathcal{O}(N_t^3)$, producing the extra prefactor N_t^2 in the computational complexity of the linear system in Tab. 9.1. Using a preconditioned iterative linear solver may reduce this by one factor of N_t and is an interesting venue for further research. Even though this step of the Dyson equation has a higher computational complexity in terms of N_T, this is not an issue when taking into account the orders of magnitude reduction of N_T enabled by the high order expansion. Furthermore, the solution of the linear system is in fact not the computational complexity bottleneck of the Dyson solver.

The main computational bottleneck of the Dyson equation is the calculation of the history integral [Eq. 9.73]. In the direct multistep method the history integral evaluation scales quadratically as $\mathcal{O}(N_T^2)$, and the real-time panel history integral in Eq. 9.73 retains the same scaling $\mathcal{O}(N_T^2) = \mathcal{O}(N_p^2 \cdot N_t^2)$ by using the recursive Legendre convolution algorithm [266]. However, in the special case of equilibrium real-time it was recently shown that the scaling of the history integral can be reduced to quasi-linear scaling [255]. The generalization of this approach to the real-time panel expansion is another promising direction for further research.

Potential computational complexity gains from the linear system and the history integral aside, the real-time panel Dyson solver algorithm presented here is already competitive for memory-limited problems. By extending the range of applicability of real-time propagation via the drastically lower number of discretization points N_T needed for a given accuracy. The same compactness property also makes the generalization of the real-time panel discretization from equilibrium real-time to non-equilibrium real-time propagation an interesting direction of further research.

9.6 Applications

As a proof of concept application of the Legendre spectral Dyson solver, we employ the solver in a quantum chemistry setting with the GF2 [230–234] method introduced in section 8.2. The calculations are using standard AO basis sets and and matrix elements from the quantum chemistry code pySCF [275, 276], which allow us to use the point group symmetry introduced in section 8.3 for optimization.

9.6.1 Dissociation energies

The highly accurate Legendre spectral Dyson solver is particularly well suited for high precision calculations. A prime example is the computation of the binding energy D_e in noble-gas dimers, where the weak bonding requires high precision calculations of total energies. The results in this subsection are published in Ref. [241].

The binding energy D_e is obtained from the minimum of the interaction energy $E_{\text{int}}(r)$ as a function of atomic separation r

$$D_e \equiv -E_{\text{int}}(r_e) \equiv -\min_r E_{\text{int}}(r) \,, \tag{9.89}$$

where r_e is the equilibrium atomic distance. The interaction energy E_{int} is in turn given by

$$E_{\text{int}}(r) \equiv E_{A_2}(r) - 2E_A(r) \,, \tag{9.90}$$

where E_{A_2} is the total energy of the dimer and E_A is the total energy of the single atom (the monomer) evaluated using the standard counterpoise correction [277]. The total energy E of the system is given by

$$E = \frac{1}{2}\text{Tr}[(h + F)P] + \text{Tr}[\Sigma * G] + E_{nn} \,, \tag{9.91}$$

where $E^{(nn)}$ is the nuclei-nuclei Coulomb energy, h is the single-particle energy, F is the Fock matrix, and P is the density matrix (see chapter 8). In the noble gases the total energies E_A and E_{A_2} are of the order of Hartrees ($\sim E_h \equiv 1\,\text{Ha}$) while the binding energy D_e is of the order of tens of micro Hartrees ($\sim 10\,\mu E_h$), hence requiring high precision calculation of the total energies.

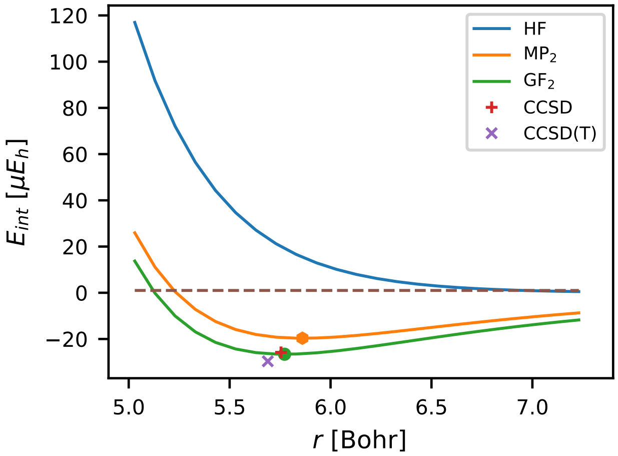

Figure 9.7: Interaction energy E_{int} as a function of atomic distance r of He$_2$ with basis aug-cc-pVQZ using HF, MP2 and GF2. The HF and MP2 results are computed with pySCF [275, 276], the GF2 results are computed using $\beta = 50\,E_h^{-1}$, $N_\tau = 192$. The CCSD and CCSD(T) results are from Ref. [278]. Figure from Ref. [241].

We use He$_2$ as a prototype system since there exist published reference results for the binding energy D_e and equilibrium distance r_e calculated with HF, second-order Møller–Plesset perturbation theory (MP2), coupled cluster singles doubles (CCSD) theory and coupled cluster singles doubles and non-iterative perturbative triples (CCSD(T)) theory [278]. The MP2 method is closely related to GF2 and uses the second order self-energy [Eq. 8.10] evaluated at the HF Green's function $G^{(\mathrm{HF})}$, $\Sigma^{(\mathrm{MP2})} \equiv \Sigma^{(\mathrm{GF2})}[G^{(\mathrm{HF})}]$. Note however that the prefactors in the total energy differ [231, 279].

Fig. 9.7 shows $E_{\mathrm{int}}(r)$ (and $-D_e$) of He$_2$ computed with HF, MP2, and GF2 in the aug-cc-pVQZ basis together with CCSD and CCSD(T) reference results on D_e [278]. The GF2 results are obtained by fitting a 4th order polynomial to 21 r-points of $E_{\mathrm{int}}(r)$ computed in a 0.1 Bohr range centered around the minimum at r_e. The GF2 results are obtained using the Legendre spectral Dyson solver while HF and MP2 are computed using pySCF [275, 276]. As seen in Fig. 9.7, He$_2$ does not bind within the HF approximation which gives a strictly positive interaction energy. Comparing to MP2, our GF2 results are a considerable improvement, using the coupled cluster CCSD and CCSD(T) as reference.

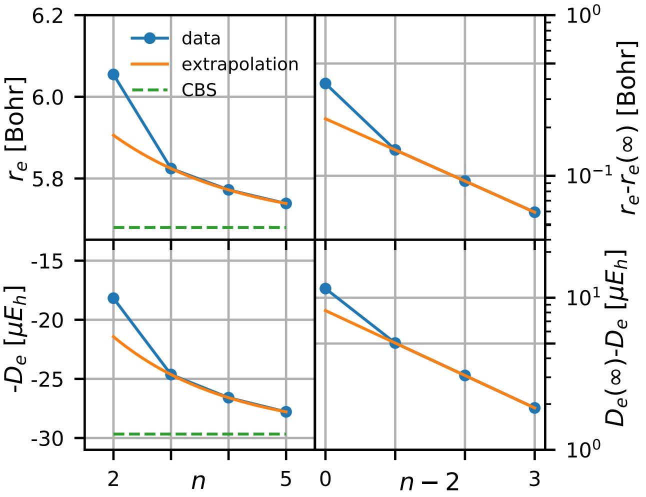

Figure 9.8: Basis extrapolation of equilibrium distance (r_e) and dissociation energy (D_e) He_2 with basis aug-cc-pVnZ with n = 2, 3, 4, 5. Left panels: raw data and fitting. Right panels: check of fitting results. Figure from Ref. [241].

9.6.1.1 Complete basis set limit

In order to extrapolate the results to the continuous basis set (CBS) limit [280, 281] we repeat the calculations using the augmented correlation consistent (aug-cc-pVnZ) basis set series with n = D, T, Q, 5 (i.e. $n = 2, 3, 4, 5$) [282–284]. This series has been shown to enable accurate extrapolation of a number of properties due to its systematic convergence in n [285–296].

D_e [μE_h]	MP2	CCSD	CCSD(T)	GF2
aug-cc-pVDZ	12.69	16.78	18.57	18.17
aug-cc-pVTZ	17.97	23.77	27.10	24.63
aug-cc-pVQZ	19.66	25.79	29.64	26.59
aug-cc-pV5Z	20.71	27.09	31.25	27.79
CBS	22.98	30.06	34.70	29.67

r_e [Bohr]	MP2	CCSD	CCSD(T)	GF2
aug-cc-pVDZ	6.1680	6.0580	6.0086	6.0547
aug-cc-pVTZ	5.9175	5.8060	5.7452	5.8244
aug-cc-pVQZ	5.8606	5.7546	5.6891	5.7722
aug-cc-pV5Z	5.8244	5.7210	5.6537	5.7388
CBS	5.769	5.672	5.607	5.680

Table 9.2: Dissociation energies D_e (top) and Equilibrium distances r_e computed by MP2, CCSD, CCSD(T), and GF2 with the basis sets aug-cc-pv$n$z, with n =D, T, Q, 5. The MP2, CCSD and CCSD(T) results are from Ref. [278].

In Tab. 9.2, we summarize the binding energy D_e and equilibrium distance r_e of He_2

computed by MP2, CCSD, CCSD(T) and GF2 using the aug-cc-pV{D,T,Q,5}Z basis sets. The aug-cc-pV{D,T,Q,5}Z GF2 energies are computed at $\beta = 50\,E_h^{-1}$ using $N_\tau = 128$, 160, 192, and 250 τ-points, respectively. The convergence in N_τ is imposed so that the absolute values of the elements in highest Legendre coefficient matrix are smaller than 10^{-10}. The zero temperature convergence (at $\beta = 50\,E_h^{-1}$) is ensured by requiring that the finite temperature MP2 total energy differ with less than 0.1 nano Hartree compared to the zero temperature MP2 total energy from pySCF.

We note that the number of τ-points N_τ used for the aug-cc-pV{D,T,Q,5}Z basis sets are of the same order as the number of atomic orbitals N_{ao}. Hence, the scaling of GF2, $\sim \mathcal{O}(N_\tau \cdot N_{ao}^5)$, is comparable to the scaling of CCSD, $\sim \mathcal{O}(N_{ao}^6)$. As seen in Tab. 9.2, the accuracy of the GF2 result for D_e is comparable to CCSD when compared to CCSD(T), while the CCSD result for r_e is closer to CCSD(T) result than GF2. This makes GF2 a considerable improvement over MP2.

With the systematic convergence of D_e and r_e as a function of basis set size n it is possible to extrapolate to the complete basis limit $n \to \infty$ [278]. We extrapolate D_e and r_e using our GF2 aug-cc-pV{T,Q,5}Z results by fitting the exponential model: $A \cdot e^{-B(n-2)} + C$, proposed in Ref. [278], where A, B, and C are parameters. The applicability of the model is checked by a logarithmic plot, see Fig. 9.8. The resulting CBS limit of our GF2 results are $D_e \approx 29.67\,\mu E_h$ and $r_e \approx 5.680\,a_0$, see also Tab. 9.2.

9.6.2 Spectral functions

As a proof-of-concept application of the equilibrium real-time Dyson equation solver, we preform real-time propagation of the mixed Green's function $G^\rceil$ for several molecules to compute their spectral functions, using GF2. The results in this subsection are published in Ref. [242].

The GF2 self-energy on the Keldysh contour is given by

$$\Sigma_{ij}^{(\mathrm{GF2})}(z, z') = \sum_{klmnpq} U_{ilnp}(2U_{kjqm} - U_{qjkm}) G_{lk}(z, z') G_{pq}(z, z') G_{mn}(z', z)\,. \tag{9.92}$$

The expressions for different components are given by the Langreth rules [256] (see Appendix A). In equilibrium real-time evolution, the mixed self-energy $\Sigma^\rceil$ is given by the direct product of three Green's functions

$$\Sigma_{ij}^\rceil(t, \tau) = \sum_{klmnpq} U_{ilnp}(2U_{kjqm} - U_{qjkm}) G_{lk}^\rceil(t, \tau) G_{pq}^\rceil(t, \tau) G_{nm}^{\rceil *}(t, \beta - \tau)\,. \tag{9.93}$$

9.6.2.1 H_2 and LiH

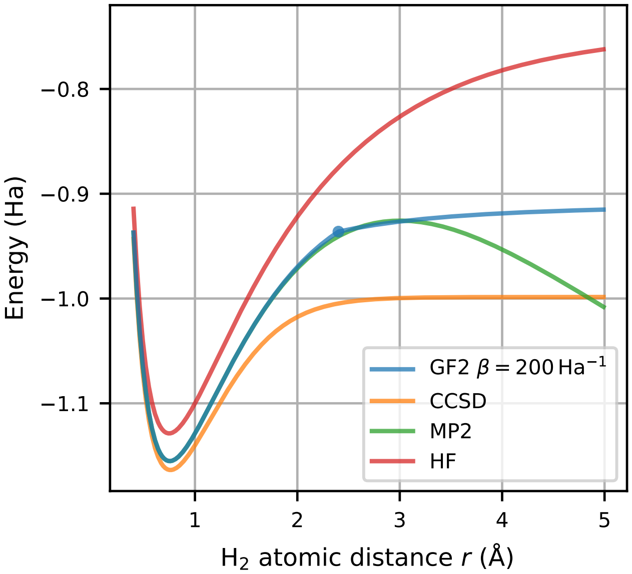

Figure 9.9: Total energy E of H_2 in the cc-pVDZ basis as a function of interatomic distance r using GF2, CCSD, MP2, and HF. Note that for H_2 with two electrons CCSD is exact. Figure from Ref. [242].

We first compute two small molecules: H_2 and LiH. Their total energies as a function of interatomic distance r in the cc-pVDZ basis and compare GF2 with HF, MP2, and CCSD are shown in Figs. 9.9 and 9.10. The total energy E is given in Eq. 9.91. Our results reproduce the well-known observation [232, 297] that the divergence of the total energy of MP2 at large r is not present in GF2, where the total energy instead levels out for large r, see Figs. 9.9 and 9.10. In the intermediate range of interatomic separation r GF2 gives two self-consistent solutions, which are adiabatically connected to the low and high r regimes. The total energy of the two solutions cross at intermediate values of r [232] and the curves in Figs. 9.9 and 9.10 show the lower energy. At the equilibrium distance r_0 the total energy $E(r)$ is minimized, and for H_2 and LiH we observe that the GF2 total energy does not improve on the MP2 result relative to the CCSD result, which is exact for H_2 with only two electrons. This is not generic, since GF2 performs significantly better than MP2 for $E(r_0)$ (relative to CCSD) in other systems like He_2 [241].

Equilibrium spectral functions

The equilibrium spectral function $A(\omega)$ are computed via equilibrium time-propagation of $G^\urcorner$ using the real-time panel algorithm (see Fig. 9.5 and section 9.5.2) using the GF2 self-energy

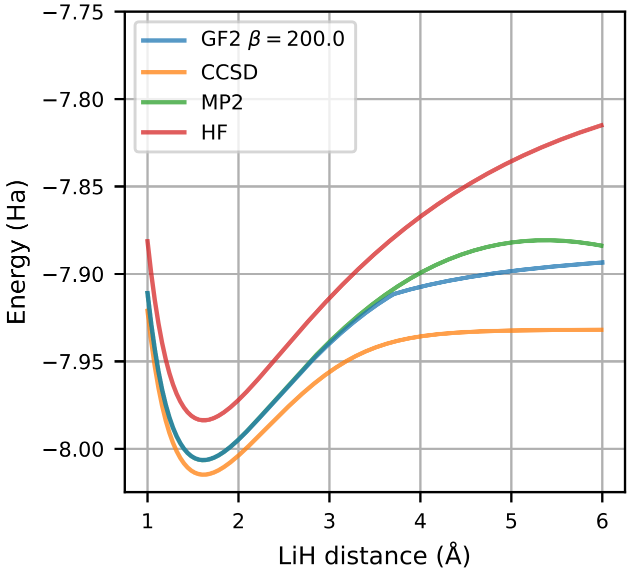

Figure 9.10: Total energy E of LiH in the cc-pVDZ basis as a function of interatomic distance r using GF2, CCSD, MP2, and HF. Figure from Ref. [242].

in Eq. 9.93, which gives the retarded Green's function G^R (see Eq. 9.9)

$$A(\omega) = -\frac{1}{\pi}\mathrm{Im}(\mathrm{Tr}[SG^R(\omega)])\,, \tag{9.94}$$

with S the overlap matrix [Eq. 2.9]. For a more detailed explanation of the relation between spectral function and Green's function see Appendix D.

For H_2 and LiH the time propagation is performed using real-time panels with 16th order Legendre expansions ($N_t = 16$) yielding floating point accuracy for the panel time step sizes $\Delta t \approx 19\,\mathrm{as}$ ($0.8\,\mathrm{Ha}^{-1}$) and $15\,\mathrm{as}$ ($0.6\,\mathrm{Ha}^{-1}$), respectively. The propagation times are $t_{max} \approx 19\,\mathrm{fs}$ ($800\,\mathrm{Ha}^{-1}$) and $29\,\mathrm{fs}$ ($1200\,\mathrm{Ha}^{-1}$), giving the frequency resolutions $\Delta\omega = \pi/t_{max} \approx 0.004\,\mathrm{Ha}$ and $0.003\,\mathrm{Ha}$. The resulting spectral functions for H_2 and LiH at the equilibrium atomic distance are shown in the upper panels of Fig. 9.11 and Fig. 9.12, together with the HF(using Koopman's theorem (KT) [298]), coupled cluster singles-doubles equation of motion (CCSD-EOM), and exact full configuration interaction (FCI) spectra at the same energy resolution. To better reveal many-body effects, the spectral function $A(\omega)$ is scaled with $\sqrt{2\pi}/(\Delta\omega)$, which causes a single-particle-state peak with a Gaussian broadening of $\sigma = \Delta\omega$ to have unit height. With this scaling the individual peaks in the HF spectra all have integer height, while many-body correlations drive peak height renormalization (away from integer values) for the methods GF2, CCSD-EOM and FCI.

Comparing the GF2 spectral function for H_2 in Fig. 9.11 with the HF, CCSD-EOM, and

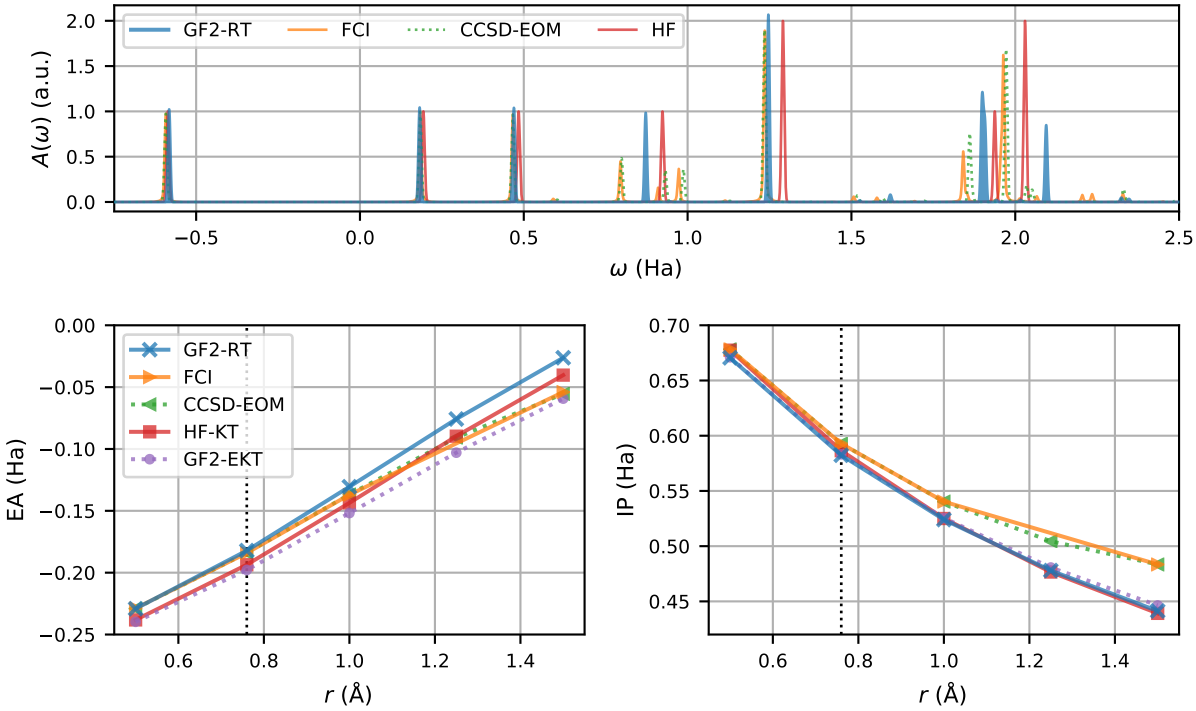

Figure 9.11: Upper panel: Spectral function of H_2 at equilibrium H-H distance $r_0 = 0.76$ Å using the cc-pVDZ basis computed with GF2, HF and the Coupled Cluster Singles-Doubles Equation of motion (CCSD-EOM). Lower left panel: Electron affinity (EA) as a function of r. Lower right panel: Ionization potential (IP) as a function of r. Figure from Ref. [242].

exact FCI results, we see that GF2 is an overall improvement comparing to HF. The position of the occupied state at $\omega \approx -0.58\,\mathrm{Ha}$ is roughly the same for all methods, though GF2 is actually slightly worse than HF when compared to the exact FCI result. For all other spectral features, GF2 is an improvement compared to HF. In GF2 the two first peaks at positive frequencies are shifted down relative to HF, in agreement with FCI. For the higher spectral features the frequency moments of GF2 are improved over HF, while the peak structure differs from FCI. We also note that CCSD-EOM agrees remarkably well with the exact FCI spectra. Thus, for LiH where FCI is out of reach we will use CCSD-EOM as the base line comparison for GF2.

For LiH, in the GF2 spectra the first peak at negative frequencies is shifted up in frequency, while the peaks at positive frequencies are shifted down relative to the HF spectra, all in agreements with CCSD-EOM. While the low frequency peak heights are only weakly renormalized, GF2 also correctly captures the strong renormalization of the spectral feature at $\omega \approx 0.275\,\mathrm{Ha}$.

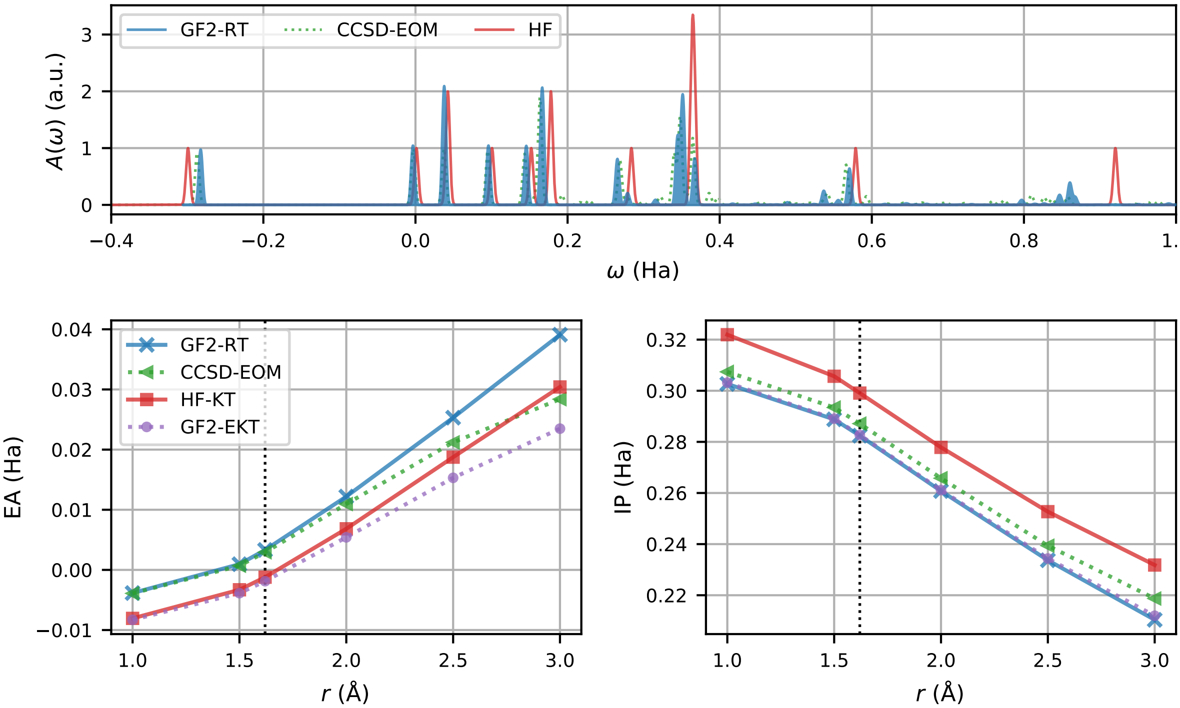

Figure 9.12: Upper panel: Spectral function of LiH at equilibrium Li-H distance $r_0 = 1.62\,\text{Å}$, $\beta = 200$ using the cc-pVDZ basis computed with GF2, HF and the Coupled Cluster Singles-Doubles Equation of motion (CCSD-EOM). Lower left panel: Electron affinity (EA) as a function of r. Lower right panel: Ionization potential (IP) as a function of r. Figure from Ref. [242].

The relatively good agreement in equilibrium spectra between GF2 and CCSD-EOM (and FCI) is promising, in particular for the application of GF2 to investigate non-linear processes in molecular systems out of equilibrium [299–302].

Comparison with analytical continuation

Within the GF2 self-energy approximation the spectral function $A(\omega)$ is obtained from real-time propagation up to the energy resolution $\Delta\omega = \pi/t_{max}$. Having the spectral function enables us to benchmark the Nevanlinna analytical continuation method [78]. Analytical continuation solves the ill posed inverse problem of determining an approximate spectral function using only the imaginary time Green's function $G^M(\tau)$ [72].

In Fig. 9.13 the GF2 spectral function for LiH (at energy resolution $\approx 0.003\,\text{Ha}$) is compared with the Nevanlinna spectral function. The Nevanlinna calculation was performed for each diagonal component of the $SG^M(\tau)$ product, c.f. Eq. 9.94, using 225 positive Legendre sparse-sampling Matsubara frequencies (see section 9.4.5) and optimized with 25 Hardy basis functions (see Ref. [78]) evaluated 0.002 Ha above the real-frequency axis.

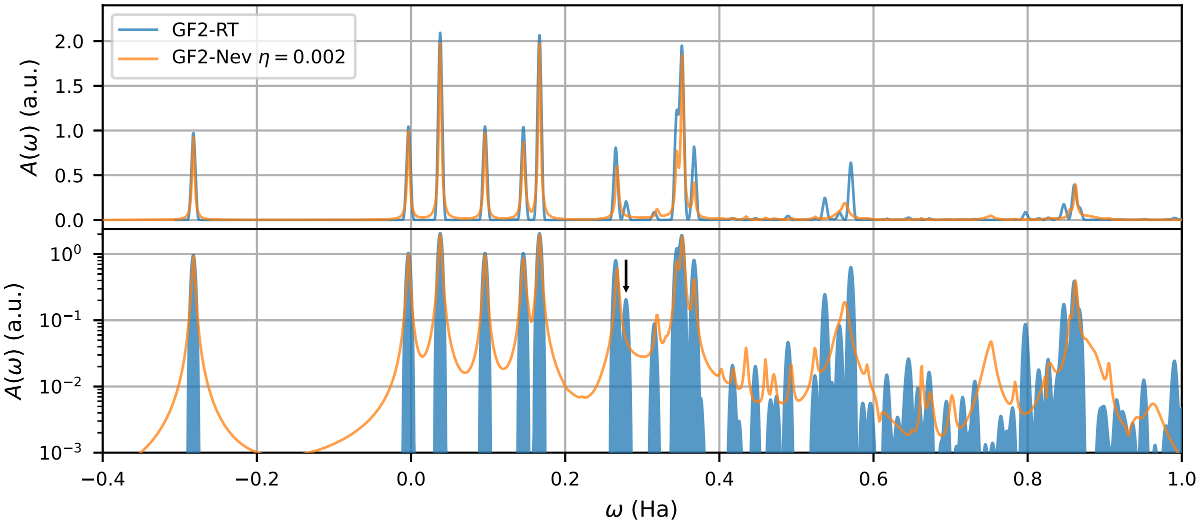

Figure 9.13: Comparison of spectral functions of LiH at equilibrium Li-H distance $r_0 = 1.62$ Å, $\beta = 200$ using the cc-pVDZ basis. The GF2 real-time result is compared with the Nevanlinna continuation result. Black arrow in the lower panel shows the first feature Nevanlinna continuation method is not able to capture. The spectral functions are scaled so that a non-degenerate single-particle state has a peak height of unity. Figure from Ref. [242].

As seen in in Fig. 9.13, peaks up to ≈ 0.20 Ha are well captured by the Nevanlinna method. However, some of the higher energy correlated resonances are missed or smeared out, such as the one at ≈ 0.275 Ha (black arrow). We stress that for diagrammatic calculations like GF2 the equilibrium real-time propagation method proposed in this chapter eliminates the need for analytical continuation.

Ionization potential and electron affinity

At positive frequencies $\omega > 0$ the spectral function $A(\omega)$ describes electron addition excitations, while negative frequencies $\omega < 0$ corresponds to electron removal excitations. The first peaks in $A(\omega)$ below and above $\omega = 0$ give the minimal energy for electron removal, the ionization potential (IP), and the minimal energy for electron addition, the electron affinity (EA), respectively. To investigate how GF2 performs in both the weakly and strongly correlated regimes, we study the IP and EA as a function of interatomic distance r for H_2 and LiH. The GF2 result is compared to the HF-KT and the CCSD-EOM results, as well as the exact FCI result in the case of H_2. With large interatomic separations $r \gg r_0$ the kinetic overlaps become exponentially small, while the long range Coulomb interaction varies weakly.

For H_2 the IP and EA are shown in Fig. 9.11 as a function of r. The overall performance of GF2 relative to the exact FCI result is better in the weakly correlated regime $r \lesssim r_0$, compared to the strongly correlated regime $r \gg r_0$. The GF2 behaviour relative to HF, however, is different for the IP and EA even in the weakly correlated regime. For the EA, GF2 constitutes a drastic improvement over HF, while for the IP, GF2 mainly follows the HF result. We note that the exact FCI result is closely followed by CCSD-EOM, which is used as baseline in comparison for LiH. The IP and EA for LiH are shown in Fig. 9.12. For both the IP and EA we find that GF2 preforms significantly better than HF relative to the CCSD-EOM result. However, the GF2 behaviour as a function of r differs between IP and EA when entering the strongly correlated regime. The EA deviates from CCSD-EOM while the IP follows the r dependence of CCSD-EOM with small offset.

In the light of the perturbation expansion order, the observed progression from HF to GF2 shows that, going from the first order dressed perturbation expansion of HF to the second order dressed perturbation expansion GF2, improves the excitation spectra in the weakly correlated regime. However, in the strongly correlated regime, with larger interaction to kinetic overlap ratios, also the second order perturbation expansion in GF2 does not suffice. Hence, GF2 is probably not well suited for studying phenomena in the $r \gg r_0$ regime like dynamical atomic dissociation. However, it is a promising level of approximation to study phenomena at $r \sim r_0$, like non-linear optical-vibronic dynamics, terahertz response, and high harmonic generation [303].

Finally we connect to previous diagrammatic perturbation theory works which compute IP and EA from the imaginary time Green's function $G^M(\tau)$ using the extended Koopman's theorem (EKT) [304–309]. Within EKT, electron addition and removal energies are computed from a generalized eigenvalue problem constructed from $G^M(\tau)$ and $\partial_\tau G^M(\tau)$ at $\tau = 0^\pm$. It has been used to compute IP and EA from both the GW [310] and GF2 [231, 311, 312] imaginary time calculations. However, how accurate the EKT approach is relative to the actual IP and EA has not been investigated. The real-time propagation approach presented here directly gives the spectral function $A(\omega)$ and alleviates the need for using EKT to compute the IP and EA. It makes it possible to investigate the accuracy of EKT by direct comparison to the exact spectral-function derived IP and EA. The real-time GF2-RT and the GF2-EKT results for the IP and EA are shown for H_2 and LiH in Fig. 9.11 and Fig. 9.12. In both cases the EA from GF2-EKT fails to reproduce the GF2-RT result, instead the EKT calculations give EAs that matches the HF results for $r \lesssim r_0$. These results raise concerns regarding the use of EKT for computing EAs.

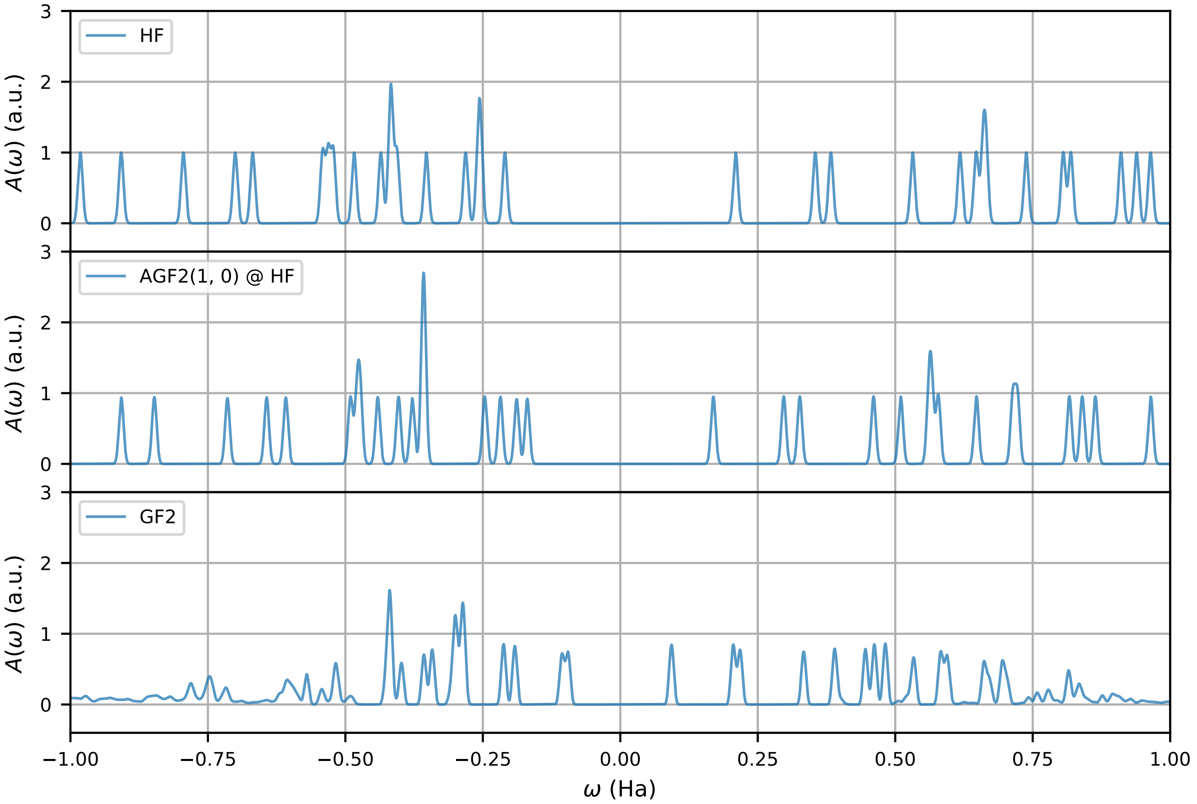

Figure 9.14: Spectral function of Benzoquinone ($C_6H_4O_2$) in the STO-3g basis from HF (upper panel), AGF2(1, 0)@HF (middle panel), and GF2 (lower panel). Figure from Ref. [242].

9.6.2.2 Benzoquinone $C_6H_4O_2$

To explore the solver in a regime that is not otherwise accessible, we compute the spectral function of the Benzoquinone molecule ($C_6H_4O_2$) in a minimal STO-3g basis (44 basis functions), with optimized MP2 geometry [313]. A previous density functional study has shown that the HOMO-LUMO gap of Benzoquinone can not be described by ab-initio density functionals like PBE [314], while HF overestimates the gap. However, a recent study [315] have shown that a self-consistent approximate formulation of GF2, called the auxiliary second-order Green's function perturbation theory (AGF2), is able to describe the experimental gap.

For the real-time propagation a 16th order real-time panel expansion was used with panel time step size $\Delta t \approx 7.3\,\text{as}$ ($0.3\,\text{Ha}^{-1}$) and a total propagation time of $t_{max} \approx 18\,\text{fs}$ ($750\,\text{Ha}^{-1}$). The minimal STO-3g basis prevents direct comparison with experiments and we compare with HF and AGF2 in this basis. The total memory foot-print of the calculation is of the order on 500 GB. The molecular point group symmetry was also used to speed up the GF2 self-energy evaluation (see section 8.3).

Figure 9.14 shows the GF2 spectral function of Benzoquinone together with the corresponding results from HF and AGF2(1,0)@HF [1].

Basis Theory	STO-3g	aug-cc-pVDZ
HF	0.420 Ha	0.410 Ha
AGF2(1,0)@HF	0.338 Ha	0.372 Ha
GF2	0.189 Ha	-
Exp.[316, 317]	0.299 Ha	

Table 9.3: HOMO-LUMO gap of Benzoquinone ($C_6H_4O_2$) at different levels of theory in the STO-3g basis (this work) and the and the aug-cc-pVDZ basis from Ref. [315].

The corresponding HOMO-LUMO gaps listed in Tab. 9.3 shows that going from first order HF, through the approximate second order AGF2(1,0)@HF result, to the full second order self-consistent GF2 result, yields a decreasing HOMO-LUMO gap.

Accounting for the aug-cc-pVDZ results for HF and AGF2(1,0)@HF from Ref. [315], see Tab. 9.3, the experimental HOMO-LUMO gap of 0.299 Ha [316, 317] is likely to be underestimated by GF2 also in the larger aug-cc-pVDZ basis.

Another distinct feature of the full GF2 spectral function is the large degree of quasi-particle renormalization, as measured in terms of deviation from unit height in the spectral function, see Fig. 9.14. This is to be compared with HF where all individual excitations come with unit height and the partial self-consistent AGF2 that only yields a small frequency-independent renormalization. The GF2 spectral function, on the other hand, displays peak-height renormalizations of the order 10-20% for the HOMO and LUMO peaks and even a loss of coherence for the spectra at frequencies. A systematic investigation of the different partial-self-consistency schemes within GF2 is an interesting venue for further research, but out of scope for the present proof of concept application of real-time propagation.

9.7 Discussion and conclusion

In this chapter, we introduced the compact representations of Green's functions based on polynomial expansions. With (piece-wise) high order expansion on the (real-) imaginary-time axis using Legendre polynomials, we reformulated the equilibrium contour Dyson equations in Legendre coefficient space. The algorithms for solving the Dyson equations use the

---

[1] See Refs. [297, 315] for details on the partial self-consistency notation: AGF2(X,Y).

Legendre spectral method [200] in combination with the recursive algorithm for Legendre convolution [266].

The equilibrium Legendre spectral Dyson solver allows us to access high-accurate energies and high-resolution spectral functions of molecules. To further improve the efficiency of the real-time Dyson solvers, generalizing the quasi-linear scaling multistep history integral method [255] to the real-time panel expansion is a promising direction. The high-order discretization of the mixed Green's also serves as an important step towards the development of compact representations of the full two-time Green's functions in non-equilibrium simulations. The combinations of the panel-based representation and the tensor compression scheme is an interesting direction of future research.

Chapter 10

Conclusion and Outlook

In the study of strongly correlated systems, numerical methods form the bridge between experimental observations and theoretical understandings. Single- and two-particle Green's functions, which describe the propagation of excitations related with one and a pair of electrons, are able to explain results measured from experiments such as angle-resolved photoemission spectroscopy and Raman scattering. Two-particle Green's functions also allow for calculating the linear response of a system to a small external perturbation, like electric fields, magnetic fields etc., and provide tools for analyzing the competing fluctuations in strongly correlated systems.

The utilization of model Hamiltonians such as the Hubbard model drastically reduces the complexity of solving many-body systems. DMFT, which maps the Hubbard model to the AIM, provides valuable insights into correlation physics such as the Mott transition. Cluster extensions of DMFT, which account for the short-range physics in the system and can be systematically improved by increasing the cluster size, provide access to momentum dependent Green's functions. With the CT-QMC impurity solvers, single- and two-particle quantities can be reliably computed within DMFT and its extensions in both the paramagnetic and superconducting state, allowing for a rigorous analysis of competing fluctuations in the model.

Ab-inito simulation with realistic Hamiltonians is another widely used approach in the study of strongly correlated systems apart from the model Hamiltonian approach. Advanced numerical methods and the simplification given by symmetry properties of the systems enable the efficient simulations of realistic systems using diagrammatic methods, which are based on perturbative expansions in the electron-electron interaction.

This thesis presents our progress in the development of numerical methods for both models and realistic systems.

The first part of the thesis provided derivations of the formalisms and methods used in the later chapters. In chapter 2, the many-body Hamiltonian, as well as the basic concepts in many-body physics were defined and reviewed. In chapter 3, we provided the generalization of the Green's function formalism in the singlet superconducting state, with a focus on the single- and two-particle Green's functions and vertex functions. In chapter 4, we first introduced the Hubbard model and the AIM, and then provided derivations for DCA and CT-AUX that are used for solving the Hubbard model. Both the models and the methods were generalized to the singlet superconducting state in this chapter.

The second part of the thesis focused on the numerical analysis of competing fluctuations and ordered states in the two-dimensional Hubbard model. Chapters 5, 6 and 7 summarized the simulation results of the two-dimensional single-band Hubbard model given by eight-site DCA. In chapter 5, we presented the simulation results of the two-dimensional single band Hubbard model in the paramagnetic state. By analyzing the intensity of magnetic, charge, and superconducting fluctuations with different symmetries, we found that the spin fluctuations are dominant around half filling, leading to an anti-ferromagnetic state as temperature decreases. By comparing the intensity of d-wave charge and superconducting fluctuations, we saw that although the fluctuations are comparable in magnitude, no area in parameter space has dominant d-wave charge fluctuations. At the parameter regime corresponding to realistic strongly correlated materials, d-wave superconducting order will emerge as temperature decreases. In chapters 6 and 7 we presented the simulations results of the two-dimensional single band Hubbard model in the d-wave singlet superconducting state. In chapter 6, we performed a quantitative study to analyze to which extent the spin fluctuations can be treated as a pairing boson within the one loop approximation. By analysing the intensity of the anomalous self-energies given by DCA and the one-loop spin fluctuation theory, we found that only a fraction of the pairing can be attributed to these fluctuations, while the other part might arise from higher order diagrams. The frequency dependence of the superconducting gap function computed from the two anomalous self-energies and the spin fluctuation spectrum further demonstrated the importance of a high-frequency non-spin-fluctuation contribution to the electron self-energy. To have a more detailed and unbiased analyze of all the fluctuations in the singlet superconducting state, we presented results from the fluctuation diagnostics method in chapter 7. From the momentum and frequency dependence of the anomalous self-energy decomposed in different physical channels, we were able to unambiguously identify spin fluctuations as the dominant contribution to the d-wave pairing. The discrepancy between the conclusion given by the fluctuation diagnostics and the conclusion given in chapter 6 can be attributed to the possibility that one-loop spin fluctuation expressions do not capture all spin fluctuation mediated processes outside the weak-coupling regime, and there are other higher order diagrams contributing to the pairing of the Cooper pairs. Identifying and analyzing these missing diagrams would give us better insights into the role of the spin fluctuations in superconductivity. We note that the cluster size in the DCA simulation performed here was chosen based on previous literature to capture the pairing and magnetic fluctuations at reasonable computational expense, but did not adequately capture phenomena such as the stripe physics. The limitation of the cluster size mainly come from the impurity solver. The CT-QMC impurity solvers suffer from increasing computational costs for simulations of large impurities and at low temperatures. The memory required for storing the two-particle Green's functions is another obstacle in the simulations. The size of the two-particle Green's functions scales as $\mathcal{O}(N_{\omega_n}^2 N_{\nu_n} N_k^3)$, which limits the number of frequencies to the order of 100. With the CT-AUX impurity solver and equidistant frequency grid, currently the largest cluster we were able to perform two-particle measurements in the singlet superconducting state (with $T_c \sim t/40$) was the eight-site cluster. Better impurity solvers and better frequency grids would allow for simulations of larger clusters and therefore reduce the finite size effects.

The third part of the thesis focused on the numerical methods used in the simulation of realistic systems. In chapter 8, we introduced the realistic Hamiltonian and basis sets for molecules, and provided two examples used in the diagrammatic self-consistent methods. We then described how point group symmetries can be used to optimize the simulation of molecules. While we only introduced simulation of molecules in this chapter, similar diagrammatic methods have been applied to the simulation of solids, in which the computational costs increase extraordinarily. Therefore, generalizing the optimizations given by group theory to the case of solids will provide great advantages.

In chapter 9, we reviewed some of the developments for efficiently representing correlation functions at finite temperature. We then derived a Legendre spectral method for solving the Dyson equations of the contour Green's functions, and presented simulation results for several molecules using the GF2 method. With the piece-wise high-order Legendre orthogonal-polynomial expansion on the real-time axis, we were able to drastically reduce the number of discretization points required to reach a fixed accuracy, and to obtain high-resolution spectral functions of molecules. While the real-time panel-based high-order Dyson solver introduced in chapter 9 was only formulated for Green's functions with time translational invariance, it serves as the first step towards high-order methods for non-equilibrium real-time evolution. Generalizing this approach to the full two-time dependent formalism is a promising direction for future research, which would reduce the memory and computational resources needed for long-time non-equilibrium simulations.

In conclusion, numerical methods plays an important role in the study of strongly correlated systems. The methods and results presented in this thesis illustrate the power of numerical simulations. Further developments will enable the simulation of larger and more complicated systems, providing access to more interesting physics phenomena.

Appendix A

Langreth Rule for Keldysh Components

In this appendix we provide the explicit forms of Langreth rules for computing convolution and product of Keldysh components used in sections 9.2 and 9.6.2. The definitions are taken from Ref. [250].

A.1 Convolution

The contour integral in Eq. 9.6 can be carried out with the Langreth rules of the convolution $C = A * B$ [250, 256]

$$C^{>} = A^{>} \circ B^{A} + A^{R} \circ B^{>} - iA^{\urcorner} \bullet B^{\ulcorner} \,, \tag{A.1a}$$

$$C^{<} = A^{<} \circ B^{A} + A^{R} \circ B^{<} - iA^{\urcorner} \bullet B^{\ulcorner} \,, \tag{A.1b}$$

$$C^{R} = A^{R} \circ B^{R} \,, \tag{A.1c}$$

$$C^{A} = A^{A} \circ B^{A} \,, \tag{A.1d}$$

$$C^{\urcorner} = A^{R} \circ B^{\urcorner} + A^{\urcorner} \bullet B^{M} \,, \tag{A.1e}$$

$$C^{\ulcorner} = A^{\ulcorner} \circ B^{A} + A^{M} \bullet B^{\ulcorner} \,, \tag{A.1f}$$

$$C^{M} = A^{M} \bullet B^{M} \,, \tag{A.1g}$$

where the two integral operators are defined as

$$C^{M}(\tau,\tau') = A^{M} \bullet B^{M} = \int_{0}^{\beta} d\bar{\tau} A^{M}(\tau,\bar{\tau}) B^{M}(\bar{\tau},\tau') \,, \tag{A.2a}$$

$$C^{R}(t,t') = A^{R} \circ B^{R} = \int_{0}^{t_{max}} d\bar{t} A(t,\bar{t}) B(\bar{t},t') \,. \tag{A.2b}$$

The Dyson equation [Eq. 9.6] related with $G^\rceil(t,\tau)$ is then in the form

$$(iS\partial_t - F)G^\rceil(t,\tau) - \Sigma^R \circ G^\rceil + \Sigma^\rceil \bullet G^M = 0\,, \tag{A.3}$$

which gives Eq. 9.11 in equilibrium.

A.2 Product

The direct products in the self-energy contraction [Eq. 9.92] can be carried out with the Langreth rules of the product $C(z,z') = A(z,z')B(z,z')$ [250, 256]

$$C^{\gtrless}(t,t') = A^{\gtrless}(t,t')B^{\gtrless}(t,t')\,, \tag{A.4a}$$

$$C^R(t,t') = A^R(t,t')B^R(t,t') + A^<(t,t')B^R(t,t') + A^R(t,t')B^<(t,t')\,, \tag{A.4b}$$

$$C^\rceil(t,\tau) = A^\rceil(t,\tau)B^\rceil(t,\tau)\,, \tag{A.4c}$$

$$C^M(\tau,\tau') = -iA^M(\tau,\tau')B^M(\tau,\tau')\,, \tag{A.4d}$$

and $C(z,z') = A(z,z')B(z'z)$ [250, 256]

$$C^{\gtrless}(t,t') = A^{\gtrless}(t,t')B^{\lessgtr}(t',t)\,, \tag{A.5a}$$

$$C^R(t,t') = A^R(t,t')B^<(t',t) + A^<(t',t)B^A(t',t)\,, \tag{A.5b}$$

$$C^\rceil(t,\tau) = A^\rceil(t,\tau)B^\lceil(\tau,t)\,, \tag{A.5c}$$

$$C^M(\tau,\tau') = -iA^M(\tau,\tau')B^M(\tau',\tau)\,. \tag{A.5d}$$

The mixed self-energy can then be written as

$$\begin{aligned}\Sigma^\rceil_{ij}(t,\tau) &= \sum_{klmnpq} U_{ilnp}(2U_{kjqm} - U_{qjkm})G^\rceil_{lk}(t,\tau)G^\rceil_{pq}(t,\tau)G^\lceil_{mn}(\tau,t)\\ &= \sum_{klmnpq} U_{ilnp}(2U_{kjqm} - U_{qjkm})G^\rceil_{lk}(t,\tau)G^\rceil_{pq}(t,\tau)G^{\rceil *}_{nm}(t,\beta-\tau)\,,\end{aligned} \tag{A.6}$$

where we used the relation between $G^\lceil(\tau,t)$ and $G^\rceil(t,\beta-\tau)$ given by Eq. 9.5.

Appendix B

Legendre and Chebyshev Quadratures

In this appendix we summarize the Gauss-type quadrature nodes and weights of Legendre and Chebysheve polynomials used in section 9.3 for representing continuous functions. The equations are taken from Ref.[200].

- Legendre-Gauss type quadratures

$$\int_{-1}^{1} dx l(x) = \sum_{i}^{N} l(x_i) w_i \,, \quad \forall\, l \in L_{2N+\delta}\,. \tag{B.1}$$

  - Legendre-Gauss quadrature ($\delta = 1$)

$$\begin{aligned} &\{x_i\}_{i=0}^{N} \text{ are zeros of } P_{N+1}(x)\,, \\ &w_i = \frac{2}{(1-x_i^2)[L'_{N+1}(x_i)]^2}\,, \quad 0 \le i \le N\,. \end{aligned} \tag{B.2}$$

  - Legendre-Gauss-Radau quadrature ($\delta = 0$)

$$\begin{aligned} &\{x_i\}_{i=0}^{N} \text{ are zeros of } P_{N+1}(x) + P_N(x)\,, \\ &w_i = \frac{1}{(N+1)^2}\frac{1-x_i}{[L_N(x_i)]^2}\,, \quad 0 \le i \le N\,. \end{aligned} \tag{B.3}$$

  - Legendre-Gauss-Lobatto quadrature ($\delta = -1$)

$$\begin{aligned} &\{x_i\}_{i=0}^{N} \text{ are zeros of } (1-x^2)P'_{N+1}(x)\,, \\ &w_i = \frac{2}{N(N+1)}\frac{1}{[L_N(x_i)]^2}\,, \quad 0 \le i \le N\,. \end{aligned} \tag{B.4}$$

- Chebyshev-Gauss type quadratures

$$\int_{-1}^{1} dx l(x) \frac{1}{\sqrt{1-x^2}} = \sum_{i}^{N} l(x_i) w_i \,, \quad \forall\, l \in L_{2N+\delta} \,. \tag{B.5}$$

  - Chebyshev-Gauss quadrature ($\delta = 1$)

$$x_i = -\cos \frac{(2i+1)\pi}{2N+2} \,, \quad w_i = \frac{\pi}{N+1} \,, \quad 0 \leq i \leq N \,. \tag{B.6}$$

  - Chebyshev-Gauss-Radau quadrature ($\delta = 0$)

$$\begin{aligned} x_i &= -\cos \frac{2\pi i}{2N+1} \,, \quad 0 \leq i \leq N \,, \\ w_0 &= \frac{\pi}{2N+1} \,, \quad w_i = \frac{2\pi}{2N+1} \,, \quad 1 \leq i \leq N \,. \end{aligned} \tag{B.7}$$

  - Chebyshev-Gauss-Lobatto quadrature ($\delta = -1$)

$$\begin{aligned} x_i &= -\cos \frac{\pi i}{N} \,, \quad w_i = \frac{\pi}{\tilde{c}_i N} \,, \quad 0 \leq i \leq N \,, \\ \tilde{c}_0 &= \tilde{c}_N = 2 \,, \quad c_i = 1 \,, \quad i = 1, \ldots N-1 \,. \end{aligned} \tag{B.8}$$

Appendix C

Fast Convolution of Legendre Polynomials

In this appendix we provide detailed derivations for Eqs. 9.57, 9.58, 9.59 in section 9.5. The derivation follows Ref. [266] but with more details and explanations. The same contents are published in the appendix of *Xinyang Dong, Emanuel Gull, Dominika Zgid, Hugo U.R. Strand "Legendre-spectral Dyson equation solver with super-exponential convergence", J. Chem. Phys. 152, 134107 (2020)* [241].

C.1 Convolution and Fourier transform

The convolution of two continuous integrable functions is defined by the integral [266]

$$h(x) = (f * g)(x) = \int_{-\infty}^{\infty} dt f(t) g(x-t)\,. \tag{C.1}$$

For the specific applications we're interested in, we consider f and g that are polynomials of finite degree and are supported on $[a, b]$ and $[c, d]$, which gives equivalent definition

$$h(x) = (f * g)(x) = \int_{\max(a,x-d)}^{\min(b,x-c)} dt f(t) g(x-t)\,, \quad x \in [a+c, b+d]\,, \tag{C.2}$$

and $h(x) = 0$ for $x \notin [a+c, b+d]$. Their Fourier transform can be written as

$$\mathcal{F}\{f\}(\omega) = \int_{-\infty}^{\infty} dx e^{-i\omega x} f(x)\,, \tag{C.3}$$

$$\mathcal{F}^{-1}\{f\}(x) = \frac{1}{2\pi}\int_{-\infty}^{\infty} dx e^{i\omega x} f(x)\,, \tag{C.4}$$

which satisfy the Fourier inversion theorem $\mathcal{F}^{-1}\{\mathcal{F}\{f\}\} = f$ and the convolution theorem [318]

$$\mathcal{F}\{f * g\} = \mathcal{F}\{f\} \cdot \mathcal{F}\{g\}\,. \tag{C.5}$$

C.2 Convolution theorem for Legendre polynomials

For the two functions f and g defined on intervals $[a, b]$ and $[c, d]$, the linear function

$$\psi_{[a,b]}(x) = \frac{2(x-a)}{b-a} - 1 \tag{C.6}$$

maps $x \in [a, b]$ back to the fundamental interval of the Legendre polynomials $\psi_{[a,b]}(x) \in [-1, 1]$. With the finite-order expansion defined in Eq. 9.14, the two functions in the convolution [Eq. (C.2] can be approximated by

$$f_M(x) = \sum_{m=0}^{M} \alpha_m P_m(\psi_{[a,b]}(x))\,, \quad g_N(x) = \sum_{n=0}^{N} \beta_n P_n(\psi_{[c,d]}(x))\,. \tag{C.7a}$$

For our specific applications, we consider two intervals of the same length $d - c = b - a$, the convolution can be computed as [266]

$$h(x) = \int_{\max(a,x-d)}^{\min(b,x-c)} dt f(t) g(x-t) = \frac{b-a}{2}(f_M * g_N)(2\psi_{[a+c,b+d]}(x))\,, \quad 2\psi_{[a+c,b+d]}(x) \in [-2, 2]\,, \tag{C.8}$$

which is the same as computing the convolution of f_M and g_N supported on $[-1, 1]$ with an extra pre-factor. For f_M and g_N supported on $[-1, 1]$, the convolution can be computed as

$$h(x) = (f_M * g_N)(x) = \int_{\max(-1,x-1)}^{\min(1,x+1)} dt f_M(t) g_N(x-t)\,, \quad x \in [-2, 2]\,, \tag{C.9}$$

which can be separated into two parts

$$h^{<}(x) = (f \overset{<}{*} g)(x) = \int_{-1}^{x+1} dt f_M(t) g_N(x-t) = \sum_{k=0}^{M+N+1} \gamma_k^{<} \, P_k(x+1) \quad x \in [-2, 0]\,, \tag{C.10a}$$

$$h^{>}(x) = (f \overset{>}{*} g)(x) = \int_{x-1}^{1} dt f_M(t) g_N(x-t) = \sum_{k=0}^{M+N+1} \gamma_k^{>} \, P_k(x-1) \quad x \in [0, 2]\,. \tag{C.10b}$$

The convolution can be computed by computing the coefficients $\gamma_k^{<}$ and $\gamma_k^{>}$. With the orthogonality of Legendre polynomials [Eq. 9.18], the two coefficients in Eq. C.10 can be computed as

$$\begin{aligned}
\gamma_k^{<} &= \frac{2k+1}{2} \int_{-2}^{0} dx P_k(x+1) \int_{-1}^{x+1} dt f_M(t) g_N(x-t) \\
&= \sum_{n=0}^{N} \beta_n \frac{2k+1}{2} \sum_{m=0}^{M} \alpha_m \int_{-2}^{0} dx P_k(x+1) \int_{-1}^{x+1} dt P_m(t) P_n(x-t) \\
&= \sum_{n=0}^{N} \beta_n B_{k,n}^{<}\,, && \text{(C.11a)} \\
\gamma_k^{>} &= \frac{2k+1}{2} \int_{0}^{2} dx\, P_k(x-1) \int_{x-1}^{1} dt f_M(t) g_N(x-t) \\
&= \sum_{n=0}^{N} \beta_n \frac{2k+1}{2} \sum_{m=0}^{M} \alpha_m \int_{0}^{2} dx P_k(x-1) \int_{x-1}^{1} dt P_m(t) P_n(x-t) \\
&= \sum_{n=0}^{N} \beta_n B_{k,n}^{>}\,, && \text{(C.11b)}
\end{aligned}$$

where we collected terms into two convolution matrices $B_{k,n}^{\lessgtr}$, which can be further simplified as

$$\begin{aligned}
B_{k,n}^{<} &= \frac{2k+1}{2} \sum_{m=0}^{M} \alpha_m \int_{-2}^{0} dx P_k(x+1) (P_m * P_n)(x) && \text{(C.12a)} \\
&= \frac{2k+1}{2} \sum_{m=0}^{M} \alpha_m \int_{-1}^{1} ds P_k(s) (P_m * P_n)(s-1)\,, \\
B_{k,n}^{>} &= \frac{2k+1}{2} \sum_{m=0}^{M} \alpha_m \int_{0}^{2} dx P_k(x-1) (P_m * P_n)(x) \\
&= \frac{2k+1}{2} \sum_{m=0}^{M} \alpha_m \int_{-1}^{1} ds P_k(s) (P_m * P_n)(s+1)\,. && \text{(C.12b)}
\end{aligned}$$

The fast convolution algorithm of the Legendre polynomials make use of the property that the Fourier transform and inverse Fourier transform of the Legendre polynomials. With the convolution theorem [Eq. C.5] and the Fourier transformation [Eq. 9.46], the convolution of Legendre polynomials can be expressed in terms of Bessel functions

$$(P_m * P_n)(x) = \frac{2(-i)^{m+n}}{\pi} \int_{-\infty}^{\infty} d\omega\, e^{i\omega x} j_m(\omega) j_n(\omega)\,, \quad x \in [-2, 2]\,, \tag{C.13}$$

the convolution matrices [Eq. C.12] can be written as

$$\begin{aligned} B^{<}_{k,n} &= \frac{2k+1}{\pi} \sum_{m=0}^{M} (-i)^{m+n} \alpha_m \int_{-1}^{1} ds P_k(s) \int_{-\infty}^{\infty} d\omega e^{i\omega(s-1)} j_m(\omega) j_n(\omega) \\ &= \frac{2(2k+1)}{\pi} \sum_{m=0}^{M} (-i)^{m+n} i^k \alpha_m \int_{-\infty}^{\infty} d\omega j_k(\omega) j_m(\omega) j_n(\omega) e^{-i\omega}\,, \end{aligned} \tag{C.14a}$$

$$\begin{aligned} B^{>}_{k,n} &= \frac{2k+1}{\pi} \sum_{m=0}^{M} (-i)^{m+n} \alpha_m \int_{-1}^{1} ds P_k(s) \int_{-\infty}^{\infty} d\omega e^{i\omega(s+1)} j_m(\omega) j_n(\omega) \\ &= \frac{2(2k+1)}{\pi} \sum_{m=0}^{M} (-i)^{m+n} i^k \alpha_m \int_{-\infty}^{\infty} d\omega j_k(\omega) j_m(\omega) j_n(\omega) e^{i\omega}\,, \end{aligned} \tag{C.14b}$$

with the only difference being the sign in the exponent of $e^{\mp iw}$.

The main property of Spherical Bessel functions used in the fast convolution algorithm is the three term recurrence relation

$$\begin{aligned} &j_{-1}(z) = \frac{\cos z}{z}\,, \quad j_0(z) = \frac{\sin z}{z}\,, \\ &j_{n+1}(z) = \frac{2n+1}{z} j_n(z) - j_{n-1}(z)\,, \quad n \geq 0\,. \end{aligned} \tag{C.15}$$

Consider the $B^{\lessgtr}_{k,n+1}$ term, applying the recursion relation of the spherical Bessel functions on n and k gives

$$\begin{aligned} (-i)^{m+n+1} i^k j_k(\omega) j_m(\omega) j_{n+1}(\omega) &= (-i)^{m+n+1} i^k j_k(\omega) j_m(\omega) \left(\frac{2n+1}{\omega} j_n(\omega) - j_{n-1}(\omega) \right) \\ &= \frac{2n+1}{2k+1} (-i)^{m+n+1} i^k \left(j_{k+1}(\omega) + j_{k-1}(\omega) \right) j_m(\omega) j_n(\omega) \\ &\quad + (-i)^{m+n-1} i^k j_k(\omega) j_m(\omega) j_{n-1}(\omega)\,. \end{aligned} \tag{C.16}$$

Since the exponent of $e^{\mp\omega}$ is unchanged when applying recursion relation, the recursion relation of the two convolution matrices can be written with one equation as

$$B^{\lessgtr}_{k,n+1} = -\frac{2n+1}{2k+3} B^{\lessgtr}_{k+1,n} + \frac{2n+1}{2k-1} B^{\lessgtr}_{k-1,n} + B^{\lessgtr}_{k,n-1}\,, \quad k, n \geq 1\,. \tag{C.17}$$

In practice this recursion relation is only stable when computing the entries of $B^{\lessgtr}_{k,n}$ below the diagonal ($k > n$). The entries of $k < n$ can be computed from the transpose relation, which can be derived from the integral expression Eq. C.14

$$B^{\lessgtr}_{k,n} = (-1)^{n+k} \frac{2k+1}{2n+1} B^{\lessgtr}_{n,k} \,. \tag{C.18}$$

The initial value to start the recursion can be computed from the Volterra integral formula for Legendre polynomials [ref]

$$\begin{aligned}
S_{a,n}(x) &= \int_a^x dt P_n(t) \,, && \text{(C.19)}\\
S_{a,0}(x) &= x - a \,, && \text{(C.20)}\\
S_{a,n}(x) &= \frac{1}{2n+1} \left[P_{n+1}(t) - P_{n-1}(t) \right]_a^x \,, && \text{(C.21)}
\end{aligned}$$

which gives the relation at $a = \pm 1$

$$\begin{aligned}
S_{\pm 1,0}(x) &= x \mp 1 = P_1(x) \mp P_0(x) \,, && \text{(C.22)}\\
S_{\pm 1,n}(x) &= \frac{1}{2n+1} \left[P_{n+1}(x) - P_{n-1}(x) \right] - \left[P_{n+1}(\pm 1) - P_{n-1}(\pm 1) \right] \\
&= \frac{1}{2n+1} \left[P_{n+1}(x) - P_{n-1}(x) \right] \,. && \text{(C.23)}
\end{aligned}$$

Using $P_0 = 1$, the first column ($n = 0$) in the convolution matrix can be written as

$$\begin{aligned}
B^{\lessgtr}_{k,0} &= \pm \frac{2k+1}{2} \sum_{m=0}^{M} \alpha_m \int_{-1}^{1} dx\, P_k(x) \int_{\mp 1}^{x} dt\, P_m(t) && \text{(C.24)}\\
&= \pm \frac{2k+1}{2} \sum_{m=0}^{M} \alpha_m \int_{-1}^{1} dx\, P_k(x) S_{\mp 1,m}(x) \\
&= \pm \frac{2k+1}{2} \left[\sum_{m=1}^{M} \frac{\alpha_m}{2m+1} \int_{-1}^{1} dx\, P_k(x) \left[P_{m+1}(x) - P_{m-1}(x) \right] \right. \\
&\qquad \left. + \, \alpha_0 \int_{-1}^{1} dx P_k(x) [P_1(x) \pm P_0(x)] \right] \,,
\end{aligned}$$

where the integral can be computed with the orthogonality relation of Legendre polynomials [Eq. 9.18] and gives

$$B^{\lessgtr}_{k,0} = \begin{cases} \alpha_0 \mp \frac{\alpha_1}{3} \,, & k = 0 \\ \pm \left(\frac{\alpha_{k-1}}{2k-1} - \frac{\alpha_{k+1}}{2k+3} \right) , & k \geq 1 \end{cases} \,. \tag{C.25}$$

Using $P_1(x) = x$, the second column ($n = 1$) of the two convolution matrices can be written as

$$\begin{aligned}
B^{<}_{k,1} &= \frac{2k+1}{2}\sum_{m=0}^{M}\alpha_m \int_{-2}^{0} dx P_k(x+1)\int_{-1}^{x+1} dt P_m(t) P_1(x-t) \\
&= \frac{2k+1}{2}\sum_{m=0}^{M}\alpha_m \int_{-1}^{1} dx P_k(x)\int_{-1}^{x} dt P_m(t)(x-t-1) \\
&= -B^{<}_{k,0} + \frac{2k+1}{2}\sum_{m=0}^{M}\alpha_m \int_{-1}^{1} dx P_k(x)\int_{-1}^{x} dt P_m(t)\int_{t}^{x} ds \\
&= -B^{<}_{k,0} + \frac{2k+1}{2}\sum_{m=0}^{M}\alpha_m \int_{-1}^{1} dx P_k(x)\int_{-1}^{x} ds \int_{-1}^{s} dt P_m(t) \\
&= -B^{<}_{k,0} + \frac{2k+1}{2}\sum_{m=0}^{M}\alpha_m \int_{-1}^{1} dx P_k(x)\int_{-1}^{x} ds S_{-1,m}(s)\,, \qquad \text{(C.26a)}\\
B^{>}_{k,1} &= \frac{2k+1}{2}\sum_{m=0}^{M}\alpha_m \int_{0}^{2} dx P_k(x-1)\int_{x-1}^{1} dt P_m(t) P_1(x-t) \\
&= \frac{2k+1}{2}\sum_{m=0}^{M}\alpha_m \int_{-1}^{1} dx P_k(x)\int_{x}^{1} dt P_m(t)(x-t+1) \\
&= B^{>}_{k,0} + \frac{2k+1}{2}\sum_{m=0}^{M}\alpha_m \int_{-1}^{1} dx P_k(x)\int_{x}^{1} dt P_m(t)\int_{t}^{x} ds \\
&= B^{>}_{k,0} + \frac{2k+1}{2}\sum_{m=0}^{M}\alpha_m \int_{-1}^{1} dx P_k(x)\int_{x}^{1} ds \int_{1}^{s} dt P_m(t) \\
&= B^{>}_{k,0} + \frac{2k+1}{2}\sum_{m=0}^{M}\alpha_m \int_{-1}^{1} dx P_k(x)\int_{x}^{1} ds S_{1,m}(s)\,, \qquad \text{(C.26b)}
\end{aligned}$$

To get recursion relation of $B^{\lessgtr}_{k,1}$, we use the derivative relation of the Legendre polynomials

$$(2k+1)P_k(x) = \frac{d}{dx}[P_{k+1}(x) - P_{k-1}(x)]\,, \quad k \geq 1\,. \qquad \text{(C.27)}$$

The two integrals in Eq. C.26 can be computed with integrate by part

$$\begin{aligned}
\int_{-1}^{1} dx P_k(x) \int_{-1}^{x} ds S_{-1,m}(s) &= \frac{1}{2k+1} \int_{-1}^{1} d[P_{k+1}(x) - P_{k-1}(x)] \int_{-1}^{x} ds S_{-1,m}(s) \\
&= \frac{1}{2k+1} \left\{ [P_{k+1}(x) - P_{k-1}(x)] \int_{-1}^{x} ds S_{-1,m}(s) \right\} \Big|_{-1}^{1} \\
&- \frac{1}{2k+1} \int_{-1}^{1} dx [P_{k+1}(x) - P_{k-1}(x)] d \left[\int_{-1}^{x} ds S_{-1,m}(s) \right] \\
&= \frac{1}{2k+1} \int_{-1}^{1} dx [P_{k-1}(x) - P_{k+1}(x)] S_{-1,m}(x) \,, \qquad \text{(C.28a)} \\
\int_{-1}^{1} dx P_k(x) \int_{x}^{1} ds S_{1,m}(s) &= \frac{1}{2k+1} \int_{-1}^{1} d[P_{k+1}(x) - P_{k-1}(x)] \int_{x}^{1} ds S_{1,m}(s) \\
&= \frac{1}{2k+1} \left\{ [P_{k+1}(x) - P_{k-1}(x)] \int_{x}^{1} ds S_{1,m}(s) \right\} \Big|_{-1}^{1} \\
&- \frac{1}{2k+1} \int_{-1}^{1} dx [P_{k+1}(x) - P_{k-1}(x)] d \left[\int_{x}^{1} ds S_{1,m}(s) \right] \\
&= \frac{1}{2k+1} \int_{-1}^{1} dx [P_{k+1}(x) - P_{k-1}(x)] S_{1,m}(x) \,. \qquad \text{(C.28b)}
\end{aligned}$$

Eq. C.26 can be simplified to

$$B^{<}_{k,1} = -B^{<}_{k,0} + \frac{1}{2} \sum_{m=0}^{M} \alpha_m \int_{-1}^{1} dx [P_{k-1}(x) - P_{k+1}(x)] S_{-1,m}(x) \,, \qquad \text{(C.29a)}$$

$$B^{>}_{k,1} = B^{>}_{k,0} + \frac{1}{2} \sum_{m=0}^{M} \alpha_m \int_{-1}^{1} dx [P_{k+1}(x) - P_{k-1}(x)] S_{1,m}(x) \,. \qquad \text{(C.29b)}$$

Comparing with Eq. C.24, and address the special case $k = 0$ explicitly using Eq. C.26, we get the recursion relation for the second row of the two convolution matrices

$$B^{\lessgtr}_{k,1} = \begin{cases} \mp B^{\lessgtr}_{1,0}/3 \,, & k = 0 \\ \mp B^{\lessgtr}_{k,0} + \frac{B^{\lessgtr}_{k-1,0}}{2k-1} - \frac{B^{\lessgtr}_{k+1,0}}{2k+3} \,, & k \geq 1 \end{cases} \,. \qquad \text{(C.30)}$$

Appendix D

Spectral Function

In this appendix we introduce the relations between the spectral function and the Keldysh Green's functions, and explain the Fourier transform routine used for computing the spectral function from the retarded Green's function G^R used in section 9.6.2. All orbital related indices and the overlap matrix are omitted in this appendix.

D.1 Definition

Single-particle spectral function is given by the imaginary part of real frequency retarded or advanced Green's function

$$A(\omega) = -\frac{1}{\pi}\mathrm{Im}G^R(\omega) = \frac{1}{\pi}\mathrm{Im}G^A(\omega)\,, \tag{D.1}$$

which represents the density of single-particle excitations at energy ω of the many-body state.

In equilibrium, all Green's function components are related to the spectral function [253]

$$G(t,t') = -i\int d\omega e^{-i\omega(t-t')}A(\omega)[\theta_C(t,t') \pm f(\omega)]\,, \tag{D.2}$$

where $f(\omega) = 1/(e^{\beta\omega} \mp 1)$ is the Bose (Fermi) occupation function, $\theta_C(t,t')$ is a step function. The imaginary part of the lesser (greater) Green's function yields the density of occupied (unoccupied) states

$$\mp\mathrm{Im}G^<(\omega) = 2\pi A(\omega)f(\omega) = 2\pi N(\omega)\,, \tag{D.3}$$

$$-\mathrm{Im}G^>(\omega) = 2\pi A(\omega)[1 \pm f(\omega)]\,. \tag{D.4}$$

D.2 Folded Fourier transform

To get the imaginary part of the real frequency retarded Green's function, we define $\tilde{G}(t)$ which is the upfolded Green's function

$$\begin{aligned}\tilde{G}(t) &= G^R(t) - [G^R(-t)]^\dagger \\ &= G^R(t) - G^A(t) = G^>(t) - G^<(t)\,.\end{aligned} \tag{D.5}$$

From the symmetry relation, $\mathrm{Re}[\tilde{G}(t)]$ is odd, and $\mathrm{Im}[\tilde{G}(t)]$ is even, which gives a pure imaginary $\tilde{G}(\omega)$ after the Fourier transform. Defining $\tilde{G}(\omega) = i\tilde{g}(\omega)$, the Fourier transfrom relations can be written as

$$\mathcal{F}\{f(t)g(t)\} = f(\omega) * g(\omega)\,, \tag{D.6}$$

$$\mathcal{F}\{\theta(t)\} = \frac{1}{i\omega} + \pi\delta(\omega)\,. \tag{D.7}$$

The spectral function $A(\omega)$ obeys

$$A(\omega) = -\frac{1}{\pi}\mathrm{Im}G^R(\omega) = -\frac{1}{\pi}\mathrm{Im}[\mathcal{F}\{G^R(t)\}]\,. \tag{D.8}$$

Using $G^R(t) = i\theta(t)\tilde{g}(t)$, the spectral function can be written as

$$\begin{aligned}A(\omega) &= -\frac{1}{\pi}\mathrm{Im}[\mathcal{F}\{i\theta(t)\tilde{g}(t)\}] \\ &= -\frac{1}{\pi}\mathrm{Im}[(\frac{1}{i\omega} + \pi\delta(\omega)) * (ig(\omega))] \\ &= -\frac{1}{\pi}\mathrm{Im}[\frac{1}{\omega} * \tilde{g}(\omega) + i\pi\delta(\omega) * \tilde{g}(\omega)] \\ &= -\tilde{g}(\omega)\,.\end{aligned} \tag{D.9}$$

Bibliography

[1] P. W. Anderson, “Twenty-five Years of High-Temperature Superconductivity – A Personal Review”, Journal of Physics: Conference Series **449**, 012001 (2013).

[2] S. Wirth and F. Steglich, “Exploring heavy fermions from macroscopic to microscopic length scales”, Nature Reviews Materials **1**, 16051 (2016).

[3] Y. Tokura, “Correlated-Electron Physics in Transition-Metal Oxides”, Physics Today **56**, 50–55 (2003).

[4] A. A. Abrikosov, L. P. Gorkov, and I. Y. Dzyaloshinskii, *Methods of Quantum Field Theory in Statistical Physics* (Pergamon, 1965).

[5] J. Negele and H. Orland, *Quantum Many-Particle Systems* (Perseus Books, 1998).

[6] G. D. Mahan, *Many Particle Physics, Third Edition* (Plenum, 2000).

[7] P. Coleman, *Introduction to Many-Body Physics* (Cambridge University Press, 2015).

[8] A. Damascelli, Z. Hussain, and Z.-X. Shen, “Angle-resolved photoemission studies of the cuprate superconductors”, Rev. Mod. Phys. **75**, 473–541 (2003).

[9] M. Fujita, H. Hiraka, M. Matsuda, M. Matsuura, J. M. Tranquada, S. Wakimoto, G. Xu, and K. Yamada, “Progress in Neutron Scattering Studies of Spin Excitations in High-Tc Cuprates”, Journal of the Physical Society of Japan **81**, 011007 (2012).

[10] D. N. Basov and T. Timusk, “Electrodynamics of high-T_c superconductors”, Rev. Mod. Phys. **77**, 721–779 (2005).

[11] R. R. Jones, D. C. Hooper, L. Zhang, D. Wolverson, and V. K. Valev, “Raman Techniques: Fundamentals and Frontiers”, Nanoscale Research Letters **14**, 231 (2019).

[12] J. Hubbard and B. H. Flowers, “Electron correlations in narrow energy bands”, Proceedings of the Royal Society of London. Series A. Mathematical and Physical Sciences **276**, 238–257 (1963).

[13] J. P. F. LeBlanc, A. E. Antipov, F. Becca, I. W. Bulik, G. K.-L. Chan, C.-M. Chung, Y. Deng, M. Ferrero, T. M. Henderson, C. A. Jiménez-Hoyos, E. Kozik, X.-W. Liu, A. J. Millis, N. V. Prokof’ev, M. Qin, G. E. Scuseria, H. Shi, B. V. Svistunov, L. F. Tocchio, I. S. Tupitsyn, S. R. White, S. Zhang, B.-X. Zheng, Z. Zhu, and E. Gull (Simons Collaboration on the Many-Electron Problem), “Solutions of the Two-Dimensional Hubbard Model: Benchmarks and Results from a Wide Range of Numerical Algorithms”, Phys. Rev. X **5**, 041041 (2015).

[14] M. Qin, T. Schäfer, S. Andergassen, P. Corboz, and E. Gull, “The Hubbard model: A computational perspective”, arXiv preprint arXiv:2104.00064 (2021).

[15] A. Georges, G. Kotliar, W. Krauth, and M. J. Rozenberg, “Dynamical mean-field theory of strongly correlated fermion systems and the limit of infinite dimensions”, Rev. Mod. Phys. **68**, 13–125 (1996).

[16] T. Maier, M. Jarrell, T. Pruschke, and M. H. Hettler, “Quantum cluster theories”, Rev. Mod. Phys. **77**, 1027–1080 (2005).

[17] A. N. Rubtsov, M. I. Katsnelson, and A. I. Lichtenstein, “Dual fermion approach to nonlocal correlations in the Hubbard model”, Phys. Rev. B **77**, 033101 (2008).

[18] A. Toschi, A. A. Katanin, and K. Held, “Dynamical vertex approximation: a step beyond dynamical mean-field theory”, Phys. Rev. B **75**, 045118 (2007).

[19] M. H. Hettler, M. Mukherjee, M. Jarrell, and H. R. Krishnamurthy, “Dynamical cluster approximation: Nonlocal dynamics of correlated electron systems”, Phys. Rev. B **61**, 12739–12756 (2000).

[20] G. Kotliar, S. Y. Savrasov, G. Pálsson, and G. Biroli, “Cellular Dynamical Mean Field Approach to Strongly Correlated Systems”, Phys. Rev. Lett. **87**, 186401 (2001).

[21] N. D. Mermin and H. Wagner, “Absence of Ferromagnetism or Antiferromagnetism in One- or Two-Dimensional Isotropic Heisenberg Models”, Phys. Rev. Lett. **17**, 1133–1136 (1966).

[22] M. Caffarel and W. Krauth, “Exact diagonalization approach to correlated fermions in infinite dimensions: Mott transition and superconductivity”, Phys. Rev. Lett. **72**, 1545–1548 (1994).

[23] N. E. Bickers, “Review of techniques in the large-N expansion for dilute magnetic alloys”, Rev. Mod. Phys. **59**, 845–939 (1987).

[24] T. Pruschke and N. Grewe, “The Anderson model with finite Coulomb repulsion”, Zeitschrift für Physik B Condensed Matter **74**, 439–449 (1989).

[25] K. Haule, S. Kirchner, J. Kroha, and P. Wölfle, “Anderson impurity model at finite Coulomb interaction U: Generalized noncrossing approximation”, Phys. Rev. B **64**, 155111 (2001).

[26] E. Gull, A. J. Millis, A. I. Lichtenstein, A. N. Rubtsov, M. Troyer, and P. Werner, “Continuous-time Monte Carlo methods for quantum impurity models”, Rev. Mod. Phys. **83**, 349–404 (2011).

[27] E. Gull, P. Werner, O. Parcollet, and M. Troyer, “Continuous-time auxiliary-field Monte Carlo for quantum impurity models”, EPL (Europhysics Letters) **82**, 57003 (2008).

[28] O. Gunnarsson, T. Schäfer, J. P. F. LeBlanc, E. Gull, J. Merino, G. Sangiovanni, G. Rohringer, and A. Toschi, “Fluctuation Diagnostics of the Electron Self-Energy: Origin of the Pseudogap Physics”, Phys. Rev. Lett. **114**, 236402 (2015).

[29] R. P. Feynman, “Space-Time Approach to Non-Relativistic Quantum Mechanics”, Rev. Mod. Phys. **20**, 367–387 (1948).

[30] J. M. Luttinger and J. C. Ward, “Ground-State Energy of a Many-Fermion System. II”, Phys. Rev. **118**, 1417–1427 (1960).

[31] M. Potthoff, "Non-perturbative construction of the Luttinger-Ward functional", Condensed Matter Physics **9**, 557–567 (2006).

[32] N. E. Bickers, "Self-Consistent Many-Body Theory for Condensed Matter Systems", in *Theoretical Methods for Strongly Correlated Electrons* (Springer New York, 2004), pp. 237–296.

[33] J. F. Rentrop, V. Meden, and S. G. Jakobs, "Renormalization group flow of the Luttinger-Ward functional: Conserving approximations and application to the Anderson impurity model", Phys. Rev. B **93**, 195160 (2016).

[34] J. Li, "Diagrammatic Methods for Strongly-Correlated Electrons in Realistic Systems", PhD thesis (University of Michigan, 2021).

[35] G. Baym and L. P. Kadanoff, "Conservation Laws and Correlation Functions", Phys. Rev. **124**, 287–299 (1961).

[36] G. Baym, "Self-Consistent Approximations in Many-Body Systems", Phys. Rev. **127**, 1391–1401 (1962).

[37] L. Lin and M. Lindsey, "Variational structure of Luttinger-Ward formalism and bold diagrammatic expansion for Euclidean lattice field theory", Proceedings of the National Academy of Sciences **115**, 2282–2286 (2018).

[38] M. Srednicki, *Quantum field theory* (Cambridge University Press, 2007).

[39] P. G. de Gennes and P. A. Pincus, *Superconductivity of Metals and Alloys* (CRC Press, 1999).

[40] G. Rohringer, "New routes towards a theoretical treatment of nonlocal electronic correlations", PhD thesis (Vienna University of Technology, 2013).

[41] N. R. Poniatowski, "Superconductivity, broken gauge symmetry, and the Higgs mechanism", American Journal of Physics **87**, 436–443 (2019).

[42] G. Rohringer, A. Valli, and A. Toschi, "Local electronic correlation at the two-particle level", Phys. Rev. B **86**, 125114 (2012).

[43] A. I. Lichtenstein and M. I. Katsnelson, "Antiferromagnetism and d-wave superconductivity in cuprates: A cluster dynamical mean-field theory", Phys. Rev. B **62**, R9283–R9286 (2000).

[44] J.-X. Zhu, *Bogoliubov-de Gennes Method and Its Applications*, Lecture Notes in Physics (Springer, Cham, 2015).

[45] D. S. Tracy and R. P. Singh, "A new matrix product and its applications in partitioned matrix differentiation", Statistica Neerlandica **26**, 143–157 (1972).

[46] H. Li, C. Fang, and K. Sun, "Diagnosis of topological nodal lines with nontrivial monopole charge in the presence of rotation symmetries", Phys. Rev. B **100**, 195308 (2019).

[47] J. Cornwell, *Group Theory in Physics*, Techniques of Physics (Academic Press, 1997).

[48] F. Iachello, *Lie Algebras and Applications*, Lecture Notes in Physics (Springer Berlin, 2015).

[49] C. Itzykson and J.-B. Zuber, *Quantum Field Theory* (McGraw-Hill International Book Company, 1980).

[50] X. Dong, L. Del Re, A. Toschi, and E. Gull, “Mechanism of superconductivity in the hubbard model at intermediate interaction strength”, arXiv preprint arXiv:2205.06286 (2022).

[51] G. Kotliar and D. Vollhardt, “Strongly Correlated Materials: Insights From Dynamical Mean-Field Theory”, Physics Today **57**, 53–59 (2004).

[52] P. W. Anderson, “Localized Magnetic States in Metals”, Phys. Rev. **124**, 41–53 (1961).

[53] T. Maier, “Nonlocal Dynamical Correlations in Strongly Interacting Fermion Systems”, PhD thesis (Universität Regensburg, 2000).

[54] H. Hafermann, “Numerical Approaches to Spatial Correlations in Strongly Interacting Fermion Systems”, PhD thesis (University Hamburg, 2009).

[55] W. Metzner and D. Vollhardt, “Correlated Lattice Fermions in $d = \infty$ Dimensions”, Phys. Rev. Lett. **62**, 324–327 (1989).

[56] E. Müller-Hartmann, “Correlated fermions on a lattice in high dimensions”, Zeitschrift für Physik B Condensed Matter **74**, 507–512 (1989).

[57] K. G. Wilson, “The renormalization group: Critical phenomena and the Kondo problem”, Rev. Mod. Phys. **47**, 773–840 (1975).

[58] R. Bulla, T. A. Costi, and T. Pruschke, “Numerical renormalization group method for quantum impurity systems”, Rev. Mod. Phys. **80**, 395–450 (2008).

[59] J. E. Hirsch and R. M. Fye, “Monte Carlo Method for Magnetic Impurities in Metals”, Phys. Rev. Lett. **56**, 2521–2524 (1986).

[60] P. Werner, A. Comanac, L. de’Medici, M. Troyer, and A. J. Millis, “Continuous-Time Solver for Quantum Impurity Models”, Phys. Rev. Lett. **97**, 076405 (2006).

[61] P. Werner and A. J. Millis, “Hybridization expansion impurity solver: General formulation and application to Kondo lattice and two-orbital models”, Phys. Rev. B **74**, 155107 (2006).

[62] E. Gull, “Continuous-Time Quantum Monte Carlo Algorithms for Fermions”, PhD thesis (ETH, 2008).

[63] P. Werner, “Diagrammatic Monte Carlo simulation of quantum impurity models – weak and strong coupling approach”, Cifar-PiTP Summer School Lecture Notes (2008).

[64] A. N. Rubtsov and A. I. Lichtenstein, “Continuous-time quantum Monte Carlo method for fermions: Beyond auxiliary field framework”, Journal of Experimental and Theoretical Physics Letters **80**, 61–65 (2004).

[65] A. N. Rubtsov, V. V. Savkin, and A. I. Lichtenstein, “Continuous-time quantum Monte Carlo method for fermions”, Phys. Rev. B **72**, 035122 (2005).

[66] S. Rombouts, K. Heyde, and N. Jachowicz, “A discrete Hubbard-Stratonovich decomposition for general, fermionic two-body interactions”, Physics Letters A **242**, 271–276 (1998).

[67] S. M. A. Rombouts, K. Heyde, and N. Jachowicz, "Quantum Monte Carlo Method for Fermions, Free of Discretization Errors", Phys. Rev. Lett. **82**, 4155–4159 (1999).

[68] E. Gull, P. Staar, S. Fuchs, P. Nukala, M. S. Summers, T. Pruschke, T. C. Schulthess, and T. Maier, "Submatrix updates for the continuous-time auxiliary-field algorithm", Phys. Rev. B **83**, 075122 (2011).

[69] N. Higham, *Accuracy and Stability of Numerical Algorithms* (Society for Industrial and Applied Mathematics, 2002).

[70] D. A. Harville, *Matrix Algebra From a Statistician's Perspective* (Springer-Verlag, 1997).

[71] E. Gull and A. J. Millis, "Energetics of superconductivity in the two-dimensional Hubbard model", Phys. Rev. B **86**, 241106 (2012).

[72] M. Jarrell and J. E. Gubernatis, "Bayesian inference and the analytic continuation of imaginary-time quantum Monte Carlo data", Physics Reports **269**, 133–195 (1996).

[73] R. Levy, J. P. F. LeBlanc, and E. Gull, "Implementation of the maximum entropy method for analytic continuation", Computer Physics Communications **215**, 149–155 (2017).

[74] A. W. Sandvik, "Stochastic method for analytic continuation of quantum Monte Carlo data", Phys. Rev. B **57**, 10287–10290 (1998).

[75] I. Krivenko and M. Harland, "TRIQS/SOM: Implementation of the stochastic optimization method for analytic continuation", Computer Physics Communications **239**, 166–183 (2019).

[76] G. A. Baker and P. Graves-Morris, *Padé Approximants*, 2nd ed., Encyclopedia of Mathematics and its Applications (Cambridge University Press, 1996).

[77] K. S. D. Beach, R. J. Gooding, and F. Marsiglio, "Reliable Padé analytical continuation method based on a high-accuracy symbolic computation algorithm", Phys. Rev. B **61**, 5147–5157 (2000).

[78] J. Fei, C.-N. Yeh, and E. Gull, "Nevanlinna Analytical Continuation", Phys. Rev. Lett. **126**, 056402 (2021).

[79] X. Wang, E. Gull, L. de'Medici, M. Capone, and A. J. Millis, "Antiferromagnetism and the gap of a Mott insulator: Results from analytic continuation of the self-energy", Phys. Rev. B **80**, 045101 (2009).

[80] X. Dong, X. Chen, and E. Gull, "Dynamical charge susceptibility in the Hubbard model", Phys. Rev. B **100**, 235107 (2019).

[81] X. Dong and E. Gull, "Short-range charge fluctuations in the two-dimensional Hubbard model", Phys. Rev. B **101**, 195115 (2020).

[82] M. Fujita, H. Goka, K. Yamada, J. M. Tranquada, and L. P. Regnault, "Stripe order, depinning, and fluctuations in $La_{1.875}Ba_{0.125}CuO_4$ and $La_{1.875}Ba_{0.075}Sr_{0.050}CuO_4$", Phys. Rev. B **70**, 104517 (2004).

[83] Y. Kohsaka, C. Taylor, K. Fujita, A. Schmidt, C. Lupien, T. Hanaguri, M. Azuma, M. Takano, H. Eisaki, H. Takagi, S. Uchida, and J. C. Davis, "An Intrinsic Bond-Centered Electronic Glass with Unidirectional Domains in Underdoped Cuprates", Science **315**, 1380–1385 (2007).

[84] C. V. Parker, P. Aynajian, E. H. da Silva Neto, A. Pushp, S. Ono, J. Wen, Z. Xu, G. Gu, and A. Yazdani, "Fluctuating stripes at the onset of the pseudogap in the high-T_c superconductor $Bi_2Sr_2CaCu_2O_{8+x}$", Nature **468**, 677–680 (2010).

[85] M. J. Lawler, K. Fujita, J. Lee, A. R. Schmidt, Y. Kohsaka, C. K. Kim, H. Eisaki, S. Uchida, J. C. Davis, J. P. Sethna, and E.-A. Kim, "Intra-unit-cell electronic nematicity of the high-Tc copper-oxide pseudogap states", Nature **466** (2010).

[86] M. Hashimoto, R.-H. He, K. Tanaka, J.-P. Testaud, W. Meevasana, R. G. Moore, D. Lu, H. Yao, Y. Yoshida, H. Eisaki, T. P. Devereaux, Z. Hussain, and Z.-X. Shen, "Particle-hole symmetry breaking in the pseudogap state of Bi2201", Nature Physics **6**, 414–418 (2010).

[87] R. Daou, J. Chang, D. Leboeuf, O. Cyr-Choinière, F. Laliberté, N. Doiron-Leyraud, B. J. Ramshaw, R. Liang, D. A. Bonn, and W. N. Hardy, "Broken rotational symmetry in the pseudogap phase of a high-T_c superconductor", Nature **463**, 519–522 (2010).

[88] P. Abbamonte, E. Demler, J. S. Davis, and J.-C. Campuzano, "Resonant soft X-ray scattering, stripe order, and the electron spectral function in cuprates", Physica C: Superconductivity **481**, 15–22 (2012).

[89] J. M. Tranquada, "Stripes and superconductivity in cuprates", Physica B: Condensed Matter **407**, 1771–1774 (2012).

[90] A. M. M. Abeykoon, E. S. Bo žin, W.-G. Yin, G. Gu, J. P. Hill, J. M. Tranquada, and S. J. L. Billinge, "Evidence for Short-Range-Ordered Charge Stripes Far above the Charge-Ordering Transition in $La_{1.67}Sr_{0.33}NiO_4$", Phys. Rev. Lett. **111**, 096404 (2013).

[91] H. Jacobsen, I. A. Zaliznyak, A. T. Savici, B. L. Winn, S. Chang, M. Hücker, G. D. Gu, and J. M. Tranquada, "Neutron scattering study of spin ordering and stripe pinning in superconducting $La_{1.93}Sr_{0.07}CuO_4$", Phys. Rev. B **92**, 174525 (2015).

[92] A. M. Merritt, D. Reznik, V. O. Garlea, G. D. Gu, and J. M. Tranquada, "Nature and impact of stripe freezing in $La_{1.67}Sr_{0.33}NiO_4$", Phys. Rev. B **100**, 195122 (2019).

[93] R. Comin, R. Sutarto, F. He, E. H. da Silva Neto, L. Chauviere, A. Fraño, R. Liang, W. N. Hardy, D. A. Bonn, Y. Yoshida, H. Eisaki, A. J. Achkar, D. G. Hawthorn, B. Keimer, G. A. Sawatzky, and A. Damascelli, "Symmetry of charge order in cuprates", Nature Materials **14**, 796–800 (2015).

[94] K. Ishii, T. Tohyama, S. Asano, K. Sato, M. Fujita, S. Wakimoto, K. Tustsui, S. Sota, J. Miyawaki, H. Niwa, Y. Harada, J. Pelliciari, Y. Huang, T. Schmitt, Y. Yamamoto, and J. Mizuki, "Observation of momentum-dependent charge excitations in hole-doped cuprates using resonant inelastic x-ray scattering at the oxygen K edge", Phys. Rev. B **96**, 115148 (2017).

[95] H. Suzuki, M. Minola, Y. Lu, Y. Peng, R. Fumagalli, E. Lefrançois, T. Loew, J. Porras, K. Kummer, D. Betto, S. Ishida, H. Eisaki, C. Hu, X. Zhou, M. W. Haverkort, N. B. Brookes, L. Braicovich, G. Ghiringhelli, M. Le Tacon, and B. Keimer, "Probing the energy gap of high-temperature cuprate superconductors by resonant inelastic x-ray scattering", npj Quantum Materials **3**, 65 (2018).

[96] E. H. da Silva Neto, M. Minola, B. Yu, W. Tabis, M. Bluschke, D. Unruh, H. Suzuki, Y. Li, G. Yu, D. Betto, K. Kummer, F. Yakhou, N. B. Brookes, M. Le Tacon, M. Greven, B. Keimer, and A. Damascelli, "Coupling between dynamic magnetic and charge-order correlations in the cuprate superconductor $Nd_{2-x}Ce_xCuO_4$", Phys. Rev. B **98**, 161114(R) (2018).

[97] M. Hepting, L. Chaix, E. W. Huang, R. Fumagalli, Y. Y. Peng, B. Moritz, K. Kummer, N. B. Brookes, W. C. Lee, M. Hashimoto, T. Sarkar, J.-F. He, C. R. Rotundu, Y. S. Lee, R. L. Greene, L. Braicovich, G. Ghiringhelli, Z. X. Shen, T. P. Devereaux, and W. S. Lee, "Three-dimensional collective charge excitations in electron-doped copper oxide superconductors", Nature **563**, 374–378 (2018).

[98] H. Miao, R. Fumagalli, M. Rossi, J. Lorenzana, G. Seibold, F. Yakhou-Harris, K. Kummer, N. B. Brookes, G. D. Gu, L. Braicovich, G. Ghiringhelli, and M. P. M. Dean, "Formation of Incommensurate Charge Density Waves in Cuprates", Phys. Rev. X **9**, 031042 (2019).

[99] K. Ishii, M. Kurooka, Y. Shimizu, M. Fujita, K. Yamada, and J. Mizuki, "Charge Excitations in Nd2-xCexCuO4 Observed with Resonant Inelastic X-ray Scattering: Comparison of Cu K-edge with Cu L3-edge", Journal of the Physical Society of Japan **88**, 075001 (2019).

[100] S. Vig, A. Kogar, M. Mitrano, A. A. Husain, V. Mishra, M. S. Rak, L. Venema, P. D. Johnson, G. D. Gu, E. Fradkin, M. R. Norman, and P. Abbamonte, "Measurement of the dynamic charge response of materials using low-energy, momentum-resolved electron energy-loss spectroscopy (M-EELS)", SciPost Phys. **3**, 026 (2017).

[101] A. A. Husain, M. Mitrano, M. S. Rak, S. Rubeck, B. Uchoa, K. March, C. Dwyer, J. Schneeloch, R. Zhong, G. D. Gu, and P. Abbamonte, "Crossover of Charge Fluctuations across the Strange Metal Phase Diagram", Phys. Rev. X **9**, 041062 (2019).

[102] P. W. Anderson, "The Resonating Valence Bond State in La_2CuO_4 and Superconductivity", Science **235**, 1196–1198 (1987).

[103] D. Scalapino, "Numerical Studies of the 2D Hubbard Model", in *Handbook of high-temperature superconductivity* (Springer New York, 2007), pp. 495–526.

[104] C. Huscroft, M. Jarrell, T. Maier, S. Moukouri, and A. N. Tahvildarzadeh, "Pseudogaps in the 2D Hubbard Model", Phys. Rev. Lett. **86**, 139–142 (2001).

[105] M. Civelli and M. Capone and S. S. Kancharla and O. Parcollet and G. Kotliar, "Dynamical breakup of the fermi surface in a doped mott insulator", Phys. Rev. Lett. **95**, 106402, 106402 (2005).

[106] T. D. Stanescu and G. Kotliar, "Fermi arcs and hidden zeros of the Green function in the pseudogap state", Phys. Rev. B **74**, 125110 (2006).

[107] H. Park, K. Haule, and G. Kotliar, “Cluster Dynamical Mean Field Theory of the Mott Transition”, Phys. Rev. Lett. **101**, 186403 (2008).

[108] A. Liebsch and N.-H. Tong, “Finite-temperature exact diagonalization cluster dynamical mean-field study of the two-dimensional Hubbard model: Pseudogap, non-Fermi-liquid behavior, and particle-hole asymmetry”, Phys. Rev. B **80**, 165126 (2009).

[109] M. Ferrero, P. S. Cornaglia, L. De Leo, O. Parcollet, G. Kotliar, and A. Georges, “Pseudogap opening and formation of Fermi arcs as an orbital-selective Mott transition in momentum space”, Phys. Rev. B **80**, 064501 (2009).

[110] M. Ferrero and P. S. Cornaglia and L. De Leo and O. Parcollet and G. Kotliar and A. Georges, “Valence bond dynamical mean-field theory of doped mott insulators with nodal/antinodal differentiation”, EPL (Europhysics Letters) **85**, 57009 (2009).

[111] S. Sakai, Y. Motome, and M. Imada, “Evolution of Electronic Structure of Doped Mott Insulators: Reconstruction of Poles and Zeros of Green’s Function”, Phys. Rev. Lett. **102**, 056404 (2009).

[112] S. Sakai, Y. Motome, and M. Imada, “Doped high-T_c cuprate superconductors elucidated in the light of zeros and poles of the electronic Green’s function”, Phys. Rev. B **82**, 134505 (2010).

[113] N. Lin, E. Gull, and A. J. Millis, “Physics of the pseudogap in eight-site cluster dynamical mean-field theory: Photoemission, Raman scattering, and in-plane and c-axis conductivity”, Phys. Rev. B **82**, 045104 (2010).

[114] T. Maier, M. Jarrell, T. Pruschke, and J. Keller, “d-Wave Superconductivity in the Hubbard Model”, Phys. Rev. Lett. **85**, 1524–1527 (2000).

[115] M. Civelli, “Doping-driven evolution of the superconducting state from a doped Mott insulator: Cluster dynamical mean-field theory”, Phys. Rev. B **79**, 195113 (2009).

[116] M. Civelli, “Evolution of the Dynamical Pairing across the Phase Diagram of a Strongly Correlated High-Temperature Superconductor”, Phys. Rev. Lett. **103**, 136402 (2009).

[117] E. Gull and A. J. Millis, “Superconducting and pseudogap effects on the interplane conductivity and Raman scattering cross section in the two-dimensional Hubbard model”, Phys. Rev. B **88**, 075127, 075127 (2013).

[118] E. Gull, O. Parcollet, and A. J. Millis, “Superconductivity and the Pseudogap in the Two-Dimensional Hubbard Model”, Phys. Rev. Lett. **110**, 216405 (2013).

[119] E. Gull and A. J. Millis, “Pairing glue in the two-dimensional Hubbard model”, Phys. Rev. B **90**, 041110(R) (2014).

[120] E. Gull and A. J. Millis, “Quasiparticle properties of the superconducting state of the two-dimensional Hubbard model”, Phys. Rev. B **91**, 085116 (2015).

[121] X. Chen, J. P. F. LeBlanc, and E. Gull, “Superconducting Fluctuations in the Normal State of the Two-Dimensional Hubbard Model”, Phys. Rev. Lett. **115**, 116402 (2015).

[122] N. Lin, E. Gull, and A. J. Millis, “Two-Particle Response in Cluster Dynamical Mean-Field Theory: Formalism and Application to the Raman Response of High-Temperature Superconductors”, Phys. Rev. Lett. **109**, 106401 (2012).

[123] L. B. Ioffe and A. J. Millis, “Quantum fluctuations and the c-axis optical conductivity of high-T_c superconductors”, Phys. Rev. B **61**, 9077–9087 (2000).

[124] A. Toschi, M. Capone, and C. Castellani, “Energetic balance of the superconducting transition across the BCS Bose Einstein crossover in the attractive Hubbard model”, Phys. Rev. B **72**, 235118 (2005).

[125] A. J. Millis, A. Zimmers, R. P. S. M. Lobo, N. Bontemps, and C. C. Homes, “Mott physics and the optical conductivity of electron-doped cuprates”, Phys. Rev. B **72**, 224517 (2005).

[126] A. Comanac, L. de’Medici, M. Capone, and A. J. Millis, “Optical conductivity and the correlation strength of high-temperature copper-oxide superconductors”, Nature Physics **4**, 287–290 (2008).

[127] M. Ferrero, O. Parcollet, A. Georges, G. Kotliar, and D. N. Basov, “Interplane charge dynamics in a valence-bond dynamical mean-field theory of cuprate superconductors”, Phys. Rev. B **82**, 054502 (2010).

[128] D. Bergeron, V. Hankevych, B. Kyung, and A.-M. S. Tremblay, “Optical and dc conductivity of the two-dimensional Hubbard model in the pseudogap regime and across the antiferromagnetic quantum critical point including vertex corrections”, Phys. Rev. B **84**, 085128 (2011).

[129] A. Macridin, M. Jarrell, T. Maier, P. R. C. Kent, and E. D’Azevedo, “Pseudogap and Antiferromagnetic Correlations in the Hubbard Model”, Phys. Rev. Lett. **97**, 036401 (2006).

[130] X. Chen, J. P. F. LeBlanc, and E. Gull, “Simulation of the NMR response in the pseudogap regime of the cuprates”, Nature Communications **8**, 14986 (2017).

[131] J. P. F. LeBlanc, S. Li, X. Chen, R. Levy, A. E. Antipov, A. J. Millis, and E. Gull, “Magnetic susceptibility and simulated neutron signal in the two-dimensional Hubbard model”, Phys. Rev. B **100**, 075123 (2019).

[132] A. Sherman and M. Schreiber, “Magnetic susceptibility of the two-dimensional Hubbard model using a power series for the hopping constant”, Phys. Rev. B **76**, 245112 (2007).

[133] S. Hochkeppel, F. F. Assaad, and W. Hanke, “Dynamical-quantum-cluster approach to two-particle correlation functions in the Hubbard model”, Phys. Rev. B **77**, 205103 (2008).

[134] Y. F. Kung, E. A. Nowadnick, C. J. Jia, S. Johnston, B. Moritz, R. T. Scalettar, and T. P. Devereaux, “Doping evolution of spin and charge excitations in the Hubbard model”, Phys. Rev. B **92**, 195108 (2015).

[135] E. Gull, O. Parcollet, P. Werner, and A. J. Millis, “Momentum-sector-selective metal-insulator transition in the eight-site dynamical mean-field approximation to the Hubbard model in two dimensions”, Phys. Rev. B **80**, 245102 (2009).

[136] W. Wu, M. S. Scheurer, S. Chatterjee, S. Sachdev, A. Georges, and M. Ferrero, “Pseudogap and Fermi-Surface Topology in the Two-Dimensional Hubbard Model”, Phys. Rev. X **8**, 021048 (2018).

[137] D. Zanchi and H. J. Schulz, “Superconducting instabilities of the non-half-filled Hubbard model in two dimensions”, Phys. Rev. B **54**, 9509–9519 (1996).

[138] C. Honerkamp and M. Salmhofer, “Magnetic and Superconducting Instabilities of the Hubbard Model at the Van Hove Filling”, Phys. Rev. Lett. **87**, 187004 (2001).

[139] Y. Deng, E. Kozik, N. V. Prokofev, and B. V. Svistunov, “Emergent BCS regime of the two-dimensional fermionic Hubbard model: Ground-state phase diagram”, EPL (Europhysics Letters) **110**, 57001 (2015).

[140] T. A. Maier, M. Jarrell, T. C. Schulthess, P. R. C. Kent, and J. B. White, “Systematic Study of d-Wave Superconductivity in the 2D Repulsive Hubbard Model”, Phys. Rev. Lett. **95**, 237001 (2005).

[141] B.-X. Zheng, C.-M. Chung, P. Corboz, G. Ehlers, M.-P. Qin, R. M. Noack, H. Shi, S. R. White, S. Zhang, and G. K.-L. Chan, “Stripe order in the underdoped region of the two-dimensional Hubbard model”, Science **358**, 1155–1160 (2017).

[142] M. Qin, C.-M. Chung, H. Shi, E. Vitali, C. Hubig, U. Schollwöck, S. R. White, and S. Zhang (Simons Collaboration on the Many-Electron Problem), “Absence of Superconductivity in the Pure Two-Dimensional Hubbard Model”, Phys. Rev. X **10**, 031016 (2020).

[143] M. Aichhorn, H. G. Evertz, W. von der Linden, and M. Potthoff, “Charge ordering in extended Hubbard models: Variational cluster approach”, Phys. Rev. B **70**, 235107 (2004).

[144] C. Husemann and W. Metzner, “Incommensurate nematic fluctuations in the two-dimensional Hubbard model”, Phys. Rev. B **86**, 085113 (2012).

[145] T. Ayral, S. Biermann, and P. Werner, “Screening and nonlocal correlations in the extended Hubbard model from self-consistent combined GW and dynamical mean field theory”, Phys. Rev. B **87**, 125149 (2013).

[146] E. G. C. P. van Loon, A. I. Lichtenstein, M. I. Katsnelson, O. Parcollet, and H. Hafermann, “Beyond extended dynamical mean-field theory: Dual boson approach to the two-dimensional extended Hubbard model”, Phys. Rev. B **90**, 235135 (2014).

[147] L. Huang, T. Ayral, S. Biermann, and P. Werner, “Extended dynamical mean-field study of the Hubbard model with long-range interactions”, Phys. Rev. B **90**, 195114 (2014).

[148] E. G. C. P. van Loon, M. Schüler, M. I. Katsnelson, and T. O. Wehling, “Capturing nonlocal interaction effects in the Hubbard model: Optimal mappings and limits of applicability”, Phys. Rev. B **94**, 165141 (2016).

[149] K. J. Kapcia, S. Robaszkiewicz, M. Capone, and A. Amaricci, “Doping-driven metal-insulator transitions and charge orderings in the extended Hubbard model”, Phys. Rev. B **95**, 125112 (2017).

[150] D. Medvedeva, S. Iskakov, F. Krien, V. V. Mazurenko, and A. I. Lichtenstein, “Exact diagonalization solver for extended dynamical mean-field theory”, Phys. Rev. B **96**, 235149 (2017).

[151] M. Jiang, U. R. Hähner, T. C. Schulthess, and T. A. Maier, "*d*-wave superconductivity in the presence of nearest-neighbor Coulomb repulsion", Phys. Rev. B **97**, 184507 (2018).

[152] H. Terletska, T. Chen, J. Paki, and E. Gull, "Charge ordering and nonlocal correlations in the doped extended Hubbard model", Phys. Rev. B **97**, 115117 (2018).

[153] J. Paki, H. Terletska, S. Iskakov, and E. Gull, "Charge order and antiferromagnetism in the extended Hubbard model", Phys. Rev. B **99**, 245146 (2019).

[154] P. Pudleiner, A. Kauch, K. Held, and G. Li, "Competition between antiferromagnetic and charge density wave fluctuations in the extended Hubbard model", Phys. Rev. B **100**, 075108 (2019).

[155] M. Schüler, E. G. C. P. van Loon, M. I. Katsnelson, and T. O. Wehling, "Thermodynamics of the metal-insulator transition in the extended Hubbard model", SciPost Phys. **6**, 67 (2019).

[156] C. Nayak, "Density-wave states of nonzero angular momentum", Phys. Rev. B **62**, 4880–4889 (2000).

[157] S. Chakravarty, R. B. Laughlin, D. K. Morr, and C. Nayak, "Hidden order in the cuprates", Phys. Rev. B **63**, 094503 (2001).

[158] S. Tewari, H.-Y. Kee, C. Nayak, and S. Chakravarty, "Spin and current correlation functions in the *d*-density-wave state of the cuprates", Phys. Rev. B **64**, 224516 (2001).

[159] D. K. Morr, "Resonant Impurity States in the *d*-Density-Wave Phase", Phys. Rev. Lett. **89**, 106401 (2002).

[160] D. K. Morr, "A Hidden Order in the Cuprate Superconductors: The d-Density-Wave Phase", Journal of Superconductivity **16**, 487–490 (2003).

[161] E. Gull, M. Ferrero, O. Parcollet, A. Georges, and A. J. Millis, "Momentum-space anisotropy and pseudogaps: A comparative cluster dynamical mean-field analysis of the doping-driven metal-insulator transition in the two-dimensional Hubbard model", Phys. Rev. B **82**, 155101 (2010).

[162] J. Lin, J. Yuan, K. Jin, Z. Yin, G. Li, K.-J. Zhou, X. Lu, M. Dantz, T. Schmitt, H. Ding, H. Guo, M. P. M. Dean, and X. Liu, "Doping evolution of the charge excitations and electron correlations in electron-doped superconducting La2-xCexCuO4", npj Quantum Materials **5**, 4 (2020).

[163] O. K. Andersen, O. Jepsen, A. I. Liechtenstein, and I. I. Mazin, "Plane dimpling and saddle-point bifurcation in the band structures of optimally doped high-temperature superconductors: A tight-binding model", Phys. Rev. B **49**, 4145–4157 (1994).

[164] O. Andersen, A. Liechtenstein, O. Jepsen, and F. Paulsen, "LDA energy bands, low-energy hamiltonians, t', t'', $t_\perp$ (k), and $J_\perp$", Journal of Physics and Chemistry of Solids **56**, 1573–1591 (1995).

[165] C. Kim, P. J. White, Z.-X. Shen, T. Tohyama, Y. Shibata, S. Maekawa, B. O. Wells, Y. J. Kim, R. J. Birgeneau, and M. A. Kastner, "Systematics of the Photoemission Spectral Function of Cuprates: Insulators and Hole- and Electron-Doped Superconductors", Phys. Rev. Lett. **80**, 4245–4248 (1998).

[166] M. Z. Hasan, E. D. Isaacs, Z.-X. Shen, L. L. Miller, K. Tsutsui, T. Tohyama, and S. Maekawa, “Electronic Structure of Mott Insulators Studied by Inelastic X-ray Scattering”, Science **288**, 1811–1814 (2000).

[167] H. Hafermann, E. G. C. P. van Loon, M. I. Katsnelson, A. I. Lichtenstein, and O. Parcollet, “Collective charge excitations of strongly correlated electrons, vertex corrections, and gauge invariance”, Phys. Rev. B **90**, 235105 (2014).

[168] W. Wu, M. Ferrero, A. Georges, and E. Kozik, “Controlling Feynman diagrammatic expansions: Physical nature of the pseudogap in the two-dimensional Hubbard model”, Phys. Rev. B **96**, 041105(R) (2017).

[169] B. Arzhang, A. E. Antipov, and J. P. F. LeBlanc, “Fluctuation diagnostics of the finite-temperature quasi-antiferromagnetic regime of the two-dimensional Hubbard model”, Phys. Rev. B **101**, 014430 (2020).

[170] O. Gunnarsson, J. Merino, T. Schäfer, G. Sangiovanni, G. Rohringer, and A. Toschi, “Complementary views on electron spectra: From fluctuation diagnostics to real-space correlations”, Phys. Rev. B **97**, 125134 (2018).

[171] A. Macridin, M. Jarrell, and T. Maier, “Absence of the d-density-wave state from the two-dimensional Hubbard model”, Phys. Rev. B **70**, 113105 (2004).

[172] N. Wentzell, G. Li, A. Tagliavini, C. Taranto, G. Rohringer, K. Held, A. Toschi, and S. Andergassen, “High-frequency asymptotics of the vertex function: Diagrammatic parametrization and algorithmic implementation”, Phys. Rev. B **102**, 085106 (2020).

[173] C. Honerkamp, M. Salmhofer, and T. Rice, “Flow to strong coupling in the two-dimensional Hubbard model”, The European Physical Journal B - Condensed Matter and Complex Systems **27**, 127–134 (2002).

[174] T. D. Stanescu and P. Phillips, “Nearest-neighbor attraction stabilizes staggered currents in the two-dimensional Hubbard model”, Phys. Rev. B **64**, 220509 (2001).

[175] X. Lu, L. Chioncel, and E. Arrigoni, “Time-reversal symmetry breaking phase in the Hubbard model: A variational cluster approach study”, Phys. Rev. B **85**, 125117 (2012).

[176] J. Otsuki, H. Hafermann, and A. I. Lichtenstein, “Superconductivity, antiferromagnetism, and phase separation in the two-dimensional Hubbard model: A dual-fermion approach”, Phys. Rev. B **90**, 235132 (2014).

[177] C. Honerkamp and W. Hofstetter, “Ultracold Fermions and the SU(N) Hubbard Model”, Phys. Rev. Lett. **92**, 170403 (2004).

[178] J.-P. Ismer, I. Eremin, and D. K. Morr, “Dynamical spin susceptibility and the resonance peak in the pseudogap region of the underdoped cuprate superconductors”, Phys. Rev. B **73**, 104519 (2006).

[179] H. Yokoyama, S. Tamura, and M. Ogata, “Staggered Flux State in Two-Dimensional Hubbard Models”, Journal of the Physical Society of Japan **85**, 124707 (2016).

[180] K. Kobayashi and H. Yokoyama, “Interplay between staggered flux and d-wave superconducting states in Hubbard model”, Journal of Physics: Conference Series **871**, 012031 (2017).

[181] X. Dong, E. Gull, and A. J. Millis, "Quantifying the role of antiferromagnetic fluctuations in the superconductivity of the doped Hubbard model", arXiv preprint arXiv:2202.10577 (2022).

[182] D. J. Scalapino, J. R. Schrieffer, and J. W. Wilkins, "Strong-Coupling Superconductivity. I", Phys. Rev. **148**, 263–279 (1966).

[183] W. L. McMillan, "Transition Temperature of Strong-Coupled Superconductors", Phys. Rev. **167**, 331–344 (1968).

[184] F. Steglich, J. Aarts, C. D. Bredl, W. Lieke, D. Meschede, W. Franz, and H. Schäfer, "Superconductivity in the Presence of Strong Pauli Paramagnetism: $CeCu_2Si_2$", Phys. Rev. Lett. **43**, 1892–1896 (1979).

[185] J. G. Bednorz and K. A. Muller, "Possible high Tc superconductivity in the Ba-La-Cu-O system", Zeitschrift für Physik B Condensed Matter **64**, 189–193 (1986).

[186] Y. Maeno, H. Hashimoto, K. Yoshida, S. Nishizaki, T. Fujita, J. G. Bednorz, and F. Lichtenberg, "Superconductivity in a layered perovskite without copper", Nature **372**, 532–534 (1994).

[187] Y. Kamihara, H. Hiramatsu, M. Hirano, R. Kawamura, H. Yanagi, T. Kamiya, and H. Hosono, "Iron-Based Layered Superconductor: LaOFeP", Journal of the American Chemical Society **128**, 10012–10013 (2006).

[188] P. W. Anderson and W. F. Brinkman, "Anisotropic Superfluidity in ^{3}He: A Possible Interpretation of Its Stability as a Spin-Fluctuation Effect", Phys. Rev. Lett. **30**, 1108–1111 (1973).

[189] K. Miyake, S. Schmitt-Rink, and C. M. Varma, "Spin-fluctuation-mediated even-parity pairing in heavy-fermion superconductors", Phys. Rev. B **34**, 6554–6556 (1986).

[190] D. J. Scalapino, E. Loh, and J. E. Hirsch, "d-wave pairing near a spin-density-wave instability", Phys. Rev. B **34**, 8190–8192 (1986).

[191] D. J. Scalapino, "Superconductivity and Spin Fluctuations", Journal of Low Temperature Physics **117**, 179–188 (1999).

[192] T. A. Maier, D. Poilblanc, and D. J. Scalapino, "Dynamics of the Pairing Interaction in the Hubbard and $t-J$ Models of High-Temperature Superconductors", Phys. Rev. Lett. **100**, 237001 (2008).

[193] C. Castellani, C. Di Castro, and M. Grilli, "Non-Fermi-liquid behavior and d-wave superconductivity near the charge-density-wave quantum critical point", Zeitschrift für Physik B Condensed Matter **103**, 137–144 (1996).

[194] C. M. Varma, "Non-Fermi-liquid states and pairing instability of a general model of copper oxide metals", Phys. Rev. B **55**, 14554–14580 (1997).

[195] M. Capone, M. Fabrizio, C. Castellani, and E. Tosatti, "Strongly Correlated Superconductivity and Pseudogap Phase near a Multiband Mott Insulator", Phys. Rev. Lett. **93**, 047001 (2004).

[196] P. W. Anderson, "Is There Glue in Cuprate Superconductors?", Science **316**, 1705–1707 (2007).

[197] T. D. Stanescu, V. Galitski, and S. Das Sarma, "Orbital fluctuation mechanism for superconductivity in iron-based compounds", Phys. Rev. B **78**, 195114 (2008).

[198] T. Saito, Y. Yamakawa, S. Onari, and H. Kontani, "Revisiting orbital-fluctuation-mediated superconductivity in LiFeAs: Nontrivial spin-orbit interaction effects on the band structure and superconducting gap function", Phys. Rev. B **92**, 134522 (2015).

[199] A. I. Lichtenstein and M. I. Katsnelson, "Antiferromagnetism and d-wave superconductivity in cuprates: A cluster dynamical mean-field theory", Phys. Rev. B **62**, R9283–R9286 (2000).

[200] L.-L. W. Jie Shen Tao Tang, *Spectral methods Algorithms, Analysis and Applications*, Vol. 41, Springer Series in Computational Mathematics (Springer, 2011).

[201] E. Gull, S. Iskakov, I. Krivenko, A. A. Rusakov, and D. Zgid, "Chebyshev polynomial representation of imaginary-time response functions", Phys. Rev. B **98**, 075127 (2018).

[202] D. Poilblanc and D. J. Scalapino, "Calculation of $\Delta(\mathrm{k}, \omega)$ for a two-dimensional $t - J$ cluster", Phys. Rev. B **66**, 052513 (2002).

[203] J. Bardeen, L. N. Cooper, and J. R. Schrieffer, "Theory of Superconductivity", Phys. Rev. **108**, 1175–1204 (1957).

[204] E. W. Huang, C. B. Mendl, H.-C. Jiang, B. Moritz, and T. P. Devereaux, "Stripe order from the perspective of the Hubbard model", npj Quantum Materials **3**, 22 (2018).

[205] A. Wietek, Y.-Y. He, S. R. White, A. Georges, and E. M. Stoudenmire, "Stripes, Antiferromagnetism, and the Pseudogap in the Doped Hubbard Model at Finite Temperature", Phys. Rev. X **11**, 031007 (2021).

[206] P. Mai, S. Karakuzu, G. Balduzzi, S. Johnston, and T. A. Maier, "Intertwined spin, charge, and pair correlations in the two-dimensional Hubbard model in the thermodynamic limit", Proceedings of the National Academy of Sciences **119**, e2112806119 (2022).

[207] D. J. Scalapino, "A common thread: The pairing interaction for unconventional superconductors", Rev. Mod. Phys. **84**, 1383–1417 (2012).

[208] C. J. Halboth and W. Metzner, "*d*-Wave Superconductivity and Pomeranchuk Instability in the Two-Dimensional Hubbard Model", Phys. Rev. Lett. **85**, 5162–5165 (2000).

[209] D. Zanchi and H. J. Schulz, "Weakly correlated electrons on a square lattice: Renormalization-group theory", Phys. Rev. B **61**, 13609–13632 (2000).

[210] S. Raghu, S. A. Kivelson, and D. J. Scalapino, "Superconductivity in the repulsive Hubbard model: An asymptotically exact weak-coupling solution", Phys. Rev. B **81**, 224505 (2010).

[211] E. Fradkin, S. A. Kivelson, M. J. Lawler, J. P. Eisenstein, and A. P. Mackenzie, "Nematic Fermi Fluids in Condensed Matter Physics", Annual Review of Condensed Matter Physics **1**, 153–178 (2010).

[212] A. Allais and T. Senthil, "Loop current order and *d*-wave superconductivity: Some observable consequences", Phys. Rev. B **86**, 045118 (2012).

[213] E. Fradkin, S. A. Kivelson, and J. M. Tranquada, “Colloquium: Theory of intertwined orders in high temperature superconductors”, Rev. Mod. Phys. **87**, 457–482 (2015).

[214] F. Šimkovic, R. Rossi, and M. Ferrero, “The Weak, the Strong and the Long Correlation Regimes of the Two-Dimensional Hubbard Model at Finite Temperature”, arXiv preprint arXiv:2110.05863 (2021).

[215] T. Schaefer and A. Toschi, “How to read between the lines of electronic spectra: the diagnostics of fluctuations in strongly correlated electron systems”, Journal of Physics: Condensed Matter **33**, 214001 (2021).

[216] T. Dahm, V. Hinkov, S. V. Borisenko, A. A. Kordyuk, V. B. Zabolotnyy, J. Fink, B. Büchner, D. J. Scalapino, W. Hanke, and B. Keimer, “Strength of the spin-fluctuation-mediated pairing interaction in a high-temperature superconductor”, Nature Physics **5**, 217–221 (2009).

[217] L. Wang, G. He, Z. Yang, M. Garcia-Fernandez, A. Nag, K.-J. Zhou, M. Minola, M. L. Tacon, B. Keimer, Y. Peng, and Y. Li, “Paramagnons and high-temperature superconductivity in mercury-based cuprates”, arXiv preprint arXiv:2011.05029 (2020).

[218] H. Chu, S. Kovalev, Z. X. Wang, L. Schwarz, T. Dong, L. Feng, R. Haenel, M.-J. Kim, P. Shabestari, H. L. Phuong, K. Honasoge, R. D. Dawson, D. Putzky, G. Kim, M. Puviani, M. Chen, N. Awari, A. N. Ponomaryov, I. Ilyakov, M. Bluschke, F. Boschini, M. Zonno, S. Zhdanovich, M. Na, G. Christiani, G. Logvenov, D. J. Jones, A. Damascelli, M. Minola, B. Keimer, D. Manske, N. Wang, J.-C. Deinert, and S. Kaiser, “Fano interference of the Higgs mode in cuprate high-Tc superconductors”, arXiv preprint arXiv:2109.09971 (2021).

[219] Z.-B. Wu, D. Putzky, A. K. Kundu, H. Li, S. Yang, Z. Du, S. H. Joo, J. Lee, Y. Zhu, G. Logvenov, B. Keimer, K. Fujita, T. Valla, I. Bo žovi ć, and I. K. Drozdov, “Homogeneous superconducting gap in $\mathrm{DyBa_2Cu_3O_{7-\delta}}$ synthesized by oxide molecular beam epitaxy”, Phys. Rev. Materials **4**, 124801 (2020).

[220] T. A. Maier, M. S. Jarrell, and D. J. Scalapino, “Structure of the Pairing Interaction in the Two-Dimensional Hubbard Model”, Phys. Rev. Lett. **96**, 047005 (2006).

[221] T. A. Maier, M. Jarrell, and D. J. Scalapino, “Spin susceptibility representation of the pairing interaction for the two-dimensional Hubbard model”, Phys. Rev. B **75**, 134519 (2007).

[222] T. A. Maier, P. Staar, V. Mishra, U. Chatterjee, J. C. Campuzano, and D. J. Scalapino, “Pairing in a dry Fermi sea”, Nature Communications **7**, 11875 (2016).

[223] T. A. Maier and D. J. Scalapino, “Pairfield fluctuations of a 2D Hubbard model”, npj Quantum Materials **4**, 30, 30 (2019).

[224] M. Kitatani, T. Schäfer, H. Aoki, and K. Held, “Why the critical temperature of high-T_c cuprate superconductors is so low: The importance of the dynamical vertex structure”, Phys. Rev. B **99**, 041115 (2019).

[225] F. Krien, P. Worm, P. Chalupa, A. Toschi, and K. Held, “Spin scattering turns complex at strong coupling: the key to pseudogap and Fermi arcs in the Hubbard model”, arXiv preprint arXiv:2107.06529 (2021).

[226] B. Nagy and F. Jensen, "Basis Sets in Quantum Chemistry", in *Reviews in computational chemistry* (John Wiley and Sons, Ltd, 2017) Chap. 3, pp. 93–149.

[227] A. Szabo and N. Ostlund, *Modern Quantum Chemistry: Introduction to Advanced Electronic Structure Theory*, Dover Books on Chemistry (Dover Publications, 1996).

[228] C. C. J. Roothaan, "Self-Consistent Field Theory for Open Shells of Electronic Systems", Rev. Mod. Phys. **32**, 179–185 (1960).

[229] W. J. Hehre, R. F. Stewart, and J. A. Pople, "Self-Consistent Molecular-Orbital Methods. I. Use of Gaussian Expansions of Slater-Type Atomic Orbitals", The Journal of Chemical Physics **51**, 2657–2664 (1969).

[230] P. García-González and R. W. Godby, "Self-consistent calculation of total energies of the electron gas using many-body perturbation theory", Phys. Rev. B **63**, 075112 (2001).

[231] N. E. Dahlen and R. van Leeuwen, "Self-consistent solution of the Dyson equation for atoms and molecules within a conserving approximation", The Journal of Chemical Physics **122**, 164102 (2005).

[232] J. J. Phillips and D. Zgid, "Communication: The description of strong correlation within self-consistent Green's function second-order perturbation theory", Journal of Chemical Physics **140**, 241101 (2014).

[233] J. J. Phillips, A. A. Kananenka, and D. Zgid, "Fractional charge and spin errors in self-consistent Green's function theory", Journal of Chemical Physics **142**, 194108 (2015).

[234] A. R. Welden, A. A. Rusakov, and D. Zgid, "Exploring connections between statistical mechanics and Green's functions for realistic systems: Temperature dependent electronic entropy and internal energy from a self-consistent second-order Green's function", The Journal of Chemical Physics **145**, 204106 (2016).

[235] C. J. Bradley and A. P. Cracknell, *The Mathematical Theory of Symmetry in Solids* (Oxford University Press, 1972).

[236] M. J. Lax, *Symmetry Principles in Solid State and Molecular Physics* (John Wiley & Sons, 1974).

[237] J.-P. Serre, *Linear Representations of Finite Groups*, Graduate Texts in Mathematics (Springer New York, 1977).

[238] M. S. Dresselhaus, G. Dresselhaus, and A. Jorio, *Group Theory: Application to the Physics of Condensed Matter* (Springer Berlin, 2008).

[239] E. P. Wigner, *Gruppentheorie und ihre Anwendung auf die Quantenmechanik der Atomspektren* (Vieweg+Teubner Verlag, 1931).

[240] G. F. Koster, "Matrix Elements of Symmetric Operators", Phys. Rev. **109**, 227–231 (1958).

[241] X. Dong, D. Zgid, E. Gull, and H. U. R. Strand, "Legendre-spectral Dyson equation solver with super-exponential convergence", The Journal of Chemical Physics **152**, 134107 (2020).

[242] X. Dong, E. Gull, and H. U. R. Strand, “Excitations and spectra from equilibrium real-time Green’s function”, arXiv preprint arXiv:2206.04181 (2022).

[243] T. Matsubara, “A New Approach to Quantum-Statistical Mechanics”, Prog. Theor. Phys. **14**, 351–378 (1955).

[244] N. Blümer, “Mott-Hubbard Metal-Insulator Transition and Optical Conductivity in High Dimensions”, PhD thesis (Universität Augsburg, 2002).

[245] A.-B. Comanac, “Dynamical mean field theory of correlated electron systems: New algorithms and applications to local observables”, PhD thesis (Columbia University, 2007).

[246] D. Hügel, P. Werner, L. Pollet, and H. U. R. Strand, “Bosonic self-energy functional theory”, Phys. Rev. B **94**, 195119 (2016).

[247] A. A. Kananenka, A. R. Welden, T. N. Lan, E. Gull, and D. Zgid, “Efficient Temperature-Dependent Green’s Function Methods for Realistic Systems: Using Cubic Spline Interpolation to Approximate Matsubara Green’s Functions”, Journal of Chemical Theory and Computation **12**, 2250–2259 (2016).

[248] G. Stefanucci and R. van Leeuwen, *Nonequilibrium Many-Body Theory of Quantum Systems A Modern Introduction* (Cambridge University Press, 2013).

[249] A. Stan, N. E. Dahlen, and R. van Leeuwen, “Time propagation of the Kadanoff–Baym equations for inhomogeneous systems”, J. Chem. Phys. **130**, 224101 (2009).

[250] M. Schüler, D. Golež, Y. Murakami, N. Bittner, A. Herrmann, H. U. Strand, P. Werner, and M. Eckstein, “NESSi: The Non-Equilibrium Systems Simulation package”, Computer Physics Communications **257**, 107484 (2020).

[251] J. Kaye and D. Golež, “Low rank compression in the numerical solution of the nonequilibrium Dyson equation”, SciPost Phys. **10**, 91 (2021).

[252] F. Meirinhos, M. Kajan, J. Kroha, and T. Bode, “Adaptive Numerical Solution of Kadanoff-Baym Equations”, SciPost Phys. Core **5**, 30 (2022).

[253] H. Aoki, N. Tsuji, M. Eckstein, M. Kollar, T. Oka, and P. Werner, “Nonequilibrium dynamical mean-field theory and its applications”, Rev. Mod. Phys. **86**, 779–837 (2014).

[254] H. U. R. Strand, M. Eckstein, and P. Werner, “Beyond the Hubbard bands in strongly correlated lattice bosons”, Phys. Rev. A **92**, 063602 (2015).

[255] J. Kaye and H. U. R. Strand, “A fast time domain solver for the equilibrium Dyson equation”, arXiv preprint arXiv:2110.06120 (2021).

[256] D. C. Langreth, “Linear and Nonlinear Response Theory with Applications”, in *Linear and nonlinear electron transport in solids* (Springer US, 1976), pp. 3–32.

[257] J. C. Mason and D. C. Handscomb, *Chebyshev Polynomials* (Chapman and Hall/CRC, 2002).

[258] N. Hale and A. Townsend, “A Fast, Simple, and Stable Chebyshev–Legendre Transform Using an Asymptotic Formula”, SIAM Journal on Scientific Computing **36**, A148–A167 (2014).

[259] J. P. Boyd, *Chebyshev and Fourier Spectral Methods* (Dover Publications Inc., 2000).

[260] S. Olver, R. M. Slevinsky, and A. Townsend, “Fast algorithms using orthogonal polynomials”, Acta Numerica **29**, 573–699 (2020).

[261] L. Boehnke, H. Hafermann, M. Ferrero, F. Lechermann, and O. Parcollet, “Orthogonal polynomial representation of imaginary-time Green’s functions”, Phys. Rev. B **84**, 075145 (2011).

[262] N. Chikano, J. Otsuki, and H. Shinaoka, “Performance analysis of a physically constructed orthogonal representation of imaginary-time Green’s function”, Physical Review B **98**, 35104 (2018).

[263] N. Chikano, K. Yoshimi, J. Otsuki, and H. Shinaoka, “irbasis: Open-source database and software for intermediate-representation basis functions of imaginary-time Green’s function”, Computer Physics Communications **240**, 181–188 (2019).

[264] J. Kaye, K. Chen, and O. Parcollet, “Discrete Lehmann representation of imaginary time Green’s functions”, arXiv preprint arXiv:2107.13094 (2021).

[265] J. Li, M. Wallerberger, N. Chikano, C.-N. Yeh, E. Gull, and H. Shinaoka, “Sparse sampling approach to efficient ab initio calculations at finite temperature”, Phys. Rev. B **101**, 035144 (2020).

[266] N. Hale and A. Townsend, “An Algorithm for the Convolution of Legendre Series”, SIAM Journal on Scientific Computing **36**, A1207–A1220 (2014).

[267] T. Barthel, U. Schollwöck, and S. R. White, “Spectral functions in one-dimensional quantum systems at finite temperature using the density matrix renormalization group”, Phys. Rev. B **79**, 245101 (2009).

[268] K. J. Burns, G. M. Vasil, J. S. Oishi, D. Lecoanet, and B. P. Brown, “Dedalus: A flexible framework for numerical simulations with spectral methods”, Phys. Rev. Research **2**, 023068 (2020).

[269] Y. Saad and M. H. Schultz, “GMRES: A Generalized Minimal Residual Algorithm for Solving Nonsymmetric Linear Systems”, SIAM Journal on Scientific and Statistical Computing **7**, 856–869 (1986).

[270] L. B. Wahlbin, *Superconvergence in Galerkin Finite Element Methods*, 1st (Springer Berlin, 1995).

[271] J. H. Bramble, A. H. Schatz, V. Thomée, and L. B. Wahlbin, “Some Convergence Estimates for Semidiscrete Galerkin Type Approximations for Parabolic Equations”, SIAM Journal on Numerical Analysis **14**, 218–241 (1977).

[272] J. Douglas, T. Dupont, and M. F. Wheeler, “A Quasi-Projection Analysis of Galerkin Methods for Parabolic and Hyperbolic Equations”, Mathematics of Computation **32**, 345–362 (1978).

[273] V. Thomée, “Negative norm estimates and superconvergence in Galerkin methods for parabolic problems”, Math. Comp. **34**, 93–113 (1980).

[274] S. Adjerid, K. D. Devine, J. E. Flaherty, and L. Krivodonova, “A posteriori error estimation for discontinuous Galerkin solutions of hyperbolic problems”, Computer Methods in Applied Mechanics and Engineering **191**, 1097–1112 (2002).

[275] Q. Sun, T. C. Berkelbach, N. S. Blunt, G. H. Booth, S. Guo, Z. Li, J. Liu, J. D. McClain, E. R. Sayfutyarova, S. Sharma, S. Wouters, and G. K.-L. Chan, "PySCF: the Python-based simulations of chemistry framework", Wiley Interdisciplinary Reviews: Computational Molecular Science **8**, e1340 (2018).

[276] Q. Sun, X. Zhang, S. Banerjee, P. Bao, M. Barbry, N. S. Blunt, N. A. Bogdanov, G. H. Booth, J. Chen, Z.-H. Cui, J. J. Eriksen, Y. Gao, S. Guo, J. Hermann, M. R. Hermes, K. Koh, P. Koval, S. Lehtola, Z. Li, J. Liu, N. Mardirossian, J. D. McClain, M. Motta, B. Mussard, H. Q. Pham, A. Pulkin, W. Purwanto, P. J. Robinson, E. Ronca, E. R. Sayfutyarova, M. Scheurer, H. F. Schurkus, J. E. T. Smith, C. Sun, S.-N. Sun, S. Upadhyay, L. K. Wagner, X. Wang, A. White, J. D. Whitfield, M. J. Williamson, S. Wouters, J. Yang, J. M. Yu, T. Zhu, T. C. Berkelbach, S. Sharma, A. Y. Sokolov, and G. K.-L. Chan, "Recent developments in the PySCF program package", The Journal of Chemical Physics **153**, 024109 (2020).

[277] S. Boys and F. Bernardi, "The calculation of small molecular interactions by the differences of separate total energies. Some procedures with reduced errors", Molecular Physics **19**, 553–566 (1970).

[278] T. Van Mourik, A. K. Wilson, and T. H. Dunning, "Benchmark calculations with correlated molecular wavefunctions. XIII. Potential energy curves for He2, Ne2 and Ar2 using correlation consistent basis sets through augmented sextuple zeta", Molecular Physics **96**, 529–547 (1999).

[279] L. J. Holleboom and J. G. Snijders, "A comparison between the Moller-Plesset and Green's function perturbative approaches to the calculation of the correlation energy in the many-electron problem", The Journal of Chemical Physics **93**, 5826–5837 (1990).

[280] D. Feller, "Application of systematic sequences of wave functions to the water dimer", The Journal of Chemical Physics **96**, 6104–6114 (1992).

[281] T. Helgaker, W. Klopper, H. Koch, and J. Noga, "Basis-set convergence of correlated calculations on water", The Journal of Chemical Physics **106**, 9639–9646 (1997).

[282] R. A. Kendall, T. H. Dunning, and R. J. Harrison, "Electron affinities of the first-row atoms revisited. Systematic basis sets and wave functions", The Journal of Chemical Physics **96**, 6796–6806 (1992).

[283] D. E. Woon and T. H. Dunning, "Gaussian basis sets for use in correlated molecular calculations. III. The atoms aluminum through argon", The Journal of Chemical Physics **98**, 1358–1371 (1993).

[284] D. E. Woon and T. H. Dunning, "Gaussian basis sets for use in correlated molecular calculations. IV. Calculation of static electrical response properties", The Journal of Chemical Physics **100**, 2975–2988 (1994).

[285] D. Feller, "Application of systematic sequences of wave functions to the water dimer", The Journal of Chemical Physics **96**, 6104–6114 (1992).

[286] D. E. Woon and T. H. Dunning, "Benchmark calculations with correlated molecular wave functions. I. Multireference configuration interaction calculations for the second row diatomic hydrides", The Journal of Chemical Physics **99**, 1914–1929 (1993).

[287] D. E. Woon and T. H. Dunning, "Calculation of the electron affinities of the second row atoms: Al–Cl", The Journal of Chemical Physics **99**, 3730–3737 (1993).

[288] D. E. Woon, "Accurate modeling of intermolecular forces: a systematic Møller-Plesset study of the argon dimer using correlation consistent basis sets", Chemical Physics Letters **204**, 29–35 (1993).

[289] K. A. Peterson, R. A. Kendall, and T. H. Dunning, "Benchmark calculations with correlated molecular wave functions. II. Configuration interaction calculations on first row diatomic hydrides", The Journal of Chemical Physics **99**, 1930–1944 (1993).

[290] S. S. Xantheas and T. H. Dunning, "Theoretical studies of sulfurous species of importance in atmospheric chemistry. 1. Characterization of the mercaptooxy (HSO) and hydroxythio (SOH) isomers", The Journal of Physical Chemistry **97**, 6616–6627 (1993).

[291] D. E. Woon, "Benchmark calculations with correlated molecular wave functions. V. The determination of accurate ab initio intermolecular potentials for He2, Ne2, and Ar2", The Journal of Chemical Physics **100**, 2838–2850 (1994).

[292] D. E. Woon and T. H. Dunning, "Benchmark calculations with correlated molecular wave functions. VI. Second row A2 and first row/second row AB diatomic molecules", The Journal of Chemical Physics **101**, 8877–8893 (1994).

[293] D. E. Woon, T. H. Dunning, and K. A. Peterson, "Ab initio investigation of the N2–HF complex: Accurate structure and energetics", The Journal of Chemical Physics **104**, 5883–5891 (1996).

[294] T. van Mourik and T. H. Dunning, "Ab initio characterization of the structure and energetics of the ArHF complex", The Journal of Chemical Physics **107**, 2451–2462 (1997).

[295] K. A. Peterson and T. H. Dunning, "The CO molecule: the role of basis set and correlation treatment in the calculation of molecular properties", Journal of Molecular Structure: THEOCHEM **400**, 93–117 (1997).

[296] K. A. Peterson, A. K. Wilson, D. E. Woon, and T. H. Dunning Jr., "Benchmark calculations with correlated molecular wave functions XII. Core correlation effects on the homonuclear diatomic molecules B2-F2", Theoretical Chemistry Accounts **97**, 251–259 (1997).

[297] O. J. Backhouse, M. Nusspickel, and G. H. Booth, "Wave Function Perspective and Efficient Truncation of Renormalized Second-Order Perturbation Theory", Journal of Chemical Theory and Computation **16**, 1090–1104 (2020).

[298] T. Koopmans, "Über die Zuordnung von Wellenfunktionen und Eigenwerten zu den Einzelnen Elektronen Eines Atoms", Physica **1**, 104–113 (1934).

[299] N. E. Dahlen, A. Stan, and R. Leeuwen, "Nonequilibrium Green function theory for excitation and transport in atoms and molecules", J. Phys.: Conf. Ser. **35**, 324–339 (2006).

[300] N. E. Dahlen, R. van Leeuwen, and A. Stan, "Propagating the Kadanoff-Baym equations for atoms and molecules", J. Phys.: Conf. Ser. **35**, 340–348 (2006).

[301] E. Perfetto and G. Stefanucci, “Some exact properties of the nonequilibrium response function for transient photoabsorption”, Phys. Rev. A **91**, 033416 (2015).

[302] E. Perfetto, A.-M. Uimonen, R. van Leeuwen, and G. Stefanucci, “First-principles nonequilibrium Green’s-function approach to transient photoabsorption: Application to atoms”, Phys. Rev. A **92**, 033419 (2015).

[303] F. Krausz and M. Ivanov, “Attosecond physics”, Rev. Mod. Phys. **81**, 163–234 (2009).

[304] D. W. Smith and O. W. Day, “Extension of Koopmans’ theorem. I. Derivation”, The Journal of Chemical Physics **62**, 113–114 (1975).

[305] O. W. Day, D. W. Smith, and R. C. Morrison, “Extension of Koopmans’ theorem. II. Accurate ionization energies from correlated wavefunctions for closed-shell atoms”, The Journal of Chemical Physics **62**, 115–119 (1975).

[306] R. C. Morrison, O. W. Day, and D. W. Smith, “An extension of Koopmans’ theorem III. ionization energies of the open-shell atoms Li and B”, International Journal of Quantum Chemistry **9**, 229–235 (1975).

[307] J. C. Ellenbogen, O. W. Day, D. W. Smith, and R. C. Morrison, “Extension of Koopmans’ theorem. IV. Ionization potentials from correlated wave functions for molecular fluorine”, The Journal of Chemical Physics **66**, 4795–4801 (1977).

[308] D. M. Chipman, “Methods for the calculation of photoionization cross sections using the extended Koopmans’ theorem”, International Journal of Quantum Chemistry **12**, 365–377 (1977).

[309] D. Vanfleteren, D. Van Neck, P. W. Ayers, R. C. Morrison, and P. Bultinck, “Exact ionization potentials from wave function asymptotics: The extended Koopmans’ theorem, revisited”, The Journal of Chemical Physics **130**, 194104 (2009).

[310] A. Stan, N. E. Dahlen, and R. v. Leeuwen, “Fully self-consistent GW calculations for atoms and molecules”, Europhysics Letters **76**, 298–304 (2006).

[311] A. R. Welden, J. J. Phillips, and D. Zgid, “Ionization potentials and electron affinities from the extended Koopmans’ theorem in self-consistent Green’s function theory”, arXiv preprint arXiv:1505.05575 (2015).

[312] M. Schüler and Y. Pavlyukh, “Spectral properties from Matsubara Green’s function approach: Application to molecules”, Phys. Rev. B **97**, 115164 (2018).

[313] R. D. Johnson, “NIST Computational Chemistry Comparison and Benchmark Database”, NIST Standard Reference Database Number 101, `10.18434/T47C7Z` (2020).

[314] L. Gallandi, N. Marom, P. Rinke, and T. Körzdörfer, “Accurate ionization potentials and electron affinities of acceptor molecules ii: non-empirically tuned long-range corrected hybrid functionals”, Journal of Chemical Theory and Computation **12**, 605–614 (2016).

[315] O. J. Backhouse and G. H. Booth, “Efficient Excitations and Spectra within a Perturbative Renormalization Approach”, Journal of Chemical Theory and Computation **16**, 6294–6304 (2020).

[316] D. Dougherty and S. P. McGlynn, “Photoelectron spectroscopy of carbonyls. 1,4-Benzoquinones”, Journal of the American Chemical Society **99**, 3234–3239 (1977).

[317] Q. Fu, J. Yang, and X.-B. Wang, “On the Electronic Structures and Electron Affinities of the m-Benzoquinone (BQ) Diradical and the o-, p-BQ Molecules: A Synergetic Photoelectron Spectroscopic and Theoretical Study”, The Journal of Physical Chemistry A **115**, 3201–3207 (2011).

[318] Y. Katznelson, *An Introduction to Harmionic Analysis* (Dover Publications, 1976).